Technische Universität München

Physik-Department, Institut E21

Forschungs-Neutronenquelle Heinz Maier-Leibnitz (FRM II)

Neutron Depolarisation Measurements of Ferromagnetic Quantum Phase Transitions

&

Wavelength-Frame Multiplication Chopper System for the Imaging Instrument ODIN at the ESS

Dipl.-Phys. Univ. Philipp Schmakat

Vollständiger Abdruck der von der
Fakultät für Physik der Technischen Universität München
zur Erlangung des akademischen Grades eines

Doktors der Naturwissenschaften (Dr. rer. nat.)

genehmigten Dissertation.

Vorsitzender:		Univ.-Prof. Dr. Martin Zacharias
Prüfer der Dissertation:	1.	Univ.-Prof. Dr. Peter Böni
	2.	Univ.-Prof. Dr. Winfried Petry

Die Dissertation wurde am 08.10.2015 an der Technischen Universität München eingereicht
und durch die Fakultät für Physik am XX.XX.2015 angenommen.

Contents

Abstract

The thesis at hand consists of two projects. In the first part, the three weakly ferromagnetic systems $CePd_{1-x}Rh_x$, $ZrZn_2$ and $Fe_{1-x}Cr_x$ were investigated. These systems undergo different kinds of ferromagnetic quantum phase transitions. For this study, most of the experiments were performed using a newly designed set up for neutron depolarisation measurements at the beam lines ANTARES and MIRA as well as POLI-HEIDI at the research neutron source Heinz Maier-Leibnitz (FRM II). By using the newly designed set up, the depolarisation technique enables to investigate the phase diagrams of weakly ferromagnetic systems as a function of the most crucial parameters in the context of quantum phase transitions which are hydrostatic pressure and an external magnetic field at lowest temperatures. Thereby, in particular the spatially resolved measurements, obtained at the neutron-imaging instrument ANTARES, provide important insights when studying the effects of these external parameters on a sample.

As an independent project that is reported in the second part of this thesis, a so-called wavelength-frame multiplication (WFM) chopper-system was designed and optimised using Monte Carlo simulations. The optimised chopper-system is foreseen to be installed at the future multi-purpose neutron-imaging instrument ODIN at the European Spallation Source (ESS). At the ESS, this type of chopper-system will offer large gain factors compared to continuous neutron sources. Considering wavelength-dependent experiments and compared to continuous neutron sources it will allow significantly shorter measuring times or provide additional information without further effort. As an example, the neutron depolarisation technique could be adapted to the instrument design, and benefit from both, the spectral properties and the time-structure as well as from the spatial resolution.

Kurzfassung

Die vorliegende Arbeit umfasst zwei Projekte. Im ersten Teil der Arbeit wurden die drei schwach ferromagnetischen Systeme $CePd_{1-x}Rh_x$, $ZrZn_2$ und $Fe_{1-x}Cr_x$ untersucht. In diesen Systemen können unterschiedliche Arten von Quantenphasenübergängen beobachtet werden. Die meisten Experimente im Rahmen dieser Studie wurden mithilfe eines neu entworfenen Aufbaus für Neutronen-Depolarisationsmessungen an den Instrumenten ANTARES und MIRA sowie POLI-HEIDI an der Forschungs-Neutronenquelle Heinz Maier-Leibnitz (FRM II) durchgeführt. Depolarisationsmessungen mit Neutronen ermöglichen es, die Phasendiagramme schwach ferromagnetischer Materialien zu untersuchen. Insbesondere der Einfluss hydrostatischen Drucks und externer Magnetfelder spielen hierbei eine wichtige Rolle und können mithilfe des neuen Aufbaus bei tiefsten Temperaturen untersucht werden. Insbesondere die hohe Ortsauflösung, welche am Neutron-Imaging Instrument ANTARES erzielt werden kann, liefert dabei wichtige Einblicke in die Effekte dieser externen Parameter auf eine Probe.

Ein davon unabhängiges Projekt wird im zweiten Teil dieser Arbeit beschrieben. In dieser Studie wurde ein sogenanntes "Wavelength-Frame Multiplication" (WFM) Chopper-System entworfen und mithilfe von Monte Carlo Simulationen optimiert. Das optimierte Chopper-System ist für den Einsatz am zukünftigen Neutron-Imaging Instrument ODIN, spezialisiert auf bildgebende Messverfahren mit Neutronen, an der Europäischen Spallationsquelle (ESS) vorgesehen. Das spezielle Chopper-System wird an der ESS insbesondere bei wellenlängen-abhängigen Experimenten und verglichen mit kontinuierlichen Neutronenquellen deutlich geringere Messzeiten erlauben oder erweiterte Informationen ohne zusätzlichen Aufwand liefern. Beispielsweise könnte der Aufbau für Depolarisationsmessungen an das Instrument-Konzept angepasst werden, wodurch sowohl von den spektralen Eigenschaften und der Zeitstruktur als auch von der Ortsauflösung profitiert werden kann.

List of Abbreviations

List I. Abbreviations used in Part I of this thesis.

AFM	antiferromagnetism, antiferromagnetic
CG	cluster-glass
FC	field-cooling
FM	ferromagnetism, ferromagnetic
FWHM	full width at half of the maximum
HFC	high-field-cooling
MIEZE	modulation of intensity with zero effort
MFL	marginal Fermi liquid
MM	meta-magnetism, meta-magnetic
PM	paramagnetism, paramagnetic
PPMS	Physical Property Measurement System
QCP	quantum critical point
QPT	quantum phase transition
RKKY	Ruderman-Kittel-Kasuya-Yosida
SANS	small angle neutron scattering
SC	superconductivity, superconducting
SDW	spin-density wave
SG	spin-glass
VSM	vibrating-sample magnetometer
ZFC	zero-field-cooling

List II. Abbreviations used in Part II of this thesis.

BP	band-pass
BPC	BP chopper
ESS	European Spallation Source
FO	frame-overlap
FOC	FO chopper
ODIN	multi-purpose imaging instrument to be build at ESS
WFM	wavelength-frame multiplication
WFMC	WFM chopper

Part I.

Neutron Depolarisation Measurements of Ferromagnetic Quantum Phase Transitions

1. Motivation For This Study

Ferromagnetism is a quantum effect which may be fundamentally explained by the electronic correlations of spins underlying the Pauli principle. The interactions between the spins may be mediated by direct exchange or indirectly for example via the RKKY interaction [1, 2]. The interactions can therefore be controlled in different ways which is of scientific as well as technological interest. The most obvious control parameter which allows to tune a system from magnetically ordered to a paramagnetic state is the temperature T. In a classical Ginzburg-Landau description the phase transition is accompanied by a change of the order parameter which takes a non-zero value below a critical value of the control parameter and is zero above this value [3, 4]. For ferromagnetic systems the magnetisation M is used as the order parameter which is zero above the Curie temperature T_C and takes a finite value below T_C. The symmetry of the system is thereby broken at the transition from the disordered to the ordered phase.

Magnetic phase transitions can be controlled by other parameters than temperature. A non-thermal control parameter such as hydrostatic pressure p, an external field B, or the concentration x of a ligand in a material can as well be used to drive a phase transition. Typically this has an effect on the overlap of the electron wave functions and consequently on the band structure. Thereby for example the ordering temperature can be influenced or the type of order can be altered. More generally one may also expect the occurrence of other correlation effects such as superconductivity to occur at lowest temperatures. Interestingly, such a transition should in principle even occur at zero temperature when using a non-thermal control parameter, which is not only an academic detail as discussed in a number of studies [5–9]. It is reasonable to conclude that such phase transitions might not be driven by thermal fluctuations alone. Instead, quantum statistical fluctuations (e.g. tunnelling-processes between two or more degenerate ground states) were considered as a mechanism to drive the phase transition and thereby the system into the new ground state [10, 11].

A magnetic phase transition at zero temperature is commonly referred to as Quantum Phase Transition (QPT). The point in the magnetic phase diagram where the transition temperature is continuously suppressed to $T_C = 0$ is referred to as Quantum Critical Point (QCP). In established theory such a QCP is thereby always connected to a second-order phase transition. Although this transition occurs at $T = 0$ it has significant influence on the properties at finite temperatures. An exemplary magnetic phase diagram describing such a QPT is sketched in Fig. 1.1a. In this case pressure p

drives the QPT at zero temperature $T = 0$ where the ground state transforms from ferromagnetic to paramagnetic. In the illustrated case the application of a magnetic field B supports the phase transition as it already reduces the symmetry of the system.

Recent discoveries in ferromagnetic (FM) as well as antiferromagnetic (AFM) systems which undergo a QPT have attracted a lot of interest. In many AFM systems it was observed that not only the ordering temperature could be suppressed but new exotic phases emerge under certain conditions in systems that are tuned towards a QCP [12–25]. The high-T_c superconductors are possibly the most prominent example among these systems where the exotic properties are observed at ambient pressure. However, also in several heavy fermion systems under applied pressure a superconducting phase was observed before suppressing the ordering temperature to zero thereby covering a putative QCP at lowest temperatures. An interesting observation was the continuity of the QPT of several AFM systems as is depicted in the phase diagram sketched in Fig. 1.1b. From the theoretical side the continuous QPT is not surprising however the emergence of exotic new phases such as superconductivity still is. Furthermore, the observed behaviour well above a putative QCP is often puzzling. Intuitively, one might expect a paramagnetic (PM) phase if T_C is suppressed to $T = 0$, however a modulated spin structure or spin-glass behaviour is often found instead, which yet cannot be explained in a unified framework.

Puzzling behaviour is also found in a large number of FM systems. For weak itinerant ferromagnets in the vicinity of a putative QCP, where T_C is suppressed by a non-thermal parameter, established theories fail to predict the most fundamental properties such as the electrical transport properties and the order of the magnetic phase transitions [26–38]. Prominent examples here include $Sr_3Ru_2O_7$ where a spin nematic phase at high magnetic fields develops accompanied by two distinct types of spin density wave (SDW) order. In some systems such as $Nb_{1-x}Fe_{2+x}$ disorder effects were found to play a significant role, however, even here a SDW phase was suggested to cover the critical regime in the phase diagram. Among the FM heavy fermion systems UGe_2 is probably the most prominent example for exotic behaviour. Here, two subsequent FM regimes were observed under hydrostatic pressure, which cover a superconducting phase at lowest temperatures.

The observed peculiarities in the vicinity of FM QPTs underscore the importance of further investigations from both theoretical and experimental side. Established theories predict a continuous suppression of the ordering temperature to zero as illustrated in Fig. 1.1a. However, this has not been unambiguously observed for any highest-purity single-crystalline ferromagnetic systems so far. Instead, there is strong evidence that only rather diluted or less pure samples show such a continuous transition and in this sense a "conventional" QCP. In clean (high-quality) samples the FM order seems to vanish always with a first-order transition at a finite temperature at a so-called tri-critical point. Inspired by this observation, several more recent theories include this

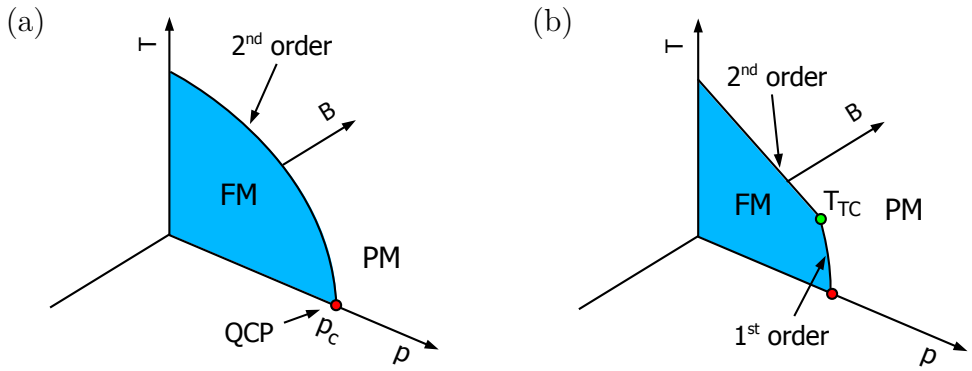

Figure 1.1.: (a) Magnetic phase diagram showing the ordering temperature T_C as function of the control parameter p and an applied magnetic field B as predicted by simple mean-field theories for weakly FM systems. The QPT is a continuous second-order phase transition which ends in a QCP at $T = 0$. (b) Generic phase diagram as predicted by more recent theories and supported by experiment. In homogeneous metallic ferromagnets the QPT is expected to be second-order up to a tri-critical point T_{TC}. For larger values of the tuning parameter p the ordering temperature is suppressed rapidly in a first-order transition and the sample takes a PM state.

feature naturally. In such theories it is argued that the FM QPT in a clean ferromagnetic sample is generically a first-order transition above a tri-critical point [9, 39, 40] as is depicted in Fig. 1.1b. Above the tri-critical point the ordering temperature is reduced more or less abruptly to $T = 0$.

The reason for this generic behaviour is a coupling of the magnetisation fluctuations to other electronic degrees of freedom which are referred to as soft-modes. In metallic systems these soft-modes are electron-hole excitations about the Fermi surface at low temperatures that are always present. As a consequence there should be generically a tri-critical point separating the regime of second-order and first-order phase transitions. As pointed out by [41, 42] the observation of the tri-critical point in their model implies the existence of a meta-magnetic (MM) transition as a function of external magnetic field above the tri-critical point. This transition line starts at the tri-critical point in zero field and terminates at a QCP at finite field. An important study by [43] showed that impurities or weak disorder effects may lower this tri-critical point eventually to zero temperature hence producing a second-order QPT or in other words a conventional QCP. Strong disorder may ultimately smear out even the second-order QPT [44, 45]. Interestingly, there are other theoretical approaches which as well predict a first-order QPT inferring a tri-critical point in clean systems [46–48]. In these models a particular change in the band structure leads to the tri-critical point. Instead of the generically expected meta-magnetic transitions, here, the emergence of completely new phases including superconductivity, spin-spiral or nematic phases is predicted. These phases are found just above the tri-critical point and thereby separate

the homogeneous FM and the PM phase.

The verification of the proposed models is a challenge for the experimentalist. This task requires to map out the magnetic phase diagrams of representative model systems using high-quality samples. In particular the phase transition needs to be tuned as a function of a non-thermal control parameter such as hydrostatic pressure or magnetic field. As the characteristic effects are expected to occur at rather low temperatures and high pressure the critical region of the phase diagram is difficult to investigate experimentally. Sample materials close to criticality need to be produced with sufficient purity. The application of hydrostatic pressure together with the unambiguous identification of weak FM order at low temperatures present further difficulties.

In this study the power of the neutron depolarisation technique is demonstrated which is used to address the scientific problem of whether FM order exists in selected materials in the critical regime of the magnetic phase diagram. As neutrons do not carry a net electric charge they interact much weaker with matter compared to electrons or positrons. However, they do carry a spin which interacts with magnetic order. Neutrons hence represent an ideal probe for the measurement of magnetic properties on the microscopic scale. While neutron scattering experiments are used to investigate reciprocal space e.g. wave vector dependent properties [49, 50], neutron transmission experiments enable to investigate properties of the sample in direct space [51]. The neutron spin is affected as well either by scattering off a magnetic moment in the sample or in transmission by interaction with local magnetic fields in the sample. Both processes deliver valuable information on the magnetic properties of a material. In scattering experiments with polarised neutrons both ferromagnetic and antiferromagnetic properties such as the spin arrangement or the spin dynamics may be investigated. In transmission experiments with polarised neutrons more specifically the ferromagnetic order in a sample can be investigated directly on a microscopic scale by evaluating the polarisation of the neutron beam [52, 53]. A signature of ferromagnetic order is a degradation of the polarisation which is caused either by a rotation of the polarisation vector away from the analysed direction or by depolarisation. A depolarisation of the neutron beam occurs if a ferromagnetic domain structure in a sample is traversed. The amount of depolarisation is connected to the microscopic properties B and δ, the magnetic flux density per domain and the average domain length in the transmitted direction, respectively. It should be emphasized that this technique does not probe the total average magnetisation such as a magnetometer but probes the internal magnetic field per domain averaged along a given path through the sample.

By using state-of-the-art technical equipment the neutron depolarisation technique enables to investigate FM samples of dimensions down to a few hundred micrometers. By using neutrons in the thermal and cold spectrum FM order on a time scale down to a few hundred nanoseconds and on a length scale of FM domains of the order of micrometers is observable as will be discussed. A particular motivation for our

neutron studies were recent results achieved with polarised neutron experiments as reported in [54–62]. The high sensitivity on FM order at both small length scales and small time scales promotes the depolarisation technique as a tool to track FM QPTs.

Three weakly FM systems $CePd_{1-x}Rh_x$, $ZrZn_2$ and $Fe_{1-x}Cr_x$ were investigated in this study which undergo different kinds of QPTs. In all cases the type of (FM) order of the underlying phase at low temperatures and in the critical regime is ambiguous regarding earlier studies. In order to address this aspect and to explore the different phase diagrams in more detail the neutron depolarisation technique was used. Conventional laboratory techniques such as susceptibility and magnetisation measurements on the samples were used to complement the neutron measurements. The main results of this study may be summarised as follows:

- In $CePd_{1-x}Rh_x$ a QPT occurs driven by chemical substitution [63, 64]. In this study a series of four samples with varying Rh content in the critical regime $x = 0.40$ to 0.80 of the phase diagram was investigated. The FM transition temperature is lowered with increasing x. Although the QPT was reported to be continuous the type of ordering on the border to PM is ambiguous [65, 66]. Furthermore, the samples are expected to show intrinsic disorder effects. At a critical concentration $x_c = 0.60$ the curvature of the phase boundary $T_C(x)$ changes sign. We have investigated two samples below and two samples above x_c. In all samples a depolarisation was found in very good agreement with published phase diagrams verifying the FM nature of the ground state. Additionally, we have investigated the samples using different magnetic field histories. A glassy behaviour was observed above x_c that develops with increasing x and is reminiscent of re-entrant spin-glasses [67, 68]. Previous studies have already suggested that a cluster glass state may form at intermediate Rh content [69]. From the difference in field-cooling and zero-field-cooling together with the fact that a depolarisation exists even in nearly zero field we conclude that FM ordered clusters evolve from the FM domains during this particular QPT which further dissolve until a spin-glass state is reached. This transition occurs continuously and ends in a non-magnetic state.

- In $ZrZn_2$ the QPT was tracked as a function of hydrostatic pressure p using a Cu:Be pressure cell. The transition temperature is reduced with increasing pressure and a first-order transition at $p_c = 16.5$ kbar was reported where the FM order vanishes [70, 71]. Small magnetic fields are sufficient to recover the phase transition which is referred to as a meta-magnetic (MM) transition. With increasing pressure the field where the phase transition occurs also increases. In this study four different pressures were applied up to $p = 18.2$ kbar. Above the nominal critical pressure a depolarisation was observed in nearly zero field which is enhanced by small applied magnetic fields. In our magnetisation measurements a MM transition was observed above p_c in agreement with earlier studies. This

indicates a partially FM state just above the critical pressure on the length and time scale which is probed by the neutron depolarisation technique. The observed FM signature may be the explanation for the $\rho = \rho_0 + AT^{3/2}$ non-Fermi liquid behaviour of the resistivity reported in independent studies [72–74]. According to this investigation the ground state is at least partially FM at p_c and also just above p_c, otherwise no depolarisation would be observed. The MM transition found in earlier studies may in this light actually be a reconfiguration of the spin (or domain) structure which prevails dominantly ferromagnetic behaviour.

- The system $Fe_{1-x}Cr_x$ undergoes another peculiar QPT on its path from pure Cr to pure Fe through chemical substitution measured using the Cr content x. In this transition the ground state changes from itinerant FM on the Fe-rich side to itinerant AFM on the Cr-rich side of the phase diagram [75–77]. In between a spin-glass region is found which is hiding a putative QCP. In this study the critical regime was investigated using eight samples in the range of x from 0.78 to 0.85. The neutron depolarisation technique was used to probe the FM contribution to the observed phases. For the highest Cr content $x = 0.78$ that was investigated a significantly broadened FM transition around 150 K was found. The intermediate concentrations show a second transition to a highly hysteretic phase reminiscent again of re-entrant spin-glasses. The underlying phase is still FM since the depolarisation is further increased below the second transition temperature. The depolarisation signature in zero external field vanishes for $x = 0.85$ where AFM nominally sets in. Interestingly, the glassy transition is still observed in the depolarisation measurements. The measurements indicate a strongly disordered state and suggest electronic phase separation on a small length scale where FM and AFM order coexists.

In all of the three investigations the neutron depolarisation technique has proven particularly useful as it enables to investigate the effect of the most crucial parameters such as pressure and magnetic field at lowest temperatures. In this study it has become clear that the technique provides a valuable tool on the route towards a better understanding of QPTs in FM materials due to the unique opportunity to interpret FM signatures spatially resolved.

The following Chapter 2 gives a more detailed introduction to FM QPTs. Sec. 2.1 gives an overview on theoretical and experimental developments in the field of QPTs. A brief overview on escape routes from conventional quantum criticality as observed in experiments and as predicted from more recent theories is given. In Sec. 2.2 the results from the conventional Ginzburg-Landau approach are summarised which describe the basic magnetic properties that are interpreted in this study. In Chapter 3 the mathematical requirements to prepare and to interpret neutron depolarisation experiments on materials that undergo a QPT are discussed. Sec. 3.1 describes details related to the set up used for measurements with polarised neutrons. Sec.

3.2 gives a review on the theory of neutron depolarisation in ferromagnets followed by newly developed methods to analyse our depolarisation data. Chapter 4 presents the experimental details and the corresponding parameters used on the different instruments in this study. The sample preparation and characterisation is described in Sec. 4.1. The technical details for the application and determination of pressure using a Cu:Be pressure cell are given in Sec. 4.2. The laboratory techniques used in this study are summarised in Sec. 4.3 while neutron instrumentation is described in Sec. 4.4. The three materials $CePd_{1-x}Rh_x$, $ZrZn_2$ and $Fe_{1-x}Cr_x$ that were investigated in this study are described separately in the Chapters 5, 6 and 7. For each material a state-of-the-art overview is given followed by the experimental findings from this study and an interpretation of the data in the context of recent theoretical predictions. Chapter 8 represents a summary of the first part of this thesis including an outlook to future studies in this field of research.

2. Ferromagnetic Quantum Phase Transitions

In elementary ferromagnets (FMs) such as iron, nickel or cobalt as well as in ferromagnetic transition metals a spontaneous magnetisation is possible due to a splitting of the corresponding electron bands. In these metallic systems the electrons can be regarded as more or less delocalised from the crystal lattice. As the spin density may vary spatially and temporally this type of magnetism is also referred to as itinerant electron magnetism. In order to understand the key features of the magnetic phase diagram of such systems it is reasonable to investigate rather weak FMs which are characterised by a low ordering temperature of only up to several tens of Kelvin. Weak itinerant FMs are often found close to a magnetic instability. The term "close" implies that the Curie temperature can be suppressed significantly e.g. by application of only a few kbar of hydrostatic pressure or by altering the chemical composition by only a few percent. The pressure p and the chemical composition x may hence be regarded as tuning parameters other than temperature that can drive a system from the FM state to a paramagnetic (PM) state. In the thermodynamic sense pressure plays the role of a control parameter in the equation of state. When driving a system from FM to PM by using such a non-thermal control parameter the phase transition is usually referred to as Quantum Phase Transition (QPT).

The following sections shortly review and summarise the theoretical basics on FM QPTs. In Sec. 2.1 the basics on QPTs are summarised. Deviations from theoretical predictions and experimentally observed escape routes from conventional quantum criticality are discussed. In Sec. 2.2 a general description of weak itinerant FMs is discussed. In Sec. 2.2.1 a short review of the Ginzburg-Landau approach for the Stoner model is given. In Section 2.2.2 the phenomenological Ginzburg-Landau approach often referred to as spin fluctuation theory is described which includes the effect of fluctuations of the magnetisation.

2.1. Quantum Phase Transitions

As discussed above temperature is not the only control parameter that may be used to drive a magnetic phase transition. Pressure is an important example, which can be used as a non-thermal parameter to tune an electron system from one ground state to another. In theory, this tuning process is even possible at zero temperature where only zero-point fluctuations are present. Altering a system by using a tuning parameter such as pressure hence suggests that the entire phase transition cannot be due to thermal fluctuations only, but may be driven by quantum mechanical fluctuations between the degenerate ground states. Therefore, such a transition is usually referred to as QPT. This kind of physics is not captured in the simple Ginzburg-Landau approach and requires different techniques of which the first one was realised and applied by Hertz [10].

The order parameter M (the magnetisation of a FM system) as function of the control parameter x (e.g. pressure) is illustrated in Fig. 2.1 (adapted from Ref. [8]). In addition, the free energy F as a function of the order parameter M is shown. The upper panels correspond to a first-order QPT as a function of the tuning parameter x. The lower panels correspond to a continuous and hence second-order QPT in x. The free energy as function of M changes its shape when x is tuned.

For a first-order QPT two local minima exist in the free energy. Tuning x through the phase transition at x_c changes the shape such that below x_c a finite magnetisation M_0 different from zero is favourable for the system. Directly at x_c both ground states are equally favourable and above x_c the PM state is assumed. An energy barrier exists separating the two states. In order to overcome the energy barrier an additional amount of energy (latent heat) must be added to the system before the phase transition occurs. As a consequence the magnetisation changes discontinuously as soon as the energy has been added.

In the case of a second-order QPT the free energy is altered in a different way. Below x_c a global minimum at finite M_0 is found, clearly defining the FM ground state. However, it smoothly transforms into a broad minimum at $x = x_c$ virtually covering a range of possible order parameter states from zero up to some finite magnetisation. Above x_c the minimum has changed its location where the order parameter is zero e.g. the PM state is reached. The transition of the order parameter $M(x)$ is hence continuous and of second-order type and more importantly this phase transition is also expected to occur for $T \to 0$. The transition can therefore not be driven by thermal fluctuations alone. Instead it may be driven by quantum mechanical fluctuations (zero-point fluctuations) between the ground states. The true ground state at x_c may then represent a superposition of several ground states. In this regime of the phase diagram interesting and yet unexplored physics may consequently be expected. In a second-order QPT the point in the phase diagram where the tuning parameter takes

the value x_c is referred to as Quantum Critical Point (QCP).

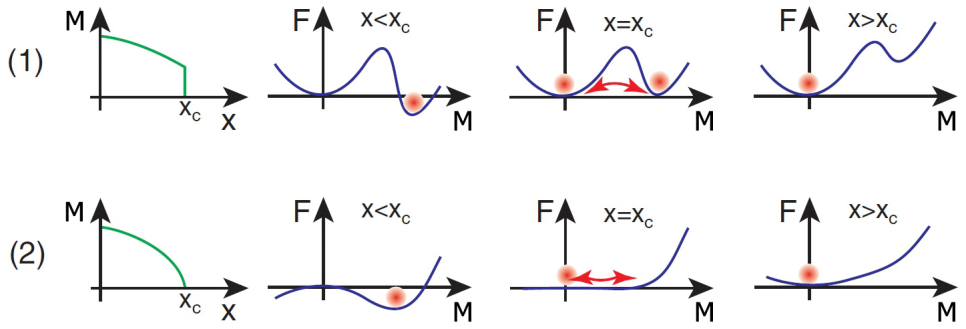

Figure 2.1.: Illustration of the difference between first-order (upper panel) and second-order (lower panel) QPT as function of a non-thermal tuning parameter x such as pressure, chemical composition or magnetic fields. On the left: order parameter (magnetisation) M as function of the tuning parameter x. Shown in the three plots on the right hand side is the free energy $F(M)$ as function of the order parameter for values of x below, directly at and above the critical point x_c. Below x_c the FM order develops with a finite M_0 favoured for the ground state. Above x_c the PM ground state is favourable. Adapted from Ref. [8].

An elegant approach to describe QPTs including quantum fluctuations in the $T = 0$ limit was found by Hertz and Millis [10, 11] using the so-called renormalisation group technique introduced by Wilson [78]. It was found that the approach is exact for sufficiently high dimensions of the electron system. As the effective dimensionality of a critical system close to a phase transition is increased by the so-called dynamic critical exponent it was originally assumed that most magnetic systems near criticality could be described by the model. In this approach the QCP is always bound to a second-order QPT where the transition temperature can be tuned continuously to $T_C = 0$. It was noticed early that due to the quantum fluctuations also the electronic transport properties should change. This implies that the standard Fermi liquid model may not be valid in the vicinity of a QCP. At least for the marginal case a conventional Ginzburg-Landau approach including spin fluctuations is applicable and an analytic description of the phase transition can be provided. The corresponding electronic ground state in the critical regime of the magnetic phase diagram can be derived in the limit $x \to x_c$ where the QCP is approached. The ground state in this limit is often referred to as marginal Fermi liquid (MFL). Predictions for a MFL on the border of FM are in particular a logarithmic dependence of the susceptibility as $\chi(T) \propto \log(T/T')$ and a $\rho \propto T^{5/3}$ resistivity [73].

Interestingly, in more recent studies such MFL behaviour is increasingly found in weak FM system which are expected to be located close to a putative QCP. Furthermore,

in sufficiently clean (high-quality) samples the second-order QPT turns always into a first-order QPT at a tri-critical point. Unfortunately, such studies also reveal that the transport properties typically change around the tri-critical point and are not well described by the $T^{5/3}$ law for the resistivity above p_c. Altogether the observations strongly indicate that another mechanism has to contribute in the vicinity and above a QCP which is neglected in the existing models.

After general reconsiderations it was suggested in the late 1990s by Belitz [79], Vojta [6] and others that the Hertz-Millis description was to some extent incomplete for the description of real metallic systems. They realised that so-called soft-modes (electron-hole excitations around the Fermi surface) which always occur in metallic systems can couple to the order parameter fluctuations. As a result a non-analytic term appears in the free energy which then not only in particular cases but generically leads to singularities which produce a first-order QPT. The formerly established prediction that QPTs are always continuous is thereby invalidated. For this generic model a phase diagram as illustrated in Fig. 2.2a was derived in [79].

This type of phase diagram applies to a number of FM systems. The continuous second-order transition changes to first-order at a tri-critical point in the phase diagram. In clean systems lines of meta-magnetic transitions defined by the critical magnetic field and the critical temperature are observed. The meta-magnetic lines end up at finite field at a QCP. A well-known example is $ZrZn_2$ [80, 72, 73]. Interestingly, in earlier studies the QPT was reported to be continuous. However, with increasing sample quality the transition at low temperatures was found to be first-order which is now established. Another system which is often cited in this context is MnSi [81–83]. Although the system is actually a weak helimagnet, the long wavelength of the modulation allows to approximate it as a weak FM. In general such a first-order QPT occurs in a large variety of materials. These include transition metals where the magnetism is carried by the $3d$ electrons such as CoS_2 , Ni_3Al and $Sr_3Ru_2O_7$ (see Refs. [84–88]) as well as $4f$ and $5f$ electron systems such as UGe_2 , U_3P_4 , URhGe , UCoAl or URhAl (see Refs. [89–91]). In some systems the first-order transition above a tri-critical point was found however the meta-magnetic wings were not observed. Examples include $Ni_{1-x}Pd_x$ and $CeSi_{1.81}$ where the QPT is most likely accompanied by moderate disorder effects [92–94]. Regarding recent theoretical approaches the above case may indeed represent the most generic case that occurs. However, empirically there are altogether four categories of phase diagrams which may be distinguished.

The occurrence of meta-magnetic transitions is only one of the four typically observed escape routes from a continuous second-order QPT. In all other cases the regime of low pressure p is mostly similar to the generic case and characterised by a continuous second-order transition. However, in the case illustrated in Fig. 2.2b the superconducting phase is observed on the border to the PM phase. Interestingly, most known systems showing this behaviour are FM metals which contain uranium.

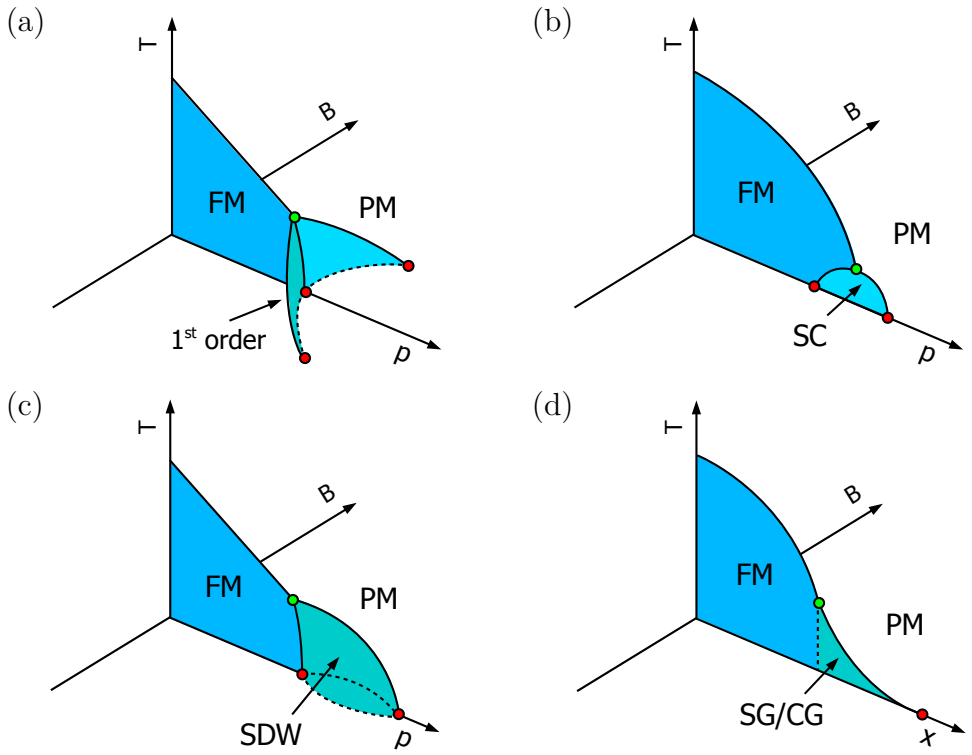

Figure 2.2.: Several examples of magnetic phase diagrams as observed for weak FM systems. (a) Possibly the most generic case where the continuous FM transition is suppressed by a tuning parameter such as hydrostatic pressure p until a tri-critical point at p_{tc} is reached. Above p_{tc} the transition changes to first-order and is rapidly suppressed to $T = 0$. Meta-magnetic first-order transitions (so-called "wings") are observed as a function of applied magnetic field B above the tri-critical point and vanish at finite field in QCPs at $T = 0$. (b) The second-order FM transition is found up to a critical value of p where a phase dome below the FM phase is found exhibiting a first-order transition into a superconducting phase. (c) A second-order FM transition at low values of p changes into a first-order transition into a SDW phase. (d) In disordered systems such as doping series the FM ground state may dissolve smoothly into a cluster glass and finally transform to a spin-glass state. Here the concentration x of a constituent of the material is used a tuning parameter. The second-order transition remains continuous until a PM state is reached.

The most prominent example is possibly UGe_2 (see Refs. [89, 95]) which besides superconductivity shows meta-magnetic transitions as illustrated in Fig. 2.2a. Other examples where superconductivity but no meta-magnetic transition was found include the systems URhGe , UCoGe (see Refs. [90, 91, 96]).

Fig. 2.2c shows another scenario where the type of order changes and a spin density wave (SDW) is stabilised above the tri-critical point. Samples of lower quality may

reveal an AFM phase emerging from the SDW phase for larger values of p. However, even in doping series the type of order is often not simply AFM but a modulated spin structure. Here the most prominent example for such a behaviour is $Nb_{1-x}Fe_{2+x}$ [97–99]. In $Sr_3Ru_2O_7$ two subsequent SDW phases are observed at finite magnetic fields [15, 87, 88, 100]. The doping series $Fe_{1-x}Cr_x$ shows a behaviour more similar to $Nb_{1-x}Fe_{2+x}$, however, instead of a SDW phase a spin-glass regime is found to separate the FM phase at low values of x and the AFM phase at larger values of x [101–105]. This type of phase diagram is also found for some f electron systems including CeRuPO , $CeAgSb_2$ or the heavy fermion system $Yb(Rh_{1-x}Co_x)_2Si_2$ (see [94, 106]).

A phase diagram which may only be observed for strongly inhomogeneous systems such as doping series is illustrated in 2.2d. Here the FM order is suppressed continuously as a function of the composition x. The tail region of the phase boundary reveals the effect of intrinsic disorder which may lead to a distribution of ordering temperatures that varies spatially on a microscopic scale. In most cases where such a phase diagram is observed a crossover into a cluster glass phase and finally into a spin-glass phase occurs for larger values of x. A prominent examples for this behaviour among the FM f electron systems are $CePd_{1-x}Rh_x$ [65, 107] which is also investigated in this study. Other examples include $CePt_{1-x}Rh_x$ or $CeNi_{1-x}Pt_x$ and some uranium based compounds (see [107–111]). However, in these systems the effect might be even enhanced due to the existence of the additional energy scale of the Kondo effect. Among the d electron systems $Ni_{1-x}V_x$ represents a case of moderate disorder [112] where the tail region is rather narrow compared to the illustration in Fig. 2.2d. In general, also the doping series $Fe_{1-x}Cr_x$ may be categorised here, as the FM phase boundary is rather similar.

Although great progress has been made in the theoretical description of the large variety of FM systems, the exact electronic behaviour determining the transport properties in the vicinity of a FM QCP is still under debate and no unified framework is known to the author. In metallic systems well above a QCP the Fermi liquid theory could be expected to predict the $T \to 0$ limit of the resistivity with a $\rho(T) = \rho_0 + AT^2$ law. However, this behaviour is rarely observed in FM materials close to a putative QCP. Instead an exponent $\alpha < 2$ in the AT^α term is often found which typically changes abruptly at the tri-critical point. It was discussed elsewhere that a particular non-Fermi liquid behaviour may hence be regarded as a precursor indicating an easily accessible QPT. An extensive review on metallic systems where a FM QPT was observed can be found in [106]. A review on metallic systems which show non-Fermi liquid behaviour is given in [113, 114] where also several of the FM systems mentioned above are included.

As the above summary is of course not exhausting we refer to the references given within the text for further details. Nevertheless, it is clear that the challenge persists to investigate weak FM materials in the context of QPTs. The theoretical challenge is to find a unified framework covering all of the discussed escape routes from a second-order

QPT. An experimental challenge is to probe the FM properties on the correct time and length scale. For the interpretation of the data in this study we rely on established models although these models are most likely to fail close to a QCP. The next Sec. 2.2 summarises the main results from a conventional Ginzburg-Landau approach to derive the magnetic properties of interest. In Sec. 2.2.1 the most simple version of the model is summarised which still helps to develop some intuitive understanding. In Sec. 2.2.2 a modification of the model including the effect of spin fluctuations is shortly reviewed.

2.2. Weak Itinerant Ferromagnetism

Weak itinerant ferromagnets can be characterised phenomenologically by a few common properties. The inverse susceptibility $\chi(T)^{-1}$ in such systems is mostly proportional to $(T - T_C)$ for temperatures T well above the Curie temperature T_C which is also known as Curie-Weiss behaviour. The spontaneous moment at zero applied field and extrapolated to zero temperature $\mu_s(T \to 0, B = 0)$ is much smaller than the effective Curie-Weiss moment μ_{eff} at high temperatures. The magnetisation $M(B)$ shows no saturation up to highest fields. So-called Arrott plots, i.e. B/M plotted against M^2 show linear behaviour over a large field range and temperature range.

Historically, weak itinerant ferromagnetism was first explained by Stoner [115] and others in the 1930s. In the Stoner model the Fermi surface of a ferromagnetic system experiences a lifting of its spin degeneracy below a critical temperature. The spin-splitting of the Fermi surface allows the spontaneous ferromagnetic polarisation of the spin ensemble by single-spin excitations from the majority band to the minority band. The first predictions were however only valid in the limit $T \to 0$. A Ginzburg-Landau approach was used later to derive the properties at finite temperatures [4, 116, 117] where a prime candidate for a model system was the weak itinerant electron magnet $ZrZn_2$. Although providing an important starting point with qualitatively correct predictions for a few selected candidates the theory failed quantitatively for most materials. More specifically the model is not able to explain the strong temperature dependencies and the magnitude of observables such as susceptibility and specific heat. Furthermore, it significantly overestimates the Curie temperature. It was found later that the collective dynamics of the spins i.e. spatial and temporal fluctuations in the spin density, which were neglected so far, were one reason for this discrepancy. It was shown in the 1980s by Moriya [118] that a model including fluctuations of the spin density could be formulated using again a Ginzburg-Landau approach. Lonzarich and Taillefer [119, 120] proposed a version of this model such that only four parameters which can be easily determined by experiment are needed for a complete description of the thermodynamic properties. By this time the model was applied to the materials MnSi and Ni_3Al at ambient pressure with remarkable agreement. However, it could not predict the behaviour for higher pressures and it failed for other materials. It took until the 1990s where a new theoretical approach by [11] was proposed that was based on the renormalisation group technique as introduced by Wilson and applied by Hertz [10, 78]. The approach was more suitable for the description of QPTs since the fluctuations driving the transition are described by quantum statistics. Nevertheless, the theory breaks down for systems close to quantum criticality as suggested from more recent experiments. In the Hertz-Millis theory the QPT is always a second-order transition and hence continuous which is in marked contrast to experimental observations. Several routes were investigated by theorists in order to solve this discrepancy. Most recent models that may provide the route towards a complete description have considered the effect of order parameter fluctuations

which couple to each other. In the last decade this has lead to a very generic picture of QPTs. In clean systems it is now predicted that the QPT is always a first-order transition above a critical value of the control parameter referred to as tri-critical point.

The Ginzburg-Landau approach based on the Stoner model for the description of weak itinerant ferromagnets at finite temperatures is summarised in the following section 2.2.1. In Sec. 2.2.2 the extension of the Ginzburg-Landau approach including spin fluctuations is discussed. Since in this study the effect of pressure on the magnetic state is investigated, the pressure dependence of the Curie temperature is considered.

2.2.1. Ginzburg-Landau Theory for Itinerant Ferromagnets

The partly phenomenological Stoner-Wohlfarth model which will be shortly reviewed in the following is microscopically based on the characteristics of the density of states around the Fermi level [115] whereas the behaviour at finite temperatures is derived using a Ginzburg-Landau approach. The Ginzburg-Landau approach for the model was extensively investigated by [116] and [117]. The model gave a first qualitatively convincing explanation for band ferromagnetism at finite temperature and was the basis of further theoretical developments. One of the archetypal ferromagnets investigated in this framework was $ZrZn_2$ which was also investigated in this study. In the Stoner description a single electron spin interacts with a mean molecular field produced by the ensemble of all other spins. The idea of such a mean field was already introduced by Pierre Weiss earlier and it is also used in the Heisenberg model for magnetic systems consisting of localised spins. In contrast to localised moments in the Heisenberg model, which for example is applicable to isolating magnets and possibly to some f-electron systems, the electron moments in band ferromagnets are not localised at the lattice points but the electrons are treated as more or less free quasi-particles in a potential imposed by the molecular field. The Fermi liquid theory or more specifically an adequate quasi-particle description is therefore in general expected to hold in metallic ferromagnets. The model assumes that spin excitations from the majority band to the minority band occur below the Curie temperature. The excitations are uncorrelated particle-hole pairs with small energy $\hbar\omega$ and small wave vector q and span the so-called Stoner continuum in $\omega(q)$ space.

The microscopic properties in this model could be derived only for the static case at $T = 0$. For the description of the magnetic properties at finite temperature a phenomenological approach was found later. This Ginzburg-Landau approach as presented below does in principle not require precise knowledge of the free energy functional. Instead the free energy is approximated as a series expansion for small changes of the order parameter characterising the phase transition. The behaviour near a phase transition can then be calculated for the change in temperature $t = \frac{T-T_C}{T_C}$ relative to the transition temperature T_C or for the volume change $\omega = \frac{V-V_0}{V}$ compared to the equilibrium volume V_0 at zero pressure. It is therefore assumed that a

thermodynamic property X such as the specific heat or magnetisation can be expressed in a form: $X(t) = a|t|^{\lambda_0}(1 + bt^{\lambda_1} + ...)$. The leading order exponent λ_0 is referred to as critical exponent which is defined by

$$\lambda_0 = \lim_{t \to 0} \frac{\log X(t)}{\log |t|} \tag{2.1}$$

Experimentally, the critical exponents may be determined by a careful analysis of the corresponding thermodynamic property and can be used to verify the model assumptions. As an example, the magnetisation $M(T)$ for values close around T_C may be plotted on a log-log scale. The slope for vanishing $t = 0$ i.e. at T_C then gives the critical exponent for the magnetisation. The critical exponents are expected to obey certain relations generically due to the thermodynamic principles. In the literature the exponents are typically named as α for the specific heat $C \propto |t|^{-\alpha}$, β for the magnetisation $M \propto (-t)^{-\beta}$ and γ for the magnetic susceptibility $\chi \propto |t|^{-\gamma}$. When approaching the critical point where $t \to 0$ the typical length scale of a fluctuation ξ (the correlation length) as well as the time scale τ (i.e. the life time or inverse decay rate) diverge as known from liquid-gas phase transitions. The correlation length is written as $\xi \propto |t|^{-\nu}$ where ν denotes the static critical exponent. The life time of the critical fluctuations can be expressed by $\tau \propto \xi^z$ where z is the dynamic critical exponent.

The general behaviour at finite temperatures can be understood by considering the free energy F for a volume V of the described system of spins. The magnetisation M plays the role of the order parameter, which takes a non-zero value in the ordered state (below the ordering temperature T_C) and vanishes in the disordered state (above T_C). The temperature T acts as control parameter. The free energy may now be written as the sum $F = F_0 + F_m$ where F_0 is the free energy for a system without magnetic interaction between the spins and F_m incorporates the magnetic interactions. For small magnetisation M the free energy can be expanded into a Taylor series. For symmetry reasons the free energy F_m should contain only even exponents of M in its expansion. From experimental observations, i.e. from so-called Arrott-plots of most archetypal ferromagnets it may be concluded that an expansion of the free energy F_m to the 4^{th} order term is sufficient to capture the essential physics. An external magnetic field H is assumed to reduce the free energy in which it couples linearly to the magnetisation M. The free energy then reads:

$$F = \frac{1}{2}a(T)M^2 + \frac{1}{4}bM^4 - HM \tag{2.2}$$

Here the coefficient $a(T)$ depends on the temperature while the coefficient b does not. The explicit assumption of such a behaviour renders the theory phenomenological. Minimisation of the free energy with respect to the magnetisation enables to determine

the coefficients a and b:

$$a(T) = \frac{1}{2\chi_0}\left(1 - \frac{T^2}{T_C^2}\right) \quad \text{and} \quad b = \frac{1}{2\chi_0 M_0^2} \tag{2.3}$$

The magnetic equation of state now reads

$$H = \frac{\mathrm{d}F}{\mathrm{d}M} = a(T)M + bM^3 \tag{2.4}$$

which resembles the behaviour observed experimentally using Arrott-plots, i.e. a plot of H/M vs. M^2. Fig. 2.3a shows typical Arrott-plots for a weak FM system at different temperatures. Directly at the ordering temperature an intersection with the origin is observed.

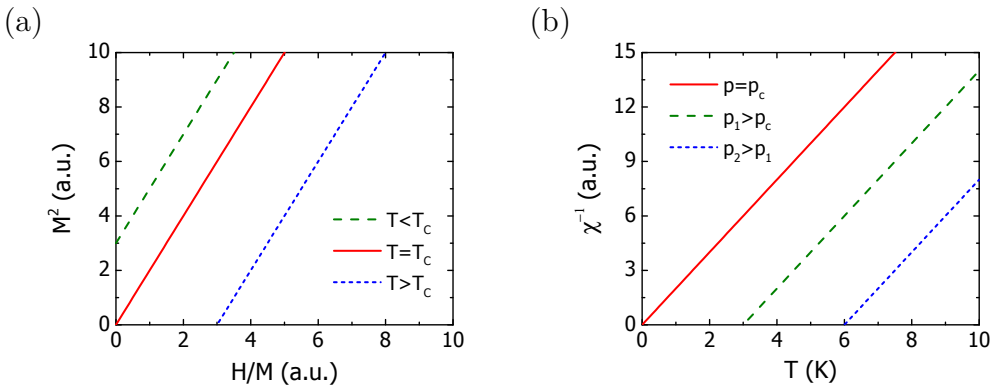

Figure 2.3.: (a) Illustration of Arrott-plots for a weak itinerant ferromagnet at different temperatures. Directly at T_C the line intersects zero and it is shifted with temperature while the slope remains constant. Below T_C a finite magnetisation exists without an external field H. (b) Inverse susceptibility as a function of temperature for different pressures. The susceptibility is shown for temperatures above T_C where a linear (Curie-Weiss) behaviour is predicted. Increasing the pressure suppresses the Curie temperature and thereby shifts the intersect $\chi^{-1}(T_C) = 0$ towards smaller temperatures. A critical point p_c is reached if the intersect is at $T = 0$.

For the spontaneous magnetisation it is found

$$M^2(T) = M_0^2\left(1 - \frac{T^2}{T_C^2}\right) \tag{2.5}$$

with $M_0^2 = -a(T = 0)/b$ is the squared equilibrium moment at $T = 0$.

Hydrostatic pressure is probably the most important parameter that can be tuned besides magnetic fields in order to fully understand the magnetic properties of a material. For some magnetic alloys the effect of pressure can be simulated by chemical substitution or dilution with a material of different atomic volume. However, this may

also lead to disorder effects and as a consequence alter the behaviour of the phase transition. The pressure dependence of the magnetic state has been investigated in a large number of ferromagnetic materials. Observations clearly indicate that the magnetisation is coupled to the elastic properties of the sample. For the description of this magneto-volume coupling a modified version of the Ginzburg-Landau free energy is hence required. In the following the pressure dependence of the Curie temperature and of the susceptibility will be derived under the assumption that only the parameter $a(p)$ of the free energy depends on pressure. The assumption is rectified by the observation from Arrott-plots M^2 vs. H/M where the intersect $a(p)$ is a function which goes approximately linear with pressure and vanishes at a critical pressure p_c. In contrast the slope of the Arrott-plots does not change significantly for varying pressure suggesting essentially no pressure dependence for the parameter b. Fig. 2.3b illustrated the typical Curie-Weiss behaviour above T_C of the static susceptibility M/H for different pressures p as observed by experiment. Typically, the application of pressure reduces the transition temperature T_C.

The pressure dependence can then be introduced using additional terms in the free energy. According to the formulation by Wohlfarth in [116] it is assumed that the free energy of a system contains an elastic energy term $\frac{1}{2\kappa}\omega^2$ (by following Hooke's law) which increases if pressure is applied. The parameter κ is the compressibility in the linear (elastic) regime and is connected to the pressure p via the relation $\omega = -\kappa p$ where $\omega = \frac{V-V_0}{V_0}$ is the relative volume change in terms of the equilibrium volume V_0 at zero pressure. In order to minimise the free energy a magneto-volume coupling term is introduced. Supported by experimental evidence it is assumed that this coupling term decreases with the squared magnetisation M^2 and linear with pressure i.e. with the relative volume change ω and hence with the volume V. The free energy then reads for the case without explicitly including spin fluctuations

$$F = \frac{a}{2}M^2 + \frac{b}{4}M^4 + \frac{1}{2\kappa}\omega^2 - HM - c\omega\left(M^2(H,T) - M^2(0,T)\right) \tag{2.6}$$

The constant c describes the strength of the magneto-volume (also called magneto-elastic) coupling.

From the free energy the magnetic equations of state for the system can be derived. For an applied magnetic field H it follows

$$H = \left.\frac{\mathrm{d}F}{\mathrm{d}M}\right|_V = aM + bM^3 - 2c\omega M \tag{2.7}$$

The application of pressure stabilises the state

$$-p = \left.\frac{\mathrm{d}F}{\mathrm{d}V}\right|_M = -c\left(M^2(H,T) - M^2(0,T)\right). \tag{2.8}$$

Experimentally either the relative volume change ω or the corresponding pressure can be measured for different $M(H,T)$ which is expected to result in a series of parallel lines with constant slope c. The application of pressure tends to reduce the Curie temperature. For the Stoner-Wohlfarth model it is found that

$$T_C(p) = T_C(0)\left(1 - \frac{p}{p_c}\right)^{-1/2} \tag{2.9}$$

with the critical pressure $p_c^{-1} = 4c\kappa\chi_0$.

This pressure dependence of the Curie temperature represents basically the most simple model of a QPT. If the pressure could be tuned continuously, the system would undergo a phase transition from a FM phase to a PM phase at zero temperature.

Successful refinements of the above theory were first elaborated by [119, 121]. The main refinement was to consider the effect of order parameter (spin) fluctuations on the magnetic equation of state in a similar way using a Ginzburg-Landau approach. However, the parameters a and b are now assumed constant with temperature and the ground state properties do not generally depend on the assumption of an underlying Fermi liquid in the magnetic state. The spin fluctuation theory will be discussed in the following section.

2.2.2. Ginzburg-Landau Theory Including Spin Fluctuations

The Stoner model and the corresponding Ginzburg-Landau approach provided a good starting point to explain the fundamental principles of band ferromagnetism. However, the Curie temperature derived from the Ginzburg-Landau formulation of the Stoner model was significantly overestimated for most real materials investigated so far. In addition, the temperature dependence of observed properties such as susceptibility and specific heat deviates from the predictions. In other words, only very few (essentially none) Stoner type ferromagnets were identified so far. As an explanation for this discrepancy collective spin fluctuations have been considered as a necessary ingredient for a full description of the phase transition and of the magnetic properties in metallic systems. In a refined Ginzburg-Landau approach these spin fluctuations couple to the magnetisation which complicates the solution [118]. It is hence favourable to include several approximations that are supported by experimental observations. Such a phenomenological version was proposed by Lonzarich and Taillefer in [122]. The assumptions simplify the model to only four free parameters a, b, c and γ which can all be determined by experiment and may in addition be derived from band structure calculations for comparison. In this model, the parameter a corresponds to the static inverse susceptibility, b denotes the so-called mode-coupling parameter, c is the spin wave stiffness and γ corresponds to the inverse life time of the spin fluctuations. The parameters a and b can be determined from magnetisation data while c and

γ can be extracted from neutron scattering data. The model introduces both longitudinal and transverse spin fluctuations with respect to the mean field direction. Both alter the temperature-dependence of physical properties in terms of the critical exponents. This section is basically a summary of the theory as reviewed in Ref. [4].

Again the Taylor series for small magnetisation M of the free energy $F = F_0 + F_m$ is used to approach the problem. In the first step the magnetisation is replaced by $M \to M + m$ where now the static average magnetisation is denoted by M and m is the fluctuating part of the magnetisation which varies as function of position. The spatial average $\langle m \rangle = 0$ vanishes as the fluctuations are assumed to be overall isotropic. However, the variance or fluctuation amplitude $\langle m^2 \rangle \neq 0$ takes a finite value which will be important for the considerations. As in the previous section it is assumed that only a quadratic and a quartic term in M occur in the free energy. However, due to the vectorial nature of the magnetisation M and of the additional fluctuating term m a more tedious expression is found

$$\begin{aligned} F_m = &\frac{a}{2}\left(M^2 + 2\langle m_\perp^2 \rangle + \langle m_\parallel^2 \rangle\right) \\ &+ \frac{b}{4}\left(M^4 + M^2(6\langle m_\parallel^2 \rangle + 4\langle m_\perp^2 \rangle) + 8\langle m_\perp^2 \rangle^2 + 3\langle m_\parallel^2 \rangle^2 + 4\langle m_\perp^2 \rangle \langle m_\parallel^2 \rangle\right) \end{aligned}$$

In contrast to the Stoner model, the parameters a and b both do not depend on temperature. However, the fluctuation-dissipation theorem predicts that the amplitude of classical (i.e. thermally induced) fluctuations scales linearly with temperature [4]. In order to include this result a condition for the fluctuation amplitude in terms of other known parameters is suitable. As a necessary requirement the inverse susceptibility $\chi^{-1}(T_C) = 0$ vanishes at T_C together with the static average magnetisation M. The inverse susceptibility

$$\chi^{-1} = \frac{\mathrm{d}^2 F}{\mathrm{d}M^2} = a + \frac{b}{2} 10 \langle m^2 \rangle \tag{2.10}$$

gives at T_C the fluctuation amplitude as $\langle m_c^2 \rangle = M_0^2/5$. In isotropic systems the simplification $\langle m_\parallel^2 \rangle = \langle m_\perp^2 \rangle = \langle m^2 \rangle$ below T_C together with the previous assumption of a linear temperature dependence leads to

$$\langle m^2 \rangle = \frac{M_0^2}{5} \frac{T}{T_C} \tag{2.11}$$

which is often referred to as Moriya formula [121, 4].

Assuming thermal equilibrium at finite T now gives

$$\frac{\mathrm{d}F}{\mathrm{d}M} = aM + bM^3 + bM(3\langle m_\parallel^2 \rangle + 2\langle m_\perp^2 \rangle) = 0 \tag{2.12}$$

The equation can be solved for the magnetisation

$$M^2 = M_0^2 \left(1 - \frac{T}{T_C}\right) \tag{2.13}$$

The static susceptibility for $T < T_C$ is derived as

$$\chi^{-1}(T) = \chi_0^{-1} \left(1 - \frac{T}{T_C}\right) \tag{2.14}$$

and for $T \geq T_C$ it reads

$$\chi^{-1}(T) = \frac{1}{2}\chi_0^{-1} \left(\frac{T}{T_C} - 1\right) \tag{2.15}$$

which, again in contrast to the Stoner model, corresponds to Curie-Weiss behaviour for temperatures above T_C.

The (stronger) temperature dependence originates from the correction terms proportional to $\left\langle |m_\parallel(q)|^2 \right\rangle$ and $\langle |m_\perp(q)|^2 \rangle$ which arise due to the thermal spin fluctuations that couple to the magnetisation.

An important parameter that can be derived from the condition $\chi^{-1}(T_C) = 0$ is the Curie temperature of the phase transition. Following the result from [119] it is given by

$$T_C = 2.387 c M_0^{3/2} \frac{(\hbar\gamma)^{1/4}}{k_B}. \tag{2.16}$$

and thereby connects all four parameters of the model. The spontaneous magnetisation may be measured directly and corresponds to $M_0 = \left(-\frac{a}{b}\right)^{1/2}$. As already mentioned, the parameters a and b can be also extracted separately from Arrott plots. The other two free parameters, i.e. the spin wave stiffness c and the inverse fluctuation lifetime γ are also required for the generalised susceptibility $\chi(q,\omega)$ as function of the wave vector q and of the excitation energy ω. The generalised susceptibility thereby includes the length and time scale that are probed. The parameters c and γ can be determined experimentally using neutron scattering. With a neutron triple-axis spectrometer the measurement of the inelastic scattering function which is proportional to $\chi(q,\omega)$ can be used where $\Gamma(q)$ is then the energy width as a function of q. The parameter c is given through the spin wave stiffness, i.e. the slope of $\hbar\omega(q)$ for small q describing well-defined spin wave excitations. Alternatively a spin echo spectrometer or MIEZE spectrometer can be used where the Fourier transform $\tau(q) = \Gamma^{-1}(q)$, i.e. the lifetime of the fluctuations is measured. In principle all four parameters a,b,c and γ can also be derived from band structure calculations for comparison. It is worth to mention that the model as formulated in [119] relies on another parameter hidden so far which is a cut-off wave vector q_c used for the complete derivation. It defines the limit above which

the excitations cannot be regarded as collective anymore. Above q_c the excitations get heavily damped and then decay completely into uncorrelated single particle-hole excitations already introduced as the Stoner continuum.

In the spin fluctuation theory the effect of pressure on the Curie temperature is assumed to arise entirely from the fluctuating part of the magnetisation and may be derived as

$$T_C(p) = T_C(0)\left(1 - \frac{p}{p_c}\right) \tag{2.17}$$

A comparison of the Stoner-Wohlfarth model and the spin fluctuation theory for the two characteristic properties magnetisation as a function of temperature and the pressure dependence of the Curie temperature is shown in Fig. 2.4.

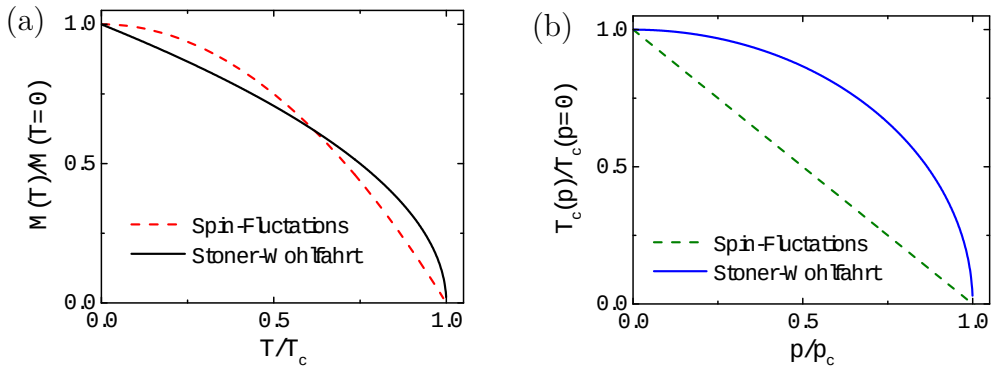

Figure 2.4.: Comparison of the Stoner-Wohlfarth theory and spin fluctuation theory according to the formulas given in the text. (a) Magnetisation as a function of temperature. The qualitative behaviour is rather similar however the quantitative predictions of the spin fluctuation theory are more accurate. (b) Pressure dependence of the Curie temperature. Quadratic behaviour vs. linear behaviour is predicted from the theories which have both been observed in experiments. Both theories predict a continuous second-order suppression of the Curie temperature to $T = 0$.

It should be noted that the model glances at ambient pressure and for low pressures. However, recent experimental findings undermine the model for larger pressures where T_C is already strongly suppressed. The theory seems to fail by predicting a second-order phase transition until a QCP is reached. It does not predict the experimentally observed first-order phase transition when approaching a putative QCP in the magnetic phase diagram. In other words the description of the QPT seems to lack some ingredient. Nevertheless, the theory constitutes an important step towards a more complete understanding of ferromagnetism. Compared to the Ginzburg-Landau theory for the Stoner model as described in the previous section the spin fluctuation theory provides much better agreement with experiment and involves only four free parameters which can be determined consistently from different measurements or calculated ab initio.

The spin fluctuation theory may in this aspect be regarded as a very successful progress.

The results from the phenomenological Ginzburg-Landau approach will be used as a basis for the interpretation of the data collected in this study. As pointed out in Sec. 2.1 the validity of this established model in the critical regime of the phase diagram is of particular interest and under investigation in this study using selected samples. The next chapter gives a summary on the mathematical basics of neutron depolarisation studies.

3. Basics Of Neutron Depolarisation Studies

This chapter gives a brief summary of the experimental requirements for neutron depolarisation measurements and of the theoretical details required for an interpretation of the neutron data. A sketch of a basic set up for neutron depolarisation measurements is shown in Fig. 3.1. For such a measurement the polarisation of the neutron beam needs to be evaluated. This is done by measuring the difference in intensities of the two opposite polarisation states ↑ and ↓ of the neutron beam as will be explained below in more detail.

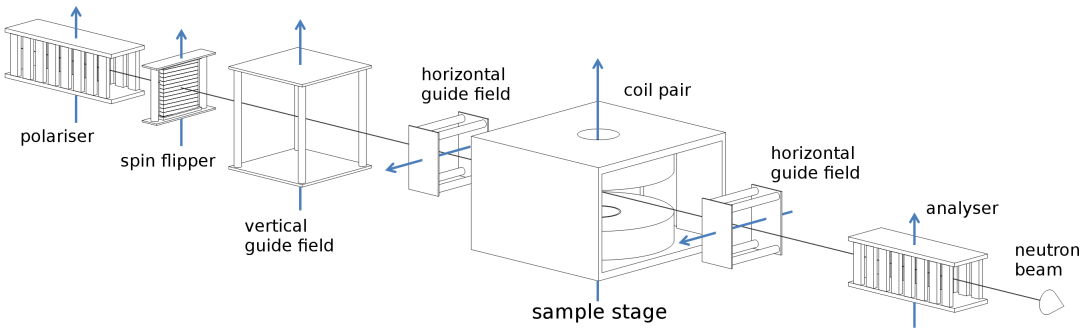

Figure 3.1.: Illustration of a typical set up for neutron depolarisation measurements. The blue arrows indicate the direction of the magnetic field in each component. The neutron beam (traversing from left to right) is first polarised using a suitable polarisation device. The polariser is followed by a spin-flipper in order to switch between ↑ and ↓ states. The polarisation is guided by static magnetic fields on the path through the sample. The sample is typically placed in a cryostat (not shown) which is surrounded by a coil pair in order to vary the temperature and to apply external magnetic fields. The polarisation is then guided to the analyser which selects the ↑ state. Finally, the neutrons are counted using a 1D or 2D detector.

For the polarisation of the neutron beam a suitable polarisation device is required, e.g. a polarising supermirror cavity [123] or a ^{3}He spin-filter cell [124, 125]. A spin-flipper device is placed behind the polariser which allows to select the spin state ↑ or ↓ required at the sample position. The beam polarisation is typically maintained by a magnetic guide field pointing along the field direction of the polariser. In order to set a desired polarisation direction at the sample position the guide field may be rotated smoothly on the neutron path from the initial polariser field direction to an arbitrary

direction. Alternatively so-called coupling coils may be used for this purpose [1]. In this case the guide field is rotated into the horizontal plane. This allows to apply magnetic fields at the sample position that are parallel or anti-parallel to the vertical axis as the polarisation vector is adiabatically guided into both directions. A smooth continuation of the magnetic field along the neutron path is required to keep the polarisation at maximum. After interaction with the sample the polarisation is guided by a magnetic field reaching to the analyser which finally selects again the initial $\uparrow$ state in order to determine the change of polarisation of the neutron beam by the sample.

The polarisation is calculated using the two measured neutron intensities $I_\uparrow$ and $I_\downarrow$ according to the spin state $\uparrow$ or $\downarrow$ selected by the spin-flipper. Imperfections of each polarisation device and of the spin-flipper have to be considered for meaningful data interpretation. These effects can be accounted for by normalisation of the data. The normalised polarisation can be calculated using the relation

$$P = \frac{1}{P_0} \cdot \frac{I_\uparrow - I_\downarrow}{I_\uparrow + I_\downarrow} \tag{3.1}$$

where P_0 is the reference polarisation measured either without the sample in the beam or with the sample hold at a temperature well above any ferromagnetic or superconducting transition. The polarisation P_0 thereby contains all influences by the set up and due to the sample environment. A normalisation to the reference polarisation P_0 exposes the pure effect of the sample on the polarisation. This formula is used throughout all measurements in order to determine the polarisation.

Two limiting cases of magnetic field transitions occur on the neutron path through our particular set up which will be discussed in some more detail. A non-adiabatic (which implies abrupt) field transition occurs in the spin-flipper coil. In total four adiabatic (smooth and continuous) transitions along the neutron path occur where the guide field direction is changed smoothly from vertical to horizontal and otherwise around. The next section gives a short summary on the mathematical description of the neutron spin in constant and spatially varying magnetic fields. Furthermore, some basic rules of thumb are given for the instrumentation with polarised neutrons.

1 For this study coupling coils had several disadvantages, i.e. they require additional power supplies and the neutron beam needs to traverse the coil wires which reduces the intensity.

3.1. Neutron Spin in Magnetic Fields

A description of the time evolution of the neutron spin in a magnetic field may be derived either in a classical way or using quantum mechanics. For the purpose of this study a classical description is used which also helps to understand the behaviour more intuitively. In this case each neutron carries a spin $\mathbf{S}$ which may point in an arbitrary direction. The polarisation of the neutron beam is then defined as $\mathbf{P} = \langle \mathbf{S} \rangle$ the ensemble average over all neutron spins and may take values between -1 and 1 with respect to a quantisation axis typically defined by the polariser and analyser guide field direction. For further theoretical details on the polarisation we refer to the literature, e.g. [50, 126, 127]. In a classical picture, the neutron spin experiences a torque if the spin and the field direction are not parallel to each other. The time evolution of the neutron spin in a magnetic field $\mathbf{B}(t)$ can be described by the Larmor equation

$$\frac{d}{dt}\mathbf{S}(t) = \gamma \mathbf{S}(t) \times \mathbf{B}(t) \tag{3.2}$$

The factor $\gamma = 183\ \mathrm{kHz/mT}$ is the gyromagnetic ratio of the neutron. For an interpretation of the Larmor equation one can now distinguish between two distinct cases: the non-adiabatic case and the adiabatic case of a magnetic field change. An illustration of a non-adiabatic and an adiabatic field transition is shown in Fig. 3.2a and 3.2b, respectively. In the non-adiabatic case the field direction changes abruptly from vertical at $t < 0$ to horizontal at $t = 0$. In the adiabatic case the field direction changes continuously from vertical at $t = 0$ to horizontal at the time t.

It is most intuitive to consider the spin in the moving coordinate system of the neutron such that only the time-dependence remains in the Larmor equation in order to derive the behaviour along the neutron path. A simple solution for the non-adiabatic case can be found by splitting the spin vector into the components $\mathbf{s}_\perp(t)$ perpendicular to $\mathbf{B}$ and $\mathbf{s}_\parallel(t)$ parallel to $\mathbf{B}$ as

$$\mathbf{S}(t) = \mathbf{s}_\parallel(t) + \mathbf{s}_\perp(t) \tag{3.3}$$

For a constant field B it follows from Eq. 3.2 that the parallel component shows no time dependence and will hence not change. The component $\mathbf{s}_\perp(t)$ perpendicular to $\mathbf{B}$ however will change in time. The solution for the case of a static field in y-direction as in Fig. 3.2 such as $\mathbf{B} = (0, B, 0)^T$ is:

$$\mathbf{s}_\perp(t) = -\mathbf{s_x} \sin(\omega_L t) + \mathbf{s_z} \cos(\omega_L t). \tag{3.4}$$

The relevant components and their signs are a result of the cross product in the Larmor equation. If the initial spin state is not parallel to $\mathbf{B}$ the polarisation vector precesses around the axis of the magnetic field with the Larmor frequency $\omega_L = \gamma B$. Hence, the spin precession sets in if an abrupt change of the field direction from the

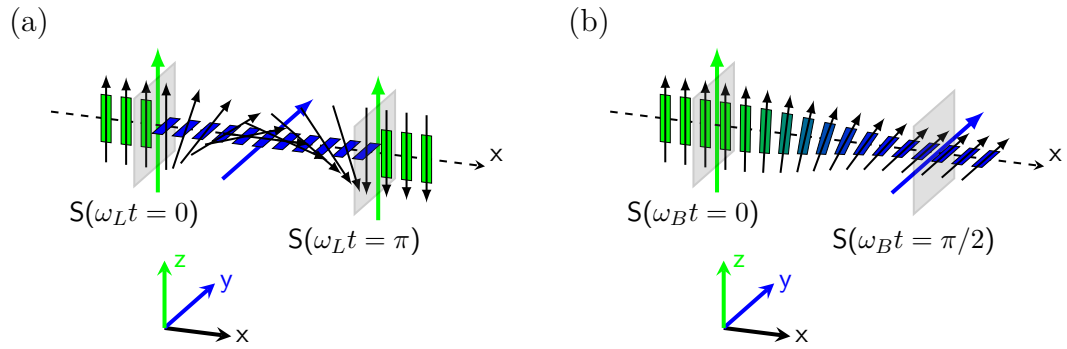

Figure 3.2.: (a) Non-adiabatic and (b) adiabatic magnetic field transition. The initial polarisation is along the guide field in z-direction while the neutron propagates in x-direction. In (a) the field changes abruptly from z-direction (green) to y-direction (blue), resulting in a spin rotation (small black arrows) within in the x-z plane around the y-axis starting at $t = 0$. A second field transition to the initial field direction occurs when a rotation by an angle $\omega_L t = \pi$ is reached. This corresponds to a spin flip. The field in (b) changes slowly from the z-direction at $t = 0$ to the y-direction where $\omega_B t = \pi/2$. The polarisation is guided along the rotating field if the angular change of the rotating field is much smaller than the angular change due to the Larmor precession around the field axis.

initial polarisation direction occurs (cf. Fig. 3.2a). The spin-flipper used for this study is a so-called Mezei-type spin-flipper which consists of two rectangular coils with perpendicular field orientations, one wound around the other. If placed in a polarised neutron beam this allows to compensate the magnetic guide field by the outer coil and at the same time to produce a field perpendicular to it using the inner coil. Since the field transition into the spin-flipper coil is in good approximation non-adiabatic the neutron spin will rotate around the axis of the perpendicular field. The field strength (the current driving the coil) is tuned such that the spin performs a rotation by 180° which corresponds to a spin flip. The behaviour is fully described by Eq. 3.4.

If the direction of the guide field varies slowly the adiabatic case needs to be considered. In general the neutron spin always performs a small amount of precession if a change in the field direction occurs. However, if the change of the field direction is small enough the major part of the polarisation will be guided along with the field direction. For a mathematical description we consider an initial magnetic field pointing along the z-direction. The magnetic field shall start to rotate at $t = 0$ in the y-z plane with frequency ω_B around the x-axis:

$$\mathbf{B} = B \begin{pmatrix} 0 \\ \sin(\omega_B t) \\ \cos(\omega_B t) \end{pmatrix} \tag{3.5}$$

After a $\pi/2$ rotation the field points along the y-direction.

It is now useful to quantify the so-called adiabaticity k by comparing the Larmor frequency ω_L to the frequency ω_B of the field change in time as

$$k = \frac{\omega_L}{\omega_B} \tag{3.6}$$

For a solution of the Larmor equation again two limiting cases may be considered. The first case $\omega_L \ll \omega_B$ and hence $k \to 0$ describes the neutron spin in a rapidly varying magnetic field. The second case $\omega_L \gg \omega_B$ which corresponds to $k \to \infty$ describes the spin in a slowly varying magnetic field. The results from [126] are used for the following calculations.

In the first limit $k \to 0$ the field change is so fast that the neutron spin can not respond if the field magnitude is low enough. Although this corresponds to the non-adiabatic limit no significant precession of the spin is expected.

In the limit $k \to \infty$ the field direction changes slowly which corresponds to an adiabatic transition as depicted in Fig. 3.2b. In this case it follows for the polarisation

$$\mathbf{P} = \begin{pmatrix} 0 \\ \sin(\omega_B t) \\ \cos(\omega_B t) \end{pmatrix} \tag{3.7}$$

which corresponds to a rotation of $\mathbf{P}$ together with the external field. This means that ideally the polarisation smoothly follows the field vector with $\mathbf{P}||\mathbf{B}$ at any moment. Only if the magnitude of the field would be decreased significantly the assumed limit would become invalid.

An exact solution of the Larmor equation for the intermediate regime involves a more tedious calculation as shown e.g. in [126]. Here only the result is given:

$$\mathbf{P} = \begin{pmatrix} \mathrm{A}_1^2 + \mathrm{A}_2^2 \cos(\Omega \mathrm{t}) \\ -A_1 \cos(\omega_B t) \sin(\Omega t) + A_1^2 \sin(\omega_B t) \cos(\Omega t) + A_2^2 \sin(\omega_B t) \\ A_2 \cos(\omega_B t) \sin(\Omega t) - A_2^2 \sin(\omega_B t) \cos(\Omega t) + A_1^2 \sin(\omega_B t) \end{pmatrix} \tag{3.8}$$

where $A_1 = \cos(\alpha)$ and $A_2 = \sin(\alpha)$ can be calculated from the relation $\tan(\alpha) = k$ using the adiabaticity k. The effective frequency $\Omega = \sqrt{\omega_L^2 + \omega_B^2}$ was introduced. Eq. 3.8 corresponds to a precession of $\mathbf{P}$ around the rotating axis of the magnetic field. There is always a component of the polarisation which is perpendicular to the field direction. As an example the y-component of the polarisation is now evaluated as a function of the angle $\phi = \omega_B t$ about which the field direction is rotated in the x-y plane after the time t. The polarisation is shown in Fig. 3.3a for different values of the adiabaticity k. For larger values of k the polarisation smoothly follows the field

direction. Complex behaviour is found for values of k in the intermediate regime. In Fig. 3.3b the y-component of the polarisation as a function of k is evaluated for a fixed angle of $\pi/2$ about which the field direction is rotated. This corresponds to a coupling of the polarisation from the initial z-direction into the y-direction. It can be derived that the adiabaticity k should be larger than 14 in order to keep more than 99 % of the polarisation and larger than 18.5 in order to guide more than 99.5 % of the polarisation. As can be concluded from the above discussion a neutron spin that passes a slowly varying magnetic field can effectively be guided into an arbitrary direction. The adiabaticity parameter k is a useful quantity that should be considered in an experimental set up for polarisation measurements.

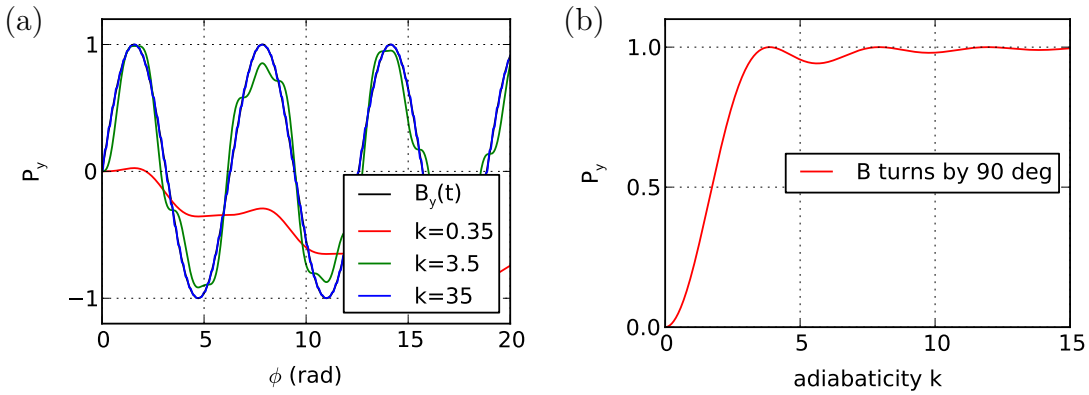

Figure 3.3.: (a) Calculated y-component of the polarisation as a function of the angle $\phi = \omega_B t$ about which the field direction is rotated according to Eq. 3.8. The polarisation is shown for three different values of the adiabaticity k. For low values of k the behaviour is rather unintuitive. For larger values of k the polarisation can be effectively guided. (b) Calculated y-component of the polarisation for a fixed angle ϕ =90° as a function of the adiabaticity k according to Eq. 3.8. As a rule of thumb the adiabaticity in a corresponding set up should be chosen larger than 14 in order to keep more than 99 % of the polarisation.

Since the precise coupling of the polarisation of a neutron beam with a finite wavelength distribution and a finite divergence can hardly be calculated analytically a Monte Carlo simulation is a convenient way to investigate the behaviour in more detail. As part of a Bachelor thesis which was supervised during this study (see Ref. [128]) the magnetic field geometry of the experimental set up was simulated using the software COMSOL Multiphysics [1] under realistic conditions. The field geometries of polariser, analyser, guide fields and of the coil pair at the sample position were mapped out using a Hall probe. The material parameters in COMSOL were tuned to reproduce the measured values. The fields simulated in COMSOL for the different components

1 http://www.comsol.de

were in excellent agreement with the measured field components along the neutron path. The bachelor thesis included an investigation of the effect of different magnetic field profiles on the neutron polarisation using Monte Carlo simulations. These were done using the software package McStas [1] which allows to model a virtual neutron instrument according to the real geometry under varying conditions. A model of the neutron instrument ANTARES at FRM II including a 2D detector was written as a basis. The depolarisation set up including all components but the sample was then implemented. The magnetic field profile resulting from a COMSOL simulation was saved as an ASCII file containing line by line the space coordinates and the corresponding three components of the magnetic field in a regular grid format which can be chosen in COMSOL. The data file was imported in McStas using a custom written function in C in the McStas instrument file. The function describing the vector field is used in the instrument file in a standard component from the McStas library called "field box". As this component requires a continuous function defining the magnetic vector field the data are interpolated using a spherical spline code yielding a continuous vector field from the discrete data points. The initial polarisation in McStas was set to the polariser field direction. The polarisation was analysed in all three direction by using the standard polarisation detectors available from the McStas library.

A simple example was chosen to demonstrate the functionality of the program code. For this demonstration a magnetic field profile similar to that of a part of our real set up was simulated in COMSOL. Two realistic guide field models rotated by 90 ° and with a distance of 60 cm to each other measured from the centre were used. The resulting total field profile along the neutron path resembles the adiabatic case shown in Fig. 3.2b. Under realistic conditions however the magnitude of B smoothly drops in between the two guide field components. In our simulation the initial polarisation was set to the initial field direction and was analysed in all three dimensions after traversing the magnetic field. By varying the neutron wavelength in McStas it was possible to scan the adiabaticity k. The result of the simulation series was as expected and is shown in Fig. 3.4. The polarisation measured along the y-axis reaches the value unity with increasing adiabaticity k which was tuned by increasing wavelength for a fixed distance of the two guide fields.

Interestingly, the real conditions including a finite beam divergence and a wavelength distribution $\Delta\lambda/\lambda = 10$ % as well a realistic field profile of the guide field as used at the instrument ANTARES have no significant effect on the coupling of the polarisation. This can be seen by a comparison with Fig. 3.3b. It is however important to note that the guide fields have to be strong enough to maintain the polarisation. The inset of Fig. 3.4 shows our simulated magnetic field profile in both the initial and the final

1 http://www.mcstas.org

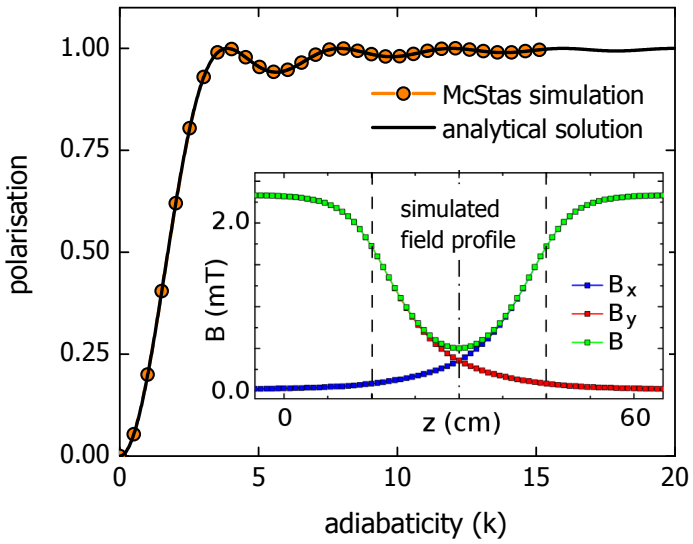

Figure 3.4.: Simulation result for the polarisation as a function of the adiabaticity parameter $k = \omega_L/\omega_B$ as measured after a $\pi/2$ rotation of the magnetic field direction along a path length of 60 cm. The imperfect guiding of the polarisation occurs for small values of k which for a fixed distance corresponds to smaller wavelengths. For realistic results a magnetic field profile as shown in the inset was used which is similar to the guide field profile produced by using two of our static guide field cages rotated by 90 degree to each other. The dashed vertical lines symbolise the edges of the guide field cages. This particular arrangement of permanent magnets produces an outer field which points in the same direction as the inner field but the magnitude decreases with increasing distance. The arrangement of the two perpendicular guide fields results in a smooth rotation of the field direction. From a comparison with the analytical solution given by Eq. 3.8 it can be concluded that neither the finite wavelength distribution $\Delta\lambda/\lambda = 10$ % and the small divergence at the instrument ANTARES nor the arrangement of the guide fields have a significant effect on the coupling of the polarisation. Data from [128].

direction which in this case were the y- and x-direction, respectively. The neutron path was along the z-direction in the simulations. As can be seen in Fig. 3.4 for short neutron wavelengths and hence small k the transition is non-adiabatic and only a fraction of the polarisation is guided with the rotating field. For larger k the transition is increasingly adiabatic and the polarisation is guided well. As a result from this study the adiabaticity should be larger than 15 in order to expect polarisation losses of less than 0.5% for the wavelength of 4.13 Å used in the experiments at ANTARES. If this condition would not be fulfilled for a given part of the set up a significant loss of polarisation must be expected. In order to optimise a given set up it is required to either increase the magnitude of the guide fields (i.e. increase the Larmor frequency $\omega_L = \gamma B$) or to vary the distance between the two guide field cages accordingly.

3.1.1. Effect of a Finite Wavelength Distribution

With an ideally polarised and monochromatic neutron beam the polarisation vector could be rotated by using non-adiabatic spin-flippers without any loss of polarisation. In any real instrument the beam is characterised by a finite wavelength distribution. For example at the instrument ANTARES a neutron velocity selector can be used to select a wavelength band with $\Delta\lambda/\lambda = 10$ % FWHM for $\lambda = 4.13$ Å. The crystal monochromator at the instrument MIRA delivers a resolution of $\Delta\lambda/\lambda = 2$ % FWHM for $\lambda = 4.59$ Å. At both instruments a Mezei-type spin-flipper was used in this study for preparing the spin state right after polarising the beam. The principle of this type of spin-flipper was described earlier (see Fig. 3.2a). The transition into the perpendicular flipper field is non-adiabatic. The polarisation for a monochromatic beam can therefore easily be calculated by

$$P(\lambda) = \cos(\gamma B \tau) = \cos(\gamma B \alpha \lambda L) \tag{3.9}$$

where B is the magnitude of the perpendicular field and τ is the transmission time given by $\tau = \alpha\lambda L$ with $\alpha = h/m_n = 252.78\ \mu\mathrm{s\ \AA^{-1}m^{-1}}$ and L being the length of the field in the beam direction. To calculate α the Planck constant h and the neutron mass m_n was used. In the tuning process of such a spin-flipper the intensity is measured for different values of the flipper current producing the field B. The resulting data should fit to a cosine function with the corresponding frequency as in Eq. 3.9. The value of B at the first minimum $\phi = \gamma B \tau = \pi$ is used to achieve a spin-flip.

If a wavelength band of finite width $\Delta\lambda$ (FWHM) is used in an experiment, a certain degree of depolarisation occurs as the spins of neutrons with different wavelengths fan out over a certain angular range. A convolution with the wavelength distribution can be used to incorporate the effect on the polarisation for the spin-flipper:

$$P(B) = \int_0^\infty P(\lambda) f(\lambda,\Delta\lambda) d\lambda \tag{3.10}$$

For a single wavelength λ_0 the distribution $f(\lambda,\Delta\lambda)$ corresponds to a delta-function $\delta(\lambda - \lambda_0)$ and the result is simplified to Eq. 3.9.

The finite wavelength distribution produced by a velocity selector or a crystal monochromator is well described by a normalised triangular function

$$f(\lambda) = \begin{cases} \frac{\lambda - \lambda_{min}}{\Delta\lambda(\lambda_0 - \lambda_{min})} & \text{if } \lambda_0 - \Delta\lambda \leq \lambda \leq \lambda_0 \\ \frac{\lambda_{max} - \lambda}{\Delta\lambda(\lambda_{max} - \lambda_0)} & \text{if } \lambda_0 < \lambda \leq \lambda_0 + \Delta\lambda \\ 0 & \text{otherwise} \end{cases} \tag{3.11}$$

where λ_0 is the centred wavelength with a width of the distribution at half of the maximum of $\Delta\lambda$ (FWHM). The minimum and the maximum wavelength found in

the spectrum are given by $\lambda_{min} = \lambda_0 - \Delta\lambda$ and $\lambda_{max} = \lambda_0 + \Delta\lambda$, respectively. The distribution is illustrated in Fig. 3.5. Although the convolution integral for this function can be solved, the resulting function has a singularity at $B = 0$ and is hence rather unstable in a fitting process using real data.

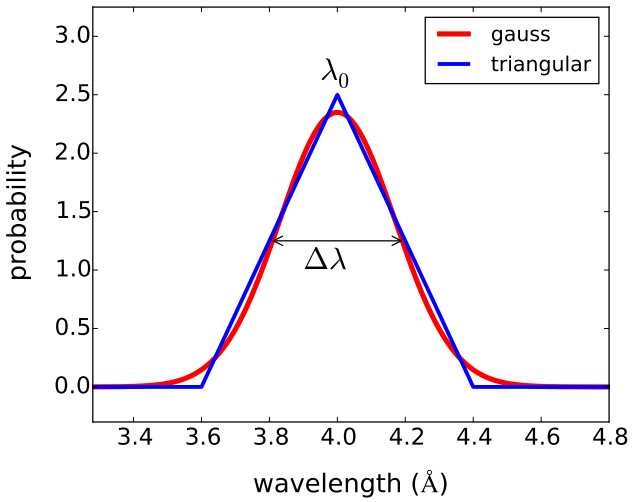

Figure 3.5.: The finite wavelength distribution produced by a neutron velocity selector or a monochromator typically corresponds to a triangular function. For the effect on the polarisation the approximation as a Gauss function is used. Both distributions are normalised with respect to the area and have the same width $\Delta\lambda$ at half of the maximum.

In contrast, the convolution of $P(B)$ with a normalised Gaussian function

$$f(\lambda) = \frac{1}{\sigma\sqrt{2\pi}} \exp\left(-\frac{\lambda^2}{2\sigma^2}\right) \tag{3.12}$$

with $\sigma = \Delta\lambda/\sqrt{8\ln(2)}$ can be calculated easily by taking the real part of the Fourier transform of the Gauss function. A normalised Gauss function approximates the triangular function reasonably well as can be seen in Fig. 3.5. Realistic values for the wavelength $\lambda_0 = 4$ Å and $\Delta\lambda/\lambda = 10$ % were used for the illustration.

As an important feature the full width of the distributions at half of the maximum is similar. When assuming a Gaussian wavelength distribution for Eq. 3.10 the resulting polarisation reads

$$P(B) = \exp\left(-\frac{\pi^2\gamma^2\alpha^2L^2B^2\Delta\lambda^2}{8\ln(2)}\right)\cos(\gamma B\alpha\lambda L) \tag{3.13}$$

which corresponds to a cosine enveloped by another Gauss function. Now, the width of

the Gauss distribution scales with the inverse width of the wavelength distribution. The product of these two functions can be fitted easily to experimental data. The effect of a finite wavelength distribution on the measured polarisation using a Mezei-type spin-flipper is illustrated in Fig. 3.6 in comparison with the perfectly monochromatic case.

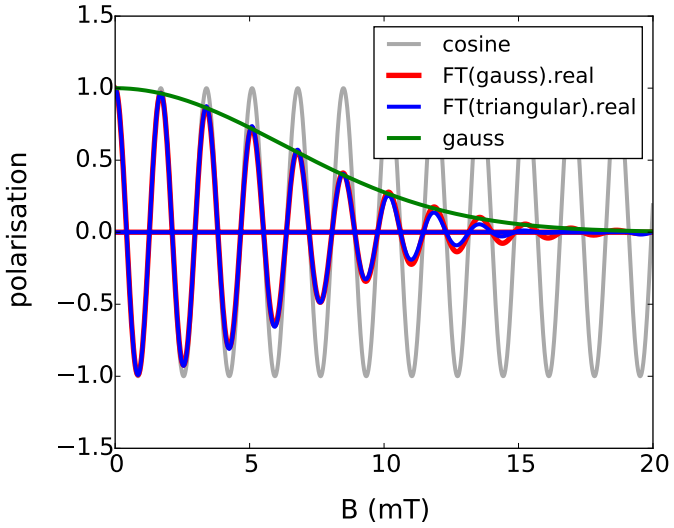

Figure 3.6.: Effect of a finite wavelength distribution on the calculated polarisation for a Mezei-type spin-flipper as described in the text. A Gaussian as well as a triangular wavelength distribution were used to calculate the polarisation according to Eq. 3.10. The oscillation of the polarisation is caused by the magnetic field in the spin-flipper that is perpendicular to the incoming polarisation. For an ideally monochromatic beam the polarisation is described by a cosine function. The effect of a finite wavelength distribution $\Delta\lambda/\lambda$ is manifested in the enveloping function of the cosine which, under the assumption of a Gauss distribution, is given by Eq. 3.13. It corresponds to the original cosine multiplied by the Fourier transform of the distribution which in this case is again a Gauss function. For the first oscillations at small fields B the enveloping Gauss function describes the behaviour for both wavelength distributions well.

An ideal perpendicular magnetic field in the spin-flipper of length $L = 2$ cm was assumed. The above shown wavelength spectrum, centred at 4 Å with $\Delta\lambda/\lambda = 10$ %, was used for the calculation. The polarisation is shown as a function of the perpendicular field B in the spin-flipper. The polarisation vector rotates around the axis of the field if the magnitude of this field is tuned continuously.

Because of the finite wavelength distribution, the single neutron spins fan out over a certain angular range depending on the wavelength and hence reduce the total

polarisation. In Fig. 3.6 the finite wavelength distribution is manifested in the function enveloping the cosine which in this particular case is a Gaussian function as in Eq. 3.13.

From Eq. 3.13 it can be concluded that such spin-flipper devices are best used for neutron beams with a rather small wavelength distribution. The effect after one single spin-flip (i.e. a rotation by an angle π) is negligible for $\Delta\lambda/\lambda = 10\%$ which is the largest $\Delta\lambda/\lambda$ used in this study at the instrument ANTARES. These results will be used later to discuss the performance of the newly designed set up at ANTARES where a velocity selector has been installed during the course of this study.

3.2. Neutron Depolarisation in Ferromagnets

In a ferromagnetic domain the ordered moments produce a net flux density per domain. In free space this field inside a single domain would be closed by an outer stray field pointing in the opposite direction. The domain structure in a ferromagnet is hence build in a way to minimise the energy of the stray fields. Without an external field the domain structure typically forms closed magnetic loops in order to minimise the free energy. In three dimensions this may lead to obscure domain formations. However, for simplicity in the following discussion it is assumed that the domain size along one specific direction through the sample is well described by the average domain length δ. It is further assumed that the orientations of the magnetic fields of all domains are distributed randomly when no additional magnetic field is present. The effects of crystal anisotropy on the magnetisation are hence neglected as well.

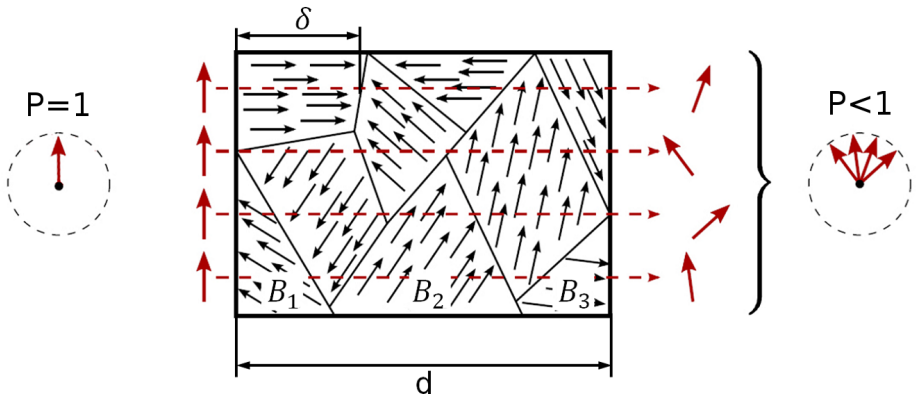

Figure 3.7.: Illustration of the depolarisation of a polarised neutron beam due to transmission through a ferromagnetic domain structure in a sample of thickness d. An average domain size δ is assumed. The internal magnetic field in each domain is denoted as B_i. In zero magnetic field the domains are assumed randomly oriented such that outer stray fields are minimised. Between two subsequent domains a non-adiabatic transition is assumed. This implies that the average domain wall thickness is small compared to the domain size. Since the spatial resolution is limited and since the beam profile shows a certain divergence and wavelength distribution each neutron takes a different path and experiences a different amount of spin precession. The averaging of all neutron spins detected leads to a decrease of the polarisation $P < 1$. Figure adapted from [58].

Neutrons passing such an arrangement of domains will traverse several volumes of randomly oriented magnetic fields of the same strength (for homogeneous materials) which are separated by domain walls. This may lead in two distinct ways to a change in the polarisation. The neutron beam is always characterised by a certain divergence

and a wavelength distribution. In addition, the polarisation is detected with a finite spatial resolution restricted by the size of one detector pixel. As shown in the previous section a finite wavelength distribution leads to a depolarisation of the beam even in the case of a non-adiabatic field transition. The divergence and the limited spatial resolution of the detector lead to an averaging over several different neutron paths through the sample which results in additional depolarisation.

The first successful description of the transmission of a polarised neutron beam through a ferromagnetic sample was developed by Halpern and Holstein in 1941 [52, 129]. A mathematical procedure was provided in order to obtain a simple formula for the polarisation which captures the essential parameters characterising the neutron beam and the ferromagnetic sample.

In this description the polarisation of a neutron beam with average wavelength λ and a corresponding neutron velocity $v = h/(m_n\lambda)$ is considered. The time-dependent evolution of the spin state is described by the solution of the Larmor equation assuming a constant field B. For the perpendicular component of the neutron spin it follows

$$\mathbf{S}_{i,\perp}(t) = \cos(\omega_i t)\mathbf{S}_{i-1,\perp} + \sin(\omega_i t)\frac{\mathbf{B_i}}{B_i} \times \mathbf{S}_{i-1,\perp} \tag{3.14}$$

where $\omega_i = \gamma B_i$ is the Larmor frequency in one domain i with magnetic field B_i. For simplicity it is assumed that all domains in transmission have the constant average length δ. For a given neutron wavelength the time τ_i for a neutron being inside the domain i can be approximated by $\tau_i = \frac{\delta}{v} = \alpha\lambda\delta \equiv \tau$. Furthermore, we assume that the magnetic field B_i has the same magnitude in each domain, i.e. $B_i \equiv B$. These assumptions result in a constant Larmor frequency for each domain as expressed by $\omega_i = \gamma B_i \equiv \gamma B \equiv \omega$. The solution of the Larmor equation describing the motion of the spin vector can now be written as:

$$\mathbf{S}_{i,\perp} = \cos(\omega\tau)\mathbf{S}_{i-1,\perp} + \sin(\omega\tau)\frac{\mathbf{B}}{B} \times \mathbf{S}_{i-1,\perp} \tag{3.15}$$

For further steps a depolarisation operator $\hat{D}_i$ is defined which operates on the spin as:

$$\hat{D}_i\mathbf{S} = \cos(\omega\tau)(1 - \hat{p}_i)\mathbf{S} + \sin(\omega\tau)\frac{\mathbf{B}_i}{B} \times \mathbf{S} \tag{3.16}$$

In the equation above $\hat{p}_i$ is a so-called projection operator which equals one if the spin direction is along the field direction and it equals zero if perpendicular to it. The operator $\hat{D}_i$ hence describes the precession of the spin $S_{i,\perp}$ experienced during transmitting the domain with an internal field $\mathbf{B}_i$:

$$\mathbf{S}_i = \hat{D}_i\mathbf{S}_{i-1} \tag{3.17}$$

Successive application of $\hat{D}$ on the vector $\mathbf{S}$ then describes the depolarisation of the

neutron beam after transmission of a series of N randomly oriented domains as follows:

$$\mathbf{S}_N = \hat{D}_N..\hat{D}_2\hat{D}_1\mathbf{S}_0 = \prod_{i=1}^{N}\hat{D}_i\mathbf{S}_0 \tag{3.18}$$

In order to calculate the depolarisation after passing a series of domains in the sample the average over the multi product of depolarisation operators needs to be calculated:

$$\mathbf{S}_N = \left\langle \prod_{i=1}^{N}\hat{D}_i \right\rangle \mathbf{S}_0 \tag{3.19}$$

By assuming a completely random distribution of independent magnetisation vectors of the domains one may write:

$$\left\langle \prod_{i=1}^{N}\hat{D}_i \right\rangle = \prod_{i=1}^{N}\langle\hat{D}_i\rangle \tag{3.20}$$

Following the procedure described in [52] the expectation value of $\langle\hat{D}_i\rangle$ may now be simplified to:

$$\langle\hat{D}_i\rangle = \frac{1}{3} + \frac{2}{3}\cos(\omega\tau) = 1 - \frac{4}{3}\sin^2\left(\frac{\omega\tau}{2}\right) \tag{3.21}$$

Please note that the index i is only required to represent the multiple application of $\hat{D}_i$ on the spins. For the further discussion the depolarisation operator can hence be regarded as a scalar factor. The effect of a successive application of $\hat{D}_i$ on the spin can be further investigated by regarding two distinct cases that eventually occur in ferromagnetic systems. These cases are discussed separately in the following two subsections.

3.2.1. Small Spin Rotation per Domain

In the first case considered the internal field per domain B is weak and hence the Larmor frequency $\omega_L \ll 2\pi/\tau$. As the depolarisation operator was already simplified to a scalar factor according to Eq. 3.21 this suggests a first-order approximation for the sine term:

$$\prod_{i=1}^{N}\langle\hat{D}_i\rangle = \prod_{i=1}^{N}\left(1 - \frac{4}{3}\sin^2\left(\frac{\omega\tau}{2}\right)\right) = \prod_{i=1}^{N}\left(1 - \frac{1}{3}(\omega\tau)^2\right) \tag{3.22}$$

The multiple product corresponds to taking the power of N which is the total number of domains traversed in the beam direction. The brackets in the last product can now be identified as the Taylor expansion of the exponential function. One may write:

$$\prod_{i=1}^{N}\left(1 - \frac{1}{3}(\omega\tau)^2\right) = \prod_{i=1}^{N}\left(\exp(-\frac{1}{3}\omega^2\tau^2)\right) = \exp(-\frac{1}{3}\sum_{i=1}^{N}\omega^2\tau^2) \tag{3.23}$$

Inserting the given parameters and assuming that the relation $\tau^2 = \alpha^2\lambda^2 d\delta$ holds for small domain sizes finally yields:

$$\mathbf{S}_N = \exp\left(-\frac{1}{3}\gamma^2 B^2 d\delta\alpha^2\lambda^2\right)\mathbf{S}_0 \tag{3.24}$$

The formula includes the average domain length δ and the thickness d of the sample in transmission direction. Furthermore, the wavelength λ and the constant $\alpha = m_n/h$ are used. It should be mentioned again that this is the quantity we measure using the polarisation of the neutron beam $P = \langle S\rangle$ as the ensemble average of neutron spin states. The temperature-dependence of the polarisation due to the sample is implicitly included by the magnetic flux density per domain. For a more intuitive interpretation it is required to insert a model function for the magnetic field $B(T)$ per domain. We may use the prediction for the magnetisation $M(T)$ according to the Ginzburg-Landau approaches as discussed in Sec. 2.2. For our purpose we use a form such as

$$M^2(T) = M_0^2\left(\frac{T - T_C}{T_C}\right)^{1/\beta} \tag{3.25}$$

which may be derived more generally for the magnetisation. For the magnetisation it is assumed that $B(T) = \mu_0 M(T)$ in order to describe the magnetic field B in each domain as experienced by the neutron spin. Furthermore, it is assumed that the average domain size δ is constant with temperature. The exponent β takes different values according to the underlying model assumptions. For example in the Stoner model $\beta = 1$ while in the spin fluctuation theory a value $\beta = 2$ is found for weak ferromagnets. In real materials the critical exponent varies according to the precise nature of the underlying magnetic interactions and more often values $\beta < 1$ are observed. Such a behaviour may not be explained by the simple mean-field models discussed here. Nevertheless, the free parameter β allows an excellent fit to the neutron data collected in this study.

For temperatures above the Curie temperature T_C the magnetisation vanishes and $B = 0$. The polarisation of the neutron beam is hence not affected when transmitting a paramagnetic sample. For temperatures $T \leq T_C$ the internal field per domain $B > 0$ increases and a decrease in the polarisation is observed according to Eq. 3.24 with decreasing temperature. The decrease of polarisation due to a ferromagnetic sample is referred to as depolarisation. In Fig. 3.8 the influence of the parameters T_C and λ and of the magnetic field $B(T)$ in Eq. 3.24 is demonstrated exemplarily for a sample of thickness $d = 1$ mm and an average domain size $\delta = 10$ μm. The exponent β in Eq. 3.25 is chosen as β=2 to produce Fig. 3.8a,b and Fig. 3.8d. The exponent β is varied in Fig. 3.8c to demonstrate the influence on the shape of the curve.

The spin fluctuation theory as summarised in Sec. 2.2.2 has shown remarkable agreement with experiment. One important prediction is the relation between ordered

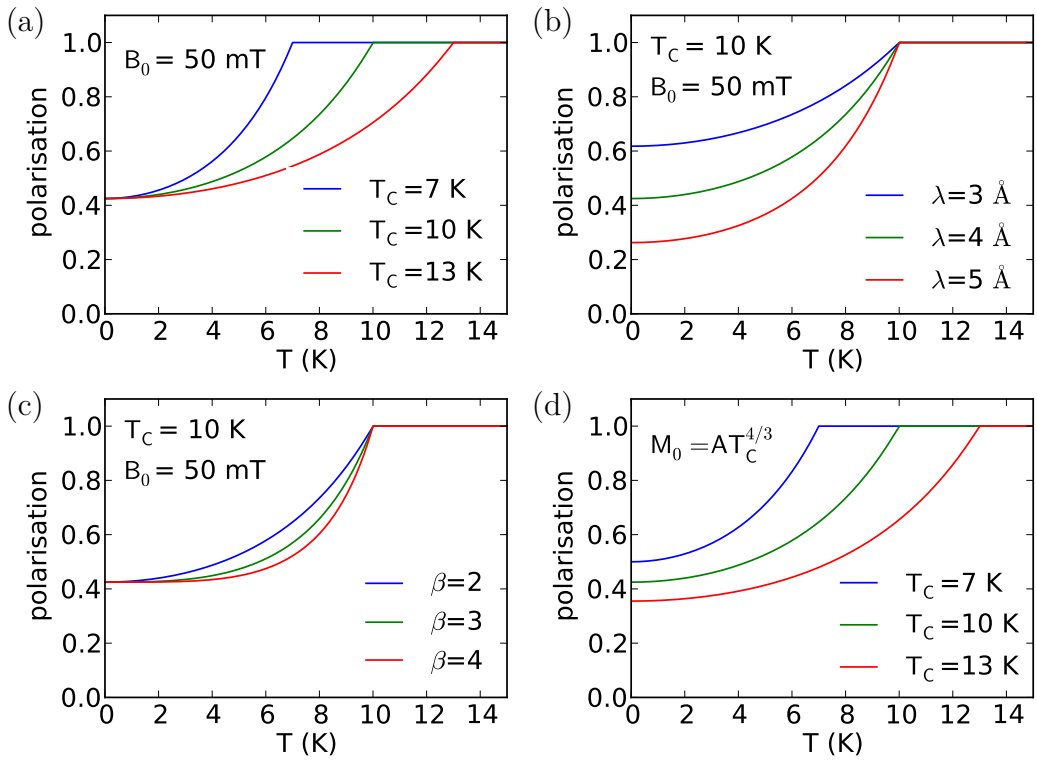

Figure 3.8.: Polarisation as a function of temperature to illustrate the influence of the different parameters used in the model in Sec. 3.2.1 for the case of small spin rotation per domain. For the variation of the internal magnetisation per domain the form $B^2 = B_0^2(1-(T/T_C)^\beta)$ was used. (a) The variation of T_C for otherwise fixed parameters shifts the transition but yields the same value for the polarisation at $T = 0$. (b) Fixed $T_C = 10$ K but using different wavelengths where the depolarisation is enhanced for longer wavelengths. (c) The shape of the curve changes when varying the critical exponent β used in the expression for B as in Eq. 3.25. Larger exponents produce a steeper transition at T_C if the other parameters are fixed. (d) Assuming the relation $B_0 = \mu_0 M = AT_C^{4/3}$ as predicted by the spin fluctuation theory described in Sec. 2.2.2 results in well separated depolarisation curves. Interestingly, the effect of hydrostatic pressure is also demonstrated by panel (d) as T_C is typically proportional to $p - p_c$ where p_c is the critical pressure.

moment $M_0 = AT_C^{4/3}$ and the ordering temperature T_C. In Fig. 3.8d this relation was used to demonstrate the effect on the neutron polarisation. Interestingly, the effect of hydrostatic pressure may then be illustrated by Fig. 3.8d as well as the ordering temperature T_C is predicted to show approximately a linear dependence $T_C \propto (p - p_c)$ on pressure up to the critical pressure p_c as summarised in Sec. 2.2.

3.2.2. Several Spin Rotations per Domain

The behaviour of the neutron polarisation is different if several spin rotations occur in each ferromagnetic domain. This may be either due to a larger internal field B in each domain or due to a larger average domain size δ. For this case $\omega_L \geq 2\pi/\tau$ and the averaging procedure used before is not valid. In this limit however $\omega\tau \geq 2\pi$ and the product of depolarisation matrices reads

$$\prod_{i=1}^{N}\langle\hat{D}_i\rangle = \prod_{i=1}^{N}\langle 1 - \frac{4}{3}\sin^2\left(\frac{\omega\tau}{2}\right)\rangle = \left[1 - \frac{4}{3}\sin^2\left(\frac{\omega\tau}{2}\right)\right]^{T/\tau} \tag{3.26}$$

The exponent T/τ is given by the ratio of time-of-flight $T = d/v$ of the neutron through the sample and the time τ spend in average in one domain. The ratio T/τ hence corresponds to the average domain count N in transmission direction. For large $\omega\tau$ one may now approximate $\sin^2\left(\frac{\omega\tau}{2}\right) = \left(\frac{1}{\sqrt{2}}\right)^2 = \frac{1}{2}$ as stated in [52] using the root mean square value. According to Eq. 3.26 this yields for the spin after traversing N domains

$$S_N = 3^{-T/\tau}S_0 = 3^{-d/\delta}S_0 = \left(\frac{1}{3}\right)^N S_0 \tag{3.27}$$

This expression does not depend explicitly on the temperature, but it is obviously only valid for temperatures close to T_C and for $T < T_C$ below the Curie temperature. The result depends only on the average domain size in other words on the average domain count in transmission direction. From a comparison it may be concluded that the first scenario considered in Sec. 3.2.1 may apply for rather weak ferromagnets where the internal field B in each domain is small. The second case considered is expected to apply if the internal field B per domain is very large. The depolarisation as a function of temperature would hence correspond to a step function positioned at the transition temperature T_C. In an experiment this would be more realistically modelled by a Gaussian error function. This function can be regarded as the convolution of a sharp step function with a Gaussian distribution. The edge of the step function is thereby smoothed and shows a finite width. A corresponding scenario is discussed in the following section.

3.2.3. Effect of a Distribution of the Curie Temperature

Even in single-crystalline metallic samples of high quality the crystal lattice may show imperfections. In the case of less pure samples the lattice spacings may vary over the entire sample volume which leads to internal stress. In ferromagnetic systems this may for example lead to a smeared phase transition. The effect of disorder may then be visualised by a distribution of different Curie temperatures in the sample.

The effect can be incorporated in the theoretical description by using a convolution

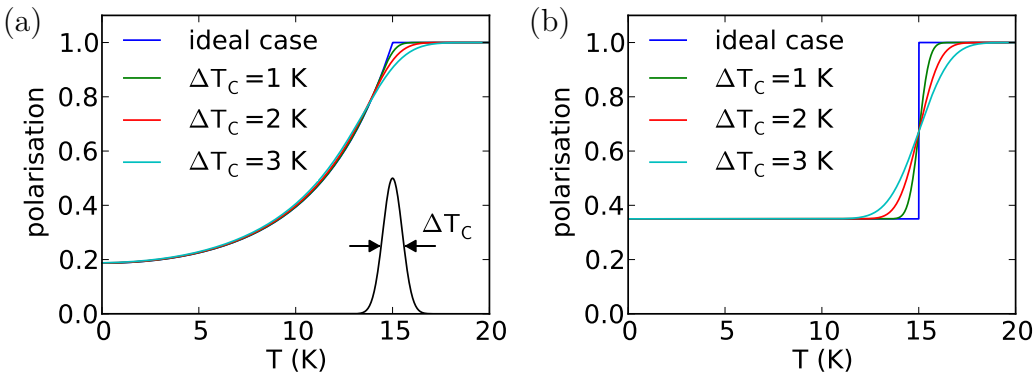

Figure 3.9.: Convolution of the theoretical depolarisation for the two limiting cases described in Sec. 3.2.1 and 3.2.2 as the ideal case (dark blue) showing a sharp transition at T_C=15 K. The sharp edge at T_C gets smoothed over a given temperature range depending on the width of the distribution ΔT_C. Shown in (a) is the case where the Larmor frequency $\omega_L \ll 2\pi/\tau$ in a domain is low and an exponential dependence is expected according to Eq. 3.24. In (b) the case $\omega_L \gg 2\pi/\tau$ is illustrated where a constant amount of depolarisation below T_C occurs as described by Eq. 3.27.

of the depolarisation model with a distribution function for T_C. For simplicity it may be assumed that a Gaussian function represents the T_C distribution in good approximation.

$$P(T) = \int_0^\infty P(T')g(T - T')dT' \tag{3.28}$$

where $g(T) = \exp(-T^2/2\sigma^2)$ is a Gaussian function. The standard deviation σ can be used to evaluate ΔT_C, the full width at half maximum (FWHM), by using $\Delta T_C = \sigma\sqrt{8\ln 2}$. The convolution can not be solved analytically, however, a numerical solution is possible and illustrates the behaviour. An according discrete convolution is then defined by

$$(P \otimes g)[t] = \sum_{t'=t_{min}}^{t_{max}} P[t'] \cdot g[t - t'] \tag{3.29}$$

where the square brackets indicate that t denotes an item of a list of discrete temperature values. For the actual data analysis a Python program was written that adapts the step size in the convolved fit function to an amount where all experimental data can be binned to without loss of precision. The numerical solution is shown in Fig. 3.9a and 3.9b for both cases of the depolarisation model expressed by Eqs. 3.24 and 3.27. The case where the internal field per domain is strong shows mainly an effect directly at the transition temperature where a smoothing occurs. For the second case the sharp step function is transformed to a Gaussian error function with a certain slope at the

transition temperature. As mentioned both cases were observed in experiments. The next chapter describes the experimental requirements to measure the depolarisation. Furthermore, the laboratory techniques used in this study are described.

4. Experimental Details

The magnetic properties of the weak ferromagnetic systems $CePd_{1-x}Rh_x$, $ZrZn_2$ and $Fe_{1-x}Cr_x$ were investigated in this study using several different experimental techniques. Of particular interest are the magnetisation as a function of temperature $M(T)$ and as a function of applied fields $M(H)$ since both are directly involved in the theoretical description of the magnetic state. These properties can be measured using different experimental techniques and are thereby probed on different time and length scales. In neutron depolarisation measurements the polarisation contains the magnetisation per domain as a microscopic property. An averaging is done along the transmission path through the sample by assuming a constant average domain size as described in Sec. 3.2. The typical time scale which is probed in transmission through a sample is of the order of nanoseconds. It is mainly determined by the neutron wavelength and the dimensions of the ferromagnetic regions in a sample. The typical length scales which can be probed using this technique is hence of the order of micrometers.

In this study a new set up for neutron depolarisation experiments was developed and tested which allows to measure the polarisation as a function of temperature and external magnetic field applied at the sample position. The new set up thereby enables to measure the depolarisation in a user-friendly way under variation of temperature and magnetic field. As was also shown in this study the set up is well-suited for the investigation of samples under hydrostatic pressure by using a clamp pressure cell.

The following section describes the technical details of the preparation and characterisation of the samples that were investigated. In Sec. 4.2 the details of the pressure cell used in this study and the method to determine the pressure is given. Bulk measurements have been carried out in the laboratories of the institute E21 at TUM. For $ZrZn_2$ the magnetisation was measured using a VSM (Vibrating Sample Magnetometer) from Oxford Instruments. For the $Fe_{1-x}Cr_x$ samples the ac-susceptibility and magnetic field loops were measured using a PPMS (Physical Property Measurement System) from Quantum Design. The technical details are described in Sec. 4.3. The depolarisation measurements were done at the research neutron source FRM II. The instruments ANTARES, MIRA and POLI, where the experiments have been carried out, and the methods used at each instrument are described in Sec. 4.4.

4.1. Sample Preparation

The $CePd_{1-x}Rh_x$ samples investigated in this study were prepared and characterised as described in [64, 65, 107]. Polycrystals were prepared by arc-melting under argon atmosphere, flipped and remelted several times. The batches were remelted in a high-frequency levitation crucible and finally annealed for 7 days at 700 °C under vacuum conditions. The Bridgman technique was used to produce single-crystalline specimen from the polycrystalline ingots using a pulling rate of 3-5 mm/h in tantalum crucibles. The single-crystals were polished afterwards to remove foreign phases. The composition was verified using energy dispersive x-ray spectroscopy (EDX). In addition we have used neutron depolarisation imaging to characterise the metallurgical homogeneity. The polycrystalline samples used in this study were cut into discs with a thickness of 1 mm and a diameter of 7-10 mm. The single-crystals were not regularly but nearly disc-shaped and approximately of the same dimensions.

Single-crystalline samples of $ZrZn_2$ were provided for this study by S. Hayden and L. Schreurs. The growth process for the sample used by Schreurs et al. and the characterisation of the crystal quality is described in [130]. This sample is roughly disc-shaped with 1 mm thickness and 6 mm diameter and was investigated under ambient pressure. For the measurements on $ZrZn_2$ under pressure the sample from S. Hayden was used. As described in [131, 132] the ingots for this sample was produced using a tungsten cell filled under argon atmosphere. The single-crystals were grown out of the polycrystals using very slow controlled cooling starting just above the melting point. The sample used in this study was a small cylindrical piece of 2.5 mm diameter and 3 mm height. It was the same sample and the same pressure cell as used in previous studies and is well characterised by [70, 71, 133].

A series of eight polycrystalline $Fe_{1-x}Cr_x$ sample was produced in this study in collaboration with A. Bauer and G. Benka as part of their PhD theses. The raw materials with a purity of 4N were used and inductively heated in a metal-sealed rod-casting furnace. From the resulting 8 g weight polycrystalline samples similar discs were cut from the centre with a diameter of around 8 mm and thickness of 1 mm. The samples were polished afterwards to remove surface artefacts from the spark-erosion cutting process. For now the ac-susceptibility and the magnetisation has been measured. The study at hand includes the first sample characterisation in terms of the metallurgical homogeneity using neutron depolarisation measurements.

4.2. Application of Pressure

For the measurements on $ZrZn_2$ hydrostatic pressure was the key parameter for the series of measurements. For this study a non-magnetic clamp pressure cell made of Cu:Be (Berylco 25) was used which is depicted in Fig. 4.1 on the left hand side. The pressure was applied using a non-magnetic Tungsten-carbide stamp with a very low Nickel content (with a total moment of the order of $4 \cdot 10^{-10}\mu_B$). The maximum pressure achievable with such cells is typically around 20 kbar. In our study on $ZrZn_2$ the cell reached its elastic limit around 19 kbar. The pressure was set using a manual hydraulic pressure station. A blocking screw was then used to hold the pressure in the cell. The sample itself is kept in a medium to transmit the pressure. In this case we have used a methanol-ethanol mixture with a 4:1 ratio. The sample and the pressure medium are kept in a small Teflon capsule which rests inside the cell.

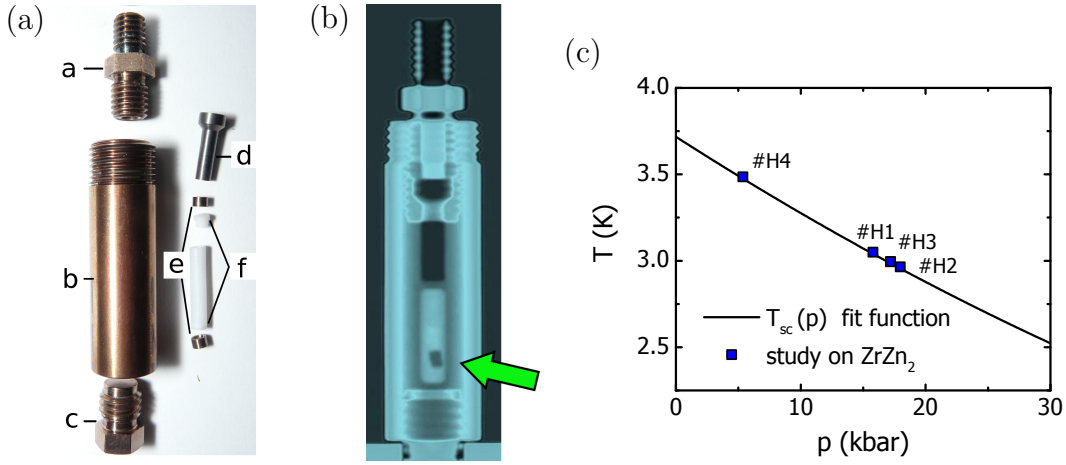

Figure 4.1.: (a) photograph of the Cu:Be clamp cell to apply hydrostatic pressure on the sample. The cell consists of [a] lock-screw, [b] the cell body and [c] a lock-nut. The pressure is applied by a tungsten-carbide piston [d] and varied using the screw. The sample itself is located in a Teflon capsule [f] which is filled with a pressure medium. Additionally, a small Sn plate is placed at the bottom of the Teflon capsule which is used to determine the pressure as described in the text. The capsule is closed by two self-cutting rings [e] when pressure is applied. (b) Neutron radiography of the mounted pressure cell including the $ZrZn_2$ sample (indicated by the green arrow). The small Sn plate is located just below the $ZrZn_2$ sample, however due the low absorption it is barely visible in the radiography. (c) Fit function for the pressure-dependence of the superconducting Sn transition (see Eq. 4.1), e.g. measured by resistivity or susceptibility. The fit function is thereby used to determine the applied pressure on the $ZrZn_2$ sample. The four data points #H1 to #H4 were determined in this study.

The pressure is first estimated using the analogue manometer of the hydraulic hand press and later determined accurately using the superconducting transition of a small

Sn sample additionally located in the bottom of the Teflon capsule. The transition is clearly visible in the magnetisation which was measured using a Vibrating Sample Magnetometer described separately in the next section. The superconducting transition as a function of pressure is known from previous studies and may consequently be used to determine the pressure in the Cu:Be cell. A reliable fit function for the superconducting transition temperature of Sn T_{sc} as a function of pressure p (in kbar) is given in Ref. [134] by

$$\begin{aligned} \Delta T_{sc}(p) &= T_{sc}(p) - T_{sc}(0) \\ &= p \cdot 4.63 \times 10^{-2}\ \mathrm{K/kbar} + p^2 \cdot 2.16 \times 10^{-4}\ \mathrm{K/kbar}^2 \end{aligned} \tag{4.1}$$

where $T_{sc}(0) = 3.74$ K at ambient pressure. Although small deviations from the absolute value of $T_{sc}(0)$ may be possible due to varying Sn sample quality and thermal coupling it is assumed that the functional dependence will not change significantly. The relative change $\Delta T_{sc}(p)$ may hence be used as verification for the pressure calibration. Shown in Fig. 4.1 on the right hand side is the superconducting transition temperature for Sn as given by Eq. 4.1 and four data points as determined in the study of $ZrZn_2$.

4.3. Laboratory Techniques

Bulk measurements were performed in the laboratories of the institute E21 at TUM in order to complement the neutron data. Specifically, the susceptibility was measured as a function of temperature for different frequencies and magnetic field histories in order to probe the static as well as the dynamic behaviour. Magnetic field loops were recorded in order to investigate hysteresis effects and to determine the saturation magnetisation.

For the magnetisation measurements on $ZrZn_2$ we have used a Vibrating Sample Magnetometer (VSM) from Oxford Instruments. In a VSM the sample is oscillating linearly (vibrating) along the central axis inside a pick-up coil. The magnetic response of the sample produces a signal in the pick-up coil. The oscillator is driven by the reference signal of a lock-in amplifier. The detected signal of the pick-up coils is fed back to the lock-in amplifier. In this way, magnetic field loops up to 9.0 T can be conducted along the central axis using a superconducting electromagnet. The VSM covers a temperature range from $T = 2.5$ K to 300 K by cooling with liquid ^{4}He. The $ZrZn_2$ sample was placed inside a Cu:Be pressure cell during these measurements. In addition, a Sn sample was located in the pressure cell. The signature in the magnetisation was used for the determination of the pressure inside the cell. The magnetisation measurements were done in collaboration with M. Halder. Further technical details on the VSM can be found e.g. in [135].

The ac-susceptibility and the magnetisation were measured on $Fe_{1-x}Cr_x$ using a Physical Property Measurement System (PPMS) from Quantum Design. For the ac-susceptibility measurements the sample was fixed at a position between the pick-up coils. An oscillating field is produced using the reference signal of a lock-in amplifier. The response of the sample is measured using pick-up coils feeding the lock-in amplifier. In magnetisation measurements the sample is pulled out of the pick-up coil to generate a signal. The PPMS covers a temperature range $T = 1.6$ K to 300 K by cooling with liquid ^{4}He. Magnetic field loops up to 9.0 T can be measured where the field is produced using a superconducting electromagnet. Further technical details on the PPMS can be found e.g. in [136].

4.4. Neutron Depolarisation Measurements

As discussed in Sec. 3.2 for neutron depolarisation measurements an initially polarised neutron beam is analysed after transmission through the sample. When passing a ferromagnetic sample, the domain structure leads to a change in the polarisation as expressed by Eqs. 3.24 and 3.27. Typically, a decrease in the polarisation is observed which is referred to as depolarisation. In contrast a purely paramagnetic sample does not affect the polarisation of the neutron beam in transmission. The depolarisation technique is sensitive to very small magnetic moments forming a domain structure. It is hence an ideal technique to track ferromagnetic Quantum Phase Transitions. As the technique uses neutrons as transmission probe it furthermore allows to easily vary essential parameters that control the magnetic state of the sample and are hence particularly important for the desired experiments. In this study these are the temperature of the sample, an applied magnetic field as well as hydrostatic pressure on the sample by using pressure cells made of an adequate material.

Neutron depolarisation measurements can be performed at an instrument which is able to detect the transmitted neutrons and they require a polarisation analysis option. A sketch of a typical set up was already shown in Fig. 3.1. In order to control the temperature a cryostat is needed for the sample under investigation. A suitable electro magnet, e.g. a coil pair in Helmholtz geometry, is required to prepare the magnetic history of the sample and to investigate the polarisation as a function of magnetic field. All of these requirements could be met at the instruments MIRA and ANTARES at FRM II where most of the depolarisation studies were carried out. A feasibility study was carried out at the instrument POLI using the 3D polarisation analysis option CryoPAD (see [125, 137–139] and references therein). The wavelength λ and the wavelength resolution $\Delta\lambda/\lambda$ together with the maximum polarisation P_0 achieved at the beam lines ANTARES, MIRA and POLI are listed in Tab. 4.1.

	λ	$\Delta\lambda/\lambda$	P_0	Polarising devices
ANTARES	4.13 Å	10 %	72 %	Two V-cavities
MIRA	4.59 Å	2 %	81 %	Solid State Bender, V-cavity
POLI	1.4 Å	1.5 %	65 %	Two ^{3}He spin filter cells

Table 4.1.: Wavelength λ and wavelength resolution $\Delta\lambda/\lambda$ used for the polarisation and analysis at the experiments at the instruments ANTARES, MIRA and POLI. In addition, the achieved maximum polarisation P_0 and the polariser/analyser devices are listed.

The experiments at ANTARES and MIRA were carried out using a specialised depolarisation set up. Several new components were developed for the study at the instrument ANTARES. At both instruments a magnetic field could be applied to the sample using

an already bespoken coil pair. In contrast, when using the CryoPAD option at the instrument POLI, it is required to keep the sample in zero magnetic field. However, this enables to set and also to analyse the neutron polarisation in an arbitrary direction and hence to investigate anisotropy effects of the sample.

The technical details for the instruments and in particular the magnetic field geometries along the neutron path are very different for the experiments done at the instruments ANTARES and MIRA compared to the instrument POLI. These details are hence described separately in the next sections.

4.4.1. The Instrument ANTARES at FRM II

ANTARES is a highly flexible neutron imaging instrument. A sketch of the instrument design is shown in Fig. 4.2. The neutrons are extracted from the cold moderator which results in a mixed spectrum of cold and thermal neutrons. The standard set up for neutron imaging (which we use as a collective term for neutron radiography and neutron tomography) can be compared to that of an optical pinhole camera. The set up consists, in this order, of the neutron source, a pinhole collimator, possibly a device to select a certain wavelength band, the sample under investigation and a 2D detector. The pinhole collimator defines the spatial resolution which is achievable to image the sample. The experiments for this study at ANTARES were performed in chamber 2 (see Fig. 4.2) where the detector-to-pinhole distance is L=9 m. We have used the pinhole collimator L/D=800 [1] which is available at ANTARES.

A high resolution scintillator/CCD detector with an active area of $150 \times 150\,\mathrm{mm}$ (2048×2048 pixels) was used. A theoretical pixel size of 75 $\mu\mathrm{m}$ was thereby achieved in our experiments, the true spatial resolution resulting from the finite beam collimation was approximately 150 $\mu\mathrm{m}$. A wavelength distribution centred at $\lambda = 4.13\,\text{Å}$ with $\Delta\lambda/\lambda$=10 % was provided using a new neutron velocity selector that was installed at ANTARES during this study.

The neutron depolarisation experiments were done using two different set up options. The most simple set up for polarised neutron imaging allows to apply a magnetic field at the sample position only in one direction. It has the advantage of a small distance between sample and detector which increases the spatial resolution. This set up is described in Sec. 4.4.1.1. A new set up was developed in this study which has the enables to measure the depolarisation for complete magnetic field loops. This set up is described in Sec. 4.4.1.3.

1 The ratio L/D denotes the pinhole-to-sample distance L divided by the pinhole diameter D. It is hence a measure for the beam divergence and can be used to calculate the sharpness of the image of a sample edge on the detector.

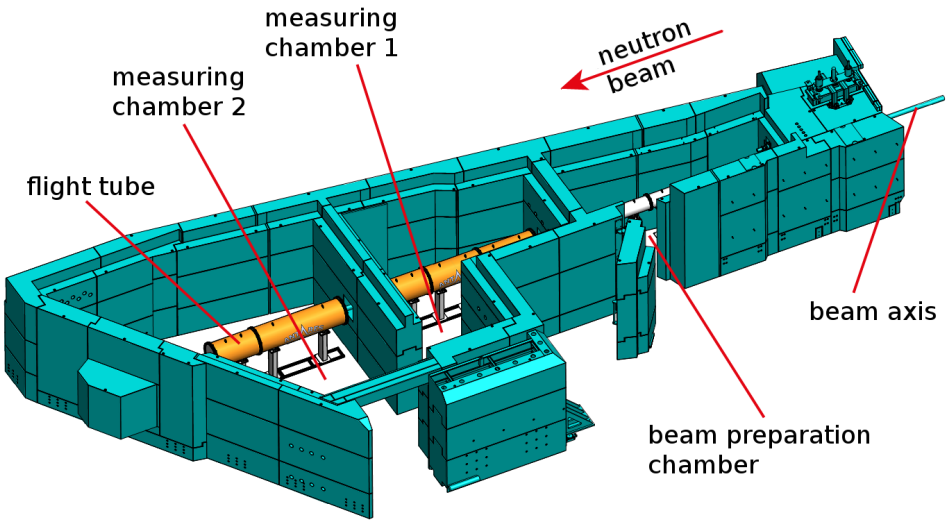

Figure 4.2.: CAD illustration of the neutron imaging instrument ANTARES. The neutron beam is collimated and prepared in the beam formation area in chamber 1. After passing flight tubes filled with ^{4}He gas in order to avoid air scattering the neutron beam is used for experiments in chamber 2 or chamber 3 depending on the desired sample environment. The figure was used with kind permission from E. Calzada.

4.4.1.1. Standard Set Up for Depolarisation Measurements

In neutron depolarisation experiments where a high spatial resolution was desirable, two ^{3}He neutron spin filter (NSF) cells were used for polarisation and analysis. The ^{3}He gas was polarised using the MEOP method at a facility at FRM II (details can be found e.g. in Refs. [125, 140]). Both cells were mounted in magnetic housings to maintain the polarisation. An additional resonance flipper coil was integrated in the polariser housing to enable a spin flip of the ^{3}He polarisation which thereby polarises the neutron beam in the opposite direction. The use of NSF cells comes with advantages especially for neutron imaging since the beam divergence is not affected by the polarisation analysis. The analyser will hence not affect the spatial resolution. However, the technique is also afflicted with some disadvantages since the ^{3}He cells depolarise with time which complicates the data evaluation. In addition, the polarised ^{3}He is very sensitive to magnetic stray fields. Therefore, it can hardly be used in experiments where magnetic fields are applied at the sample position which is located close to the analyser.

In the most simple version of the set up the polarisation is guided using vertical magnetic fields as illustrated in Fig. 4.3. For our experiments the guide fields were of the order of $B = 2$ mT. This basic set up allows to vary the magnetic field at the sample position parallel to the guide field direction. For several measurements on $CePd_{1-x}Rh_x$ we have used an already bespoken coil pair in Helmholtz geometry which

is able to provide a magnetic field up to 30 mT. An iron yoke was used to reduce outer stray fields.

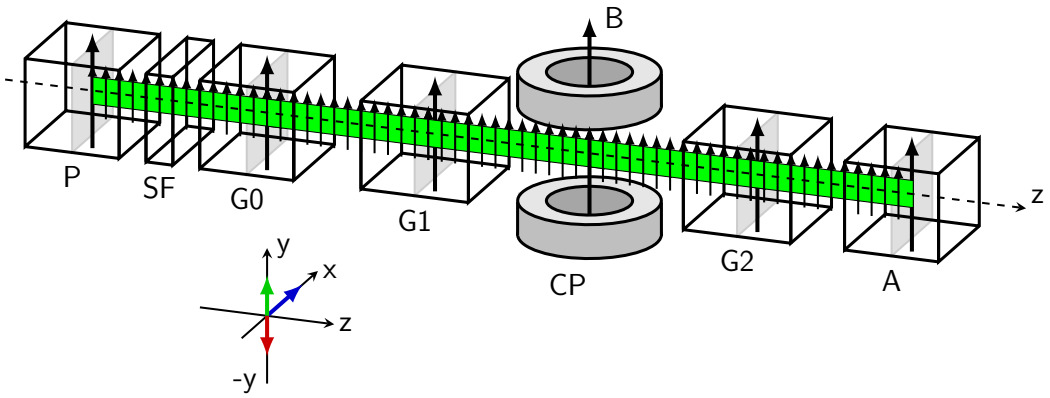

Figure 4.3.: Standard components and idealised magnetic field profile in a conventional depolarisation set up including polariser (P), spin-flipper (SF), guide fields (G0, G1 and G2) and an analyser (A). The sample is located in a coil pair (CP) which can be used to apply a magnetic field B along the guide field direction at the sample position. The magnetic guide field always points into the y-direction which requires that the applied field B points in the same direction as a zero field region would occur otherwise. The neutrons are counted behind the analyser using a scintillator/CCD based detector (not shown).

The detection limit of the depolarisation technique with the described set up is estimated as 1% of detectable depolarisation. The limit depends on the exposure time required for one set of spin-up and spin-down images which is typically between 10 and 60 seconds and it depends on initial polarisation of the neutron beam. The resolution further depends on the sample thickness and on the strength of the magnetic field per domain. According to Eq. 3.24 for a typical sample thickness of $d = 1$ mm a depolarisation of 1% corresponds to $B(T)^2\delta \approx 2{\times}10^{-10}$ Tm $= 200$ mT$^2\mu$m. For a typical average domain length of 2 μm this corresponds to a magnetic field $B = 10$ mT.

All measurements were performed using a closed-cycle cryostat from the sample environment group at FRM II, providing temperatures down to 3.5 K. In addition, for temperatures down to 0.5 K a ^{3}He-insert and down to 50 mK a ^{3}He/^{4}He dilution-insert was used. A photograph of the set up as installed at the instrument ANTARES is shown in Fig. 4.4.

4.4.1.2. New Depolarisation Set Up for Hysteresis Loops

The above set up is restricted to magnetic fields at the sample position which point only in one direction. By switching the magnetic field in the electro magnet a zero-field

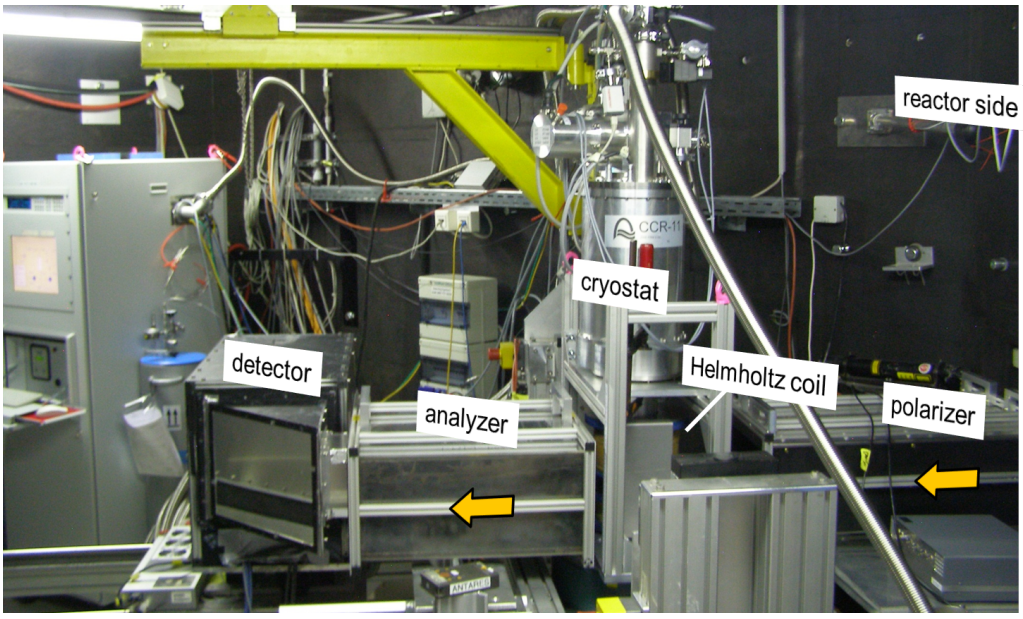

Figure 4.4.: First prototype of the depolarisation set up installed at ANTARES. The neutron beam is collimated in the beam preparation area on the right hand side (not visible). A ^{3}He NSF cell located in a guide field box is used for polarisation. The sample is placed in a closed-cycle cryostat which is surrounded by a Helmholtz coil in order to apply vertical magnetic fields. A second ^{3}He NSF cell is used for polarisation analysis. The scintillator/CCD based detector allows high-resolution imaging of the sample properties.

region would occur on the neutron path from the guide field into the coil pair which causes a depolarisation of the beam. A new set up was designed and constructed in this study to measure complete field loops $P(\pm B)$ by circumventing the zero-field crossing. A solution to avoid the zero-field region was found by introducing additional horizontal guide fields. The field geometry is shown in Fig. 4.5. This new set up rotates the polarisation vector adiabatically before and after the electro magnet into the horizontal plane.

This field geometry allows to apply magnetic fields at the sample which can be parallel as well as anti-parallel to the vertical direction as depicted in Fig. 4.5 since the polarisation is always guided in both cases. If the adiabaticity condition is fulfilled for the spatially rotating guide field the polarisation vector at the sample position can be considered as always parallel to the applied magnetic field at the sample position.

For the experiments using this set up we have used so-called V-cavities which are based on polarising supermirrors [1] (as described e.g. in Ref. [123]) to polarise and

1 www.swissneutronics.ch

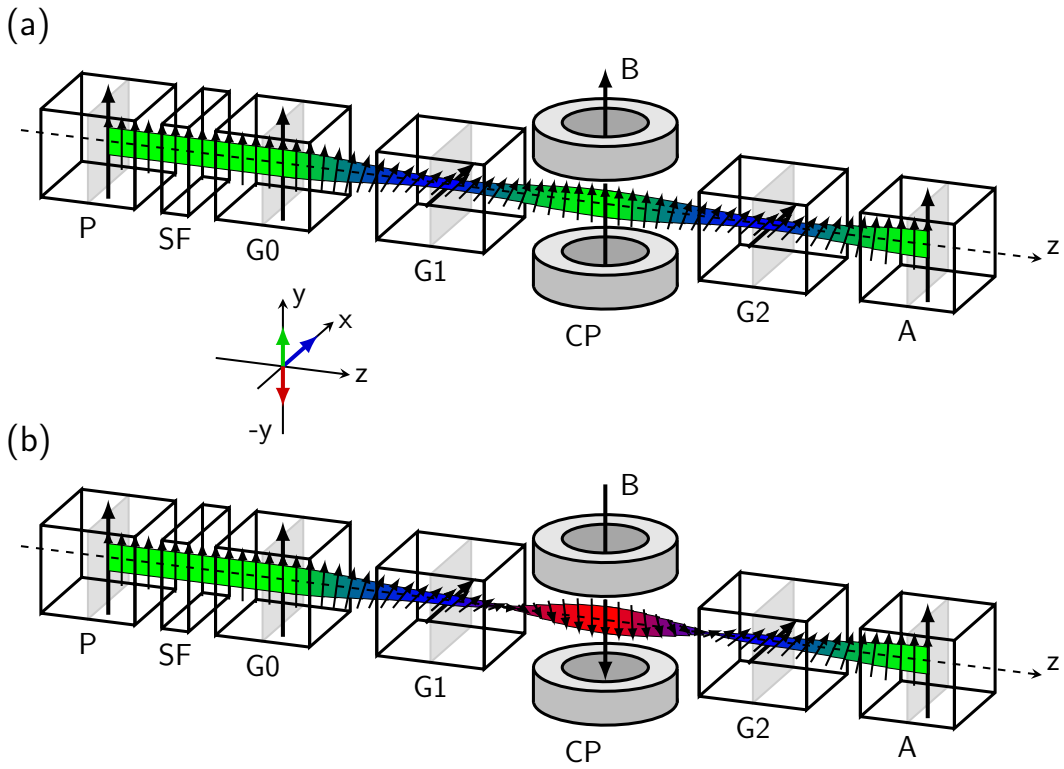

Figure 4.5.: Set up to measure complete magnetisation loops using the neutron depolarisation technique. After the polariser (P) and the spin-flipper (SF), two guide fields (G0 and G1) rotate the polarisation adiabatically into and out of the field of the coil pair (CP). A third guide field (G2) is used to turn the polarisation again adiabatically back into the field direction of the analyser (A). The analysed neutron beam is detected using a scintillator/CCD based 2D detector (not shown). The colour-coded band indicates the guide field direction along the neutron path through the set up. In the upper panel (a) the applied field in the coil pair points upwards (coloured green), in the lower panel (b) the applied field points downwards (coloured red).

to analyse the neutron beam. The already bespoken V-cavities were kindly provided for this study by the instrument scientists of RESEDA and MIRA at FRM II. The polariser (the V-cavity from RESEDA) contained five V-arrangements side-by-side that polarise a beam window of $4 \times 4\ \mathrm{cm}^2$ (width $\times$ height). The analyser (from the instrument MIRA) contained three V-shaped arrangements of supermirrors allowing a beam window of $3 \times 5\ \mathrm{cm}^2$. Both devices are optimized for cold neutrons which brought us to select a wavelength of $\lambda = 4.13$ Å as a compromise of high polarisation and high neutron flux. Although ANTARES is specialised for cold neutron imaging the maximum of the wavelength spectrum is around 2 Å and then decreases for longer wavelengths.

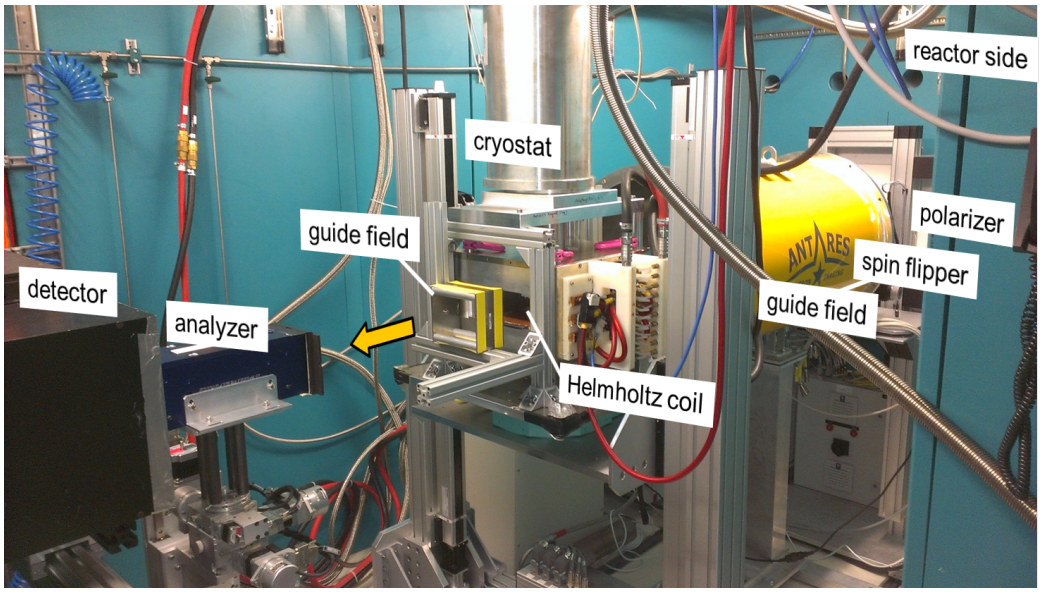

Figure 4.6.: The new set up for measuring complete field loops using the depolarisation technique. The beam is collimated and a wavelength range is selected before entering the chamber. The well-defined beam is entering from the reactor side and is then polarised using a V-cavity (not visible in the picture). The spin-flipper and a vertical guide field is located in the yellow flight tube. The sample is located in the cryostat which is surrounded by a Helmholtz coil. The guide field is rotated into and out of the horizontal plane before and after the Helmholtz coil in order to allow both directions (up and down) of the magnetic field to be applied during the measurements.

Magnetic fields up to $B = 250$ mT were applied to the sample using an already bespoken normal-conducting and water-cooled coil pair in Helmholtz geometry as sketched in Fig. 4.3. The outer magnetic field of the coil pair was closed by an iron yoke (not shown in the figure) in order to minimize stray fields on the neutron path. The magnetic field was aligned along the vertical direction which in our set up corresponds to the y-axis. A picture of the newly designed set up is shown in Fig. 4.6.

4.4.1.3. Neutron Velocity Selector

A mechanical Neutron Velocity Selector (NVS) from EADS ASTRIUM [1] was installed at the instrument ANTARES during the course of this study. This enabled us to use solid state polarisation devices such as the supermirror based V-cavities described above. These polarising devices are typically performing best in a selected wavelength range. The NVS allows to select an arbitrary wavelength λ with a given wavelength resolution and hence allows an optimised use of the V-cavities. The mounted and

1 http://www.space-airbusds.com

shielded NVS at ANTARES is shown in Fig. 4.7a.

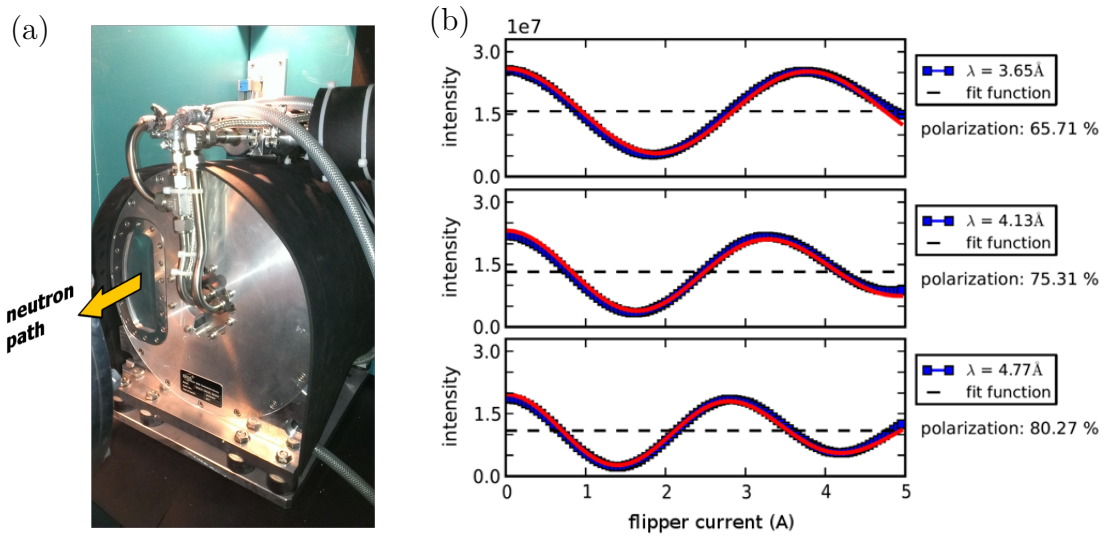

Figure 4.7.: (a) Installation of the new neutron velocity selector at the beam line ANTARES. A minimum wavelength of $\lambda_{min} = 2.95$ Å can be selected by using the maximum rotator speed of 21.000 rpm. (b) Spin rotation curves for three different wavelengths $\lambda = 3.65$ Å, 4.13 Å and 4.77 Å as set by the velocity selector. The spin-flipper current driving the field perpendicular to the polarisation was varied to produce the data. The resulting polarisation was averaged over a detector area of 8 mm by 8 mm and is shown on the right hand side for each wavelength. As can be seen from the data the polarisation gets enhanced for longer wavelengths. This is most likely an effect due to the coating of the particular supermirrors used in the V-cavities.

The NVS is a turbine-like device where a number of twisted blades rotate around an axis parallel to the neutron beam. The blades of the rotator are coated with a strongly neutron-absorbing material, in this case ^{10}B. The equidistant blades form channels for the neutron beam to pass through. The twisting angle of each channel increases linearly with the path length along the neutron beam. The twisting angle thereby defines the velocity of a neutron required to pass the NVS. The number of channels and consequently their width depends only on the number of blades (and the blade thickness) used for the rotator. A well-defined velocity distribution is hence produced by choosing the number of blades accordingly. The NVS at ANTARES possesses 144 blades with a tilting angle of 23.5 deg. This results in a triangular wavelength resolution of $\Delta\lambda/\lambda$ =10 % (FWHM). The wavelength can be selected during an experiment by choosing the corresponding rotation frequency of the rotator.

The given channel width implies that the average wavelength varies spatially across

the neutron beam cross section which has to be taken into account in experiments on large samples. A series of measurements was done in order to demonstrate the performance of the selector and to characterise the spatial wavelength variation. The set up for depolarisation measurements was used for this purpose. For a demonstration the intensity was measured for varying the transverse field in the spin-flipper and a fixed wavelengths. This results in a spin rotation as a function of magnetic field which is shown in Fig. 4.7b for the wavelengths $\lambda = 3.65$ Å, 4.13 Å and 4.77 Å.

The corresponding fit function is in the ideal case a cosine convolved with the known wavelength distribution provided by the NVS as described in Sec. 3.2.3. As an approximation a Gaussian function may be used to describe the wavelength distribution. By assuming that the desired wavelength is found at the centre position of the beam one may calculate the wavelength shift over the beam window at the detector. As can be seen from the fit in Fig. 4.7 the polarisation gets enhanced for longer wavelengths. This is most likely connected to the particular Fe:Si coating of the supermirrors which are used in our V-cavities and to the absorption layers which should stop the reflected neutrons in the V-cavities. There is a clear wavelength dependence which suggests that the absorbing layers are slightly too thin for wavelengths below about 4 Å . However, as the intensity of the wavelength spectrum at FRM II decreases with increasing wavelength we have decided to use 4.13 Å at ANTARES as a good compromise between intensity and good polarisation.

The spin rotation curves were measured with higher statistics for the wavelengths 3.65 Å and 4.13 Å. The resulting spatial wavelength distributions are shown in Fig. 4.8. As expected from the orientation of the NVS a gradient of the wavelength distribution is observed mainly in the vertical direction. The horizontal variation is due to an interplay of the small horizontal wavelength gradient produced by the velocity selector and of the two V-cavities which produce a horizontal pattern in the polarisation due to the V-arrangement of the supermirrors. The beam window covers approximately one single V-shape made of two supermirrors. Since we have used a divergence of about 0.7° of the neutron beam at ANTARES, it is clear that such a V-shape produces a horizontal stripe pattern due to the varying reflectivity. One of these stripes can be identified in Fig. 4.8a at the horizontal position $x = 5$ mm.

In most depolarisation measurements this effect is negligible as the samples are typically very small. For other experiments the effect may even be desired for a fine wavelength scan realised by scanning the vertical position of a small sample along the wavelength gradient in the field of view.

4.4.2. The Instrument MIRA at FRM II

MIRA is a multi-purpose beam line which can easily be adapted to many different configurations. The instrument is located in the neutron guide hall west of FRM II and

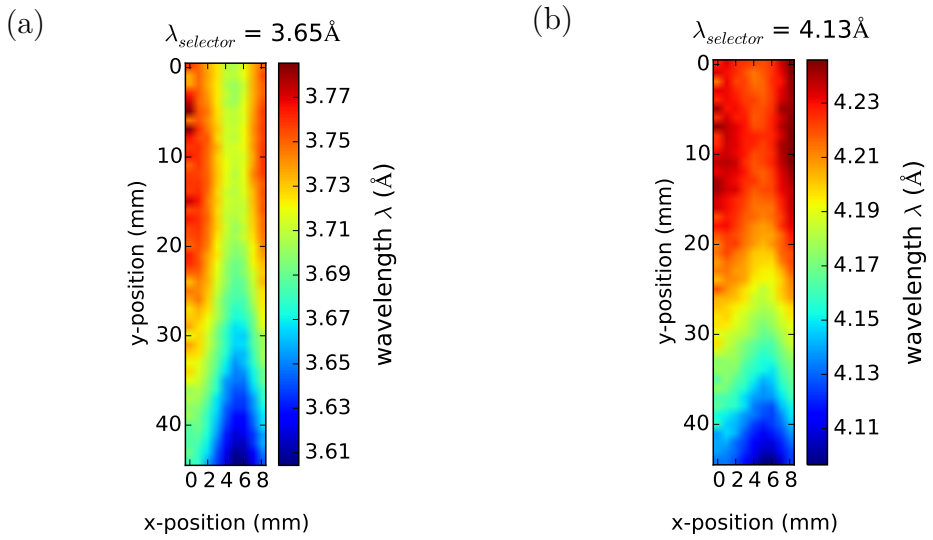

Figure 4.8.: Wavelength distribution at the detector position as produced by the neutron velocity selector at ANTARES. The data were produced for the two wavelengths (a) $\lambda = 3.65$ Å and (b) $\lambda = 4.13$ Å. An area of 8 mm by 45 mm set by the beam limiter was covered. The wavelength for each coordinate was extracted from the corresponding fit of a spin rotation curve (see text) and is represented as colour map.

provides a cold neutron spectrum. A crystal monochromator (pyrolytic graphite PG 002) was used at MIRA for selecting a wavelength of $\lambda = 4.59$ Å with a wavelength distribution $\Delta\lambda/\lambda$ =2 %.

For this study we have used a four-blade beam limiter as a pinhole approximately providing L/D=400. A so-called CASCADE detector (see [141, 142]) with an active area of 200×200 mm (128×128 pixels) was used yielding a pixel size of 1.56 mm. The neutron depolarisation set up is described in the following section.

4.4.2.1. Depolarisation Setup For Hysteresis Loops

The components and the magnetic field geometry were similar to that already described in Sec. 4.4.1.2. However, the prototype of the set up for measuring magnetic field loops by neutron depolarisation was first tested at the instrument MIRA. The polarisation of the beam was done using a solid state bender which produces a high polarisation of $P \geq 95\%$. A Mezei-type spin-flipper is mounted directly after the polariser in order to set the polarisation.

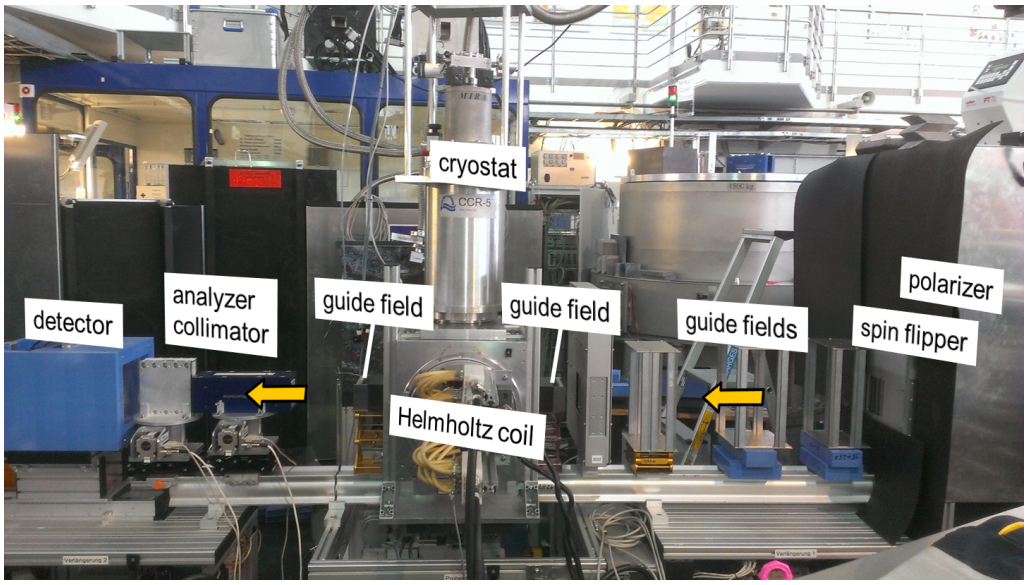

Figure 4.9.: Prototype of the depolarisation set up for measuring complete field cycles which was installed at the instrument MIRA. After the monochromator (not visible in the right hand side of the picture) the beam is polarised using a solid state bender. The polarisation is maintained by magnetic guide fields. The sample is placed in a cryostat which is surrounded by a Helmholtz coil producing a field in the vertical direction. The polarisation is rotated adiabatically from the vertical direction into the horizontal plane right before and after the Helmholtz coil to enable complete field loops without changing the guide field direction. The neutron beam is analysed using a V-cavity. A CASCADE detector (see [141, 142]) is used to allow the direct imaging of the sample.

The sample was placed in a standard closed-cycle cryostat surrounded by the already bespoken water-cooled normal-conducting coil pair in Helmholtz geometry. The coil pair allowed to apply magnetic fields up to $B = 250$ mT parallel as well as anti-parallel to the vertical direction. A V-cavity as already described in Sec. 4.4.1.1 was used to analyse the polarisation of the neutron beam. A photograph of the set up at MIRA is shown in Fig. 4.9.

4.4.3. The Instrument POLI at FRM II

A measurement on $CePd_{1-x}Rh_x$ was done at the instrument POLI at FRM II in order to investigate the magnetic anisotropy. POLI is a zero-field polarimeter with a 3D polarisation analysis option based on a CryoPad [125, 137–139]. The basic components and the geometry of the guide field is sketched in Fig. 4.10.

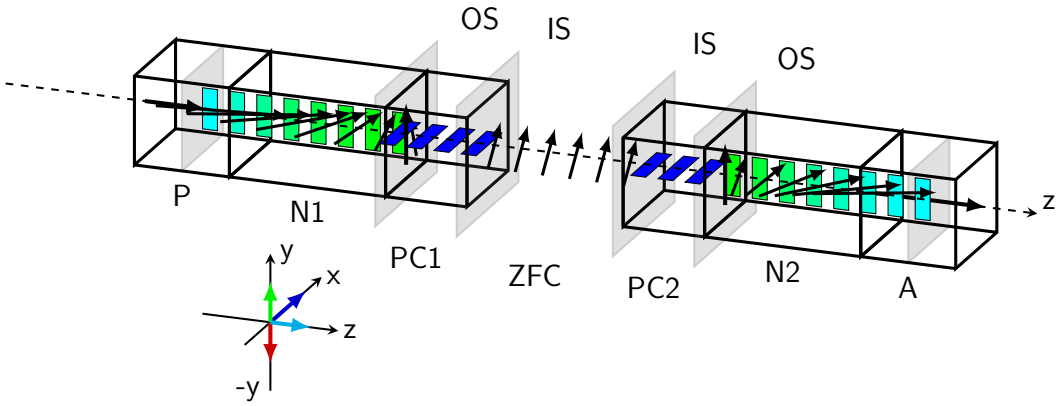

Figure 4.10.: Depolarisation set up at the instrument POLI using the CryoPAD zero-field option. The polariser (P) contains a ^{3}He NSF cell. The polarisation direction is along the beam direction which corresponds to the z-axis. The polariser is followed by a nutator (N1) which turns the polarisation adiabatically into the x-y plane. The angle is set mechanically using a stepper motor. The CryoPAD is surrounded by a cylindrical outer mu-metal shield (OS) and an inner shield (IS) made of superconducting niobium. A precession coil (PC1) at the entry window located between the two shields allows to turn the polarisation set by the first nutator to an arbitrary direction. The polarisation direction is then maintained in the zero-field chamber (ZFC) inside the inner shield where the sample is placed. A second precession coil (PC2) at the exit window again located between the two shields turns the polarisation vector back into the x-y plane. A second nutator (N2) adiabatically turns the polarisation vector into the z-direction. The analyser (A) consists of a second NSF cell which analyses in z-direction.

The neutron beam is polarised and analysed in z-direction using ^{3}He NSF cells located in longitudinal guide fields. The neutrons is guided through a device called nutator in which the polarisation direction is changed adiabatically to lie in the x-y plane. The nutator can be rotated by a stepper motor around the beam axis and thereby allows to define the angle of the polarisation in the x-y plane. The polarisation vector may then be rotated into an arbitrary direction in space by a precession coil. In contrast to the conventional depolarisation set up with a guide field along the neutron path, the sample environment is shielded by a superconducting Nb cylinder and an additional mu-metal cylinder. The precession coils are hence located in zero-field regions and no compensation field is required. As the sample is also located in a zero-field region this set up does not allow the application of magnetic fields to the sample without affecting the functionality of the instrument. However, the set up allows to investigate the directional dependence of the depolarisation caused by a possibly anisotropic domain structure. After passing the sample in the zero-field region the superconducting Nb shield is transmitted again and a second precession coil together with a second nutator is used to define the analysed polarisation direction. The polarisation can hence be set and analysed in all three dimensions in space before and after interaction with the

sample. A photograph of the complete set up is shown in Fig. 4.11.

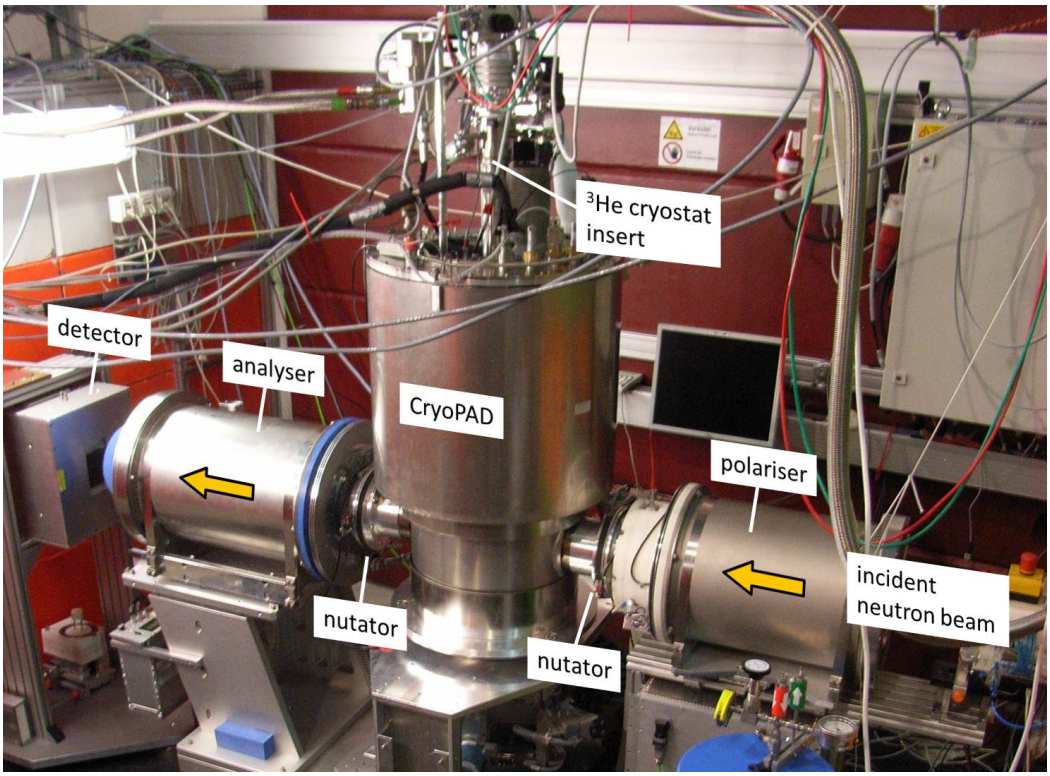

Figure 4.11.: Depolarisation set up at the instrument POLI. Polariser and analyser contain a ^{3}He NSF cell where the magnetic guide field points along the beam direction. The nutator uses an adiabatic transition to turn the polarisation into the plane perpendicular to beam. The angle is set by rotating the nutator mechanically using a stepper motor. A precession coil in the beam entry window of the CryoPAD case is used to turn the polarisation into an arbitrary direction. The sample is located in the zero-field region of the CryoPAD. A second precession coil at the exit window and another nutator are then used to analyse the polarisation in a particular direction. A ^{3}He counter tube is used as detector.

4.4.4. Data Evaluation

An evaluation tool kit was implemented using the programming language Python during the course of this study. The tool kit allows to evaluate the 1D detector data from the instrument POLI as well as the 2D detector data from ANTARES and MIRA. The evaluation of the 2D detector data is based on calculating the polarisation for each pixel by

$$P(x,y) = \frac{I_{\uparrow}(x,y) - I_{\downarrow}(x,y)}{I_{\uparrow}(x,y) + I_{\uparrow}(x,y)} \tag{4.2}$$

where the intensity depends on the position (x,y) at the detector. The CASCADE detector which was used at the instrument MIRA provides the number of neutron counts and the instrument parameters for each measurement are saved in an additional log file. The combination allows to evaluate the data as a function of a desired scan parameter such as magnetic field B or temperature T. The CCD based detector at ANTARES records the intensity in a dynamic range which is chosen accordingly to the required exposure time. In addition, the data are saved adding a constant background in the intensity (for technical reasons which are discussed elsewhere) which must be subtracted before data evaluation. At ANTARES the instrument parameters are included in the header information of each image and can therefore directly be used for data evaluation. For the 1D data measured at the instrument POLI a log file containing both the number of counts detected as well as the currently scanned instrument parameter was generated for each measurement. Parsing the log file yields the corresponding initial and final polarisation direction together with the count values as a function of the desired scan parameter.

4.4.4.1. Map of the Curie-temperature

If a detector with a high spatial resolution is used in neutron depolarisation measurements the homogeneity of a sample can be investigated. When using a CCD detector such as used at the instrument ANTARES each pixel represents only a very small part of the sample. By using longer exposure times the statistics can be increased until each pixel or at least small pixel group (e.g. using a 2x2 or 4x4 binning) can be evaluated separately. When measuring the polarisation $P(T)$ as function of temperature, the corresponding fit function may then be applied to the polarisation of each pixel individually. For temperature sweeps a fit then gives as a result the transition temperature T_C. By using a conventional radiography of the sample, i.e. by taking the sum of the polarised intensities $I_{total} = I_\uparrow + I_\downarrow$ a mask of the sample region can be created using a suitable threshold in intensity. The threshold thereby defines the sample shape. The determined transition temperature T_C found for each pixel can now be saved at the corresponding pixel position in a new 2D array resulting in a so-called T_C-map. The technique is demonstrated in the study on $CePd_{1-x}Rh_x$ where the metallurgical homogeneity plays a particular role for the magnetic properties in the context of QPTs as will be discussed in the following chapter.

The next three chapters may be regarded as independent studies in the context of QPTs. First in Chap. 5 the system $CePd_{1-x}Rh_x$ is investigated in which a so-called Kondo-Cluster-Glass formation takes place when altering the chemical composition. The role of the metallurgical homogeneity is therefore considered. In Chap. 6 the itinerant FM $ZrZn_2$ is investigated under application of hydrostatic pressure which tunes a QPT. In Chap. 7 the FM QPT in the system $Fe_{1-x}Cr_x$ is investigated which occurs by diluting the Fe host system with Cr. Chap. 8 gives a global summary of the scientific results of these studies and of the instrumental developments.

5. Kondo-Cluster-Glass Formation in $CePd_{1-x}Rh_x$

The compound $CePd_{1-x}Rh_x$ is one of the very few ferromagnetic Kondo lattice systems that have been identified so far. This inspired early studies [143, 63] as the coexistence of screened magnetic moments due to the Kondo effect and FM order seem to exclude each other at first sight [41]. $CePd_{1-x}Rh_x$ undergoes a quantum phase transition as a function of chemical composition defined by the Rh content x. The substitution of Pd by Rh content leads to a continuous suppression of the ferromagnetic ordering temperature. As can be seen from the phase diagram in Fig. 5.1 the ordering temperature is $T_C = 6.5$ K for the clean system CePd and the lowest measured transition temperature of 25 mK has been observed at $x = 0.87$ [144, 107].

The magnetic moment is carried by the cerium $4f$ electrons. The system features additional energy scales as compared to transition metal ferromagnets, namely the Kondo temperature below which a screening of the magnetic moments occurs and the RKKY interaction which mediates magnetic order through the polarisation of surrounding conduction electrons. In Fig. 5.1 the right scale corresponds to the paramagnetic Pauli temperature $|-\Theta_P|$ which should compare in magnitude to twice the Kondo temperature T_K as explained e.g. in [69]. Disorder accompanies the substitution of Pd by Rh as these elements are not iso-electronic which most likely influences the shape of the phase boundary $T_C(x)$ that would be expected for a clean ferromagnetic system under pressure. The curvature of the phase boundary of $CePd_{1-x}Rh_x$ changes sign at $x^* = 0.65$ which indicates strong quenched disorder as discussed in Sec. 2.1. Above x^* the magnetisation dynamics inferred from ac-susceptibility measurements change and indicate a glassy state. From the frequency dependence of the susceptibility it was suggested that the dynamics result from larger clusters of spins that decay and thereby decrease in size with further increasing the Rh content [65].

Below x_v the Kondo temperature is low and ferromagnetic order is favourable. Above x_v, the Kondo temperature is rapidly increasing far above the temperature where ferromagnetic order is stabilised. However, due to the intrinsic disorder the Kondo effect plays the important role of inhibiting long range order by screening a fraction of the magnetic moments. The name Kondo-Cluster-Glass was found by [65] to compile all observations in one term. For intermediate Rh content x the interplay of ferromagnetic order and the Kondo effect leads to the formation of ferromagnetic clusters surrounded by Kondo-screened moments. The clusters decrease in size with increasing Rh content, thereby transforming the system into a state comparable to that of a spin-glass. The microscopic details in this pre-critical regime was illustrated

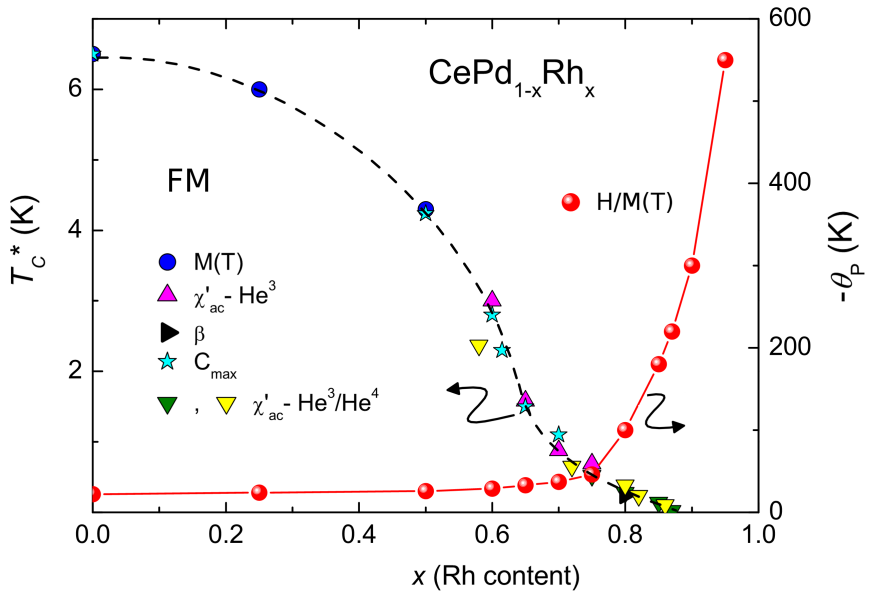

Figure 5.1.: Magnetic phase diagram of $CePd_{1-x}Rh_x$ showing the ordering temperature denoted as $T_C^*(x)$ on the left hand scale. T_C^* was determined using magnetisation $M(T)$, ac-susceptibility $\chi'(T)$, thermal expansion $\beta(T)$ and specific heat $C(T)$ measurements for varying Rh content x. The right hand scale denotes the absolute value of the paramagnetic (Pauli) temperature $|-\Theta_P|$ which is commonly used as an estimate for the Kondo temperature as described e.g. in [69]. Interestingly, the value of Θ_P is negative even in the FM regime. Three characteristic concentrations were identified in [107]. At $x^* = 0.65$ the curvature of the phase boundary changes sign. At $x_v = 0.70$ strong valence fluctuations were suggested by a rapid increase of the Kondo temperature (right scale). At the critical concentration $x_c = 0.87$ the ferromagnetism is completely suppressed. Figure adapted from [106].

by [69] as in Fig. 5.2.

The temperature decreases in the four panels from (a) to (d). In panel (a) the moments are not screened and fluctuate as for a normal paramagnetic system. If, as depicted in panel (b), the temperature falls below the average Kondo temperature T_K some magnetic $4f$ moments are screened while clusters of unscreened paramagnetic clusters survive. As depicted in panel (c) below the ordering temperature $T_{cluster}$ these cluster order ferromagnetically and the susceptibility is dominated the rather slow dynamics of entire spin clusters. As illustrated in panel (d) a freezing temperature T_C is introduced where the clusters freeze in a certain constellation that is strongly influenced by the magnetic field history.

The illustration was proposed for elevated Rh content above x^* but below x_c. It was further proposed that this picture may in principle remain valid up to x_c where the volume of the ferromagnetic clusters is reduced with further increasing Rh content.

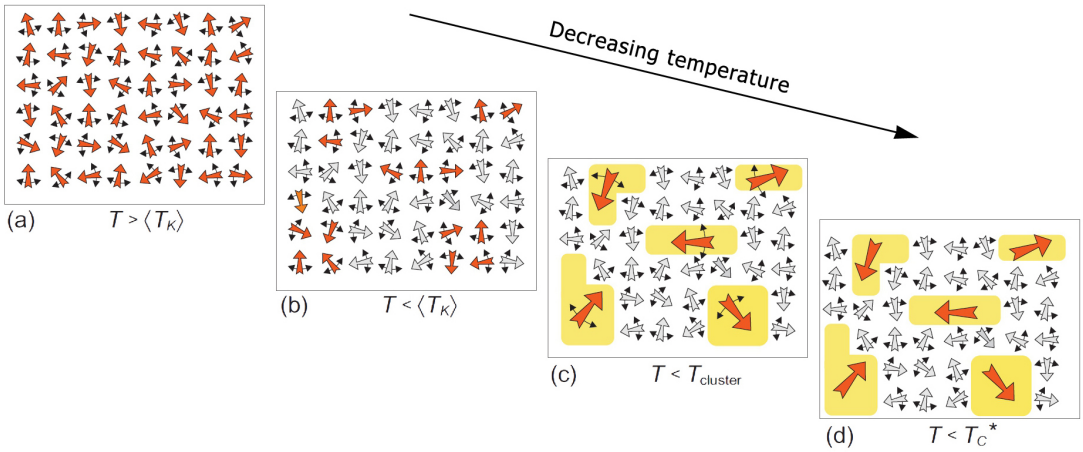

Figure 5.2.: Illustration of the cluster glass formation with decreasing temperature from (a) to (d) in $CePd_{1-x}Rh_x$ for elevated Rh content in the tail region of the magnetic phase diagram. (a) Paramagnetic state where all $4f$ moments (large red arrows) are unscreened and thermally fluctuating (indicated by small black arrows). (b) Cooling below the average Kondo temperature leads to a spatial variation of screened (grey arrows) and unscreened (red arrows) $4f$ moments where thermal fluctuation still affect the single spins. (c) Below a characteristic temperature ferromagnetic short-range order stabilises in the regions of unscreened moments. These ferromagnetic clusters are still dynamic on a somewhat slower time scale compared to the single spins. (d) Below a freezing transition the thermal fluctuations are overcome by the interaction between the clusters which then lock in a certain constellation. Figure adapted from [69].

In the CeRh limit the system is assumed non-magnetic in a sense that all magnetic moments are screened by the Kondo effect. These findings call for further investigation regarding the length and time scale of the ferromagnetic clusters on the route towards the critical concentration.

Inspired by first test experiments (see [61]) we have used the neutron depolarisation technique to investigate the effect of the metallurgical homogeneity on the magnetisation properties and on the distribution of ordering temperatures T_C over the entire sample volume of a series of $CePd_{1-x}Rh_x$ crystals. In addition, the mechanism of the spin cluster freezing for intermediate Rh content was explored using an external magnetic field. A series of well characterised $CePd_{1-x}Rh_x$ samples [64, 65, 107] with different Rh content $x = 0.40$, 0.60, 0.65 and $x = 0.70$ was used in this study. A state-of-the-art overview on the compound and thereby a characterisation of the samples under investigation is given in the following section. The experimental results of this study are summarised in the subsequent section.

5.1. State of the Art

The sample series provided for this study consisted of both polycrystalline samples which were characterised in [65, 107] and single-crystals which were characterised in [64, 65] as also described in Sec. 4.1. As was verified by x-ray powder diffraction $CePd_{1-x}Rh_x$ shows an orthorhombic CrB crystal structure for all Rh contents x. Increasing x has a negative volume effect and hence compares to pressure as is shown in Fig. 5.3.

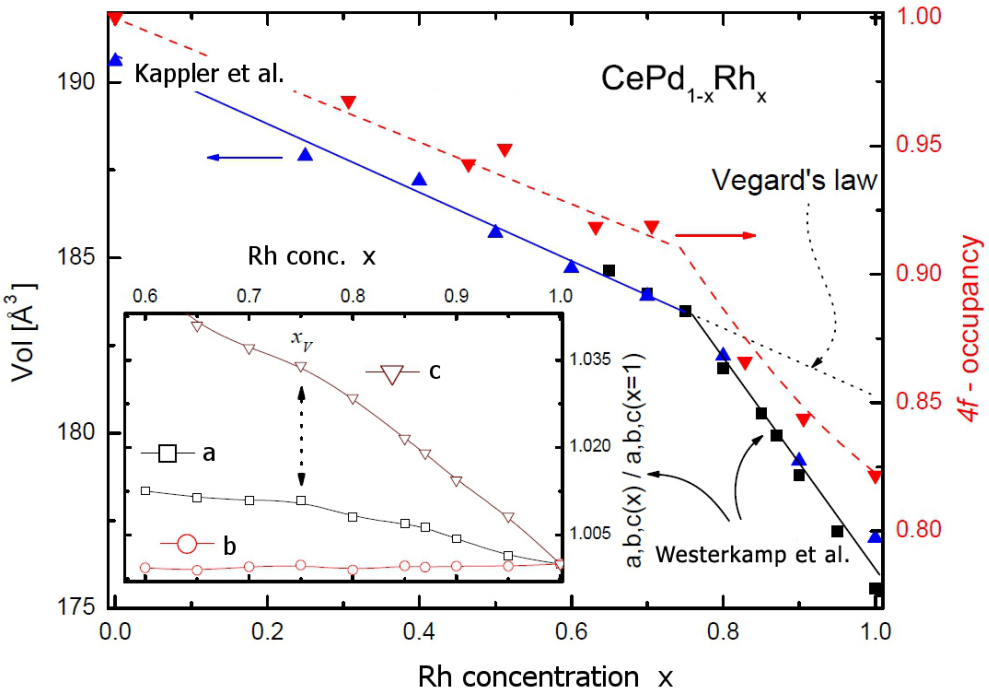

Figure 5.3.: Unit cell volume (left scale) as calculated from x-ray diffraction measurements and $4f$ electron occupancy (right scale). The inset shows the lattice constants determined for samples in the tail region of the phase diagram. Increasing x acts linear on the volume and may hence be regarded as chemical pressure. The characteristic $x_v = 0.70$ was identified where a super-linear drop of the volume accompanied by a drop of the $4f$ occupancy (right scale) is observed. Figure adapted from [69].

In addition, the $4f$ occupancy is decreased with increasing x with a similar evolution as the volume. The drop in the $4f$ occupancy is accompanied by a pronounced enhancement of the Kondo temperature as shown already in Fig. 5.1 above $x_v = 0.70$ indicating the onset of strong screening effects. From magnetisation measurements as in Fig. 5.4 it is observed that the system behaves almost Ising-like for low and intermediate Rh content where the axis of the magnetisation is the crystallographic c-axis. Fig. 5.4 shows exemplarily magnetisation loops from samples with Rh content $x = 0.40$ and $x = 0.60$ which is in the intermediate (pre-critical) regime. No hysteresis

is observed for both concentrations.

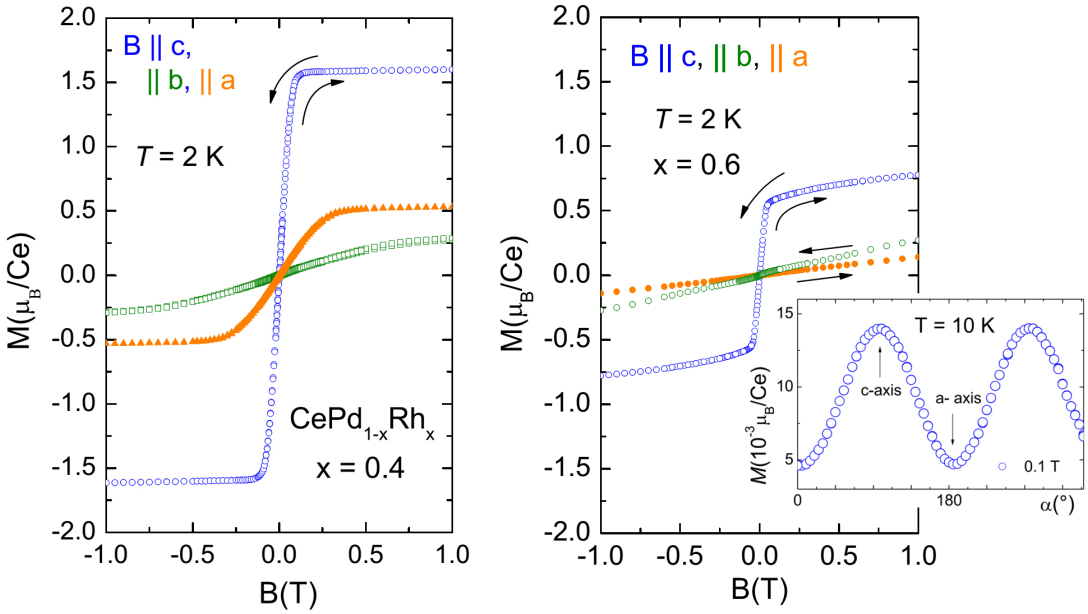

Figure 5.4.: Magnetisation loops for the three different crystallographic axes measured on two single-crystalline samples with $x = 0.40$ and $x = 0.60$. The system behaves almost Ising-like where the easy axis of the magnetisation is along the crystallographic c-axis. The inset for $x = 0.60$ shows the magnetic anisotropy at $T = 10$ K visualised by a magnetisation measurement using a sample rotator. The maximum is found if the probed field direction is parallel and anti-parallel to the easy axis of the magnetisation. Figures adapted from Ref. [64]

Although the system is non-magnetic in the CeRh limit the inverse magnetisation (the dc susceptibility) is enhanced for $T \to 0$ above the critical concentration $x_c = 0.87$ where the lowest transition temperature $T = 27$ mK was observed. The ac-susceptibility shows a pronounced peak at the transition temperature as shown in Fig. 5.5 with a similar shape for both polycrystalline and single-crystalline samples [69]. The frequency dependence of the ac-susceptibility is shown in Fig. 5.5 in the lower inset. As explained by [65] the frequency shift is characteristic for ferromagnetic spin-glasses and suggests the existence of large ferromagnetic clusters with slow dynamics at low temperatures.

The specific heat initially shows a sharp lambda-shaped anomaly at the phase transition for small Rh content which transforms into a logarithmic temperature dependence without a distinct peak at the critical concentration $x_c = 0.87$. The peak position in the specific heat is found in good agreement with the transition temperature determined from other thermodynamic properties. The temperature dependence finally changes to power law behaviour for large Rh contents above x_c. From the specific

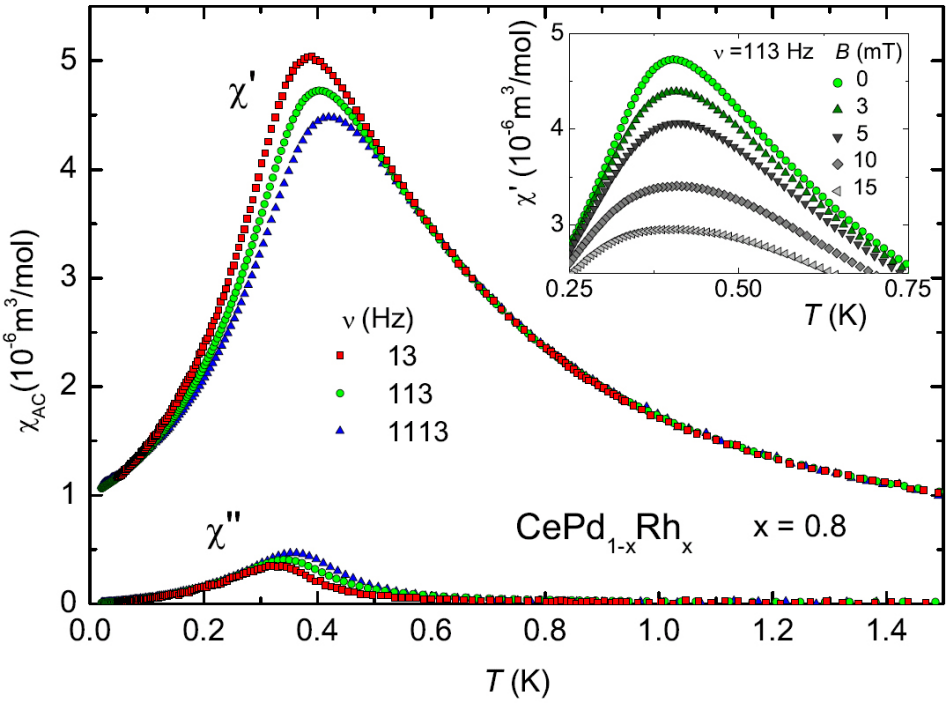

Figure 5.5.: Frequency-dependence of the ac-susceptibility χ_{ac} from a single-crystalline sample with $x = 0.80$ measured along the crystallographic c-axis. With increasing frequency a shift of the maximum is observed. The inset shows the magnetic field dependence of $\chi_{ac}(T)$. Small external fields smoothly suppress the sharp peak. Both observations are typically interpreted as a spin-freezing effect on a certain time scale below the transition temperature. Figure adapted from Ref. [69]

heat data [63] have extracted the fraction of magnetic moments that are screened by the Kondo effect and found that above the critical concentration more than 90% of the moments are screened and can therefore not contribute to the FM properties. However, a certain amount of unscreened moments survives up to high Rh content which may still allow for FM correlations.

As reported by [66] power law behaviour may not only be identified in the specific heat but also in the susceptibility and the magnetisation above x_c. This was attributed to the coexistence of ferromagnetic order and highly (Kondo) hybridised quasi-particles. As an argument for such a coexistence the inhomogeneous distribution of magnetic coupling constants and Kondo temperatures over the sample was considered. The logarithmic C/T dependence just below x_c could be explained by conventional QCP scenarios [11, 145]. However, as noticed the Grueneisen ratio does not diverge when approaching the nominal critical point (see Ref. [69]) which invalidates these scenarios at first sight. The Sommerfeld ratio is large in the paramagnetic regime for large x indicating strong correlation effects. However, neither in the ferromagnetic nor in the Kondo-screened regime conventional $\rho(T) \propto T^2$ Fermi liquid behaviour was observed

[65, 146]. From these findings disorder seems a most important effect which effectively leads to a distribution of relevant energy scales in the material. In some cases this may allow the coexistence of different phases that are spatially distributed in a material. The observed power laws in the specific heat and in the magnetisation may then be attributed as in [66] to an emerging quantum Griffith phase (see [147–149]) above the ferromagnetic tail region of the phase diagram at $T = 0$. In this scenario the existence of FM clusters which are often referred to as rare regions is considered. Different rare region models (see [41, 149–151]) were discussed in the context of the properties observed for $CePd_{1-x}Rh_x$ in [65].

As one of the key questions concerns the precise manifestation of disorder and how the corresponding length scales and transition temperatures evolve in the system the metallurgical homogeneity was investigated in this study using the neutron depolarisation technique on a series of samples. The following section summarises the experimental results from the neutron depolarisation measurements. An interpretation of our data in the context of the known results from other studies is given in the subsequent section.

5.2. Experimental Results

As the magnetic ordering temperature varies strongly with the chemical composition, a spatially resolved map of ordering temperatures over the sample can be used to determine the metallurgical homogeneity. To generate the desired T_C maps for the samples under investigation the polarisation was measured as a function of temperature and afterwards fitted pixel-wise to the models discussed in Sec. 3.2. Exemplary depolarisation data with the corresponding fit function are shown in Fig. 5.6. The data have been fitted to Eq. 3.27 where as a result the ordering temperature T_C and the value of the product $B_0^2\delta$ is found.

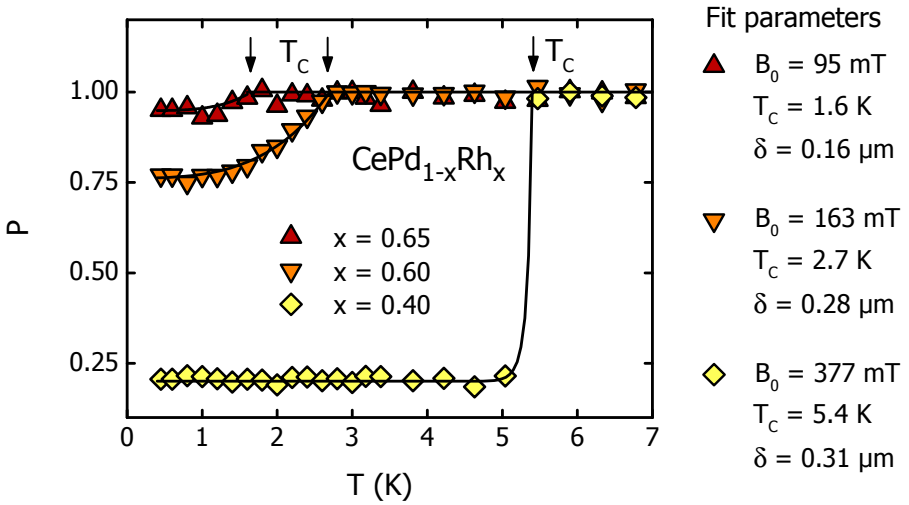

Figure 5.6.: Exemplary depolarisation data of the $CePd_{1-x}Rh_x$ samples with Rh content $x = 0.40$, $x = 0.60$ and $x = 0.65$ as function of temperature without an external field $B = 0$. The data were produced by evaluating a 4x4 pixel group (corresponding to 300x300 μm^2) at an arbitrary position within each of the samples. The exponential temperature-dependence of the depolarisation as described by Eq. 3.27 was used to fit the data. The fit parameters are the ordering temperature T_C and the value of the product $B_0^2\delta$. Inserting a known value for the field B_0 allows to estimate the average domain size δ probed in transmission direction of the neutron beam. The values of B_0 were estimated from magnetisation measurements by $B_0 = \mu_0 M(T \to 0)$ in [69] and set as fixed parameter for the corresponding fit. The domain size δ is hence a result of the fit.

As discussed in Sec. 3.2 the field B_0 is the averaged magnetic field in each ferromagnetic domain and δ is the average domain size probed in the direction of the neutron beam.From Fig. 5.6 a first result may be noted. According to the estimated values of B_0 the data suggest that the average size δ of the ferromagnetic domains decreases with increasing Rh concentration x. It should also be noted however that this is only a rough estimate of B_0 and consequently of δ which is solely due to the number of

approximations that are included in the model. However, the ordering temperature T_C is also determined from the fit and may be regarded as more accurate.

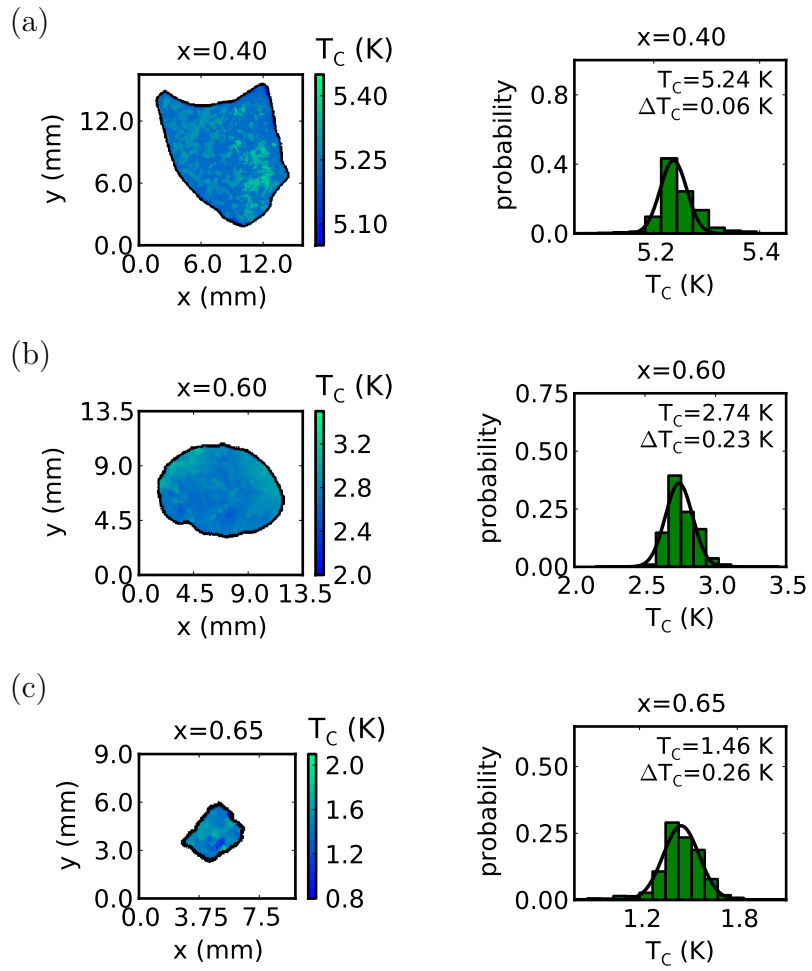

Figure 5.7.: Left column: T_C maps of the $CePd_{1-x}Rh_x$ samples with Rh content (a) $x = 0.40$, (b) $x = 0.60$ and (c) $x = 0.65$ generated from temperature scans without an external field $B = 0$. The gradient colour bar beside each map decodes the transition temperature T_C. Right column: The histogram beside each map illustrates the corresponding distribution ΔT_C (FWHM) of the transition temperatures as determined by the fitting procedure described in Sec. 4.4.4.1.

The T_C maps that were derived from the measurements on the samples with Rh content $x = 0.40$, $x = 0.60$ and $x = 0.65$ are shown in Fig. 5.7. A small magnetic field of $B = 0.5$ mT was applied during the corresponding temperature scans to guide the neutron polarisation. For the sample with $x = 0.70$ the depolarisation effect in such a small field was too low to allow for a meaningful fit. Further measurements

using different magnetic field histories are already planned. The histograms show the distribution of the ordering temperature over the sample. The colour coding represents the corresponding transition temperature.

The transition temperature of all samples varies over a very small range. As can be seen from the histograms the width of the distribution of transition temperatures ΔT_C (FWHM) increases from $x = 0.40$ to $x = 0.65$ while T_C decreases. It should be noted that the samples with $x = 0.40$ and $x = 0.65$ are nominal single-crystals while the sample with $x = 0.60$ is polycrystalline. Nevertheless, the data suggest that the inhomogeneity in the samples increases in terms of the distribution of transition temperatures ΔT_C. At the same time the typical size of the ferromagnetic domains decreases with increasing x as discussed above for Fig. 5.6.

For all of the samples the effect of field-cooling was investigated. Fig. 5.8 shows the depolarisation data measured for the samples with $x = 0.40$, $x = 0.60$ and $x = 0.65$, where different magnetic field histories were applied before measuring. The samples were heated and thereby measured in the same magnetic field as they were cooled down which is abbreviated as fc-fh (field cooled - field heated). Data were recorded for three different applied fields of $B = 7.5$ mT, $B = 15$ mT and $B = 22.5$ mT. For comparison a zero-field measurement abbreviated as zfc-zfh (zero field cooled - zero field heated) was performed, which is also shown in Fig. 5.8 for each sample.

The applied magnetic fields lead only to a small enhancement of the depolarisation for the sample with $x = 0.40$. This sample shows typical behaviour expected of a ferromagnet in the multi-domain state in zero or weak magnetic field. The averaged spontaneous magnetisation per domain stabilises at the transition temperature T_C, saturates fast and remains constant for $T \to 0$. Different fields affect the depolarisation only slightly.

In contrast, for the sample with $x = 0.60$ and $x = 0.65$ the small field of 7.5 mT enhances the depolarisation remarkably. In the sample with $x = 0.65$ the depolarisation nearly vanishes after zero-field-cooling. This suggests that for this concentration the long-range order is virtually suppressed in zero field. However, a small external magnetic field $B = 7.5$ mT drastically increases the depolarisation and further increasing the field in this range still enhances the signature. This indicates a form of FM order which stabilises at very small critical fields.

Additional depolarisation measurements were done on zero-field-cooled (zfc) as well as field-cooled (fc) samples during field-heating (fh). Fig. 5.9 shows depolarisation data from zfc-fh and zfc-zfh measurements on the four $CePd_{1-x}Rh_x$ samples with Rh concentrations $x = 0.40$, $x = 0.60$, $x = 0.65$ and $x = 0.70$, that were under investigation.

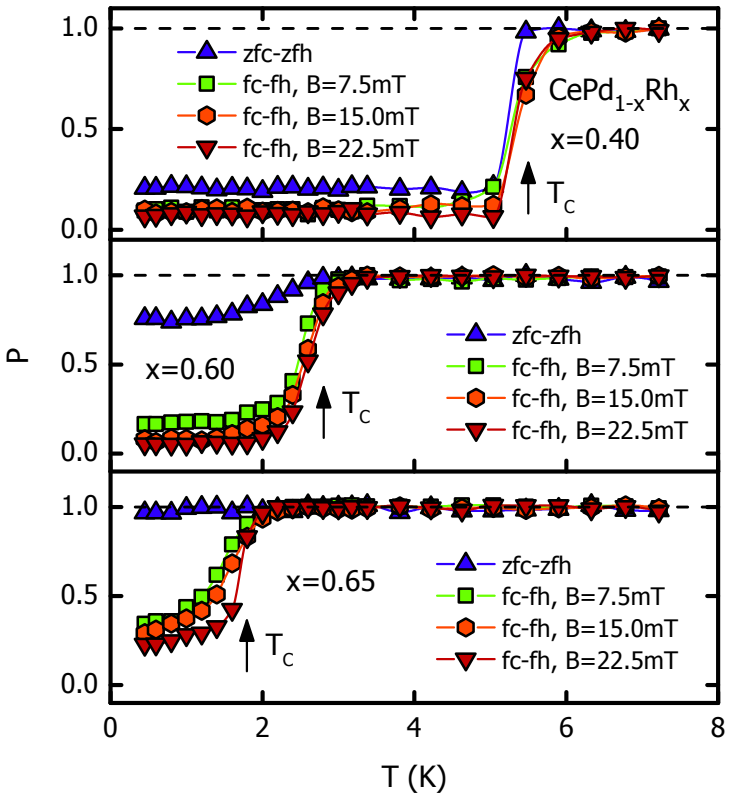

Figure 5.8.: Depolarisation measured as a function of temperature extracted from zfc-zfh and fc-fh data of $CePd_{1-x}Rh_x$ samples with Rh content $x = 0.40$, $x = 0.60$ and $x = 0.65$. The curves have been extracted from a 8x8 pixel region centred in each sample. Three data sets were recorded using different external magnetic fields $B = 7.5$ mT, $B = 15$ mT and $B = 22.5$ mT for field-cooling, respectively. For comparison a zero-field measurement was done. As can be seen from the data the depolarisation increases with increasing external field $B||P$ parallel to the polarisation while the transition smears out. The arrows indicate the position of T_C as determined from the zero-field data.

The measurements on the sample with $x = 0.40$ suggest the onset of a slowly developing spin-freezing transition of the magnetic configuration under zero-field-cooling. This smooth transition from the zfc state to the fc state occurs at the temperature denoted as T_F in Fig. 5.9. The shape of the zfc-zfh curve changes for the sample with $x = 0.60$. However, the shape of the fc-fh data is essentially unchanged. The zfc-fh data now clearly expose the broad transition around T_F. If a small magnetic field of 7.5 mT is applied after zero-field-cooling the depolarisation remains nearly constant. Increasing the temperature restores the depolarisation as measured under fc-fh conditions with the same applied field of 7.5 mT.

The sample with $x = 0.65$ shows similar behaviour under fc conditions although the

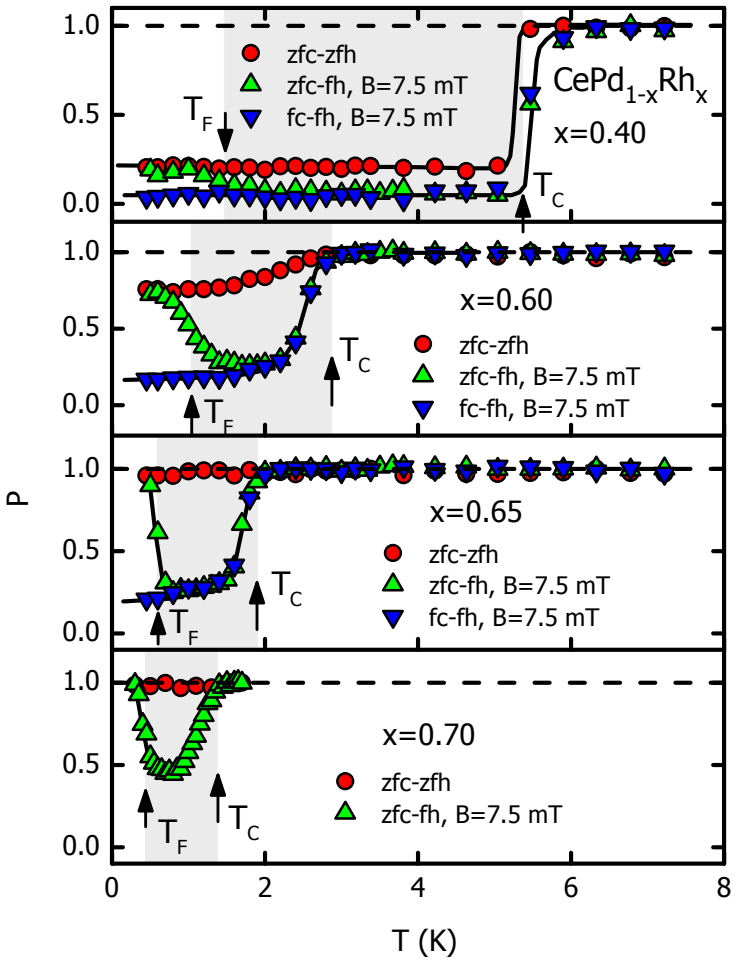

Figure 5.9.: Comparison of zfc-zfh and zfc-fh data recorded from $CePd_{1-x}Rh_x$ samples with Rh concentrations $x = 0.40$, $x = 0.60$, $x = 0.65$ and $x = 0.70$, respectively. The samples were cooled down in zero applied field. For the zfc-fh measurements a field of 7.5 mT was then applied at the lowest temperature. The FM ordering temperature T_C is indicated by arrows. The signature of a cluster glass formation is associated with the decrease of depolarisation below the splitting of the curves. This transition is indicated by the arrows at T_F and may be interpreted as a spin-freezing effect. The ferromagnetic behaviour of the field-cooled state is only observed in a small temperature window for larger Rh concentrations.

freezing transition at T_F now appears sharper. Interestingly, the signature under zfc conditions is already very small compared to the lower concentrations. Finally, for the sample with $x = 0.70$ the depolarisation vanishes after zero-field-cooling and essentially does not change even if a small external field $B = 7.5$ mT is applied. Interestingly, when increasing the temperature the ferromagnetic behaviour is still re-entrant in a finite temperature interval. The freezing transition at T_F is again somewhat broadened compared to $x = 0.65$. At the slightly higher transition temperature T_C the system transforms to the paramagnetic state where the depolarisation vanishes. The ordering temperature T_C was extracted from the data by fitting. The temperatures T_F of the presumed spin-freezing transition were estimated from the zfc-fh data. We have determined T_F by using the value where the curvature (the second derivative) changes sign. The extracted temperatures will be used to generate a revised phase diagram which will be shown in the next section enclosing the discussion.

For the single-crystals with a Rh content $x = 0.40$ and $x = 0.60$ strong magnetic anisotropy was observed in magnetisation measurements as shown in Fig. 5.4 for $x = 0.40$ which was discussed in the previous section. For a direct comparison a measurement of the anisotropy of the depolarisation was performed at the instrument POLI at FRM II using the 3D polarisation analysis set up option CryoPAD discussed in Sec. 4.4.3.

The sample was oriented such that the crystallographic a-c plane was in the plane perpendicular to the neutron beam which is the x-y plane in polarisation coordinates. Fig. 5.10 shows an illustration of the coordinate system.

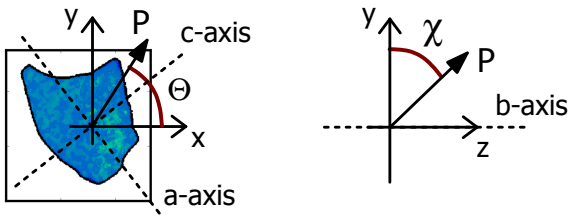

Figure 5.10.: Coordinate system of the neutron polarisation showing the crystallographic a- and c-axis of the $CePd_{1-x}Rh_x$ sample with Rh concentration $x = 0.40$ as determined by Laue diffraction. The crystallographic a- and c-axis of the sample lie in the x-y plane perpendicular to the neutron beam. The b-axis points roughly along the z-direction. The CryoPAD device at the instrument POLI allows to set and to analyse the polarisation in an arbitrary direction defined by then angles Θ in the x-y plane and χ in the y-z plane.

The magnetic easy axis of the system is the crystallographic c-axis and hence lies in this plane. The y-axis of the set up is the vertical axis while the x-axis is horizontal in real space.

The instrument POLI allows to continuously scan both angles Θ and χ which hence define polar coordinates for the neutron polarisation vector. The angle Θ is measured clock-wise in the x-y plane where $\Theta = 0$ corresponds to the y-direction. The angle χ is measured in the y-z plane starting also at $\chi = 0$ in the y-direction. For the measurements we have set and analysed the polarisation always in the same direction, in order to expose the depolarisation effect. Therefore, both nutator angles Θ and both angles χ set by the precession coils have always the same value, respectively. Measurements were so far only done for the single-crystalline sample with $x = 0.40$. The angular scans of the polarisation are shown in Fig. 5.11a and 5.11b. Both scans show that the polarisation is constant above T_C as expected for the paramagnetic sample. Below the transition temperature however a sinusoidal variation is observed. The variation in χ is much smaller than the variation in Θ which resembles the fact that the easy axis of the magnetisation is almost out of this particular plane.

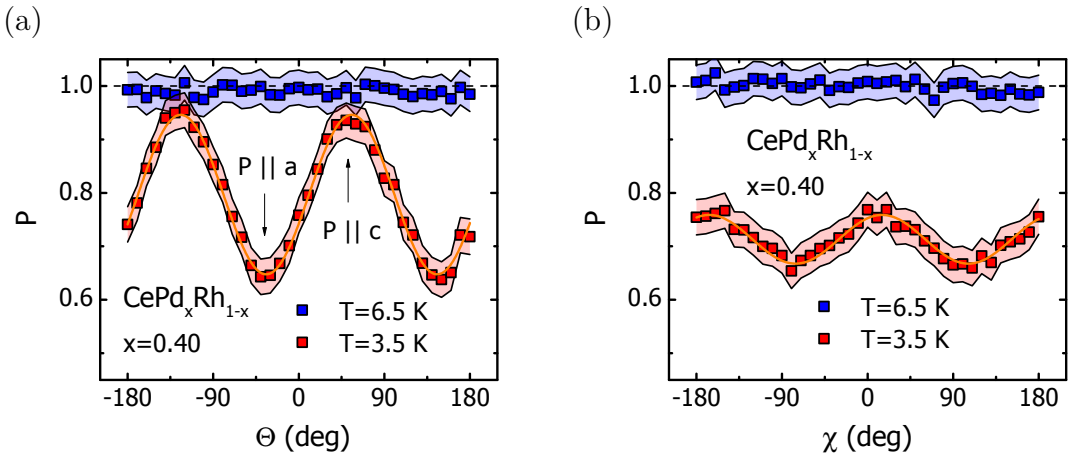

Figure 5.11.: Anisotropic behaviour of the depolarisation for a single-crystal of $CePd_{1-x}Rh_x$ with Rh concentration $x = 0.40$. For the measurements shown in (a) and (b) the angles Θ and χ have been scanned separately. The polarisation was thereby always set and analysed in the same direction. (a) The angle Θ lies in the crystallographic a-c plane of the sample which is almost perpendicular to the neutron beam. As can be seen from small phase shift in the oscillation the easy axis of the magnetisation is rotated roughly by an angle of 55° from the x-axis. (b) The angle χ defines the angle of the polarisation in the y-z plane where $\chi = 90°$ corresponds to the beam direction and roughly to the crystallographic b-axis of the sample.

In the angular scan of χ there is also a small oscillation which indicates that the sample surface (i.e. the crystallographic a-c plane) was not oriented perfectly perpendicular to the neutron beam. This is however not surprising as a 1D detector was used

to record the data [1]. Two well-defined minima and maxima are observed during a complete angular scan of the polarisation vector. The maxima correspond to the case where the easy axis of the magnetisation (in this case the crystallographic c-axis) is almost parallel or anti-parallel to the polarisation vector. The minima correspond to a maximum in depolarisation where the polarisation vector is almost perpendicular to the preferred magnetisation axis.

An interpretation of our data and the conclusions are given in the next section.

1 Compared to the case of a 2D imaging detector where the sample shape can be observed

5.3. Formation of Ferromagnetic Clusters

The fact that a signature in neutron depolarisation measurements is visible strongly suggests the existence of ferromagnetic volumes inside the sample. We have traced a signature so far up to a Rh concentration $x = 0.70$ using the depolarisation technique, thereby verifying the ferromagnetic nature of the ground state even at this large value of x. As suggested from the T_C maps the distribution of the ordering temperature varies only slightly over the samples with a rather sharp defined transition temperature. However, the depolarisation in zero magnetic field vanishes for $x \geq 0.65$ while small fields still recover the depolarising effect. The state after cooling a sample in this regime of x in zero field may be considered as an ensemble of small clusters which show FM order on a short length scale below our resolution limit as discussed in Sec. 4.4 (i.e. without significantly increasing the measurement times). The behaviour of the samples is clarified in Fig. 5.12a which shows the product $B_0^2\delta$ of the squared average field per domain B_0 and the average domain size δ as a function of the external field $B = \mu_0 H$. Fig. 5.12b shows $B_0^2\delta$ as a function of Rh content x.

As can be concluded from Fig. 5.12a very weak magnetic fields enhance the depolarising effect significantly. We suggest that the orientation of neighbouring ferromagnetic clusters gets more aligned by the external field, thereby effectively leading to larger ferromagnetic clusters that depolarise the neutron beam. Another possibility would be that the Kondo screened moments directly surrounding the ferromagnetic clusters are reactivated (unscreened) to take part in the FM order. However, as the average Kondo temperature in this regime was reported to be an order of magnitude larger in [107], i.e. $k_B T_K \approx k_B \Theta_P \gg T$, the effect of destroying Kondo hybrid states which then contribute to the ferromagnetism and essentially increase the cluster size is more unlikely. From Fig. 5.12b it can be seen that the signature after zero-field-cooling vanishes at $x = 0.70$ which implies that $B_0^2\delta \to 0$. However, after field-cooling in a small field $B = 7.5$ mT the FM behaviour persists up to larger values of x. The slope suggests to intersect at $B_0^2\delta = 0$ close to the CeRh limit $x \to 1$.

The temperature scans from this study were fitted to the model discussed in Sec. 3.2 and the corresponding temperatures found were combined with data from [69] to generate a new phase diagram. As can be seen in the revised phase diagram in Fig. 5.13 the ferromagnetic ordering temperatures found from this study are in very good agreement with earlier measurements. However, an additional freezing transition well below T_C for $x > 0.4$ was observed which we ascribe to the freezing of the ferromagnetic clusters in a random constellation in zero magnetic field.

In agreement with earlier studies it was observed that the ferromagnetism in $CePd_{1-x}Rh_x$ is suppressed in a continuous way with increasing x. For the sample with a low Rh concentration of $x = 0.40$ we observe a nearly constant amount of depolarisation below the ferromagnetic transition which resembles a magnetisation measurement at low

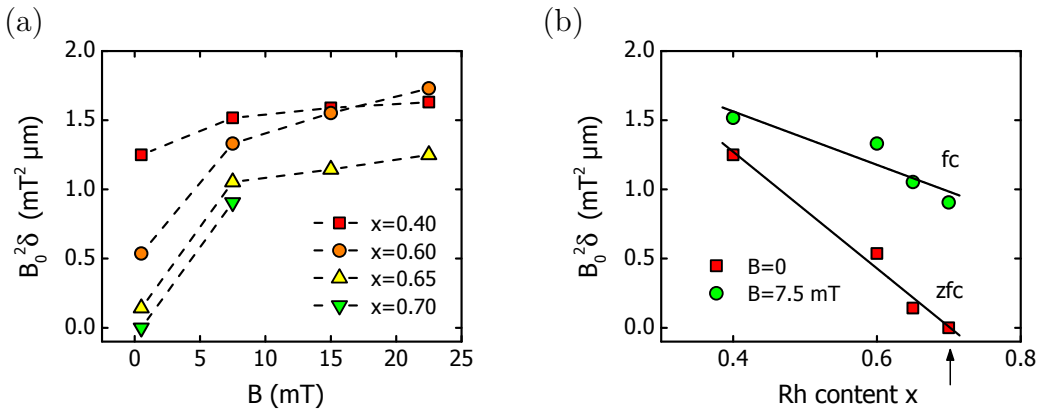

Figure 5.12.: (a) Product $B_0^2\delta$ of average flux density per domain B_0 in the $T \to 0$ limit and average domain length δ in transmission direction as a function of external magnetic field $B = \mu_0 H$. The behaviour is monotonic, however with increasing Rh content x the initial value at zero applied field vanishes for $x > 0.65$. (b) The product $B_0^2\delta$ shown as function of Rh concentration x derived from zero-field measurements and under an applied field B =7.5 mT for each concentration. The signature after zero-field-cooling vanishes at $x = 0.70$ which implies that $B_0^2\delta \to 0$.

magnetic fields and consequently in the multi-domain state of the sample. The sample is hence clearly ferromagnetic on length scales in the micrometer range as suggested by the depolarisation measurements. For larger Rh concentrations x a smoothly developing onset of a splitting of the fc-fh and zfc-fh depolarisation curves which is reminiscent of spin-glass behaviour is observed. Since disorder in this concentration range presumably leads to a distribution of Kondo temperatures it was already proposed that ferromagnetic clusters survive in a surrounding of Kondo-screened moments. These clusters may thereby interact weakly presumably through RKKY or dipolar interactions. It would hence be interesting to investigate the corresponding energy scales theoretically and experimentally for a comparison.

The random distribution of clusters suggests frustration effects between the clusters and a freezing temperature is thereby introduced where the cluster dynamics slow down significantly. At lowest temperatures the clusters freeze in a random constellation in zero field. Our measurements strongly support these considerations and allow the conclusion that for larger Rh content a state comparable to a superparamagnet is realised in $CePd_{1-x}Rh_x$ under zero-field-cooling which transforms to a ferromagnetic cluster glass in small applied fields. The magnetic field may in this case slow down the dynamics of the ferromagnetic clusters that survived which are then static (slow) enough to depolarise the neutron beam.

In Fig. 5.14 we try to give an illustration of the microscopic behaviour under zero-field-cooled (left column) and field-cooled conditions (right column). The Rh content x is

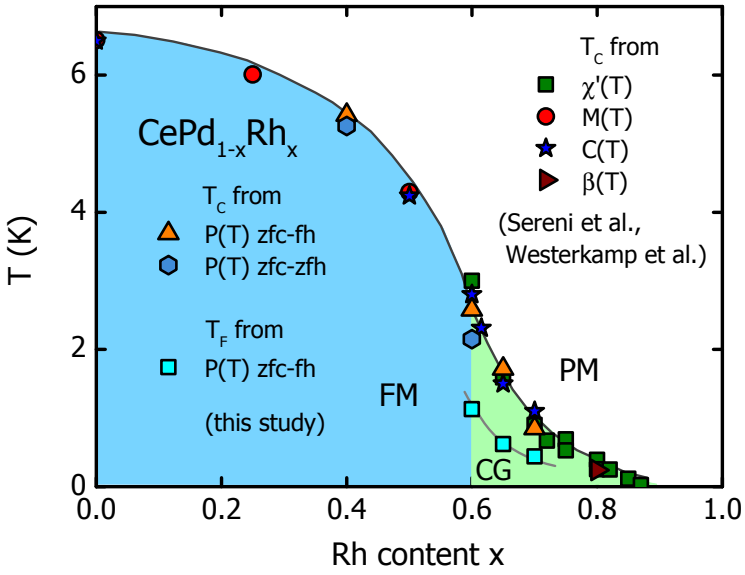

Figure 5.13.: Magnetic phase diagram of the ferromagnetic Kondo system $CePd_{1-x}Rh_x$ showing the ordering temperature $T_C(x)$ as a function of the Rh concentration x. Data from [69] were reused which include T_C as determined from susceptibility, magnetisation, specific heat and thermal expansion (right hand legend). The temperatures determined in this study from the signature in the neutron polarisation $P(T)$ are in good agreement (left hand legend). While ferromagnetism is suppressed continuously, a ferromagnetic cluster glass forms before reaching the quantum critical point. A temperature T_F where the clusters freeze in a random constellation was identified in this study. The curvature of the phase boundary changes sign at $x = 0.65$ which indicates the presence of disorder in the system leading to a distribution of characteristic temperatures. In the tail region of the phase boundary $T_C(x)$ a spin-glass state is formed from the ferromagnetic cluster glass before the non-magnetic state is reached in the CeRh limit.

assumed to increase in Fig. 5.14 from top to bottom. According to the depolarisation measurements it is assumed that ferromagnetic regions exist under zero-field-cooling for elevated Rh concentrations up to $x = 0.65$. In the regime of lower values of x the sample may be viewed on a microscopic scale like a normal ferromagnet (with some impurities) as illustrated in panels (a) and (e). Here the domain walls are assumed to be rather narrow compared to the domain size.

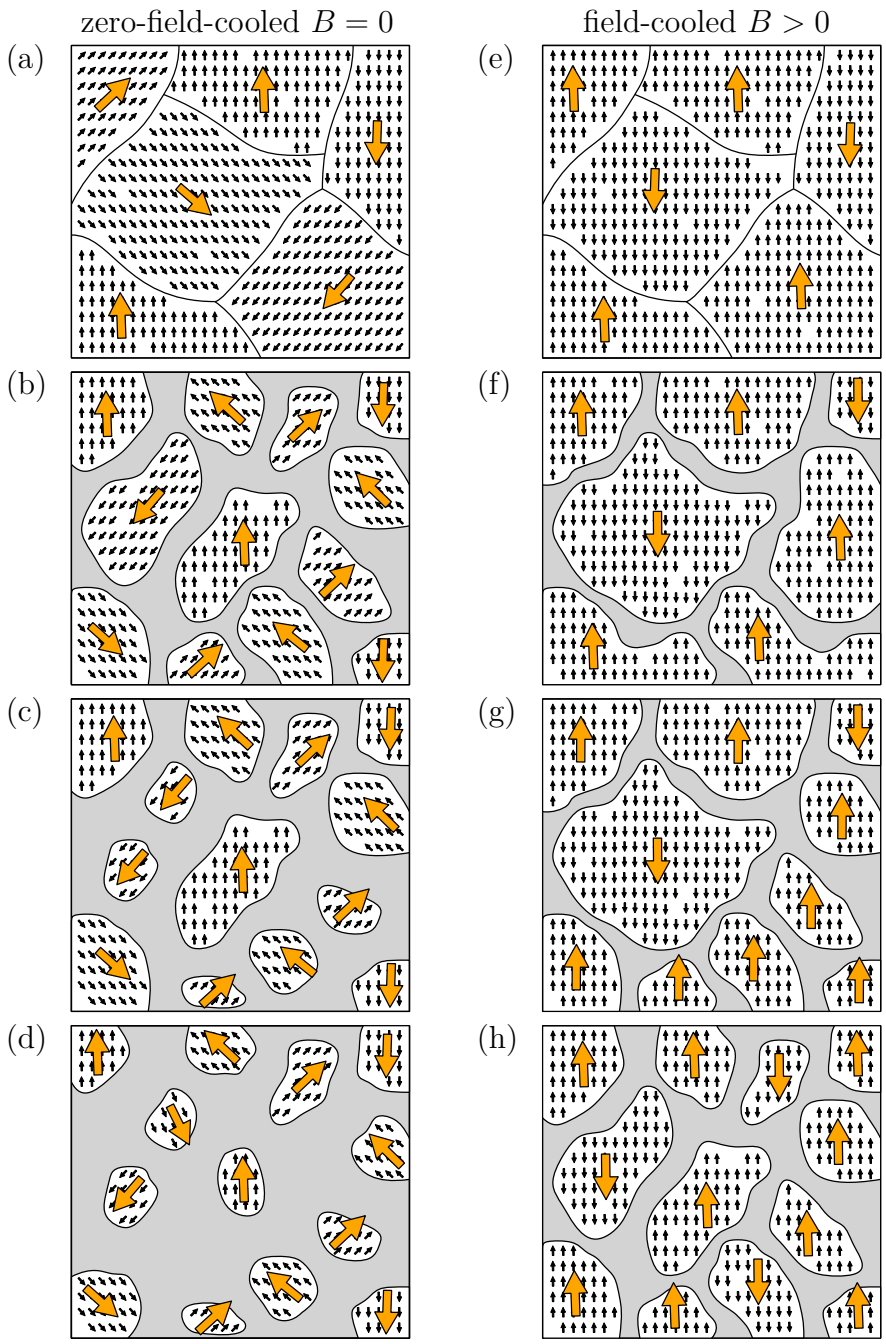

Figure 5.14.: Illustration of the cluster-glass formation in $CePd_{1-x}Rh_x$ with increasing the Rh content x from top to bottom. The left column, i.e. panels (a) to (d), corresponds to the case where the sample has been cooled in zero external magnetic field $B = 0$ (zfc). The right column with the panels (e) to (h) illustrate the state after field-cooling with $B > 0$ (fc). The upper most row shows the behaviour of a normal ferromagnet after zfc and fc, respectively. With increasing x the ferromagnetic domains decrease in size and disconnect from each other in a surrounding of screened magnetic moments due to the Kondo effect. In the fc state the average size of the increasingly independent ferromagnetic clusters is increased.

For moderate Rh content the ferromagnetic clusters decrease in size and disconnect from each other due to the surrounding moments which are screened due to the Kondo effect. The behaviour is shown in the panels (b) and (f). Further increasing x leads to a further decrease of the cluster size while at the same time the distribution of cluster volumes broadens as illustrated in panels (c) and (g). This effect may be particularly due to the intrinsic disorder in the elevated range of x which is assumed to be present mostly on a microscopic scale. Further increasing x leads to the formation of small clusters of only a few spins while the magnetic interaction between the distant clusters essentially vanishes. The panels (d) and (h) illustrate the proposed behaviour.

It is interesting to note that long-range interactions between the spin clusters could modify the dynamics of the system and may introduce an additional freezing temperature T_F below the ordering temperature T_C. It may be assumed that at T_C the FM order in each cluster stabilises. However, the entire clusters are still able to fluctuate on a slower time scale. This resembles virtually a superparamagnet where long-range interactions between the entire clusters are overcome by thermal fluctuations. Below T_F however the interactions between the clusters overcome the thermal fluctuations, as a consequence the dynamics slow down rapidly below T_F. Since each cluster orders ferromagnetic at an individual temperature depending on the cluster size, the ordering temperature T_C as well as the freezing temperature T_F of the system follow a distribution around their respective average values.

Further studies are required to characterise in particular the tail region of the system $CePd_{1-x}Rh_x$ in more detail. Additional depolarisation measurements on samples with elevated Rh concentration $x > 0.65$ are planned to investigate the field-dependence of the depolarisation. Small angle neutron scattering measurements may be used in order to identify the typical length scale of the ferromagnetic clusters. Further measurements of the spin dynamics using for example neutron spin-echo techniques may be used to investigate the time scales on which the ferromagnetic clusters exist.

The next chapter represents a study of the quantum phase transition in a clean system, the itinerant d-electron ferromagnet $ZrZn_2$, which is tuned by hydrostatic pressure. Disorder effects such as the formation of ferromagnetic clusters that are possibly characteristic for $CePd_{1-x}Rh_x$ are therefore not expected to occur in $ZrZn_2$ at first sight.

6. Itinerant Ferromagnetism in $ZrZn_2$ under Pressure

The binary compound $ZrZn_2$ may be considered as one of the archetypal weak itinerant ferromagnets. The first study on the ferromagnetic properties of $ZrZn_2$ was done by [152] who were also interested in the fact that both pure Zr and pure Zn get superconducting at low temperatures and the compound does not. For the magnetism the situation is just the opposite - only the compound is ferromagnetic while the pure elements are not magnetic. In subsequent studies it was observed that the application of hydrostatic pressure on $ZrZn_2$ leads to a continuous suppression of the ferromagnetic ordering temperature [153–155] to $T = 0$ which was in agreement with theory by this time [156]. However, although the ferromagnetic phase diagram as a function of pressure seemed qualitatively understood the quantitative predictions failed by orders of magnitude. This motivated several further theoretical and experimental studies [157–160, 117, 161].

Among early theories the Stoner-Wohlfarth model was found to describe the low-temperature and low-pressure magnetic behaviour of $ZrZn_2$ reasonably well. In these studies the qualitative behaviour was very similar, however, the set of parameters varied strongly for studies on different samples. From a more recent point of view it is now important to notice that the crystals produced at that time are not supposed to match the sample quality achieved nowadays [80, 70, 132] and varied significantly. Although $ZrZn_2$ in its magnetic properties was originally one of the model systems for Stoner theory the discrepancy between experiment and theory grew with increasing sample quality. For clean samples and high pressure the predicted second-order nature of the quantum phase transition was not observed and instead a first-order transition was found. Furthermore, a line of meta-magnetic transitions was identified in clean samples above a critical pressure referred to as tri-critical point. A phase diagram including these transitions is shown in Fig. 6.1 which is taken from Ref. [74]. The phase diagram was derived from ac-susceptibility data.

Interestingly, more recent theoretical approaches (see [42]) predict such a type of phase diagram generically for itinerant electron ferromagnets as already discussed in Sec. 2.1. Most thermodynamic properties of $ZrZn_2$ may be described well in this framework. However, to complicate the puzzle again two peculiar types of non-Fermi liquid behaviour are found at low temperatures for the electrical resistivity below and above the critical pressure. In particular the temperature dependence above the critical

pressure is not compliant with any of the mentioned theories. There is indication that the unusual resistivity may be the result of partial order which exists well above the tri-critical point. However, the typical length and time scale of this form of order is yet unclear.

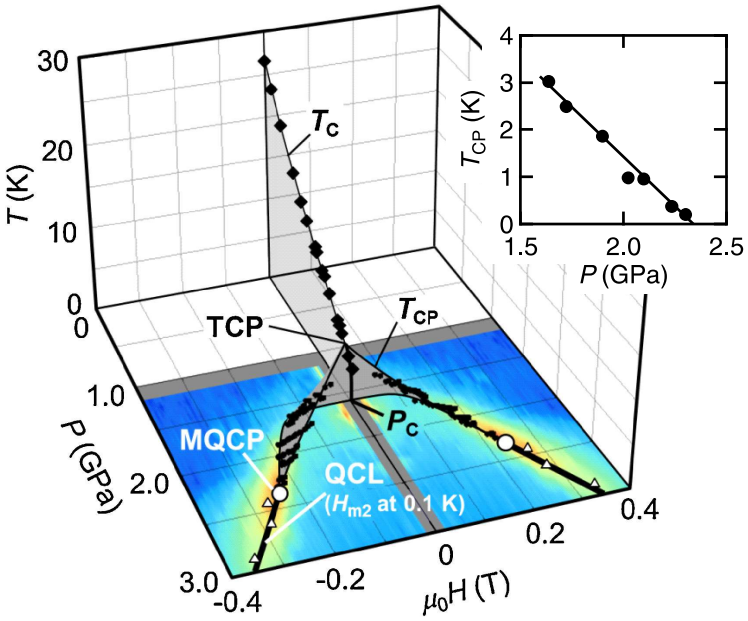

Figure 6.1.: Magnetic phase diagram of the itinerant ferromagnet $ZrZn_2$ showing the temperature versus pressure and external magnetic field as inferred from ac-susceptibility measurements. A line of second-order transitions at the temperature $T_C(p)$ is found for pressures p below the tri-critical point TCP at p_c =16.5 kbar. Above p_c meta-magnetic wings of first-order transitions indicated by the transition temperature $T_{cp}(p,B)$ are observed as a function of external magnetic field B and pressure. The upper right inset shows a detail of $T_{cp}(p)$. The meta-magnetic lines terminate at so-called called multiple quantum-critical points (MQCP) at 23.5 kbar and $T = 0$ at finite field B = 250 mT. The real part of the ac-susceptibility is visualised as colour plot in the base plane. The enhanced susceptibility above 23.5 kbar was associated with a quantum critical line (QCL) of so-called Lifshitz transitions which extends the line of first-order transitions in the $T = 0$ plane. Figure from [74] were further details can be obtained.

The magnetic phase transition in the critical regime and above the tri-critical point is under investigation in this study. We have used neutron depolarisation measurements in order to investigate the nature of the magnetic order with increasing hydrostatic pressure on the sample. As discussed in Sec. 3.2 the depolarisation technique is

particularly sensitive to the existence of small ferromagnetic domains or clusters and allows measurements under very small applied magnetic fields. It is hence a very useful probe to track the phase boundary $T_C(p)$ and to unambiguously verify the ferromagnetic nature of the underlying phase.

6.1. State of the Art

$ZrZn_2$ crystallises in a cubic C15 Laves phase with a lattice constant of 7.39 Å at ambient pressure. The Curie temperature in clean samples is found at 28.5 K with a small ordered moment of $\mu_s = 0.17\mu_B$. The effective moment μ_{eff} derived from the high-temperature susceptibility is about a factor of 11 larger than μ_s (e.g. [70]). The ferromagnetism is according to numerical band structure calculations a result from the spin-split electronic 4d bands formed by the Zr orbitals in the lattice. The band nature of the ferromagnetism is supported by the robustness of the high-field ferromagnetic properties against doping with iron or titanium [162, 163]. The magnetisation as function of field from $ZrZn_2$ can be evaluated using Arrott plots to demonstrate the typical behaviour of a weak ferromagnet as predicted by a Ginzburg-Landau theory with mean-field exponents (see [164]). In a more recent study on a clean $ZrZn_2$ sample at ambient pressure the mean-field exponents could be verified by a scaling analysis of the magnetisation [132]. In the same study a peculiar non-Fermi liquid behaviour of the electrical resistivity was observed for a sample under ambient pressure. The resistivity was found to follow a $T^{5/3}$ temperature dependence which compares to marginal Fermi-liquid (MFL) behaviour as discussed in Sec. 2.1.

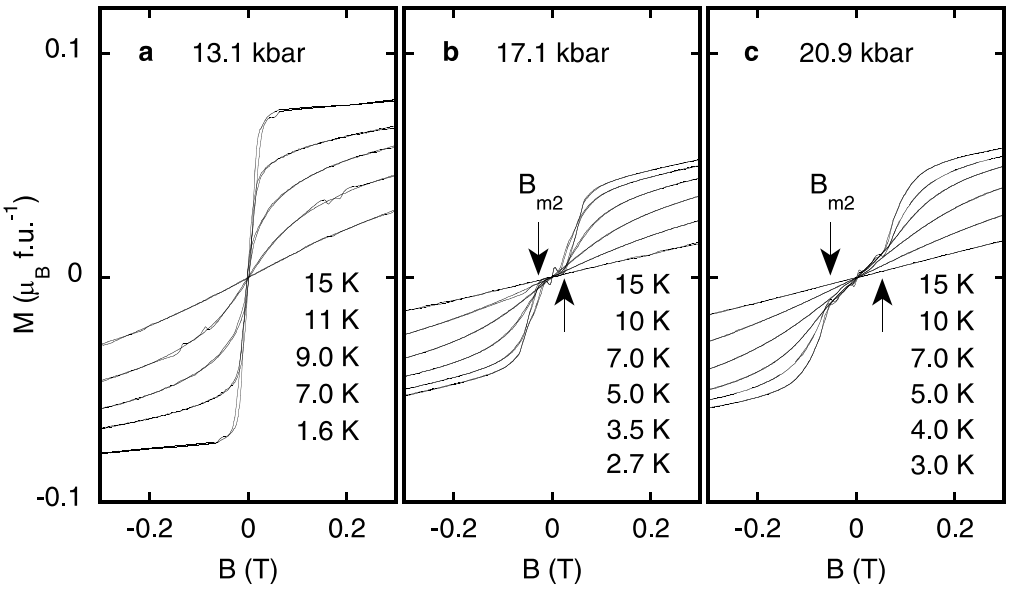

Figure 6.2.: Hysteresis loops measured in $ZrZn_2$ for three different pressures, one below and two pressures above the tri-critical point at p_c =16.5 kbar. The hysteresis is not visible for all pressures. Above p_c meta-magnetic transitions were identified by the shoulder (indicated by arrows) which evolve to larger fields with increasing pressure. Figure from [70].

A $ZrZn_2$ sample of excellent quality was investigated in detail by [71]. The sample was pressurised in a non-magnetic Cu:Be clamp cell. The same sample and the same pressure cell were used for the present study as described in Sec. 4.2. It was confirmed that the Curie temperature decreases linearly with pressure up to a tri-critical point at $p_c = 16.5$ kbar. The phase transition then changes to a first-order transition where T_C together with the spontaneous magnetisation rapidly drop to zero. Above p_c a line of meta-magnetic (MM) transitions was observed. Exemplary magnetisation data which show this MM transition are shown in Fig. 6.2. The magnetisation is shown for one pressure below and two pressures above p_c. The meta-magnetic transition is associated with the kink at finite field well below saturation.

Interestingly, the extrapolated inverse susceptibility to $\chi(T)^{-1} = 0$ indicates the existence of ferromagnetic correlations up to a pressure of 20.5 kbar, which is higher than the tri-critical point around 16.5 kbar. The extrapolated points which were extracted from VSM measurements in a small field $B = 100$ mT are shown in Fig. 6.3a. Magnetisation data were also used to estimate the effective moment which is shown in Fig. 6.3b. For comparison the effective moment was additionally determined in a very small external field $B = 0.1$ mT where it seems to disappear in a first-order manner at the tri-critical point.

The electrical resistivity of $ZrZn_2$ under pressure was investigated in detail up to 32 kbar as reported in [72]. The study showed that the low-temperature resistivity behaviour as function of temperature changes more or less abruptly from $\rho(T) \propto T^{5/3}$ for pressures below 14 kbar to a $\rho(T) \propto T^{3/2}$ dependence for pressures above 18 kbar. Both exponents of the temperature are not compatible with Fermi liquid theory without further modification. At least the $T^{5/3}$ behaviour could be explained assuming a so-called marginal Fermi liquid for the electronic state in the vicinity of the quantum critical point. However, the $T^{3/2}$ resistivity above p_c remained unexplained.

The electrical and thermal resistivity of $ZrZn_2$ under pressure was investigated in [73] where essentially the same theoretical framework was given to explain the temperature-dependencies below the critical pressure. It was explained that the metallic behaviour is generically altered by the coupling of the magnetic order parameter fluctuations to electronic soft-modes (as in [42]). This leads for clean systems to a tri-critical point at finite temperature before reaching a quantum critical point at $T = 0$. In this regime a marginal Fermi liquid description may be suitable to explain the transport propertied. Unfortunately, no explanation was found for the $3/2$ exponent of the resistivity above the critical pressure.

The study was continued by [74] under pressure up to 32 kbar using magneto-resistance and susceptibility measurements. The authors traced the meta-magnetic transition at lowest temperatures and concluded the existence of critical end points of the meta-magnetic transition at $T = 0$ which occur at 23.5 kbar under an applied magnetic field

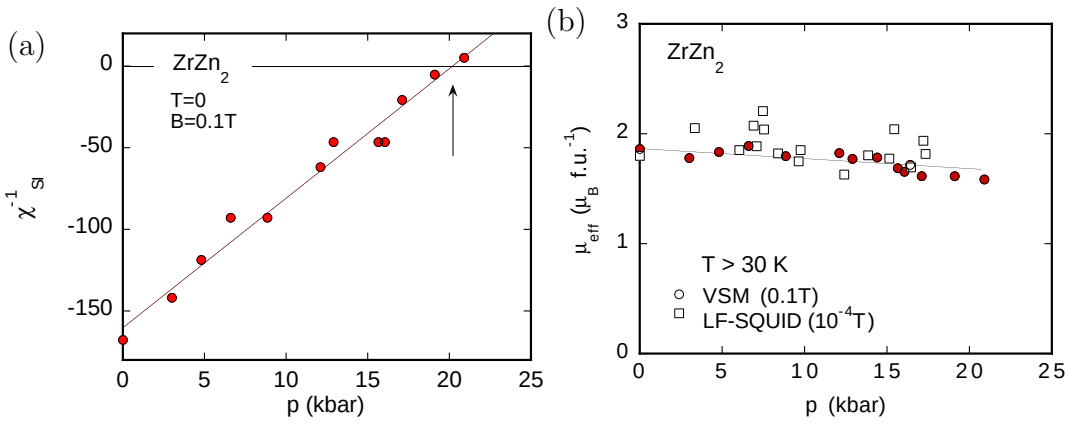

Figure 6.3.: (a) Inverse static susceptibility $\chi^{-1} = B/M(T)$ (in SI units) as a function of pressure. The continuous line is a linear fit, the intersection is at 20.5 kbar. (b) Effective magnetic moment μ_{eff} derived from magnetisation data measured with a VSM in 0.1 T and with a SQUID magnetometer at 0.1 mT. Data from [165].

of 250 mT. For even higher pressures a line of first-order transitions is then fixed at $T = 0$ which the authors associated with a Lifshitz transition. Again the $5/3$ to $3/2$ drop of the exponent in the resistivity was confirmed at the tri-critical point around 16.5 kbar. As an explanation for the non-Fermi liquid behaviour above p_c the proximity to the Lifshitz transition was discussed which may produce complicated fluctuations between two configurations of the Fermi surface. Such fluctuations would certainly explain deviations from conventional Fermi liquid behaviour. However, a model which includes these effects on the transport properties was not given by [74] and is not known to the author.

Another interesting observation in [74] is the negative slope of the meta-magnetic line dT_c/dH which may indicate at least short-range order below the critical field. As noticed by [94] a $T^{3/2}$ resistivity is more commonly found for antiferromagnetic systems close to a quantum critical point. This allows the conclusion that above the tri-critical point in $ZrZn_2$ additional antiferromagnetic fluctuations may contribute or even dominate the transport behaviour. Such a conclusion is also supported by recent theoretical work by [166, 47, 48] which suggests that a modulated phase (e.g. a spin-spiral) and a nematic phase (essentially a melted version of the modulated phase) may pre-empt the paramagnetic phase when suppressing uniform ferromagnetic order by using pressure.

We have performed neutron depolarisation measurements on $ZrZn_2$ under high pressure in order to explore the ferromagnetic correlations of the underlying phase in the critical regime in more detail. The results of the study at hand are given in the next section which are afterwards interpreted in the line of findings described above.

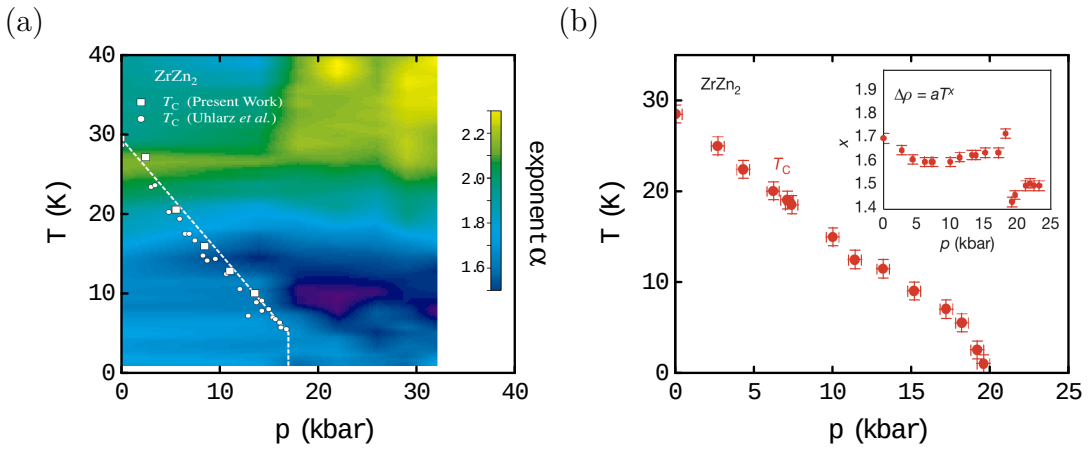

Figure 6.4.: Magnetic phase diagrams showing $T_C(p)$ for $ZrZn_2$. (a) Figure adapted from [72]. The resistivity exponent α from $\rho(T) \propto T^{\alpha}$ was extracted by taking the logarithm and is shown as colour map. The behaviour changes at $p_c = 16.5$ kbar where the magnetisation in zero-field vanishes according to Ref. [70]. (b) Magnetic phase diagram adapted from Ref. [73] who were able to trace a feature in the resistivity which indicates that the phase transition vanishes at 19.5 kbar. However, the phase transition changes from second-order to a weak first-order transition at 16.5 kbar. The inset shows the resistivity exponent changing from 5/3 to 3/2 at 19.5 kbar.

6.2. Experimental Results

In this section we report on the experimental results from bulk measurements recorded using a Vibrating Sample Magnetometer (VSM) as described in Sec. 4.3 and from neutron depolarisation measurements as explained in Sec. 4.4. We have used the depolarisation technique for our study on $ZrZn_2$ in the vicinity of the critical pressure p_c. We have adjusted four different pressures which are abbreviated as H1 (p=16 kbar), H2 (p=18.2 kbar), H3 (p=17.5 kbar) and H4 (p=5.6 kbar) and recorded data for each pressure first in the VSM and then at the neutron source FRM II. The pressure for each measurement was determined as explained in Sec. 4.2 from the susceptibility drop due to the superconducting Sn transition. The first derivative and a moving average smoothing was applied to determine the superconducting transition temperature by using the peak position as shown in Fig. 6.5. Additionally, a sample abbreviated as S1 was investigated under ambient pressure without a pressure cell for comparison.

6.2.1. Magnetisation

The magnetisation $M(T)$ was measured for each pressure as a function of temperature up to 30 K for the higher pressures H1, H2, H3 and up to 50 K for the lower pressure H4. The data are shown in Fig. 6.6a. As expected from the adjusted pressure the

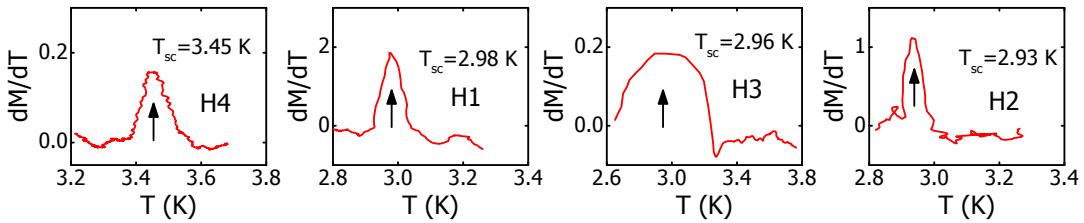

Figure 6.5.: The pressure on the $ZrZn_2$ sample is determined from the superconducting transition $T_{sc}(p)$ of a Sn piece which is located in the same pressure cell as the $ZrZn_2$ sample under investigation as described in Sec. 4.2. The transition at T_{sc} is observed in the magnetisation $M(T)$ measured with an external field $B = 0.5$ mT which allows for a precise determination of the pressure on the sample. The peak position of the first derivative $\mathrm{d}M/\mathrm{d}T$ was used to determine the transition temperature. The same sample and the same pressure cell as in [70] were used for this study. The labels H1 to H4 indicate the order of measuring the pressure cell. The pressure cell reached its mechanic limit at H3 where the pressure was actually meant to be slightly larger than for H2. The broadened Sn transition for H3 suggests a pressure gradient (a uni-axial pressure component) in the pressure medium. The transition temperature determined from this measurement may hence be considered as ambiguous.

up rise in M is suppressed to a lower temperature from H1 to H2. The pressure for H3 was meant to be slightly higher than for H2, however the pressure cell was on its mechanical limit and lost some pressure instead. For H4 the pressure was released to around 6 kbar.
A convenient method to provide an estimate for the ferromagnetic ordering temperature T_C is to extrapolate the inverse susceptibility $\chi_{dc}^{-1}(T) = B/M(T)$ to zero and use the intercept with the temperature axis which is shown in Fig. 6.6b. For temperatures well above T_C a linear behaviour is observed as expected from a Curie-Weiss law. The extrapolation to zero lets us estimate the values of T_C as listed in Tab. 6.1.

The magnetisation $M(B)$ was recorded as a function of an external magnetic field at $T = 3.25$ K. The data of the four pressures are shown in Fig. 6.7. The hysteresis is negligible for all pressures and is hidden by the negative hysteresis error from the superconducting magnet in the VSM of approximately 3 mT. With increasing pressure the saturation magnetisation decreases which is consistent with earlier studies as in

	H1	H2	H3	H4
hydrostatic pressure p	16.0 kbar	18.2 kbar	17.5 kbar	5.6 kbar
T_C from $B/M(T)$	6.3 K	4.5 K	5.1 K	18.8 K

Table 6.1.: Pressure p and ordering temperature T_C of the $ZrZn_2$ sample as estimated from the inverse magnetisation $B/M(T)$ extrapolated to zero.

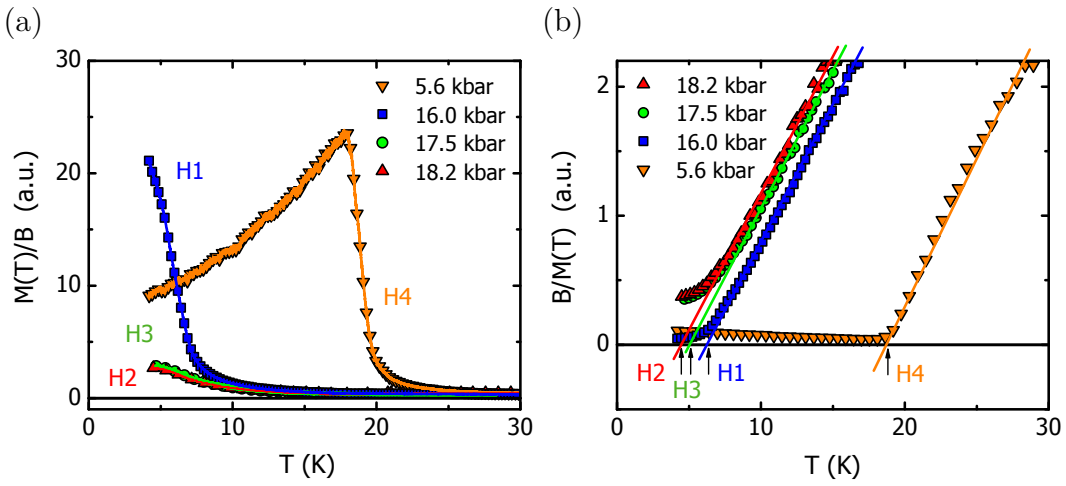

Figure 6.6.: (a) Magnetisation $M(T)/B$ as a function of temperature measured in a VSM for the pressures $p = 16$ kbar (H1), $p = 18.2$ kbar (H2), $p = 17.5$ kbar (H3) and $p = 5.6$ kbar (H4). The up-rise indicates the ferromagnetic ordering. (b) Inverse susceptibility $B/M(T)$ as a function of temperature. According to a Curie-Weiss law the intersect with the temperature axis gives an estimate of the ordering temperature.

[165]. For H2 where $p > p_c$ the slope of the curve changes with a kink at a field around $B_{mm} = 25$ mT indicating the meta-magnetic transition as expected from earlier studies [165, 74]. The data for H3 do not clearly show the meta-magnetic transition in $M(B)$ indicating that the actual pressure was only very close above the tri-critical pressure. By taking the derivative we have estimated a value $B_{mm} = 10$ mT. A misleading feature which can be observed in all of the hysteresis loops is a small kink around 50 mT. This is an instrumental issue which has not been solved so far. However, as it was also observed for completely different samples, we may safely ignore it in the data analysis. These findings will be combined with the neutron data described in the following section.

6.2.2. Neutron Depolarisation

The signature of ferromagnetic correlations in a sample that is observed in neutron depolarisation measurements can be used to provide microscopic information. It will be used to complement the laboratory data. As discussed in Sec. 3.2 the depolarisation of the neutron beam through the sample indicates the existence of ferromagnetic domains or clusters. The polarisation $P(T)$ was recorded as a function of temperature for different external fields B. Additionally, the polarisation $P(B)$ as function of magnetic field was investigated. The temperature scan shown in Fig. 6.8a was recorded for the sample S1 at ambient pressure in a field $B = 0.5$ mT. The curve reflects the behaviour for a normal ferromagnet as expected from the phase diagram from [70] and follows

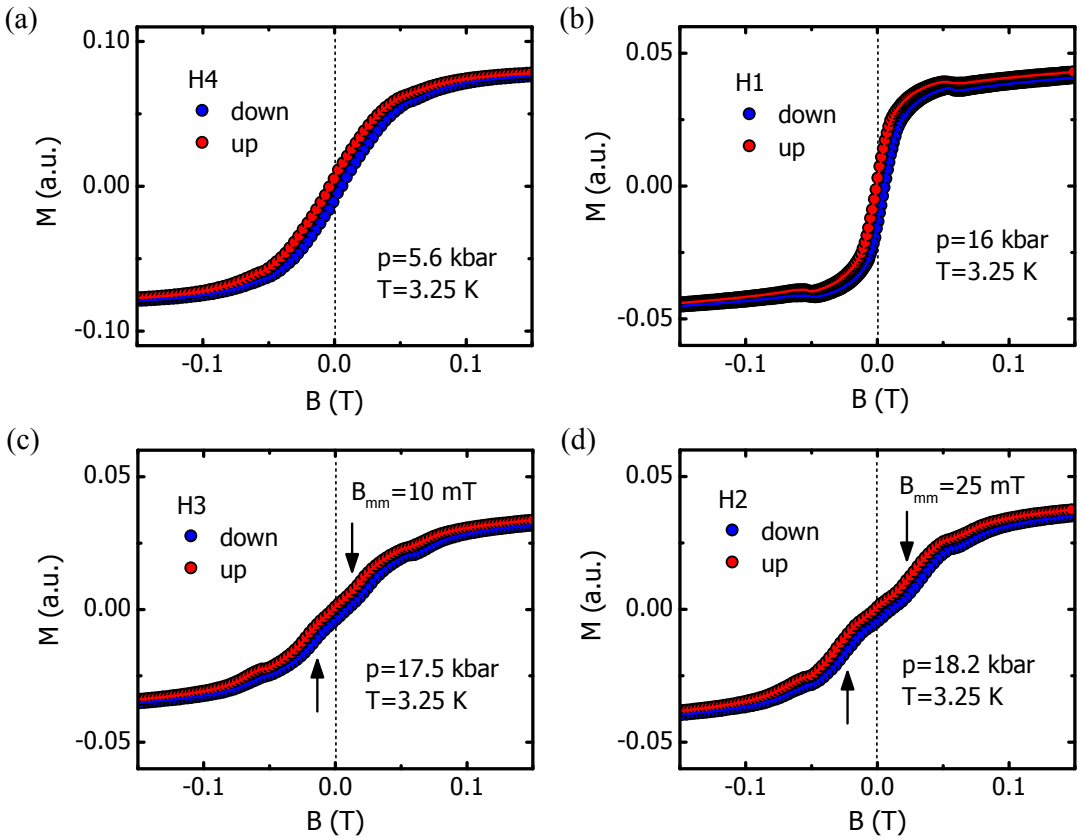

Figure 6.7.: Magnetisation loops measured at $T = 3.25$ K in a VSM. The pressures adjusted for the four measurements were $p = 16$ kbar (H1), $p = 18.2$ kbar (H2), $p = 17.5$ kbar (H3) and $p = 5.6$ kbar (H4). The negative hysteresis seen between sweep-up and sweep-down is due to the superconducting magnet of the VSM. However, the sample shows essentially no hysteresis as confirmed by high-precision SQUID measurements in an earlier study. The kink at $B_{mm} = 10$ mT for H3 and at $B_{mm} = 25$ mT for H2, which is indicated by the arrows, is associated with the meta-magnetic transition. A small kink around 50 mT is observed in all plots and is ascribed to an instrumental issue as explained in the text.

in general the theoretical predictions given in Sec. 3.2 for the depolarisation in weak ferromagnets.

A linear relation between M^2 and T^2 was found from magnetisation measurements of $ZrZn_2$ which is not observed in the neutron depolarisation. This can be seen by taking the logarithm $-\log(P)$ of the polarisation which should then be proportional to the product $B^2\delta$ as shown in Fig. 6.8a. In the product $B^2\delta$ now B denotes the average field in each domain with a mean value δ for the domain size. As it does not behave linear versus T^2 this suggests on the one hand that the domain size may depend on temperature. On the other hand this reminds us that the magnetisation

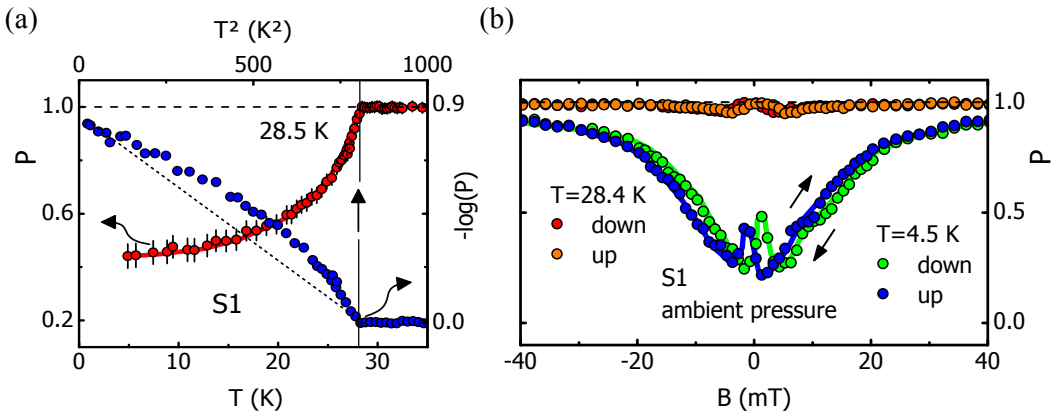

Figure 6.8.: Depolarisation data for the sample S1 under ambient pressure. (a) Depolarisation measured as a function of temperature (left scale, red data points). In addition, the value of $-\log(P) \propto B^2\delta$ extracted from the data and plotted versus the squared temperature T^2 is shown using the top scale together with the right hand scale. The dashed line corresponds to a linear relation between B^2 and T^2 as suggested by magnetisation data in [165]. (b) Depolarisation as a function of external magnetic field measured at $T = 4.5$ K which was the lowest temperature in this measurement, and measured at $T = 28.4$ K which is just 0.1 K below the Curie temperature. A hysteresis is observed at the lower temperature. In addition, a small oscillation occurs at small fields below 10 mT which may be explained by a magnetic anisotropy (a magnetic easy axis) in the sample.

which is probed by the neutron depolarisation technique is not exactly the same as the bulk magnetisation but may be regarded as a scaled version of the magnetisation with a non-linear relationship. The field loops in Fig. 6.8b show an interesting feature. In particular in the field loop recorded at 4.5 K the small hysteresis of about 2.5 mT is clearly observed with a small oscillation occurring in the range of small fields up to 10 mT. The small oscillation may however be an artefact of stray fields which dominate the behaviour if the guide field direction at the sample position changes its sign.

A similar signature in the depolarisation as for the sample S1 at ambient pressure was also observed in the other measurements on the $ZrZn_2$ sample under hydrostatic pressure (H1, H2, H3 and H4). The data are shown in Fig. 6.9a to 6.9d for increasing pressure. Again the left column shows the temperature dependence of the polarisation using the left hand scale. The right column in Fig. 6.9 shows the corresponding field sweeps recorded for each pressure. For the field sweeps a separate scale on the right hand side is used for better readability.

At the moderate pressure $p = 5.6$ kbar as shown in Fig. 6.9a the value of $T_C = 19$ K determined from the depolarisation is in good agreement with the value estimated from the inverse susceptibility. Both measurements suggest that the magnetic order

stabilises rapidly below T_C. A small hysteresis of the order of 2 mT is visible in the field loop shown on the right hand side which compares to the measurement S1 under ambient pressure shown above. Again the oscillation at small fields is observed which suggests that the effect is a subtle interplay of the low-field susceptibility of the sample and our particular field geometry in the depolarisation set up.

For the measurement H1 shown in Fig. 6.9b we have adjusted a pressure $p = 16$ kbar which is just below the tri-critical point $p_c = 16.5$ kbar. Temperature sweeps were recorded for fields in the range $B = 0.5$ - 37 mT. The curves collapse at $T_C = 6.5$ K above which the sample is paramagnetic. The small field of 37 mT is already sufficient to fully align the domains along the polarisation direction. Therefore, the signature below T_C vanishes. In the field loop on the right hand side the small oscillation observed for 5.6 kbar is less pronounced. The colour data points correspond to the sweep-up with increasing field while the open white circles in the background correspond to the sweep-down. As both datasets are essentially identical within the statistics one may conclude that the hysteresis has vanished. However, the measurements were only possible down to 3.0 K, a small hysteresis might have been observed at lower temperatures.

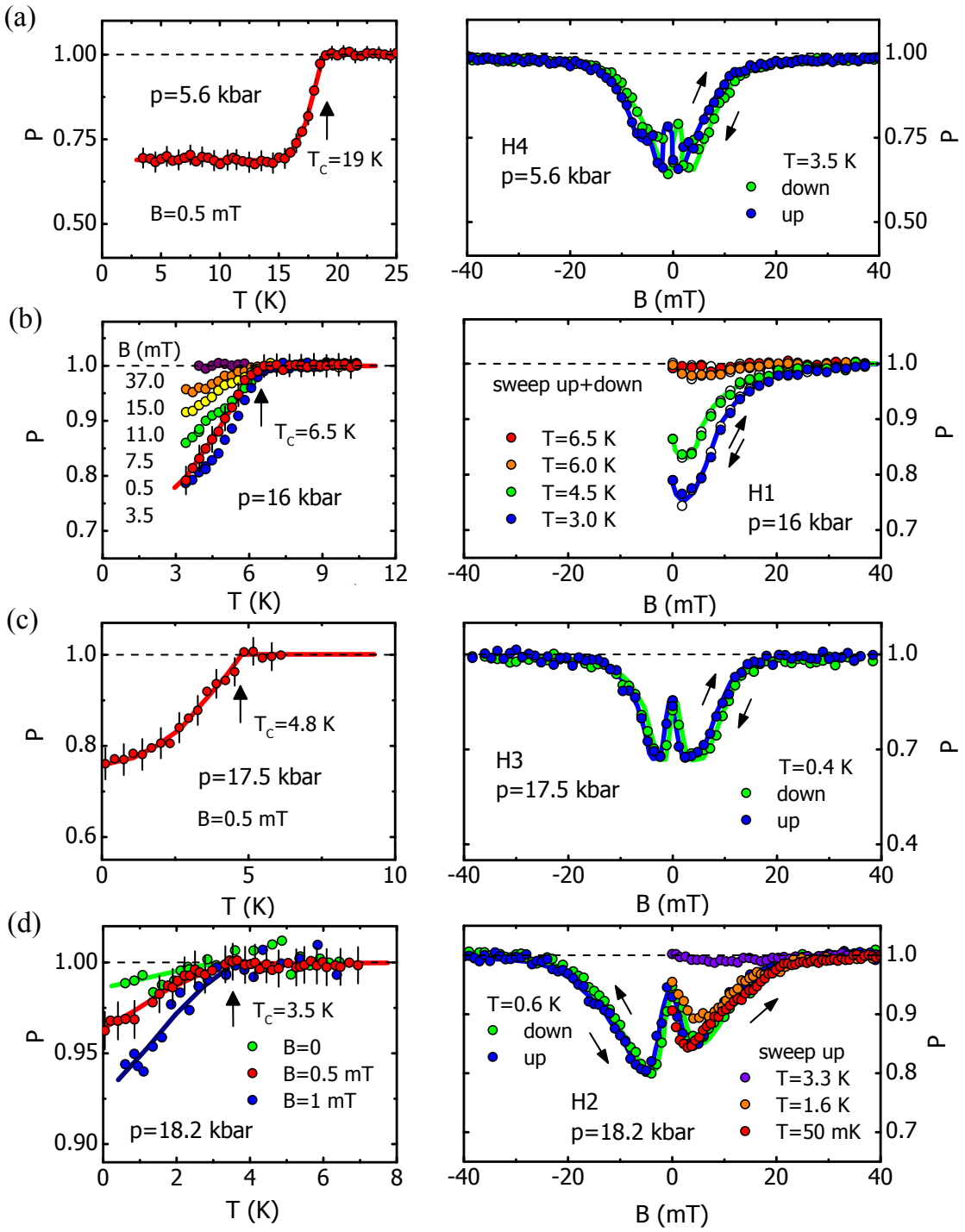

Figure 6.9.: Depolarisation data from the measurements of the $ZrZn_2$ sample under hydrostatic pressure where (a) $p = 5.6$ kbar (measurement called H4), (b) $p = 16$ kbar (H1), (c) $p = 17.5$ kbar (H3) and (d) $p = 18.2$ kbar (H2). Left column: depolarisation as a function of temperature (red circles for $B = 0.5$ mT and coloured circles for larger values of B) using the left hand scale for the polarisation. The ordering temperatures T_C are indicated by vertical arrows. Right column: depolarisation as a function of external magnetic field applied along and anti-parallel to the polarisation direction. The depolarisation at $B = 0$ rapidly decreases with increasing the pressure above 16 kbar. However, small magnetic fields recover the depolarising effect significantly. Notice the change of the scale of the polarisation for each pressure.

At a pressure of 17.5 kbar which is closely above the tri-critical point we have determined $T_C = 4.8$ K as can be seen in Fig. 6.9c on the left hand side. As for the other pressures the red circles correspond to the temperature sweep in a field $B = 0.5$ mT. The signature in the polarisation is very similar to the lower pressures. The transition is clearly observed even at this low field. In the field loop shown on the right hand side in Fig. 6.9c the shift of the sweep up and down curves indicate again a small hysteresis of the order of 1 mT. The depolarisation at $B = 0$ is decreased compared to $p = 16$ kbar. However, small values of B enhance the depolarisation significantly producing a minimum value in the polarisation at finite values of B which is not so pronounced for the lower pressures. In terms of our model for the depolarisation due to the ferromagnetic domain structure this indicates a remarkable increase of the product $M_0^2\delta$ of the average magnetisation M_0 in each domain and the average domain size δ probed in transmission direction.

Interestingly, for $p = 18.2$ kbar we have still observed a depolarisation below a transition temperature of 3.5 K as shown in Fig. 6.9d on the left hand side. We have recorded the data without external field $B = 0$ and after field-cooling in a field $B = 0.5$ mT and 1 mT for comparison. For these small fields the signature in the depolarisation is increased. However, the effect of depolarisation is still in the percent range. The statistic for the measurement at $B = 0$ are rather bad which is likely due to the weak guide field at the sample position as seen by the neutrons. In this case very small external stray fields dominate the behaviour of the polarisation. For this pressure $p = 18.2$ kbar we have recorded field sweeps in one direction using the simple set up described in Sec. 4.4.1.1 at three different temperatures and a complete field loop using the new set up as described in Sec. 4.4.1.2. The data indicate that in principle both configurations produce similar results for positive values of B. The depolarisation nearly vanishes at 3.3 K which is in good agreement with the temperature sweep shown on the left in 6.9d. From the complete field loop which was recorded at $T = 0.4$ K one can still observe a small hysteresis between sweep up and sweep down which is more pronounced at finite values of B compared to very small fields around $B = 0$.

The conclusions taken from our results are discussed in the next section in the light of previous studies.

6.3. Traces of Ferromagnetic Order above the Critical Pressure

We have investigated a $ZrZn_2$ sample at ambient pressure and a $ZrZn_2$ sample at four different pressures using a clamp pressure-cell. The pressures were determined to be $p = 5.6$ kbar, $p = 16$ kbar, $p = 17.5$ kbar and $p = 18.2$ kbar. The tri-critical point as observed in previous studies was reported to be located at $p_c = 16.5$ kbar [70, 72, 74]. We have observed a signature of ferromagnetic domains or clusters in the depolarisation for the pressures below p_c as well as for the pressures above p_c. This indicates a form of ferromagnetic order persisting closely above the tri-critical point.

The measurements at 18.2 kbar may be considered the most conclusive in this study. The pressure lies above p_c. Nevertheless, a signature of depolarisation occurs below $T_X = 3.5$ K. The field-dependence of the depolarisation still suggests the existence of ferromagnetic correlations in the sample. For a comparison of the behaviour for the different pressures the slope dP/dT of the polarisation obtained by a linear fit of the polarisation just below T_C is considered. Due to the derivative it represents a measure of the critical exponent for the temperature dependence of the magnetisation and should scale with the magnetisation. The values are plotted in Fig. 6.10a. Although a quantitative analysis is not conclusive due to the unknown average domain size, a qualitative consideration of the plot suggests a rapid decrease of dP/dT just above the tri-critical point at $p_c = 16.5$ kbar.

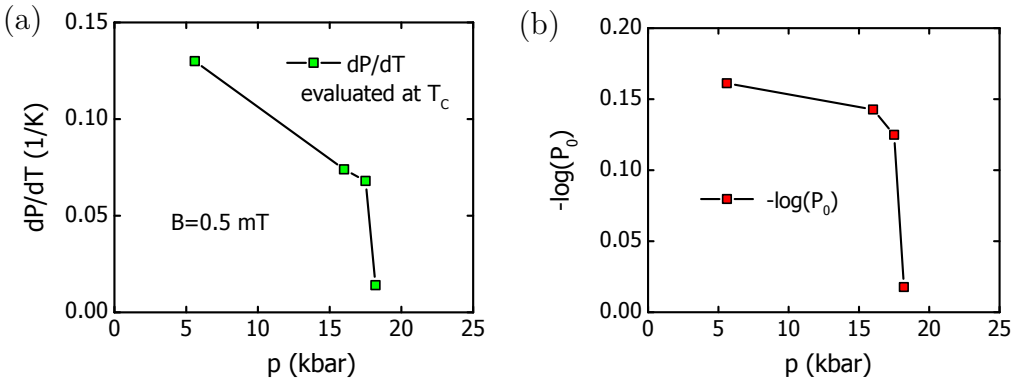

Figure 6.10.: (a) Slope of the polarisation $dP/dT(T_C)$ evaluated at the transition temperature T_C for the different pressures. A rapid decrease of the slope is observed above the tri-critical point. (b) The value of the polarisation $P_0 = P(T \to 0)$ extrapolated to zero temperature shows the evolution of the product $B_0^2\delta$ with pressure. The behaviour compares to the magnetisation measurements by [70] and suggests a QPT which changes from second-order to first-order at the tri-critical point around 16.5 kbar.

For a comparison we have also estimated the polarisation as extrapolated to the $T = 0$

limit. The negative logarithm of this value should be proportional to the squared magnetisation and the average domain size in the $T = 0$ limit as described in Sec. 3.2. The values of $-\log(P_0)$ are plotted in Fig. 6.10b. It must be noted that these data points represent only an estimate, nevertheless, the tendency is clearly similar to the behaviour of the magnetisation as discussed in the previous section. Just above the tri-critical point the value drops rapidly towards $B_0^2\delta \to 0$ which suggests a first-order transition. However, there is still a depolarisation in very small fields which are nominally well below the critical field B_m of the meta-magnetic transition.

Increasing the external magnetic field leads for small values first to a stronger depolarisation which may be the result of an increased domain size or mean field per domain. Further increasing the field then leads to a decrease in depolarisation. This indicates that the domain structure is aligned mostly parallel and anti-parallel to the applied field direction. For high fields the multi domain state transforms to a single-domain state. For the neutron spin this corresponds essentially to a smooth continuation of the guide field, which explains why the depolarisation vanishes at elevated fields but below the saturating field as estimated from magnetisation measurements.

Together with the observed meta-magnetic transition in earlier studies this leads to the conclusion that $p_c = 16.5$ kbar in fact denotes a tri-critical point in the phase diagram. At this point the order of the phase transition as a function of temperature changes from second-order to weakly first-order. Meta-magnetic first-order transitions are found in the magnetisation which were not as clearly observed in the neutron depolarisation. A possible reason could be the rather slow sweep rate at which we have recorded the neutron data compared to the magnetisation measurements. A faster sweep could in principle allow to resolve the meta-magnetic transition as well. Nevertheless, we have observed a small depolarising effect at a pressure $p = 18.2$ kbar even in nearly zero external field which implies the existence of residual ferromagnetic order on a short length scale and possibly also short time scale.

We have included the transition temperatures which were determined from the neutron depolarisation measurements in a field $B = 0.5$ mT to extend the magnetic phase diagram from [71] which is shown in Fig. 6.11. The transition temperatures are in good agreement. Above the tri-critical point a rapid decrease of the ordering temperature is suggested.

Since the ordering transition above p_c is not clearly visible in magnetisation data this might suggest that a sort of modulated spin structure forms at this high pressure. According to our results the meta-magnetic transition above p_c could be a reconfiguration of the domain structure. However, it requires further investigation in particular in the high-pressure regime where the ordering temperature is almost suppressed to $T = 0$. As our first pressure-cell was not able to apply higher pressures we have already loaded a new clamp pressure cell and adjusted the pressure to approximately $p = 16$

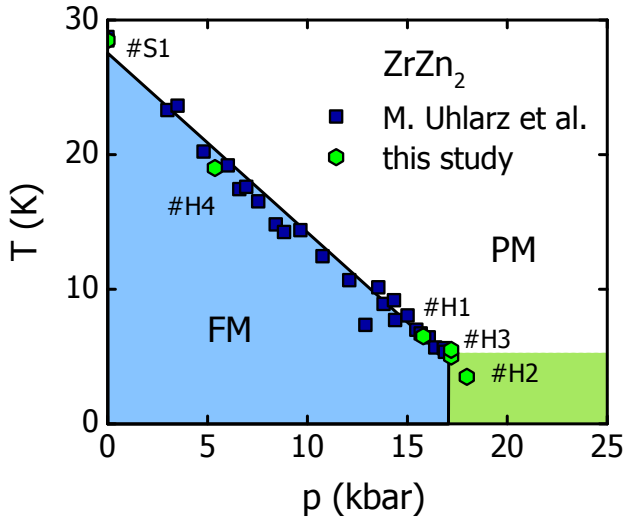

Figure 6.11.: Temperature versus pressure phase diagram of the itinerant ferromagnet $ZrZn_2$. A line of first-order transitions is found below the tri-critical point at p_c =16.5 kbar. Above p_c the ordering temperature drops rapidly indicating a first-order transition. However, even slightly above the tri-critical point a weak signature of ferromagnetic order exists in weak magnetic field well below the critical field of the meta-magnetic transition. Data from [71] were reused.

kbar. Further depolarisation measurements are thereby planned as part of the Master thesis by M. Seifert. In addition, a SANS study will be performed using different applied fields for the regime of higher pressures in order to investigate a possible spin texture of the sample which might form just above the tri-critical point as suggested e.g. in [42, 166, 47, 48] as a generic feature for clean itinerant ferromagnets. Further measurements may hence be collected following the theoretical predictions for such a modulated phase existing at high pressures.

Recent studies in this light have been done also on $Nb_{1-x}Fe_{2+x}$ or $Sr_3Ru_2O_7$ (see e.g. [98, 88]) where also meta-magnetic transitions have been observed. Particularly interesting is the similarity of the meta-magnetic transitions in the SDW phase of $Nb_{1-x}Fe_{2+x}$ which strongly resemble the behaviour observed in $ZrZn_2$. However, in $Nb_{1-x}Fe_{2+x}$ the phase transition is driven by the precise chemical composition. Still both materials show the same behaviour in the electrical resistivity $\rho(T) = \rho_0 + AT^{3/2}$ in the critical regime where ferromagnetism is almost suppressed. This could hence be a strong indication that such a form of non-Fermi liquid behaviour is in fact a precursor to the existence of a modulated or nearly anti-ferromagnetic phase emerging above the QCP. It may suggest that in rather clean and itinerant ferromagnetic systems such a behaviour is generic. Consequently, the magnetic moments may not simply vanish but will at some point form a certain structure which is different from a simple

ferromagnetic domain structure to save energy. According to the results by [74] a first-order QPT without such a behaviour may in fact be only possible if a topological reconstruction of the Fermi surface occurs. This would imply that also the lattice constants might show a sharp drop at this first-order transition. It would therefore be also very conclusive to investigate the lattice constants as a function of pressure in the critical regime using a high-resolution technique such as Larmor-diffraction with polarised neutrons. Similar studies have been performed on the itinerant helimagnet MnSi e.g. in [167] or more recently on the system UGe_2 for a comparison with the theoretical predictions.

7. From Ferromagnetism to Antiferromagnetism in $Fe_{1-x}Cr_x$

An interesting QPT is observed in the doping series $Fe_{1-x}Cr_x$ where the type of magnetic order changes from itinerant electron FM to itinerant AFM by substitution of Fe by Cr atoms. As a tuning parameter the percentage x of Cr is used. Increasing x has a similar effect as pressure since the bcc crystal structure is unchanged for the entire range from iron to chromium. As the volume of the unit cell is thereby increased this would correspond to the application of negative pressure. However, Cr has one $3d$-electron and one $4s$-electron more than Fe which suggests also a deformation of the band structure with increasing x. Pure Fe shows a Curie temperature $T_C =$ 1043 K which is suppressed with increasing Cr content. In contrast pure Cr shows antiferromagnetic order with $T_N =$ 311 K which can be easily tuned to spin density wave order by application of weak hydrostatic pressure or doping [168, 169, 76].

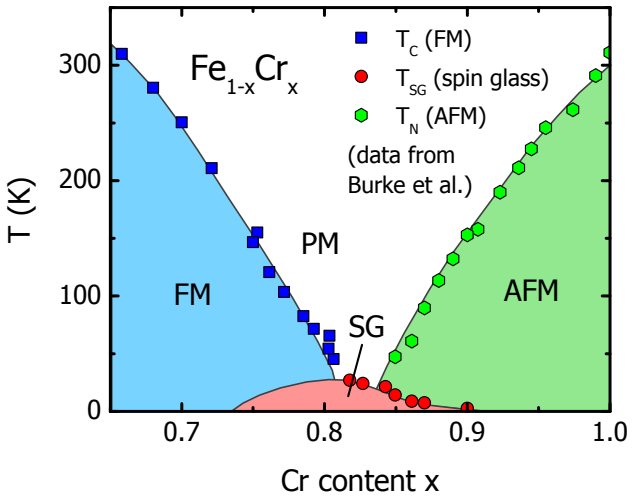

Figure 7.1.: Magnetic phase diagram of $Fe_{1-x}Cr_x$ showing the ordering temperature as a function of the Cr content x. Pure Fe orders at $T_C =$ 1043 K. The ordering temperature is lowered with increasing x. For elevated Cr content around $x = 0.8$ the FM order vanishes and a spin-glass phase is observed which extends into the surrounding FM and AFM phase. Above $x = 0.85$ the magnetic order changes to AFM where further increasing of x now increases the Neel temperature T_N. Pure Cr undergoes an AFM transition at $T_N =$ 311 K. Data from [104].

Early studies have been done on $Fe_{1-x}Cr_x$ sample series using neutron scattering in order to map out the phase diagram as shown in Fig. 7.1 (data from [104]). The FM phase boundary was determined from the temperature dependence of the SANS intensity around the direct beam. The AFM phase boundary was derived from neutron diffraction experiments. In the critical regime where the Curie temperature is already well below room temperature a spin-glass phase was found to cover a putative QCP around the concentration $x = 0.83$. Interestingly, the phase boundary of the spin-glass state extends into the surrounding FM and AFM phases.

7.1. State of the Art

Inspired by our studies on the cluster glass formation in $CePd_{1-x}Rh_x$ we have investigated the critical regime of $Fe_{1-x}Cr_x$ using the neutron depolarisation technique. As the technique is particularly sensitive to the existence of FM domains or clusters, the phase boundaries of the FM phase as well as the underlying SG phase should be detectable. For this purpose a series of $Fe_{1-x}Cr_x$ samples in the range $x = 0.70$ to $x = 0.90$ was prepared in collaboration with A. Bauer and G. Benka at the institute E21 at TUM as described in Sec. 4.3. First magnetisation and susceptibility measurements were done on selected samples. Here, we show preliminary results from the measurements using laboratory techniques and the results of our neutron depolarisation measurements.

7.2. Experimental Results

For the characterisation of our samples the magnetisation $M(T)$ and $M(H)$ as well as the ac-susceptibility $\chi(T)$ were measured using a PPMS as described in Sec. 4.3. The temperature- and field dependence of the neutron polarisation was investigated as described in Sec. 4.4 to obtain microscopic information.

7.2.1. Magnetisation and Susceptibility

We have measured magnetisation loops for the samples with $x = 0.75$, 0.80, 0.85 and $x = 0.90$ at a temperature of $T = 2$ K. The complete magnetisation loops are shown in Fig. 7.2a while Fig. 7.2b shows a close-up of the data. The sample $x = 0.75$ shows a saturation magnetisation of about $0.4\ \mu_B$ and essentially no hysteresis is observed (see Fig. 7.2b). In contrast, a significant hysteresis is visible for $x = 0.80$ and $x = 0.85$. The saturation moment is decreased smoothly with increasing x. The coercive field increases rapidly with increasing x. Interestingly, a small saturation moment of about $0.04\ \mu_B$ is still observed for the sample $x = 0.90$ which is nominally in the AFM regime of the phase diagram.

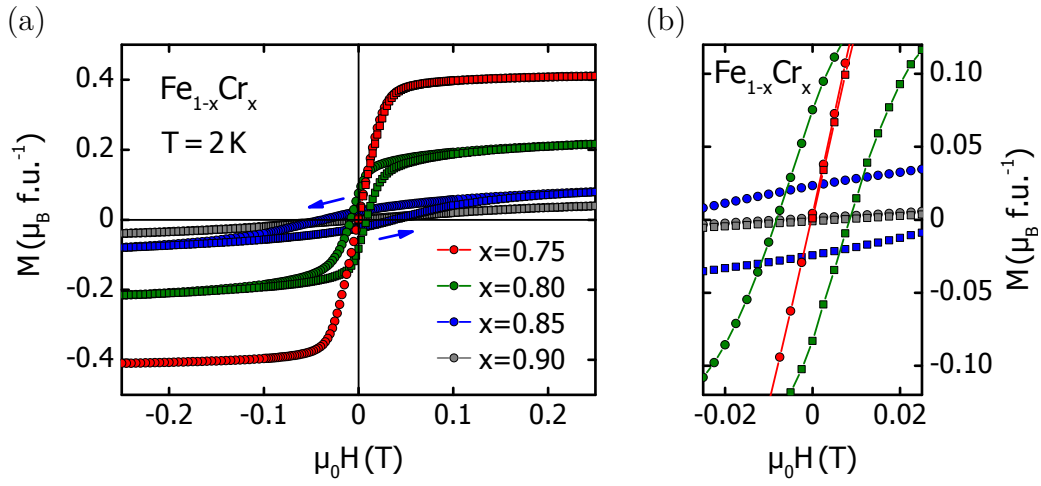

Figure 7.2.: (a) Magnetisation loops for $Fe_{1-x}Cr_x$ samples with $x = 0.75$, 0.80, 0.85 and $x = 0.90$. The sample with $x = 0.75$ is clearly ferromagnetic, however, no hysteresis is visible. The samples with $x = 0.80$ and $x = 0.85$ in contrast show a hysteresis. (b) Close up of the data. With a concentration $x = 0.90$ the sample is nominally AFM however a very small hysteresis is still observed which indicates residual ferromagnetism.

The temperature dependence of the magnetisation is shown in Fig. 7.3a for the samples with $x = 0.75$, 0.80, 0.85 and $x = 0.90$. The magnetisation was recorded for each sample under zero-field cooling (zfc). For a comparison with the neutron data

shown in the next section we have also recorded the magnetisation after field-cooling in an external field $B = 10$ mT (fc) and a higher field of $B = 250$ mT (hfc), respectively for each sample. For $x = 0.90$ the magnetisation is essentially zero on this scale and shows only a very small up-rise at lowest temperatures which can be identified in the close-up of the data in Fig. 7.3b. For the concentrations in the range $x = 0.75$ to 0.85 a splitting of the curves with different field histories is observed.

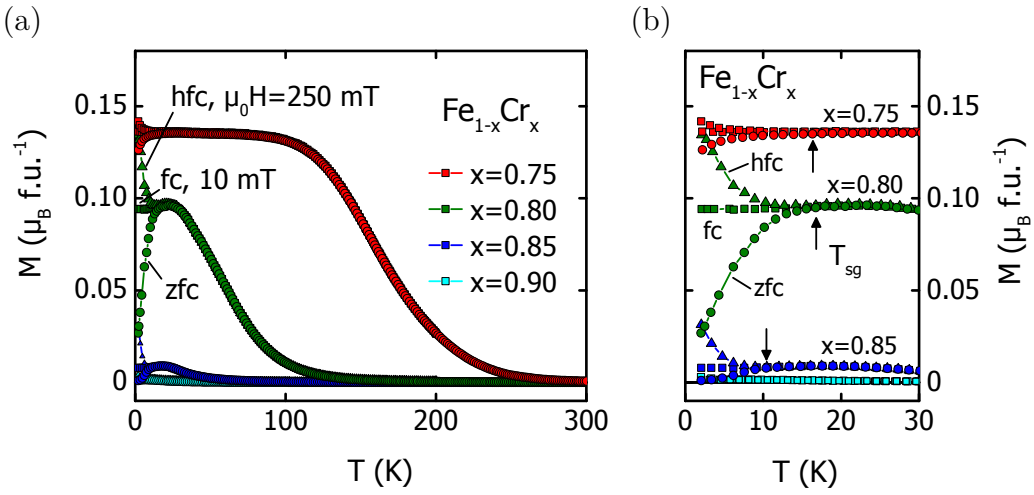

Figure 7.3.: (a) Magnetisation data for the three different concentrations $x = 0.75$, $x = 0.80$ and $x = 0.85$ measured after zero-field-cooling (zfc) and field-cooling (fc) with an external field $B = 10$ mT and $B = 250$ mT (hfc). A splitting of the curves of different field histories is most pronounced for $x = 0.80$. (b) Close-up of the low-temperature part. The splitting indicates a glassy transition well below the ferromagnetic ordering temperature.

The splitting is most pronounced for $x = 0.80$ which is close to the border of ferromagnetism. We denote the temperature where the splitting occurs with T_{sg} and associate it with the spin-glass transition found in earlier studies.

The ac-susceptibility was already recorded for several of our samples. In further studies in particular the frequency dependence will be investigated in more detail in order to characterise the nominal spin-glass regime. A preliminary evaluation of first data measured in zero external field and at a frequency f =10 Hz is shown in Fig. 7.4 as a contour plot. The missing data points were linearly interpolated. From the contour plot the phase boundary may be visualised. The FM phase is characterised by a strongly enhanced susceptibility. Interestingly, the boundary of the spin-glass phase is also clearly visible. The phase boundary of $T_{sg}(x)$ starts around $x = 0.76$ and is covered by the FM phase. With increasing x the two phase boundaries approach each other until the FM phase is suppressed at a finite temperature around $T = 25$ K

at $x = 0.83$. A slightly enhanced susceptibility is visible even for larger values of x forming a single line of transitions that may be traced until $x = 0.89$.

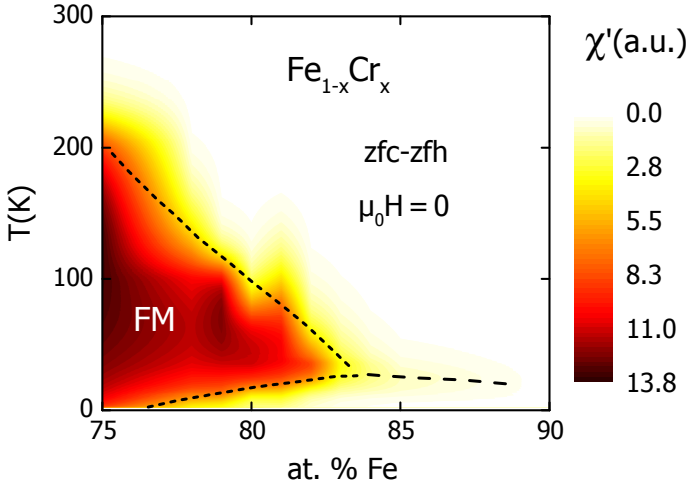

Figure 7.4.: Contour plot of the real part $\chi'(T)$ of the ac-susceptibility as a function of temperature and increasing Cr content x (and thereby decreasing Fe content). The data where measured under zero external field. The contour plot suggests a small gap corresponding to a second phase transition at lower temperatures in the critical regime for concentrations $x > 0.76$. Ferromagnetism is virtually suppressed at $x = 0.83$. However, the ac-susceptibility shows a broad peak even for $x = 0.90$ which is associated with a spin-glass transition.

7.2.2. Neutron Depolarisation

Temperature sweeps and field loops were measured for the samples with concentrations in the range $x = 0.78$ to $x = 0.85$ using different field histories while cooling down. The samples were cooled and then measured in zero magnetic field. For a comparison with the magnetisation the samples were also measured without an applied field, after cooling in an external field $B = 250$ mT (fc-zfh).

The left column in Fig. 7.5 shows the polarisation as a function of temperature for the entire datasets while the right column shows a close-up of the data at small temperatures.

The sample with $x = 0.78$ shows a smooth ferromagnetic transition around $T_C = 200$ K. The smeared transition indicates a broad distribution of transition temperatures with a width of approximately $\Delta T_C = 70$ K. At a temperature around 80 K a small kink is visible which we refer to as T_X. At $T_{sg} = 25$ K a second drop is observed which we as-

sociate with the spin-glass transition. No significant difference between zfc and fc data can be observed. The sample with $x = 0.79$ shows essentially the same three features. However, here T_C and T_X are suppressed while T_{sg} is slightly higher than for $x = 0.78$. In addition, a splitting of the zfc and fc data which sets in approximately at T_X is visible.

As can be seen from Fig. 7.5 the transition at T_X vanishes for $x = 0.80$ while T_C is further suppressed to about 130 K. The splitting below T_{sg} is not clearly observed for all samples in the spin-glass regime which might be a consequence of demagnetisation effects due to varying sample shapes. The kink at T_{sg} is only slightly varying with x across the concentration range $x = 0.80$ up to $x = 0.84$ while the ordering temperature T_C is continuously suppressed.

The depolarisation measured in zero field and extrapolated to $T = 0$ vanishes continuously for the series of samples. Almost complete depolarisation to a value $P = 0$ is found for $x = 0.78$ while the sample with $x = 0.84$ shows only a weak effect of 5% depolarisation to a value $P = 0.95$. The depolarisation for $x = 0.85$ essentially vanishes within the statistics of our measurement after zfc. This concentration nominally marks the border to AFM. The splitting of zfc and fc data at T_{sg} may however still be identified. Interestingly, it can be seen further that the depolarisation is reentrant in a small temperature window. Nevertheless, the effect is visible by about 1% depolarisation which for this particular measurement compares to the statistical uncertainty.

Magnetic field loops in the range $\mu_0 H$ = -250 mT to 250 mT were recorded at $T = 3.5$ K for each sample for later comparison with the magnetisation data. The field loops are shown in Fig. 7.6. Here, the sample with $x = 0.78$ shows a behaviour similar to the magnetisation measurement where no hysteresis is visible. The depolarisation is at maximum for $B = 0$ while increasing the field leads to a decrease of the depolarisation. The depolarisation is expected to vanish already before saturation is reached at a state where essentially all domains are either parallel or anti-parallel to the applied field. For $x = 0.79$ a small hysteresis opens up as can be seen in more detail in Fig. 7.6b.

The hysteresis effect increases with further decreasing the Fe content x which can be seen by the shift of the minimum in the polarisation to finite value of B. The hysteretic behaviour is different for $x = 0.82$ and $x = 0.83$. Here the minimum of the polarisation again occurs at $B = 0$. However, the hysteresis develops only in a small field interval. The behaviour changes again below $x = 0.84$ where the ferromagnetic signature i.e the depolarisation in zero field is essentially suppressed. For small fields however the hysteretic behaviour can still be observed at small fields.

The most recent results collected in this study are summarised and interpreted in the following section.

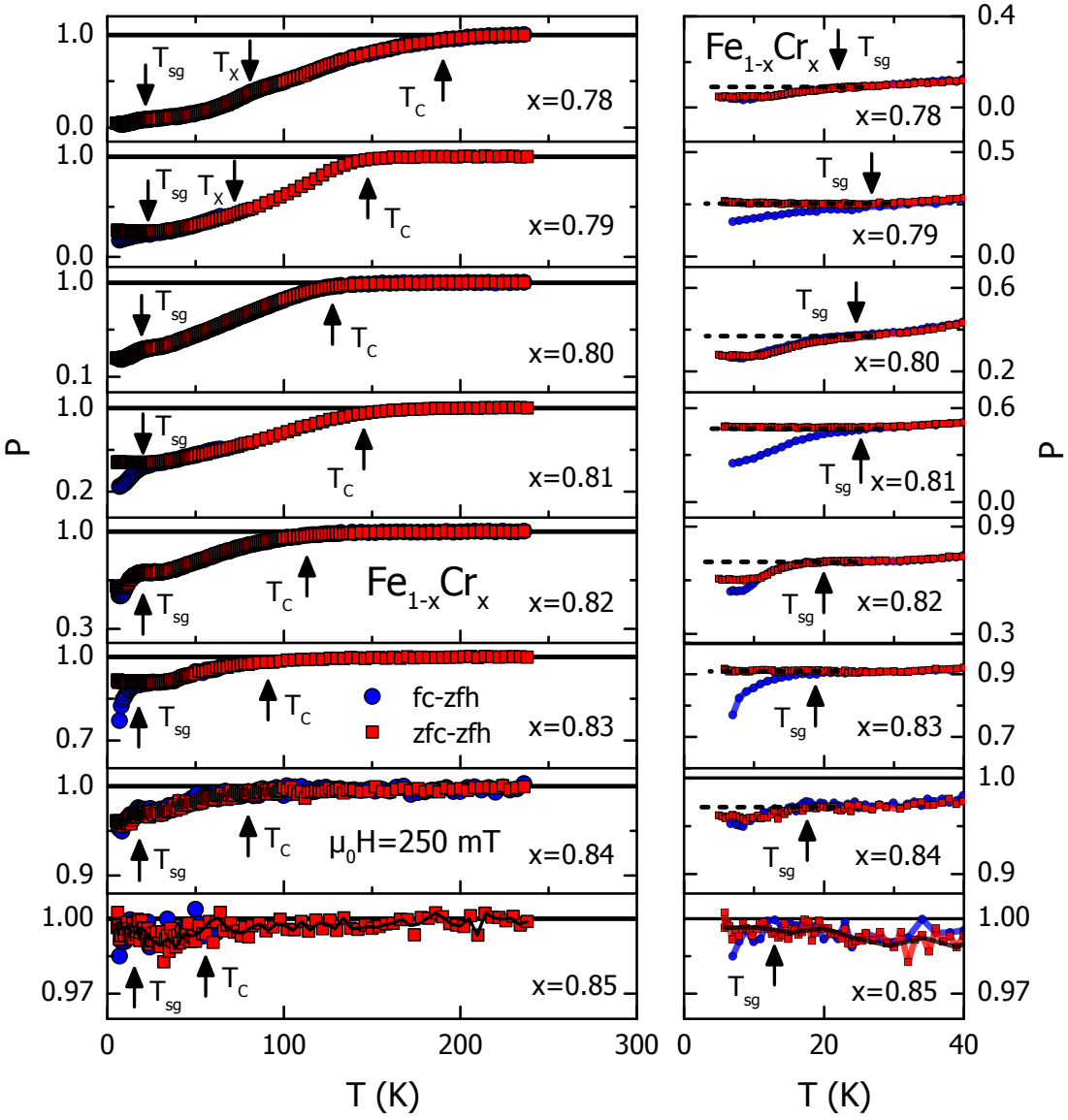

Figure 7.5.: Depolarisation as a function of temperature for the series of $Fe_{1-x}Cr_x$ samples. Data were recorded in the controlled heating process without an external field (zfh). For comparison the measurement was done for two different field histories, after zero-field cooling (zfc) and after field-cooling (fc) using a field $B = 250$ mT. The left column shows the entire datasets while the right column shows a close-up at small temperatures. For $x = 0.78$ a smooth ferromagnetic transition is observed indicating a broad distribution of transition temperatures. A kink indicated by T_X at intermediate temperatures is visible. A second drop is found at a lower temperature denoted by T_{SG} around 20 K which is associated with the spin-glass transition. For $x = 0.79$ a splitting of the curves sets in at T_X. For $x = 0.80$ and larger values of x the kink at T_X has vanished after zfc, however the splitting of the zfc and fc curves is observed together with a drop at T_{SG}. A signature of ferromagnetic ordering is observed up to $x = 0.84$. For the sample with $x = 0.85$ the depolarisation vanishes after zfc and is only slightly visible in a small temperature window.

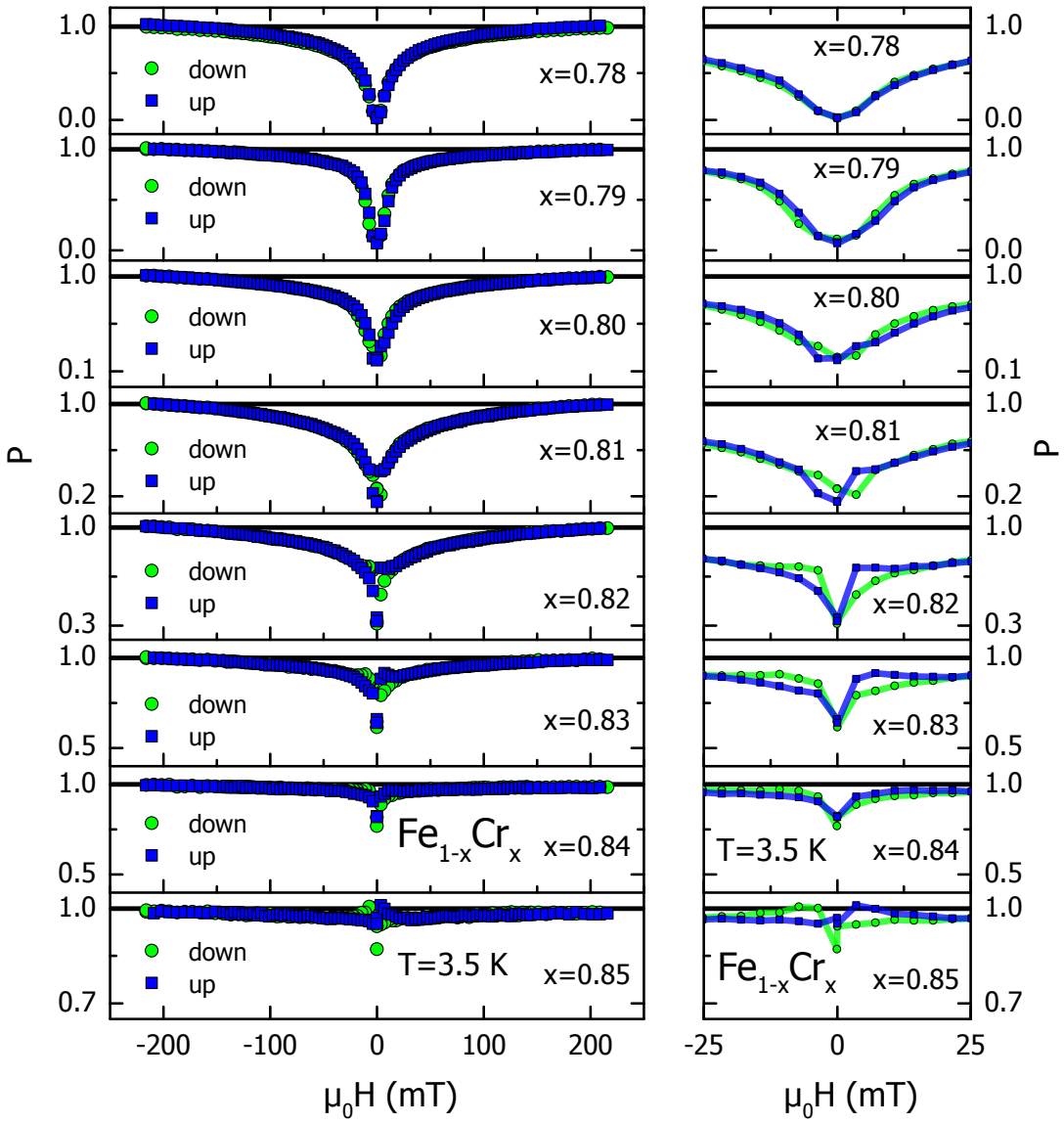

Figure 7.6.: Field loops on $Fe_{1-x}Cr_x$ measured using the neutron depolarisation technique. For large Fe content $x = 0.78$ the shape of the curve is as expected for a weak ferromagnet with vanishing hysteresis. At zero magnetic field the domain structure is formed such that a maximum in depolarisation occurs. Increasing the field leads to smooth reorientation of the domains along and anti-parallel to the field axis while at the same time the domains in field direction grow at the cost of others. For $x = 0.79$ and below an increasing hysteresis is visible. Interestingly, the behaviour of the hysteresis changes rather unexpectedly Below $x = 0.81$ where the switching of the magnetic field has a much more pronounced effect. The depolarisation at zero field vanishes smoothly at $x = 0.85$ which is nominally at the border to AFM. However, a depolarisation signature is still visible and the hysteretic behaviour is still pronounced indicating partially ferromagnetic order.

7.3. Residual Ferromagnetism in the Spin Glass Phase

In the following we will interpret our most recent results in the context of previous studies. The transition temperatures determined from our depolarisation measurements were combined with these earlier results in order to create the revised phase diagram shown in Fig. 7.7. The phase boundary of the spin-glass regime as determined from our measurements is in good agreement with the temperatures determined in [104]. The FM transition at T_C as determined from the depolarisation measurements show a more or less constant offset of about 50 K compared to the data from [104].

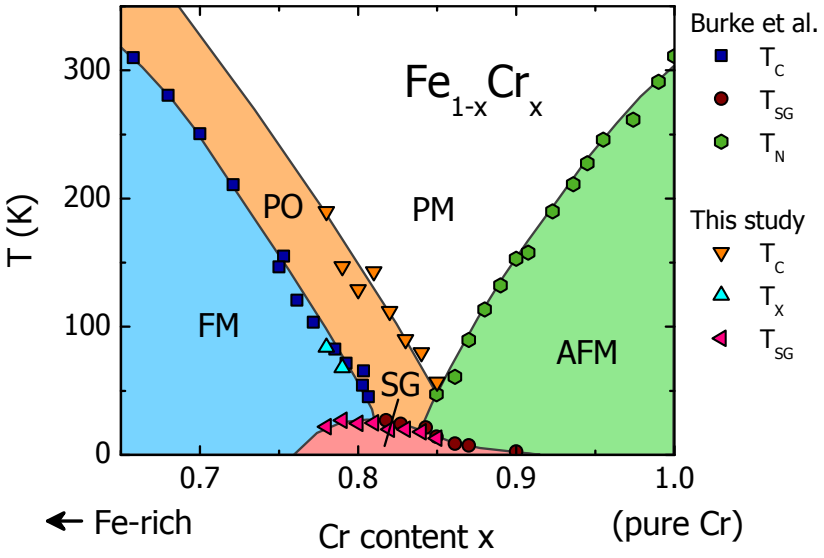

Figure 7.7.: Revised magnetic phase diagram for $Fe_{1-x}Cr_x$ showing the FM ordering temperature T_C and the freezing temperature T_{SG} associated with the spin-glass transition. Data from [104] were reused which in addition show the AFM ordering temperature T_N. The spin-glass transition determined using neutron depolarisation data is in good agreement with earlier studies. However, the ferromagnetic ordering sets in at a higher temperature as concluded from our data. The transition is very broad indicating strong inhomogeneity effects. The region shaded in orange may hence be described as a regime of partial order (PO) where ferromagnetism begins to stabilise and is already detectable by the neutron depolarisation technique.

We interpret this as a consequence of the different methods which were used to determine T_C. As the neutron depolarisation measurements are very sensitive on FM order on a short length and time scale we conclude that our values for T_C reflect the onset of the ordering process. The order stabilises rapidly with decreasing temperature. As magnetisation measurements probe rather static behaviour averaged over a longer time scale this might explain why the values of T_C found in this study are systematically higher than these found by [104].

From the temperature sweeps measured using the depolarisation technique one may deduce that the samples are intrinsically rather inhomogeneous. This can be illustrated by comparing the standard fit function used for the results on $ZrZn_2$ or $CePd_{1-x}Rh_x$ with the depolarisation model including a distribution $\rho(T_C)$ of transition temperatures as discussed in Sec. 3.2.3. As the fit method for this model is still work in progress and numerically unstable we show only exemplary results for the sample with $x = 0.82$ in Fig. 7.8. The red curve represents the simple model for the depolarisation as described in Sec. 3.2 assuming that a small amount of spin rotation occurs in each ferromagnetic domain. For this fit the low-temperature part below 25 K has been skipped. In this simple model a sharp transition at T_C is expected below which the order stabilises. The blue curve corresponds to the same model equation, now convolved with a Gauss distribution of transition temperatures as described in Sec. 3.2.3. For this dataset it was possible to extend the fit by using the product of two polarisation curves with different transition temperatures in order to capture the second transition at T_{sg}. The fit requires rather accurate initial parameters and is unstable if more than three parameters are fitted. However, if one assumes that the simple model at least predicts the polarisation, extrapolated to $T = 0$, correctly one may fix this parameter. The resulting fit agrees much better with the data. The resulting transition temperature $T_C = 80.3$ K with a distribution with a FWHM of $\Delta T_C = 68.8$ K was found.

It is interesting to note that this inhomogeneity is not seen on a macroscopic scale, i.e. there is no such variation in T_C of the depolarisation curves in neighbouring detector pixels of the illuminated area of the sample. This means that the disorder manifests on a much smaller length scale and may be rather compared to an inhomogeneous distribution of strain in the sample. It is further interesting that the depolarisation increases further below T_{sg}. In the simple model for the depolarisation in ferromagnets this suggests that the spin structure either stabilises (the dynamics slow down) or that the domain size increases below this temperature. It seems more likely that the spin structure stabilises when considering the fact that an AFM regime follows for larger values of x. The intrinsic disorder may then have the effect that the AFM ordering temperature lies below the FM ordering temperature (i.e. there might be a phase coexistence). If the AFM coupling increases to an amount which compares to the FM coupling strength this might produce such a behaviour. This may be compared to the behaviour found in $CePd_{1-x}Rh_x$ with the difference that AFM coupling sets in instead of a screening of the magnetic moments due to the Kondo effect. Here, the FM domains form below T_C but the domains are surrounded (or partly dissolved) by fluctuating moments. These fluctuating moments experience an AFM ordering transition below T_{sg} which leads to a frustration of the FM domains and thereby to a freezing of the spin configuration.

The depolarisation measurements may already be sufficient to suggest a simple scenario using the RKKY interaction to explain the observed behaviour. Most importantly

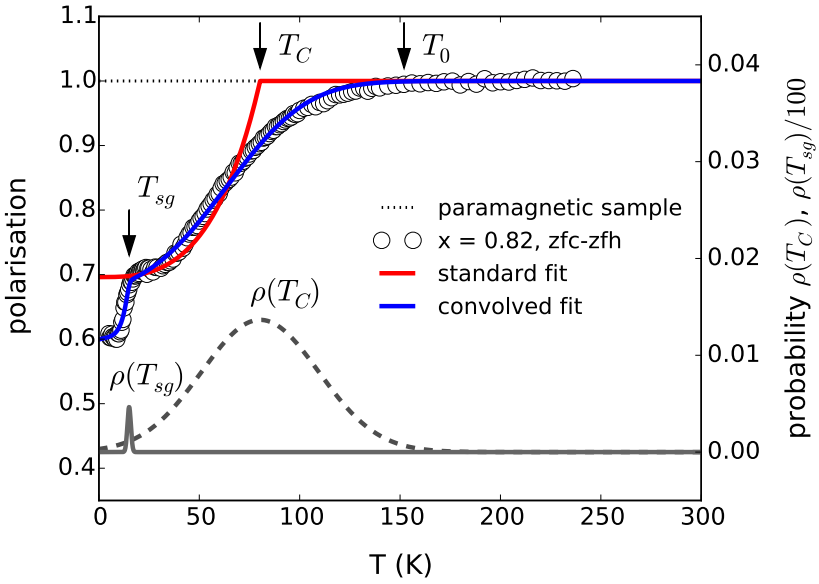

Figure 7.8.: Exemplary depolarisation data from the zfc-zfh temperature sweep on the $Fe_{1-x}Cr_x$ sample with $x = 0.82$ (open circles). The red curve corresponds to the standard depolarisation model by [52] as discussed in Sec. 3.2 including one transition at T_C. By incorporating a distribution of transition temperatures in the model using a convolution the agreement of the fit (blue curve) is much better. For this dataset it was even possible to fit the product of two depolarisation curves which allowed us to capture the second transition at T_{sg}. From this fit a $T_C = 80.3$ K and the FWHM of the distribution $\Delta T_C = 68.8$ K was found. The glassy transition was determined at $T_{sg} = 15.1$ K with a distribution $\Delta T_{sg} = 2$ K The corresponding Gauss distributions are shown in grey and use the right hand scale. For better readability the distribution $\rho(T_{sg})$ was scaled down by a factor of 100. Both temperature distributions were normalised.

the topology of the free-energy landscape should be considered then. If on the one hand the energy landscape is rather flat, implicating a truly itinerant system, the application of hydrostatic pressure might infer some modulated spin structure as the only escape route away from a first-order transition. However, if the energy landscape is rather coarse in a sense that several local minima arise (possibly influenced by the crystal field) the spin density might also follow this imprinted structure. The important aspect might be to consider finally the influence of the spin density on the type of order.

In the following discussion we assume only the RKKY interaction to determine the type of magnetic order, resulting in one of the two extreme cases FM or AFM. However, the RKKY interaction depends on the average distance between two spins which is related to the spin density in the system. If the spin density is homogeneous only one of the

two states FM or AFM may be expected. However, an inhomogeneity of the spin density may cause the formation of FM and AFM islands in a surrounding of frustrated spins. An important question which then arises is the length scale on which these variations of the spin density can occur. If a system is intrinsically disordered due to the metallurgical inhomogeneity the variations could be expected to occur on a rather large length scale. This case might be regarded as most likely to occur in substitution series of compound systems. If in contrast hydrostatic pressure is applied to a clean system this kind of phase separation could occur on the atomic scale involving only a number of spins.

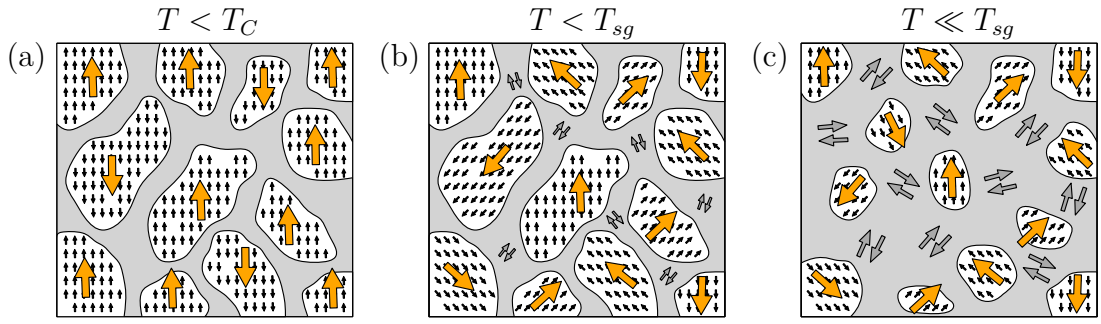

Figure 7.9.: Illustration of the cluster glass evolution in $Fe_{1-x}Cr_x$ for elevated Cr content of the order of $x = 0.80$. Panels (a) to (c) show the putative evolution with decreasing temperature of the system in the nominal spin-glass regime which separates the FM and AFM regime as a function of x. (a) Below the FM transition temperature T_C a soft domain structure is formed where the domains are separated by fluctuating moments. (b) At temperatures below T_{sg} remaining fluctuating moments experience an AFM coupling. (c) Cooling down further increases the average size of AFM regions at the cost of FM regions. This process may be accompanied by an effective freezing of the FM clusters in an AFM surrounding with respect to the dynamics of the entire FM clusters.

The suggested scenario may be illustrated as in Fig. 7.9 for a sample in the intermediate regime of the phase diagram which is nominally in the FM phase but close to the nominal spin-glass regime. The panels (a) to (c) show the putative temperature evolution with decreasing temperature. In panel (a) the temperature is just below the ordering temperature T_C below which most of the ferromagnetic domains (clusters) are already ordered. The ordered regions may however by surrounded by fluctuating moments in contrast to a conventional FM domain structure where domain walls are formed. If the system is cooled down further below T_{sg} as depicted in panel (b) the remaining fluctuating moments experience an AFM transition which strongly enhances the interaction between the FM clusters and may cause a frustration. When cooling down further the AFM surrounding stabilises and possibly grows at the cost of some FM clusters. The dynamics of the spin system are thereby expected to slow down significantly which suggests that T_{sg} might as well be called a freezing transition.

The next chapter gives a global summary of the study on the three systems $CePd_{1-x}Rh_x$, $ZrZn_2$ and $Fe_{1-x}Cr_x$ and summarises the technical developments along this line of investigations.

8. Summary and Conclusion

A global summary of this study may be divided into instrumental developments and scientific results. A standard set up for depolarisation measurements which allows to apply external fields at the sample position along the polarisation direction was build as a prototype set up at the instrument ANTARES. At the beam line MIRA the prototype for the newly designed set up was constructed which allows to measure complete field cycles. A user-friendly version of the newly designed set up was then constructed for the instrument ANTARES. At ANTARES the set up is now fully integrated into the instrument control system and can easily be build up and tuned within half a day.

The optimisation of the set up and the construction of some of the components was part of the bachelor thesis of S. Mayerhofer which was supervised during this study. The new set up will be used and further adapted to specific requirements as part of the master thesis of M. Seifert and of the PhD thesis of P. Jorba-Cabre which is already work in progress.

We have used the different options at the instrument ANTARES and MIRA to investigate in particular the ferromagnetic correlations in the three different materials $CePd_{1-x}Rh_x$, $ZrZn_2$ and $Fe_{1-x}Cr_x$ which all can be tuned through different types of quantum phase transitions. The samples were characterised using conventional laboratory techniques such as magnetisation and susceptibility to complement the neutron data.

In the study of the Kondo-Cluster-Glass formation in $CePd_{1-x}Rh_x$ we have investigated four samples in the range $x = 0.4$ to $x = 0.7$ of Rh concentrations. These are located in the tail region of the magnetic phase diagram $T_C(x)$ where earlier studies have suggested the formation of FM clusters in a surrounding of Kondo-screened magnetic moments. We have determined the T_C distribution of the samples using the T_C maps generated from the neutron depolarisation measurements. Thereby we have found that all of the samples show a rather narrow distribution and may hence be considered as metallurgical homogeneous on the probed length scale of about 150 μm. This suggests that the average size of the presumed FM clusters is some orders of magnitude smaller. However, our measurements indicate that the width of the distribution of cluster sizes increases with increasing the Rh concentration x in this regime. From temperature sweeps using different field histories we have furthermore observed a freezing transition of the FM clusters which occurs at a temperature T_f well below the ordering temperature T_C. Our measurements suggest that either (i) the dynamics

of the entire spin clusters slow down rapidly at T_f such that a depolarisation of the neutron beam occurs or (ii) the cluster size changes significantly at this temperature which could be due to AFM fluctuations. Further measurements of the spin dynamics on different time scales using neutron spin-echo techniques might by required to decide for one particular scenario. Small angle neutron scattering experiments may allow to estimate the typical length scales of the spin clusters.

The itinerant ferromagnet $ZrZn_2$ was investigated which undergoes a quantum phase transition as a function of pressure. We have adjusted four different pressures on our high-quality sample using a Cu:Be pressure cell and we have further used a second sample of the same quality which was investigated at ambient pressure. The system $ZrZn_2$ shows a peculiar magnetic phase boundary $T_C(p)$ where ferromagnetism is suppressed almost discontinuously above a tri-critical point at p_c=16.5 kbar. Above p_c the phase boundary $T_C(p,B)$ continues only at finite fields. The transition at $T_C(p,B)$ for a fixed pressure is a meta-magnetic transition which is indicated by a characteristic kink at B_m in the magnetisation measurements. In this study we have adjusted two pressures below p_c and two pressures just above p_c. We have measured the magnetisation as well as the neutron depolarisation for each pressure. Interestingly, we have observed a depolarisation above p_c however even in nearly zero external field and hence well below the critical field B_m at which the meta-magnetic transition was observed. From our study we therefore conclude that residual ferromagnetic correlations remain even above the tri-critical point at very small magnetic fields. In the light of recent theoretical results this may indicate the existence of a (possibly dynamic) modulated spin structure or a spin texture which can easily be polarised. Our study suggests that even at very small fields a domain-like structure is formed which in turn leads to a small depolarisation of the neutron beam. The critical field B_m may therefore indicate a reconfiguration of this domain structure. We propose that this could provide a hint to an explanation for the unusual resistivity behaviour observed in $ZrZn_2$ below and above the critical pressure.

Inspired by the study on $CePd_{1-x}Rh_x$ we have investigated a series of $Fe_{1-x}Cr_x$ samples. The quantum phase transition in $Fe_{1-x}Cr_x$ is accompanied by strong disorder effects which makes it in some sense similar to $CePd_{1-x}Rh_x$. However, in $Fe_{1-x}Cr_x$ the FM order is suppressed with increasing the Cr concentration x and an AFM phase emerges in the Cr limit. The putative quantum critical point is in this compound hidden by a spin glass regime. In our measurements using the neutron depolarisation technique we have identified the phase boundary of this spin glass regime up to a Cr concentration $x = 0.85$ which provides strong evidence that the spins are clustered as in $CePd_{1-x}Rh_x$. However, the FM clusters may in this case be surrounded by an AFM background due to the Cr content. This could hide the freezing transition which was observed in $CePd_{1-x}Rh_x$ and lead to an immediate freezing of the cluster configuration below the ordering temperature. Further measurements will include the ac-susceptibility and in particular the frequency and field dependence of the signal in order to investigate

the spin glass behaviour in more detail. The study will be complemented by further neutron depolarisation measurements using different field histories for samples with higher Cr content $x > 0.85$. If FM correlations still exist at this high Cr content, this would enable us to track the ferromagnetic phase boundary even further reaching the nominally AFM regime of the phase diagram, thereby suggesting a phase coexistence in a broad regime of the phase diagram.

The newly designed set up for neutron depolarisation measurements which now allows to measure the polarisation for complete magnetic field cycles provided a particularly sensitive probe of ferromagnetic correlations in the samples at low temperatures as well as high pressures. This promotes the depolarisation technique as a valuable tool in the investigation of ferromagnetic quantum phase transitions which remains a puzzling and highly interesting field of research.

The following part of this thesis may regarded as an independent study. Although it concerns neutron instrumentation the focus is on an analytical model for a so-called WFM (wavelength-frame multiplication) chopper system with optically blind choppers. Furthermore, Monte Carlo simulations are used to investigate the performance under realistic conditions in the multi-purpose imaging beam line ODIN which has been proposed to be build as a day-one instrument at the European Spallation Source. To bridge the two distinct parts of this thesis one may in fact consider a neutron depolarisation measurement at this future imaging beam line. At a continuous neutron source such as the FRM II the technique requires a velocity selector or a monochromator which selects only a small wavelength band out of the broad spectrum provided by the moderator. The WFM chopper system produces a continuous wavelength band where the wavelengths are ordered in time at the detector position. By evaluating the depolarisation for every wavelength bin separately using a time-sensitive detector this could increase the efficiency in terms of measurement time by orders of magnitude. However, it will be a future challenge to design a corresponding set up for depolarisation measurements which may be regarded as an outlook for further studies.

Part II.

Wavelength-Frame Multiplication Chopper System for the Imaging Instrument ODIN at the ESS

9. Introduction

The European Spallation Source (ESS) is designed to be the world's brightest pulsed neutron source where neutrons are produced in a spallation target hit by a pulsed proton beam [170]. The resulting neutron pulses allow for taking full advantage of time-of-flight methods in order to separate neutrons in time according to their wavelengths. The combination of intrinsic wavelength resolution and the high brilliance render the ESS hence an ideal source for modern wavelength-dependent neutron imaging techniques. The imaging beam line ODIN was therefore proposed as a day-one instrument to become operational together with the source in 2019 due to potentially very high gain factors for wavelength dependent techniques compared to existing beam lines [1]. Prominent examples of imaging techniques requiring a range of different wavelength resolutions are Bragg edge imaging for strain mapping ($\Delta\lambda/\lambda \leq$ 0.5%), texture and micro-structure investigations and imaging with polarization analysis (around 1.0%), as well as depolarisation imaging and dark field imaging (up to 10%) [51, 56, 57, 171–174]. As the ESS in contrast to all other existing spallation sources will deliver rather long neutron pulses of 2.86 ms duration (in contrast to around 10 - 300 μs at existing sources [175–177]) at a low frequency of 14 Hz, new requirements to a chopper system arise to utilize the time structure in an efficient way [178–181]. In this study we discuss a highly flexible chopper system based on the concept of wavelength frame multiplication (WFM), which is able to access a broad wavelength band with the envisaged adjustable wavelength resolution $\Delta\lambda/\lambda$ at the detector position [178, 182, 183]. The proposed chopper system combines the WFM technique with a pair of optically blind chopper discs [184] and thereby allows to adjust the wavelength resolution by varying the distance of the chopper discs. In addition, the concept of an optically blind chopper pair for pulse shaping results in a constant wavelength resolution over the utilized spectrum which is meanwhile state of the art for modern TOF reflectometers and SANS instruments at continuous sources [185–189].

The chopper arrangement has been designed and specified first analytically by calculating and constructing time-of-flight (TOF) diagrams. We have implemented the corresponding parameters into a virtual instrument using the Monte Carlo simulation software McStas [190]. The virtual instrument allowed to optimize the WFM chopper system and to refine the resulting time structure at the detector position which is

1 Instrument Proposal for the beam line ODIN at the European Spallation Source

necessary due to several approximations initially used for the analytical calculations. This study therefore presents a basis for an assessment and for further optimization of the wavelength frame multiplication concept and may be regarded as a benchmark for similar instrument concepts that could be proposed for a long-pulse neutron source such as the ESS.

The focus of this study is hence the design of the basic chopper system following the outlined concept and boundary conditions and the implementation of the chopper system into a virtual instrument in the Monte Carlo software package McStas together with the optimisation process. In the following section 9.1 we will discuss the requirements imposed by the desired applications. In section 9.2 we will briefly describe the WFM chopper concept. Section 10 compiles the mathematical description for an idealized instrument using the proposed WFM technique and the construction of the corresponding TOF diagrams. In section 11 the results of our simulations are shown and discussed. In section 12 we give a conclusion and an outlook to the results of on-going studies on the optimisation of the chopper system.

9.1. Requirements for an Imaging Beam Line at the ESS

Standard imaging applications typically require a thermal or cold neutron spectrum [51, 191, 192]. Therefore, the desired spectrum for an imaging beam line at the ESS was chosen to cover a similar range starting at 2 Å for coarse-resolution measurements and starting at 1 Å for high-resolution measurements.

A specialized neutron guide system is required in order to access the spectral properties homogeneously over the desired detector area. The maximum divergence desired at the sample position, which is accessible by selecting a corresponding pinhole for collimation and choosing the pinhole-to-sample distance, determines the required guide system. More precisely it determines the curvature and the index m of the supermirrors used for the guide system (see e.g. [123]). Such a guide system for an imaging instrument at the ESS has been proposed elsewhere [193]. A sketch of the guide system used for the simulations is shown in Fig. 9.1. The sketch includes the gaps for the required chopper discs that will be introduced in the next section.

The required length of the beam line is determined by the coarsest desired resolution for the shortest wavelength in the chosen wavelength band. This natural wavelength resolution for an instrument without choppers and assuming an idealized rectangular source pulse in time, can be calculated as

$$\frac{\Delta\lambda}{\lambda} = \frac{\Delta t}{t} = \frac{t_{\mathrm{P}}}{\alpha\lambda z_{\mathrm{det}}} \tag{9.1}$$

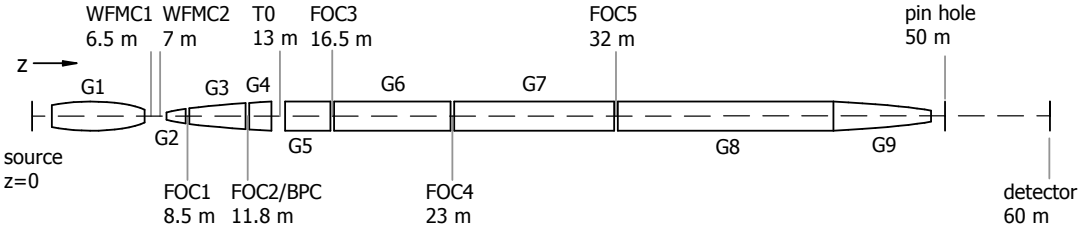

Figure 9.1.: Schematic of a guide system as proposed in [193] for an imaging beam line at the ESS. The first guide G1 focusses the beam at the centre position between the WFM choppers. The beam is defocussed again from G2 to G4 using either elliptical or parabolic guide shapes. The guides G5 to G8 correspond to a straight section. The guide G9 finally focusses the beam again at the pinhole position. The guide system includes the gaps for the WFM chopper pair as well as for five frame overlap (FO) choppers, one T-zero (T0) chopper and a band pass (BP) chopper as described in the text. The WFM chopper position is chosen as close as possible to the source. The FO chopper positions may be calculated from the WFM chopper positions and the base parameters as will be discussed in the text.

where t_P is the source pulse length, $\alpha = m_n/h = 252.78$ s^{2}Å^{-1}m^{-1} and z_{det} is the distance from the source to the detector. Consequently, the wavelength resolution depends on the wavelength.

Including the above requirements a 10 % resolution at 2 Å results in an instrument length of about 60 m for the ESS source pulse. Together with the source frequency of 14 Hz a wavelength band of 1 to 5.6 Å can be covered at this instrument length. By blocking every second source pulse the spectrum can be extended to a range 1 - 9.25 Å. In addition, for the imaging techniques requiring finer resolutions, the WFM chopper system can be used for this wavelength band. A diagram illustrating the wavelength band versus time-of-flight is given in detail in the next section. For the base parameters given above, the accessible range of resolutions with the WFM chopper system is from 0.2 to 0.9% (when assuming the detector fixed at the 60 m position from the source), as will be shown in the next paragraph.

9.2. Wavelength-Frame Multiplication using Optically Blind Choppers

In the wavelength-frame multiplication (WFM) concept [182, 178] each source pulse is chopped into a number of sub pulses (also called wavelength frames), where each frame contains a subsequent part of the spectrum of the source pulse. Fig. 9.2 illustrates the principle for two arbitrary wavelength frames created by the WFM chopper (WFMC). A frame overlap chopper (FOC) that reshapes the wavelength frames at a given time

was introduced for later considerations.

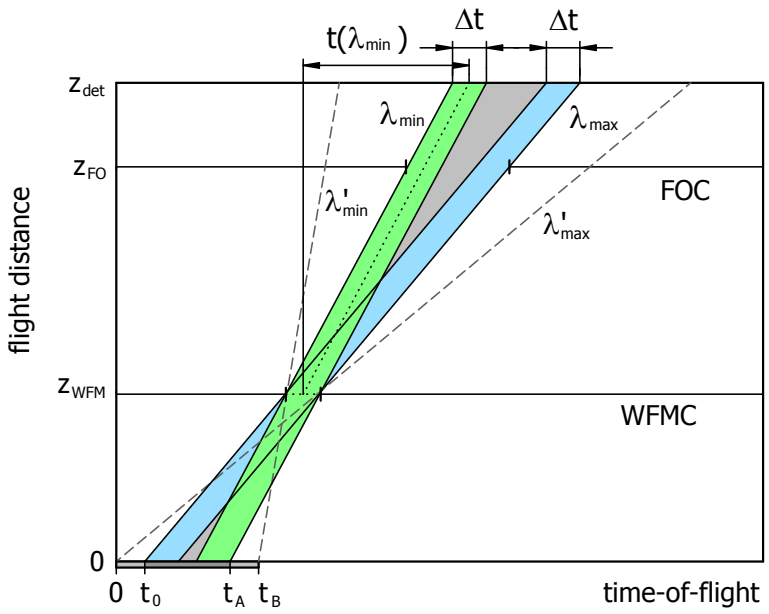

Figure 9.2.: Illustration of one arbitrary wavelength frame created by a single WFM chopper disc at position z_{WFM} with one opening window defining the burst time Δt. Each wavelength at the detector position z_{det} is then found in a time window Δt as indicated on the top scale. The desired wavelength range is from λ_{min} to λ_{max}. The source pulse is not sharply limited in time but has a rising edge in intensity from $t = 0$ to t_0 and a falling edge from $t = t_A$ to t_B. This undesired part of the source pulse produces additional frame overlap as indicated by the dashed lines. The edges of the wavelength frame therefore have to be reshaped in time which is why a frame overlap chopper at position z_{FO} is introduced. When using this simple concept the wavelength resolution $\Delta\lambda/\lambda = \Delta t/t$ decreases within the wavelength frame for each wavelength.

For designing the chopper system we assume a rectangular part of the source pulse, starting at time t_0 with a duration of $t_P = t_A - t_0$. The tail region of the source pulse is assumed from t_A to t_B. The spectral width of each frame is defined by the chopper burst time Δt and the distance z_{WFM} of the WFM chopper pair from the source. The main reason to use a WFM chopper is to decrease the effective burst time Δt (see Fig. 9.2) and hence to tune the wavelength resolution which can be seen from Eq. 9.1. The WFM chopper acts like a virtual source and thereby at the same time redefines the effective burst time Δt and reduces the effective time-of-flight to the detector to $t = \alpha\lambda(z_{\mathrm{det}} - z_{\mathrm{WFM}})$ which together can be used to decrease $\Delta\lambda/\lambda = \Delta t/t$. The WFM concept thereby enables to decouple wavelength resolution and the wavelength

range from the given source pulse time structure. However, the wavelength resolution still depends on λ.

When considering this aspect, the WFM concept can be improved by using a pair of optically blind WFM chopper discs at a certain distance to each other [184, 180, 181], which results in a constant wavelength resolution over the entire utilized spectrum.

Fig. 9.3 shows the TOF diagram for the first wavelength frame of two optically blind WFM chopper discs at a certain distance $d = \Delta z_{\mathrm{WFM}}$ to each other. The resolution can now be calculated by using

$$\frac{\Delta\lambda}{\lambda} = \frac{\Delta t}{t} = \frac{\Delta z_{\mathrm{WFM}}}{z_{\mathrm{det}} - z_{\mathrm{WFM}}} \tag{9.2}$$

with z_{det} being the distance of the detector from the source and z_{WFM} the distance of the center position of the WFM chopper pair from the source [184]. Since the effective chopper burst time now scales linearly with wavelength just like the time-of-flight, the resolution becomes independent of the wavelength within one wavelength frame. For an idealised instrument, the time window covered by a wavelength frame at the detector position is limited by λ_{N} and $\lambda_{\mathrm{N+1}}$ as shown in Fig. 9.3.

As an additional feature of this concept, the wavelength resolution can be adjusted by changing only the distance d between the two pulse shaping WFM chopper discs, thus modifying the effective chopper opening time for each wavelength. Shortening the distance between the WFM chopper discs implies a better wavelength resolution at the cost of intensity by effectively reducing the time window in which each wavelength can pass. To cover the desired wavelength band at the detector, several wavelength frames must be produced successively from a single source pulse. In order to obtain a continuous spectrum the maximum wavelength of a subframe must equal the minimum wavelength of the succeeding frame. This means technically that several different chopper windows with increasing size have to be cut out of one chopper disc thereby constricting the maximum chopper rotation speed (see [181]) as will be explained below.

For the diagrams and consequently the calculations above, the exact time structure of the source pulse was not taken into account in detail. However, in a real chopper system the rising and falling edges of the source pulse lead to a broadening of the wavelength frames compared to the ideal case with a rectangular shaped pulse. This will cause additional frame overlap in time of the ideally distinct wavelength frames. To minimize the effect of frame overlap, additional frame overlap choppers (FOCs) have to be introduced, which prevent neutrons from one subframe from penetrating into a neighbouring subframe in the TOF diagram. Since the subframes broaden again after reshaping the pulse with a FOC, a series of FOCs may be needed depending on the instrument length. The positions of the FOCs are determined by the amount

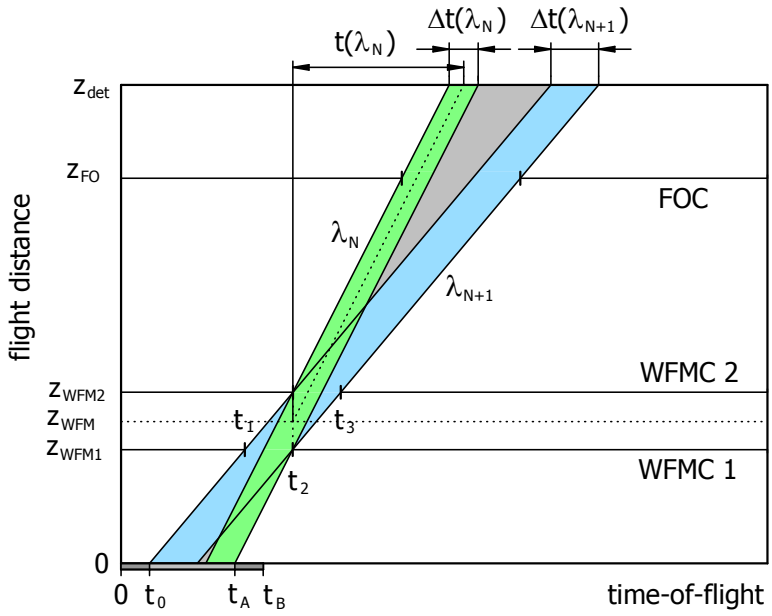

Figure 9.3.: One arbitrary frame of a WFM chopper system with two optically blind chopper discs at positions z_{WFM1} and z_{WFM1}. The wavelength resolution is constant within the range λ_{N} to $\lambda_{\mathrm{N+1}}$ of the limiting wavelengths. This can be seen from the burst time Δt_N (see top scale) which now increases linearly with λ and hence gives a constant $\Delta\lambda/\lambda = \Delta t/t$ within each frame denoted by the index N. The times t_0 to t_3 can be used to derive general equations to calculate the WFM chopper discs as described in the text. The FOC re-limits the wavelength frame at a given time.

of broadening. Since the ideal construction neglects the finite opening and closing time of the chopper window due to the finite frequency, an optimization of the FOC positions is necessary for a real instrument which is addressed in a subsequent section in detail. Given the source frequency of the ESS of 14 Hz and the instrument length of 60 m, three wavelength frames covering a wavelength band from 1 - 5.6 Å (the so-called three-frame mode) can be fit in between two subsequent source pulses.

In order to extend the wavelength range to longer wavelengths, every second source pulse may be skipped, thereby allowing six wavelength frames to fit in between two subsequent pulses producing a wavelength band in the range 1 - 9.25 Å (the six-frame mode). Following these considerations, the chopper system was constructed to support six wavelength frames. A bandpass chopper which is rotated at 14 Hz for the three-frame mode and at 7 Hz for the six-frame mode was introduced to select the desired wavelength range and also to suppress every second source pulse in the six-frame mode. Resulting from this particular realisation, the wavelength range in the three-frame

mode can be chosen within the given limits of the six-frame mode by shifting the phase of the bandpass chopper. By stopping all choppers but the bandpass chopper in an open position, the natural resolution mode is accessible. Again, the wavelength band can be chosen by adjusting the phase and the frequency of the bandpass chopper.

Shown in Fig. 9.4 are TOF diagrams of the WFM chopper system, implemented into a 60 m long instrument at the ESS, tuned for a resolution $\Delta\lambda/\lambda = 0.93\%$ by setting the WFM chopper distance to the maximum distance of 0.5 m. We have decided to position the WFM chopper discs at 6.5 m and 7.0 m from the target center, which is just outside the foreseen target shielding monolith and therefore still allows access for maintenance. The chopper concept is realised with five FOCs and one band pass chopper in order to support the different modes of operation. In Fig. 9.4a the band pass chopper is operated at the ESS source frequency, transmitting only three of six possible wavelength frames which are created by the WFM choppers. This permits using every source pulse, resulting in a smaller wavelength band in the range 1 - 5.6 Å. By rotating the band pass chopper at half the ESS source frequency, all six wavelength frames created by the pulse shaping WFM choppers reach the detector but every second source pulse is skipped. The corresponding TOF is shown in Fig. 9.4b. In this mode, the wavelength band 1 - 9.25 Å can be utilized at the detector position.

By decreasing the distance between the two WFM chopper discs while maintaining their center position, the wavelength resolution can be increased to cover a $\Delta\lambda/\lambda$ in the range 0.19 - 0.93%. For the best resolution a minimum distance of 0.1 m was assumed.

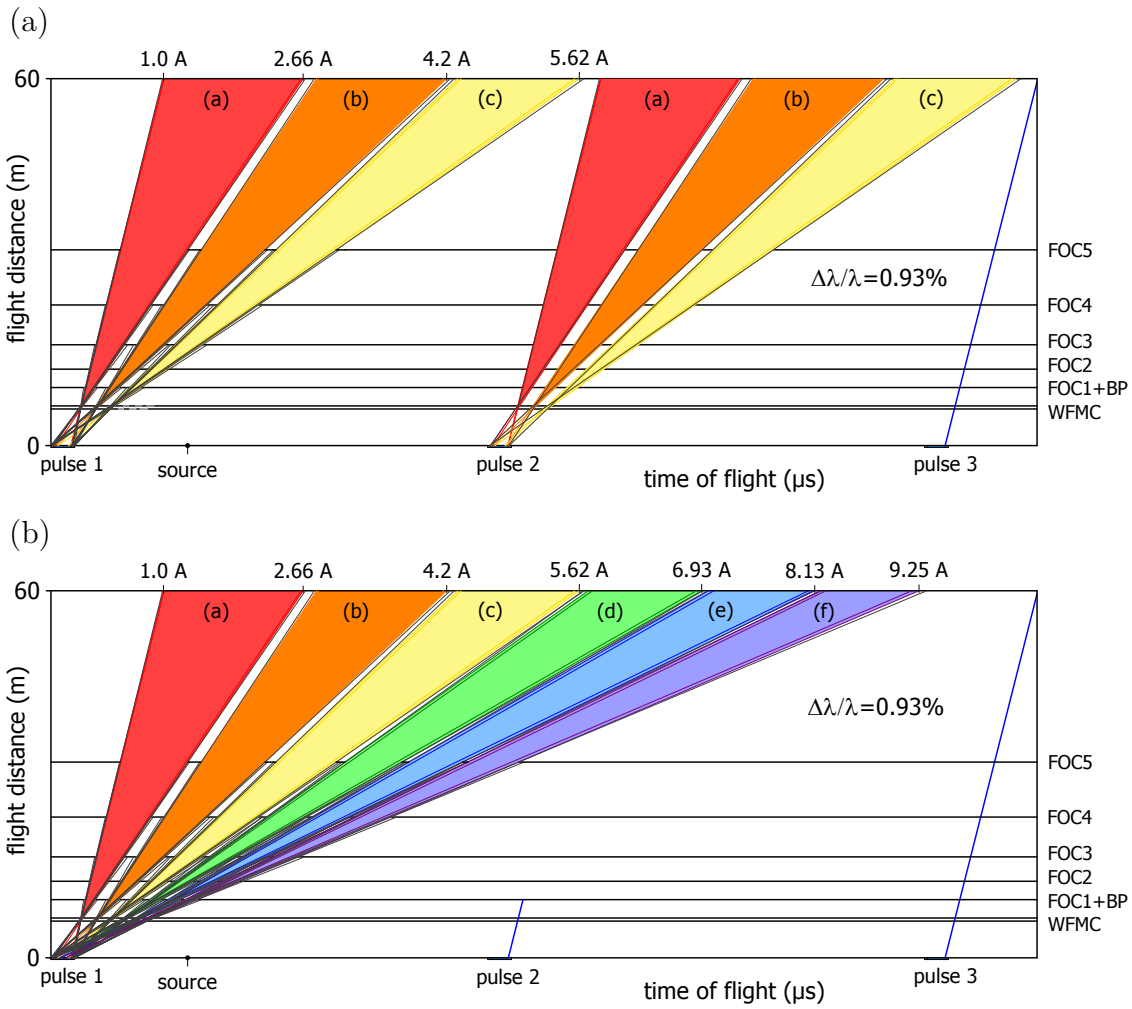

Figure 9.4.: TOF diagram for the 60 m long WFM chopper instrument at the ESS, tuned to a wavelength resolution of 0.93 % by setting the WFM choppers to the maximum distance of 0.5 m. (a) By rotating the band pass chopper at the ESS source frequency, three wavelength frames can be selected and accessed from each source pulse. The blue line starting at the third source pulse corresponds to the wavelength $\lambda = 1$ Å and hence indicates the beginning of the next pattern of three wavelength frames. (b) When skipping every second source pulse by rotating the band pass chopper at half the source frequency, six wavelength frames can be produced, covering a broader spectrum in the range 1 - 9.25 Å.

Fig. 9.5 illustrates the two low-resolution modes achieved without using the WFM choppers. In this case, all choppers except the band pass chopper are stopped in an open position. By adjusting the band pass chopper phase, the wavelength band at the detector can be selected as can also be concluded from Fig. 9.5a.

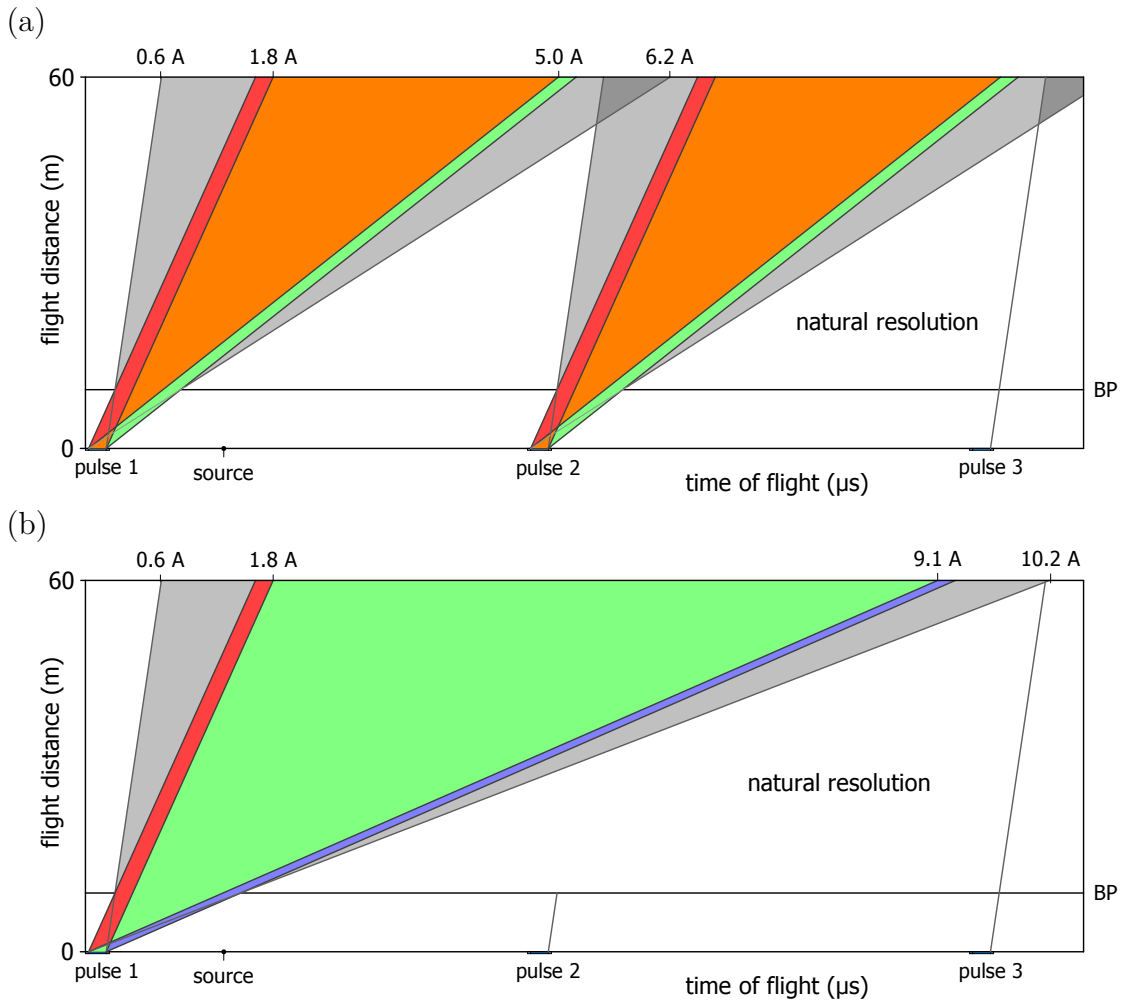

Figure 9.5.: TOF diagram for the instrument configured for the natural wavelength resolution (where all choppers despite the band pass are out of operation and parked in an open position with respect to the beam). (a) Every source pulse can be used by rotating the band pass chopper at the ESS source frequency. (b) By skipping every second source pulse with the band pass chopper, a broader wavelength band can be selected. In general, also lower fractions could be used for the band pass chopper frequency in order to expand the wavelength band to even longer wavelengths.

Similar to the WFM mode, by skipping every second source pulse (see Fig. 9.5b) a broader wavelength band can be accessed at the detector position. In principle, also $1/3$ of the source frequency could be used in the low-resolution mode. This allows to expand the accessible wavelength band to longer wavelengths but it also implies that two out of three source pulses need to be skipped. For $1/4$ and smaller fractions of the source frequency, the band pass chopper can not further block all but one source pulse per turn. Hence, the wavelength ordering at the detector would be destroyed.

As the chopper discs in this instrument have a pattern of six different opening windows the most simple realisation would be to rotate them at the source frequency. However, since the source frequency is rather low it is useful to rotate the discs as fast as possible. It is clear that only integer multiples of the source frequency can be used. For a better illustration of this issue, a zoom into the time-of-flight diagram of the six-frame mode is shown in Fig. 9.6. The largest integer multiple N of the source frequency is used where the pattern of the six opening windows still can be realised on the chopper disc.

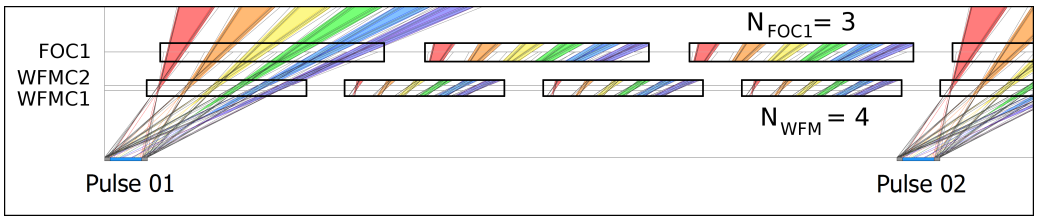

Figure 9.6.: Zoom into the time-of-flight diagram for the six-frame mode showing the opening windows of the WFM chopper discs and of the first FOC. The frequency of the chopper discs only integer multiples of the source pulse frequency can be used. The largest integer value is used where the patterns are still well separated such that the guide window at the WFM chopper position is closed between two cycles. No neutrons are expected to pass the opening windows of the choppers that are cycled through between two subsequent source pulses as (i) there are no neutrons produced by the source at this time and (ii) the BP chopper limits the wavelength band to the desired range.

10. Mathematical Description of the Chopper Discs

In this section we will discuss how the parameters of the chopper system can be calculated analytically for an idealized instrument with infinitesimally small beam cross section. The construction of the full TOF diagram, i.e. creating the subsequent wavelength frames is an iterative process. The superscript N shall denote the frame number for which the values are calculated. As base parameters we use the ESS source pulse constants t_0 and t_P, the distances z_{WFM1}, z_{WFM2} from the WFM choppers to the source and the minimum desired wavelength of the instrument $\lambda_{min} = \lambda_1$ which are defined in Fig. 9.3. To calculate the chopper parameters, we start with the first frame $N = 1$ and iterate through all six frames using the general equations given below. The longest wavelength of each frame with index N (which is equal to the shortest wavelength of frame $N + 1$) can be calculated using the equation:

$$\lambda_{N+1} = \frac{t_P + \alpha \lambda_N z_{\mathrm{WFM1}}}{\alpha z_{\mathrm{WFM2}}}. \tag{10.1}$$

Here, $\alpha = h/m_n$, where h is the Planck constant and m_n is the neutron mass. By using these variables we can calculate the chopper opening angles and phases of the required choppers which were already introduced above. The angles can be calculated using the corresponding times t_0 to t_5 introduced in Fig. 9.3. For clarity Fig. 10.1 shows a chopper disc and defines the angles Θ and the phase ϕ of frame N. An exemplary second frame $N + 1$ is shown in addition.

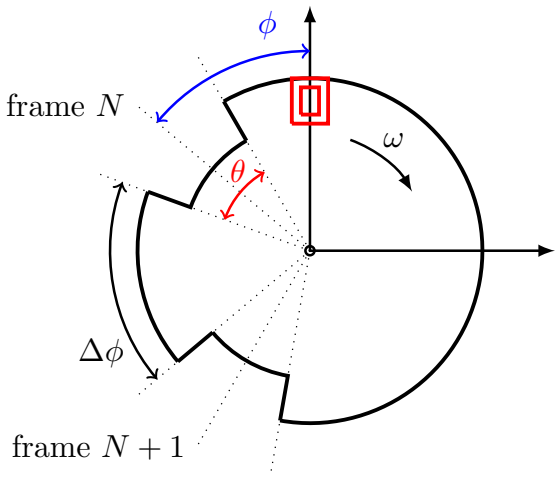

Figure 10.1.: Illustration of a chopper disc with one window of angular width Θ centred at the angle ϕ descring the phase as used in the text and in the calculations. The small rectangular window (red) corresponds to the cross section of the neutron guide.

10.1. Wavelength Frame Multiplication Chopper

The angles θ^N_{WFM1}, θ^N_{WFM2} and the corresponding phases ϕ^N_{WFM1}, ϕ^N_{WFM2} for a WFM chopper disc can be derived from Fig. 9.3. For each subframe denoted by the index $N = 1$ to $N = 6$ the angle and phase is given by

$$\theta^N_{\mathrm{WFM1}} = \theta^N_{\mathrm{WFM2}} = \omega_{\mathrm{WFM}}(t_P + \alpha(\lambda_N - \lambda_{N+1})z_{\mathrm{WFM1}}) \tag{10.2}$$

$$\phi^N_{\mathrm{WFM1}} = \omega_{\mathrm{WFM}}(t_0 + \frac{1}{2}t_P + \frac{1}{2}\alpha(\lambda_N + \lambda_{N+1})z_{\mathrm{WFM1}}) \tag{10.3}$$

$$\phi^N_{\mathrm{WFM2}} = \omega_{\mathrm{WFM}}(t_0 + \frac{3}{2}t_P + \frac{1}{2}\alpha(3\lambda_N - \lambda_{N+1})z_{\mathrm{WFM1}}) \tag{10.4}$$

For the construction, the first subframe is created by choosing the minimum required wavelength, the maximum distance of the WFM chopper discs and their position. These base parameters, together with the instrument length, define the coarsest resolution achievable in the WFM mode (see Eq. 10.1). Fig. 10.2 illustrates the chopper discs of the WFM chopper pair as constructed using Eqs. 10.2 to 10.4. It rotates at four times the source frequency as this is the largest integer multiple where all wavelength frames still fit on one chopper disc as discussed above (see Fig. 9.6). The positions were chosen to be 6.5 m and 7 m from the centre of the source.

The set of parameters calculated using the above equations and the current parameters obtained after the optimisation process (which is described in the next section) are

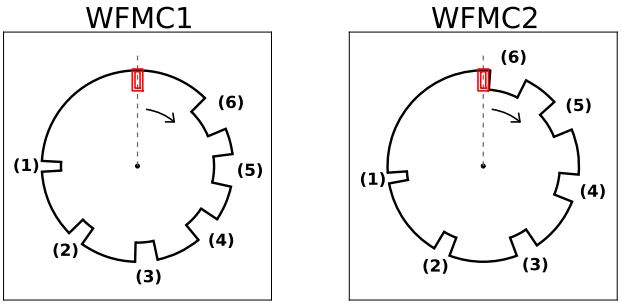

Figure 10.2.: Illustration of the WFM chopper discs as constructed using Eqs. 10.2 to 10.4. Left: first WFM chopper disc. Right: The second optically blind WFM chopper disc. The labels (N=1) to (6) denote the corresponding wavelength frame as described in the text. The red rectangle depicts the guide (beam) cross section at the chopper position.

listed in the Appendix in Tab. A.6 and Tab. A.7. As will be shown, the optimisation requires to decrease only some of the chopper windows for larger wavelengths by only a few percent. The equations given above hence represent a rather accurate starting point when developing such a chopper system.

From the definition of the angles used in our calculation (cf. Fig. 10.1) it can be derived that the angular separation $\Delta\phi$ between two subsequent chopper windows N and $N+1$ can be calculated by

$$\Delta\phi = (\phi_{N+1} - \frac{1}{2}\theta_{N+1}) - (\phi_N + \frac{1}{2}\theta_N) \tag{10.5}$$

It is important to note that the angular separation should always be wide enough to completely close the neutron guide cross section.

10.2. Frame Overlap Chopper

The initial Frame Overlap Chopper opening angles θ^N_{FOC} and the corresponding phases ϕ^N_{FOC} can be calculated for any FOC at respective position z_{FOC} by:

$$\theta^N_{\mathrm{FOC}} = \omega_{\mathrm{FOC}}(t_P + \alpha(\lambda_{N+1} - \lambda_N)(z_{\mathrm{FOC}} - z_{\mathrm{WFM1}} - z_{\mathrm{WFM2}})) \tag{10.6}$$

$$\begin{aligned}\phi^N_{\mathrm{FOC}} = \omega_{\mathrm{FOC}}(t_0 + \frac{3}{2}t_P + \frac{1}{2}\alpha(3\lambda_N - \lambda_{N+1})z_{\mathrm{WFM1}} \\ + \frac{1}{2}\alpha(\lambda_N + \lambda_{N+1})(z_{\mathrm{FOC}} - z_{\mathrm{WFM2}}))\end{aligned} \tag{10.7}$$

Note that these angles and phases are calculated for the case where the chopper

rotates at the single ESS source frequency. In a real chopper instrument, the finite neutron guide cross section leads to finite rising and falling edges of the subframes. Therefore, the actual chopper speed should be as large as possible. A high chopper speed most efficiently restricts the subframes in time. The maximum speed that can actually be used is given by taking the integer value of the fraction of the period between two ESS pulses divided by the length of one complete six-frame pattern at the WFM chopper position in time. The real angles on the chopper disc are then given by the angles calculated above multiplied by this specific integer factor. Fig. 10.3 illustrates the five FO chopper discs as constructed using Eqs. 10.6 and 10.7.

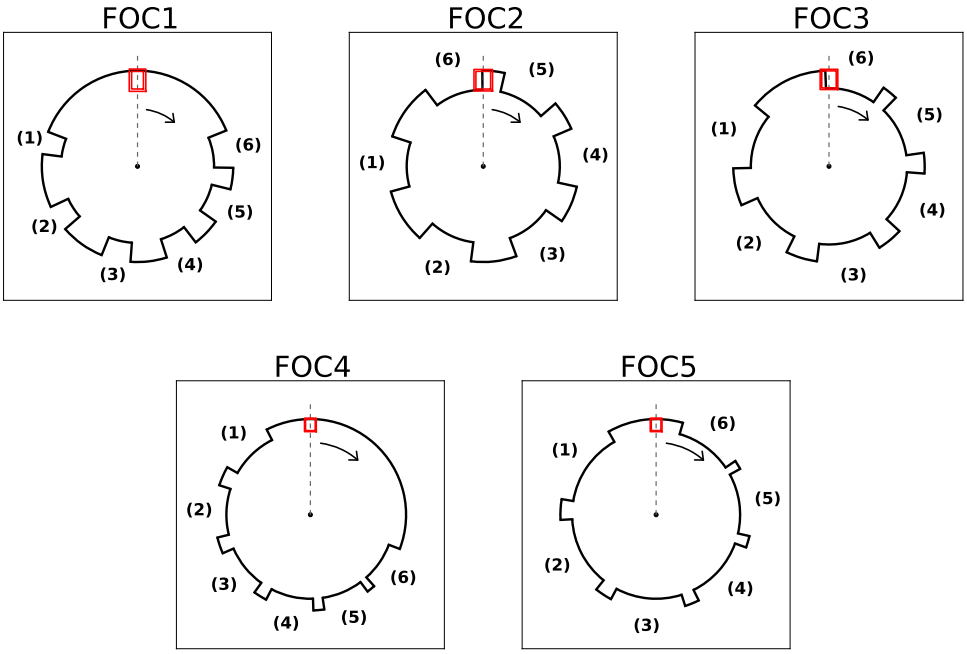

Figure 10.3.: The five frame overlap chopper discs on the path from source to detector as constructed using Eqs. 10.6 and 10.7 in the text. (N=1) to (6) denote the corresponding wavelength frame. The red rectangle depicts the guide cross section next to the chopper.

Tab. A.8 to Tab. A.12 in the Appendix tabulate the calculated parameters describing the five FO choppers.

As can be seen from the Fig. 10.3, the last two FO chopper discs take rather big dimensions in order to function properly. As mentioned the large radii are required due to the slow rotation frequency. They at least slightly compensate the resulting edge effects in the transmission as a function of time.

10.3. Band Pass and T0 Chopper

As discussed above for the proposed instrument modes, the band pass chopper (BP) rotates at two different frequencies namely at the source frequency f_{ESS} in the three-frame mode and at half of it in the six-frame mode. If only one disc should be used for both modes the calculation needs to be done for the six-frame mode. As half of the time window of the six wavelength frames will always be sufficient to pass any of three subsequent subframes the calculated band-pass will generally allow the three-frame mode.

The band pass chopper opening angles θ_{BP} and the corresponding phase ϕ_{BP} can be calculated for the position z_{BP} by:

$$\begin{aligned}\theta_{\mathrm{BP}} = \omega_{\mathrm{BP}}(t_P + \alpha(\lambda_3 - \lambda_4 - \lambda_2)z_{\mathrm{WFM1}} + \alpha(\lambda_4 - \lambda_1)z_{\mathrm{BP}} \\ + \alpha\lambda_1 z_{\mathrm{WFM2}} + 2\beta_{corr})\end{aligned} \tag{10.8}$$

$$\phi_{\mathrm{BP}} = \omega_{\mathrm{BP}}(t_0 + \alpha(\lambda_2 z_{\mathrm{WFM2}} + \lambda_1(z_{\mathrm{BP}} - z_{\mathrm{WFM2}}))) + \frac{1}{2}\theta_{\mathrm{BP}} - \beta_{corr} \tag{10.9}$$

where for better readability

$$\beta_{corr} = \arctan\left(\frac{w_{guide}}{2R_{BP} - h_{BP} - w_{guide}}\right) \tag{10.10}$$

is used in both formulas. The term β_{corr} represents the angle about which the chopper needs to rotate in order to completely open or close the neutron guide window. The width w_{guide} of the guide window, the total chopper radius R_{BP} and the height h_{BP} of the window in the chopper disc are used for the calculation.

Due to the slow rotation frequency of the choppers the band pass as well as the T0 chopper need careful considerations. The opening and closing time of the guide cross section by the chopper is significant and was therefore accounted for in the Eqs. 10.8 and 10.9. More details on the derivation are described In Fig. 10.4 the band pass chopper disc is shown on the left hand side. The parameters have been calculated using the above equations.

The T0 chopper is meant to prevent high-energetic neutrons and gamma radiation (including the so-called after-glow), which are emitted and would instantly arrive at the detector during the time of the source pulse, from contaminating measurements excessively. As the naming implies this chopper should hence be closed at $t = 0$ where the pulse is produced. It should be noted that also the neutron guide should be shielded from these neutrons in order to reduce the otherwise resulting background due to moderated neutrons and gamma radiation. It is assumed that guides upstream

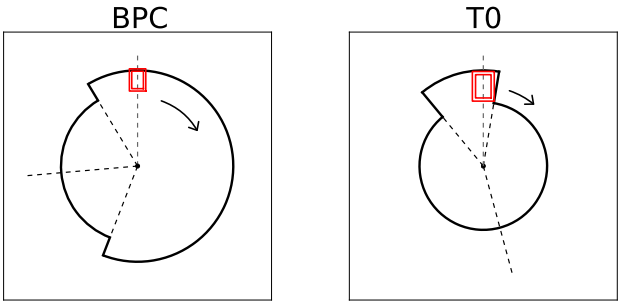

Figure 10.4.: Sketch of the chopper discs for (a) band pass chopper, constructed using Eqs. 10.8 and 10.9 and (b) the T0 chopper using Eqs. 10.11 and 10.12.

of the T0 chopper at ESS will have metal substrates instead of otherwise used glass. Hence, for the phase of the T0 chopper the thickness of the neutron guide walls are also taken into account for the calculation as they cannot stop such radiation efficiently. The opening angle (the inverse hammer size) and the phase are given by

$$\theta_{\text{T0}} = 2\pi - \omega_{\text{T0}} t_p - 2\arctan\left(\frac{w_{guide}/2}{\sqrt{R_{T0}^2 - (w_{guide}/2)^2} - h_{guide}}\right) \tag{10.11}$$

$$\phi_{\text{T0}} = \frac{1}{2}\omega_{\text{T0}} t_p - \pi \tag{10.12}$$

The above formulas contain the width w_{guide} and height h_{guide} of the outer guide dimensions (which means the guide window plus the guide walls). Furthermore, the total radius R_{T0} of the T0 chopper and its frequency ω_{T0} together with the source pulse length t_p (for which the WFM chopper system is designed) are used.

The right hand side of Fig. 10.4 shows the T0 chopper cross section as calculated using Eqs. 10.11 and 10.12. Instead of a disc as for common choppers the T0 chopper is actually more a cylinder of at least 30 cm thickness. The parameters as calculated from the above equations and as determined after the optimisation process for the instrument ODIN are listed in the Appendix in Tab. A.5.

11. Results of Monte Carlo Simulations

The time-of-flight diagrams shown above do not take into account the finite beam cross section and the true shape of the source pulse, which both imply that frame overlap increases. However, an analytical description of these effects is complicated. In order to work properly the chopper system needs to be optimised for the guide system as well as to a more realistic neutron source. A conceptual sketch of the guide system for the proposed instrument was already shown in Fig. 9.1. An elliptic guide pointing towards the source extracts the desired neutrons and focusses the neutron beam at a position of 6.75 m. This is the first possible (center) position for a chopper pair and will be used for the pulse shaping WFM choppers. The neutron beam is then defocussed using an elliptic guide part which ends up in a long straight guide section. Along this path several gaps are introduced for the choppers. Around 34 m distance from the centre of the source the straight guide is continued by a final guide section which focusses the beam at the pinhole distance of 50 m from the source. The pinhole will be adjustable to allow for different collimation values which is required for the broad range of neutron imaging applications. The detector can be positioned between 52 m and 64 m from the source with a standard position of 60 m. Regarding these conditions the guide system is far from an idealised system with infinitely small cross section and the real source pulse will not be an idealised rectangular pulse. Therefore, the theoretical instrument parameters require corrections which can most practically be figured out using Monte Carlo simulations.

In order to optimize the chopper parameters under realistic conditions, the Monte Carlo simulation package McStas (originally version 1.12c and later version 2.1, see [190]) was used. The full WFM chopper system as described analytically including FOCs and the band pass chopper together with the neutron guide system has been implemented into a virtual instrument in McStas. The calculations for chopper frequencies, opening times and phases have been implemented as functions depending only on the base parameters, as described above. A realistic pulse shape of the ESS source pulse as shown in Fig. 11.1 has been taken into account in the simulations. This resulted in a flexible virtual set up, where the different modes of operation but also different parameters and geometries of the chopper system can be tested and further optimized.

The McStas standard ESS (cold and thermal mixed) moderator with the idealised dimensions of 10x10 cm^2 was used for the simulations. Although the divergence effects may therefore not be perfectly realistic this should resemble at least the time structure and the spectral properties to a sufficient accuracy. Fig. 11.1 shows the

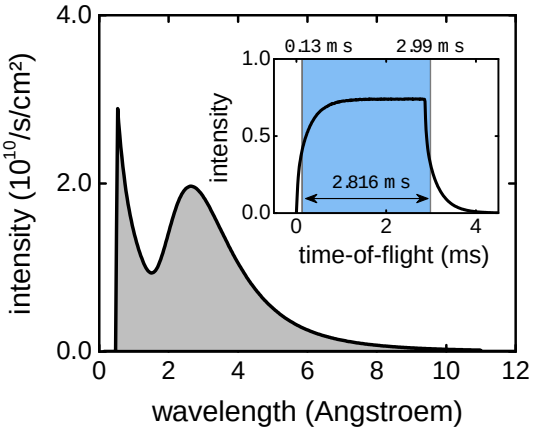

Figure 11.1.: Mixed cold and thermal ESS source spectrum as used for the McStas simulations. High energy neutron wavelengths below 0.5 Å were not simulated as they can essentially not be transported in the proposed guide system. The inset shows the time structure of one source pulse which occurs at a rate of 14 Hz. The pulse time used for the proposed chopper system is 2.86 ms. Adapted from [194].

wavelength spectrum of the simulated ESS moderator. Such a spectrum may be produced by pointing the guide system towards both, thermal and cold moderator of the source. A so-called bi-spectral extraction system as in Ref. [195, 196] will be used for this purpose. In this concept the neutron guide is pointing towards the thermal moderator and a number of neutron super mirrors (for a review see [123]) is used to deflect cold neutrons originating from the cold moderator into the guide system.

The part of the source pulse which is used for the proposed instrument is 2.86 ms long, the rising edge is rather short with about 0.13 ms while the falling edge continues much longer with an exponential decrease. The pulse is repeated at a rate of 14 Hz. The inset in Fig. 11.1 shows the source pulse as simulated in McStas using a realistic shape. The limited rectangular area shaded in blue corresponds to the part of the source pulse which is used for the theoretical values of the chopper parameters. These theoretical parameters are used as a basis for the optimisation process. Both time-of-flight diagram as well as the wavelength spectrum are a result of the current ESS base parameters (see Ref. [170]).

The guide system was originally implemented using a quadratic cross section of the guides. It was shown that the height of the guides may be easily increased by several percent in order to increase the illuminated detector area as well as the total intensity without significant implications on the time-of-flight spectrum. Additionally, the asymmetric guide cross section destroys some of the divergence gaps that are produced due to the guides, resulting in a more homogeneously illuminated detector area. This is shown in Fig. 11.2 where on the left hand side a position sensitive detector and a divergence monitor for the symmetric (quadratic) guide cross section is shown and

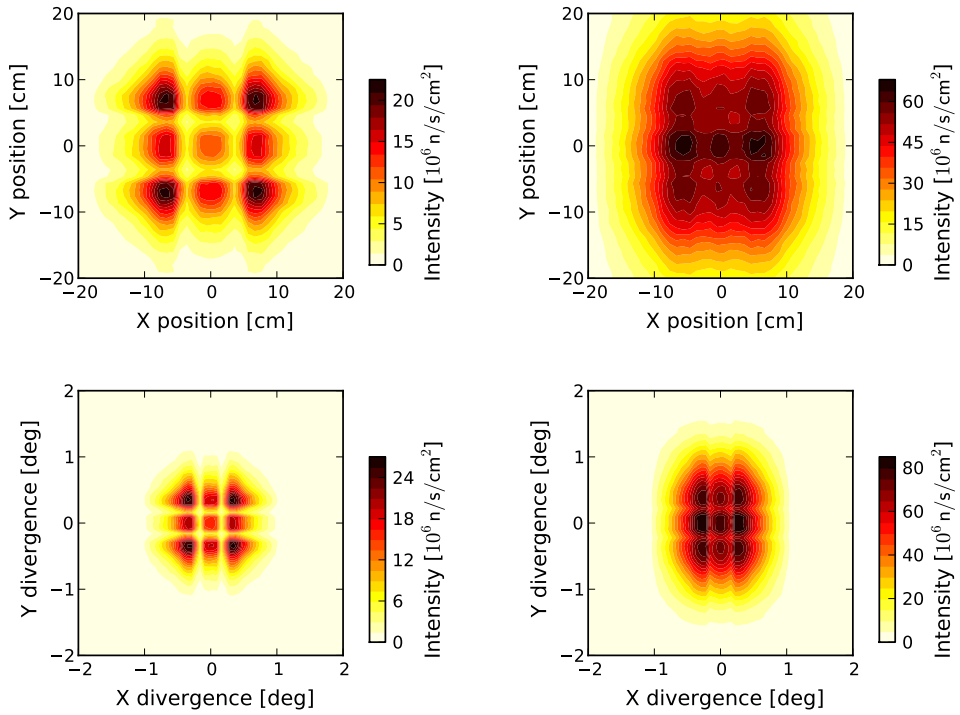

Figure 11.2.: Comparison of the detector homogeneity achieved using a quadratic guide cross section of 9x9 cm^2 on the left and an asymmetric guide cross section of 9x12 cm^2 on the right hand side. Both guide systems show certain divergence gaps which indicates that further optimisation of the neutron optics may be required after finalising the chopper optimisation.

on the right hand side for the asymmetric cross section. Interestingly, the spatial homogeneity seems to be improved for the asymmetric guide system which should be investigated in more detail.

Using the analytically calculated chopper parameters leads to an overlap of the frames in time as shown exemplary for the two neighboured frames (e) and (f) in Fig. 11.3a. The intensity in the spectrum at the limiting wavelengths of the frames is thereby increased as shown in Fig. 11.3b (red dashed lines in Fig. 11.3a and 11.3b). The overlap arises due to the finite chopper speeds and guide cross sections which are not taken into account in the analytical description. To optimize the performance of the chopper system, the chopper windows can be decreased to achieve a separation of the frames in time while at the same time providing a continuous spectrum. In this context a certain amount of overlap can be accepted in the time gaps between two subsequent frames where no data is acquired (compare Fig. 11.3a). Decreasing the chopper window size then leads to a small intensity drop in the wavelength spectrum as shown in Fig. 11.3b. It may be noted that the intensity in the simulations is given by

the number of neutrons which are counted by the detector in a desired area which here had the dimensions of 40x40 cm^2. We have always simulated two subsequent source pulses in order to investigate the occurrence of undesired wavelength contamination. However, the intensity per time is automatically included by the source component in McStas.

In general the optimisation required to reduce frame overlap needs to be done only once for the six-frame mode (see Fig. 9.4b) since only the bandpass chopper frequency and phase are changed to operate in the three-frame mode. Hence, the shape of the transmitted spectrum is similar in the given wavelength range. The development of the optimisation procedure was also part of a bachelor thesis [194] supervised during this study and will be discussed in a subsequent publication [197]. Here the most recent results of the ongoing optimisation process are shown.

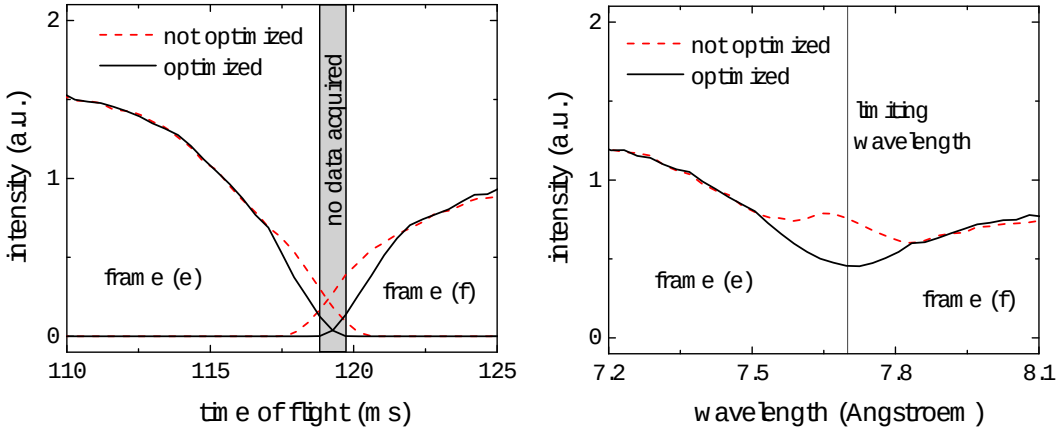

Figure 11.3.: Left: zoom into the time-of-flight spectrum showing the time gap between the last two wavelength frames. The optimisation of the chopper system requires a clear separation in time of the frames. The shaded area indicates the time window where no data is acquired in such a chopper instrument. Right: In the wavelength spectrum one can observe a drop in intensity in this time window. This is a result of the optimisation procedure where the opening angles Θ_i of the corresponding chopper windows are reduced.

In the following we show the simulations of the distinct modes of the instrument to demonstrate the performance of the optimized chopper system and to show the limitations given by the analytical calculations. We have configured the virtual instrument to achieve a theoretical resolution $\Delta\lambda/\lambda = 0.93\%$ corresponding to a WFM chopper distance of 0.5 m, since this mode is the most difficult one to optimize. The calculated chopper parameters as described in the previous Sec. 10 were used as a starting point. Optimizing the chopper system for the coarsest resolution implies that the same or even better performance is reached for finer resolutions. Fig. 11.4 shows the resulting intensity vs. time-of-flight diagram and the corresponding wavelength

spectrum for each foreseen mode of operation of the chopper system. The WFM mode using six wavelength frames and every second ESS pulse is shown in panel 11.4a, the setting with three frames using every ESS pulse is shown in panels 11.4b to 11.4e. Panel (b) shows the results for the lowest accessible part of the spectrum i.e. the first three frames (1 - 5.6 Å), in panels (c) to (e) the band pass chopper is used to access the subsequent three frames respectively. Panel 11.4e shows the highest accessible part (5.6 - 9.25 Å) of the spectrum corresponding to the last three frames.

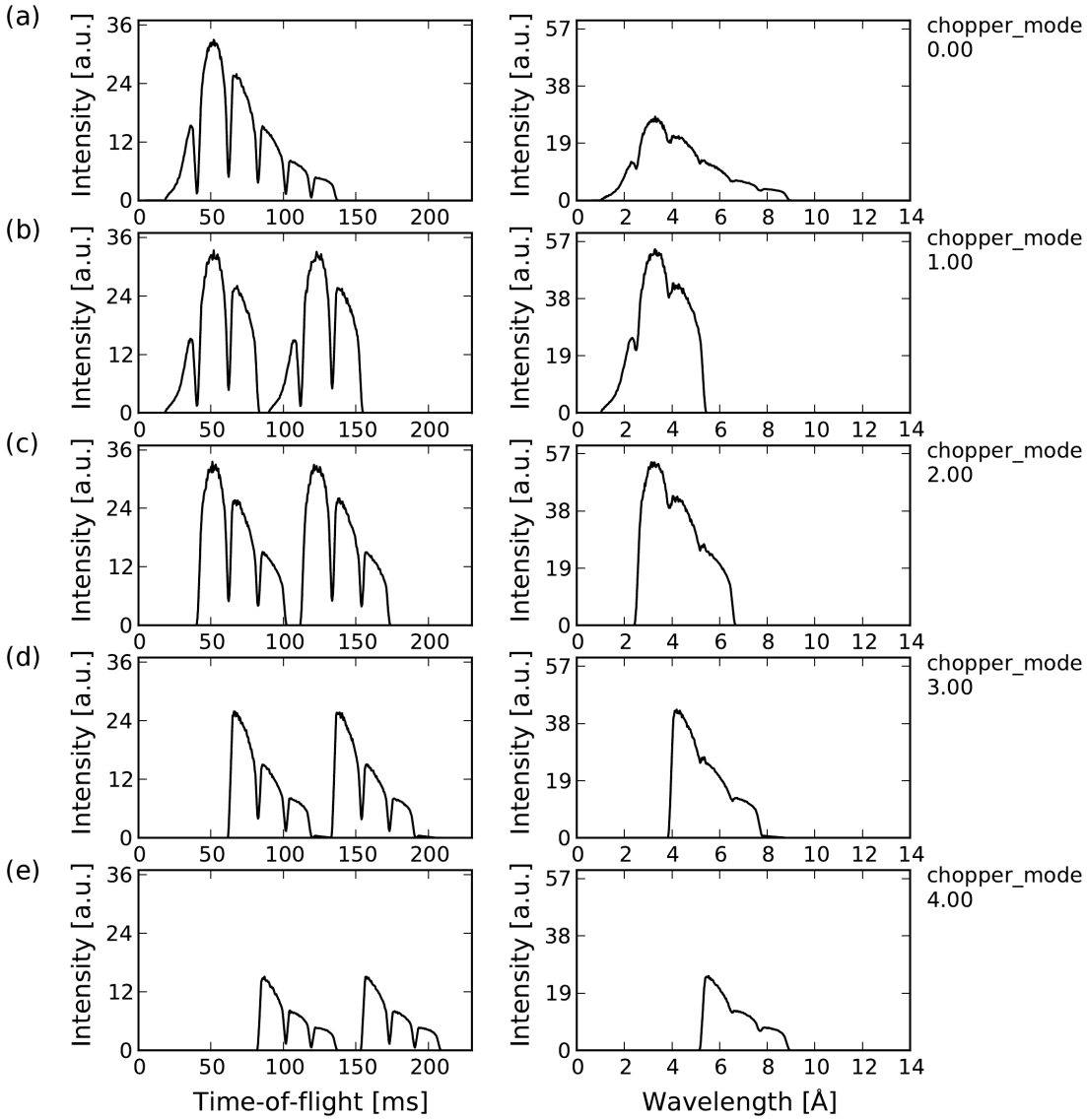

Figure 11.4.: Simulation results of the intensity vs. the time-of-flight (left column) and of the wavelength spectrum (right column) for the distinct modes of the instrument after the optimisation process as described in the text. (a) WFM mode with a resolution $\Delta\lambda/\lambda = 0.93\%$ using six subframes by skipping every second source pulse. (b) to (e) WFM mode using only three subframes but every source pulse. (b) shows the lowest part of the spectrum (1 - 5.6 Å). The band pass is used to access three subsequent frames out of six. (c) starting with the second frame and (d) starting with the third frame. (e) shows the upper part of the spectrum (5.6 - 9.25 Å) by selecting the last three frames. The variable called "chopper_mode" which is shown on the right hand side of each wavelength spectrum can be set in our virtual McStas instrument in order to adapt the corresponding chopper parameters.

For all modes the spectrum at the detector is continuous as desired. However, in the WFM mode dips in intensity down to 20 % are visible at the limiting wavelengths of the single frames. The dips in the spectrum and the slight overlap in time can be explained by taking into account the optimisation procedure required due to the finite chopper speed and the finite guide cross sections as explained in Fig. 11.3. In the optimization process the chopper windows were decreased to an amount below the detection limit within the statistics (we have used 10^{11} neutrons in McStas).

From a comparison of the intensities in the spectra in Fig. 11.4 it can be seen that the intensity in the six-frame mode is half of the intensity of the three frame mode as only one source pulse is used instead of two. The maximum around 3.5 Å is a result of the incoming spectrum and due to the properties of the guide system. The time-of-flight diagrams in the left column show a good separation of the single frames in time with only slight overlap in the gaps between the frames where no data will be acquired. Note that only two subsequent source pulses have been simulated, while actually a continuous sequence of frames will be produced. As already seen in the spectrum in the simulation, neutrons with the upper limiting wavelength (5.6 Å) of the selected band will arrive almost at the same time at the detector as the shortest wavelength of the subsequent three frames of the next source pulse.

For the natural-resolution mode of the instrument only the BP chopper is rotated while the other choppers are stopped in an open position. The intensity vs. time-of-flight and the wavelength spectrum for the different natural-resolution modes is shown in Fig. 11.5 on the left and on the right hand side respectively. In the natural resolution mode a smooth spectrum is observed which is mainly shaped by the transport properties of the guide system as can be seen in Fig. 11.5b. It can be observed that the intensity for shorter wavelengths is significantly larger in the six-frame WFM mode in Fig. 11.4a compared to the natural-resolution mode shown in Fig. 11.5a. This is a result of the optically blind WFM choppers which effectively adapt the burst time Δt for each wavelength as described in Sec. 10.1 in order to achieve a constant wavelength resolution. As this time window is smaller for shorter wavelengths, the intensity at shorter wavelengths is more reduced in the WFM mode compared to the natural-resolution mode.

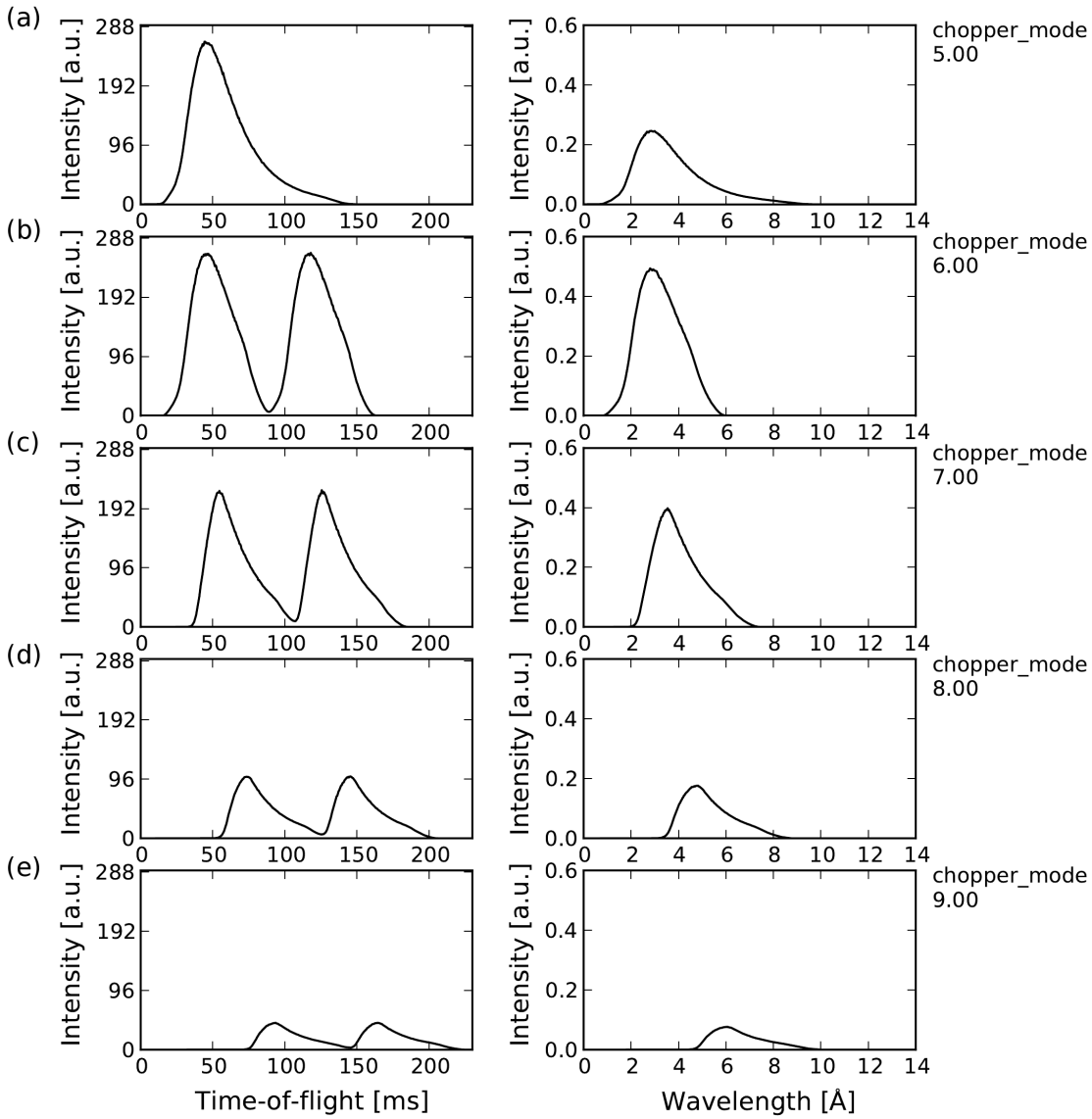

Figure 11.5.: Simulation results of the intensity vs. the time-of-flight (left column) and of the wavelength spectrum (right column) for the natural-resolution modes. The wavelength resolution $\Delta\lambda/\lambda$ scales linearly with λ in the range 10% down to 2% for 1 - 9.25 Å. Panel (a) shows the mode of operation where the BP chopper is rotated at 14 Hz and all other choppers are stopped in an open position. Each second source pulse is thereby skipped. In the panels (b) to (e) the BP chopper is rotated at 7 Hz which allows to use every source pulse at the cost of bandwidth. As for the WFM mode the wavelength band can be selected by adjusting the phase of the BP chopper.

The wavelength resolution of the different modes was determined from simulated data using a fitting routine written in the programming language Python. A comparison with the theoretically expected values as calculated for an ideal (and hence not optimised) chopper system is shown in Fig. 11.6. The corresponding theoretical values $\Delta\lambda/\lambda$ are shown in the caption. From the average wavelength resolution for each mode (shown as a dashed horizontal line in each panel in Fig. 11.6) it can be seen that the theoretical prediction overestimates the values slightly. However, this may be due to the way the resolutions were determined.

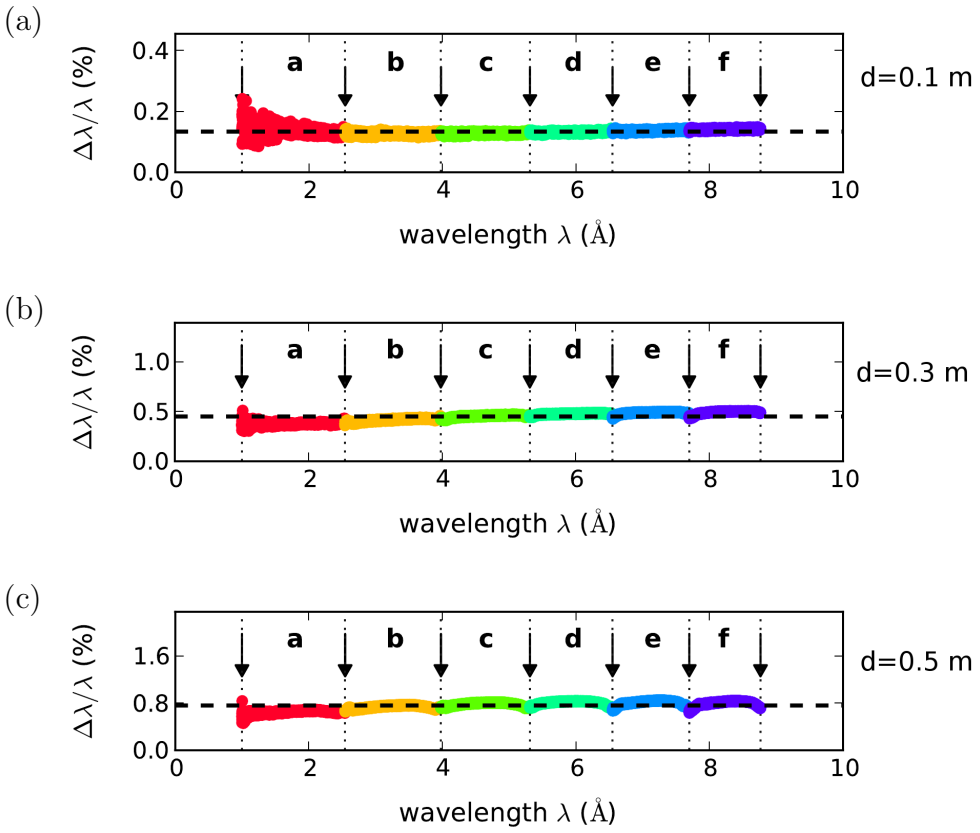

Figure 11.6.: Simulation data were used to fit the resolution $\Delta\lambda/\lambda$ for three different distances (a) d=0.1 m, (b) d=0.3 m and (c) d=0.5 m of the WFM chopper discs to each other. The expected resolutions for an idealised and unoptimised instrument would be for (a) $\Delta\lambda/\lambda = 0.19$ %, for (b) $\Delta\lambda/\lambda = 0.56$ % and for (c) $\Delta\lambda/\lambda = 0.93$ %. It can be seen from the fitted data that the resolution has a slightly lower value, i.e. it is finer than calculated for an idealised instrument. Small dips in the wavelength resolution are observed on this scale only for the coarsest resolution $\Delta\lambda/\lambda = 0.93$ %. The noise of the data for smaller wavelength is due to the rather low statistics for this part of the spectrum.

The reduced wavelength resolution in the simulated instrument compared to the analytically calculated instrument may be for two reasons. First the optimisation requires several windows of the frame overlap choppers to be decreased by a small amount which decreases the effective burst time Δt and hence reduces the value of the resolution in particular for the wavelengths that are limiting the six frames [1]. This explains the small drops indicated by the vertical arrows. Furthermore, the slow opening and closing times of the choppers are involved in these dips.

Therefore, the values in Fig. 11.6 were determined from a fit of a smeared rectangular pulse to the intensity as a function of wavelength. The wavelength resolution was then calculated by $\Delta\lambda/\lambda$ where the FWHM value was used for $\Delta\lambda$. The smeared pulse gives a good approximation although the theoretically expected value is derived for a rectangular pulse and infinitesimally small guide cross section. The fitted wavelength resolution is hence expected to be smaller than the theoretical resolution for an unoptimised chopper system. The noise which can be seen in Fig. 11.6 for smaller wavelengths is due to the rather low statistics in this wavelength regime.

An important aspect for an imaging beam line is of course the beam homogeneity at the detector position. A position-sensitive detector was used to investigate the behaviour separately for each frame. The results are shown in Fig. 11.7 for two high-resolution WFM modes. The two resolutions were set by using WFM chopper distances of 0.1 m and 0.5 m. This results theoretically in $\Delta\lambda/\lambda = 0.19\%$ and $\Delta\lambda/\lambda = 0.93\%$, respectively. The intensity distributions at the detector position were integrated over the corresponding wavelength band of each frame. It can be seen that the WFM chopper system does slightly influence the spatial homogeneity in particular the left-right symmetry of the intensity for all modes which is due to the low rotation frequency of the frame overlap choppers. The grid pattern is mainly for smaller wavelength which obviously suffer some divergence gaps. This basically means that there is still room for further optimisation of the geometry of the guide system or to use e.g. a graphite filter in order to smear out the divergence gaps.

1 It should be noted again that a small value of the bandwidth $\Delta\lambda/\lambda$ corresponds to a fine resolution while a large value corresponds to a coarse resolution.

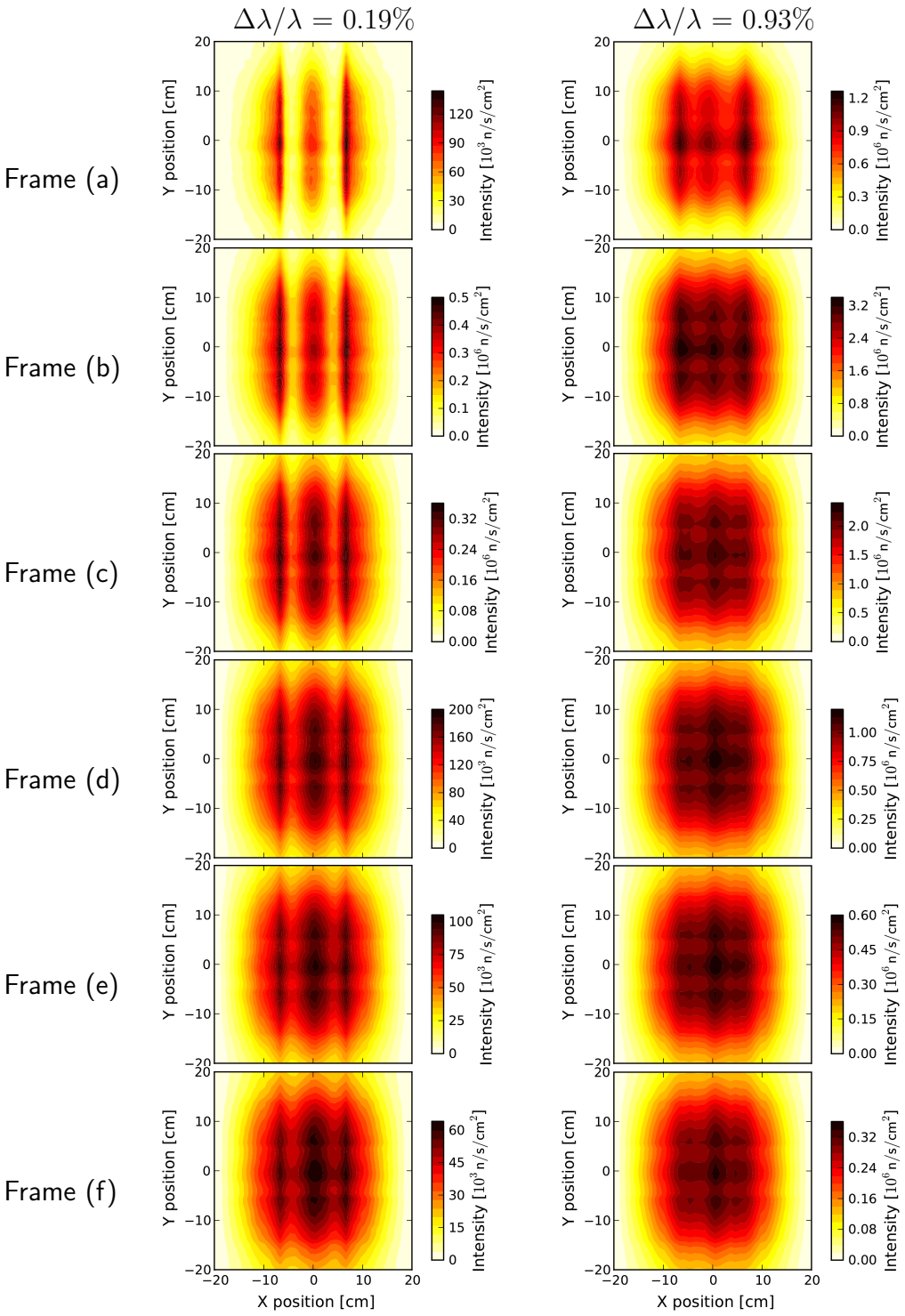

Figure 11.7.: Simulation results showing the intensity on position-sensitive detectors separately for each wavelength frame (a) to (f) in the six-frame WFM mode. The set up was tuned for the lower and the upper resolution limit by adjusting the distance d of the WFM chopper discs to each other. The left column corresponds to a theoretical bandwidth $\Delta\lambda/\lambda = 0.19\%$. The right column shows the results for a theoretically expected value $\Delta\lambda/\lambda = 0.93\%$. For smaller wavelengths in particular for the finer wavelength resolution a more pronounced inhomogeneity of the intensity distribution due to the yet unoptimised guide system is observed.

12. Summary and Outlook

A WFM chopper system adapted to the requirements of an imaging beam line at the ESS was discussed and optimised using an analytical model and Monte Carlo simulations. The advantage of the chosen chopper concept with optically blind WFM chopper discs is the constant but variable wavelength resolution over the entire spectrum and the opportunity to investigate samples using a continuous range of wavelengths within a single measurement (i.e. a multi-spectral analysis). That guarantees highest possible efficiencies by resolutions tailored to the requirements of specific measurements. An analytical description of the chopper parameters was given which completely models the proposed instrument. Using these calculations a virtual instrument has been implemented in the Monte Carlo software package McStas. The simulations allow to take into account finite guide cross sections and rotation speeds of the choppers which lead to frame overlap. The amount of contaminating wavelengths due to frame overlap was successfully reduced to achieve the desired high resolution. The optimisation was done by decreasing the size of the chopper windows by a few percent. This optimisation is judged sufficient regarding the targeted imaging applications. Tab. A.1 to Tab. A.12 in the Appendix tabulate the optimised chopper parameters for the proposed neutron guide system.

This study predicts an outstanding performance of the instrument in the high resolution (WFM) modes as well as in the natural-resolution modes and shows that our optimisation procedure of the chopper parameters can successfully eliminate frame overlap effects. According to the results the wavelength resolution in the WFM mode is not expected to be perfectly constant over the entire wavelength band in a real instrument. This is due to the optimisation steps that affect the time window where the choppers pass the neutron beam. Since a reduction of the chopper windows will shorten the time where a wavelength at the limits of each frame would pass, the wavelength resolution is expected to be smaller (i.e. finer) than the average value in these regions. However, these variations in the resolution can be considered as negligible compared to the insufficient statistics in the affected wavelength regimes and could also be accounted for in measurements. In summary the discussed chopper system shall be implemented in the multi-purpose imaging beam line ODIN at the ESS. However, other types of instruments could certainly benefit from the constant but tunable wavelength resolution.

List of Publications

- P. Schmakat, M. Wagner, R. Ritz, A. Bauer, M. Brando, M. Deppe, W. Duncan, C. Duvinage, C. Franz, C. Geibel, F.M. Grosche, M. Hirschberger, K. Hradil, M. Meven, A. Neubauer, M. Schulz, A. Senyshyn, S. Süllow, B. Pedersen, P. Böni, and C. Pfleiderer. Spin dynamics and spin freezing at ferromagnetic quantum phase transitions. *The European Physical Journal Special Topics*, 224 (6):1041–1060, 2015. ISSN 1951-6355. doi: 10.1140/epjst/e2015-02445-4. URL http://link.springer.com/10.1140/epjst/e2015-02445-4

- F. Kargl, M. Engelhardt, F. Yang, H. Weis, P. Schmakat, B. Schillinger, A. Griesche, and A. Meyer. In situ studies of mass transport in liquid alloys by means of neutron radiography. *Journal of physics. Condensed matter : an Institute of Physics journal*, 23(25):254201, 2011. ISSN 0953-8984. doi: 10.1088/0953-8984/23/25/254201

- M. Schulz, P. Schmakat, C. Franz, A. Neubauer, E. Calzada, B. Schillinger, P. Böni, and C. Pfleiderer. Neutron depolarisation imaging: Stress measurements by magnetostriction effects in Ni foils. *Physica B: Condensed Matter*, 406(12): 2412–2414, June 2011. ISSN 09214526. doi: 10.1016/j.physb.2010.10.079. URL http://linkinghub.elsevier.com/retrieve/pii/S0921452610010355

- C. Pfleiderer, P. Böni, C. Franz, T. Keller, A. Neubauer, P. G. Niklowitz, P. Schmakat, M. Schulz, Y.-K. Huang, J. a. Mydosh, M. Vojta, W. Duncan, F. M. Grosche, M. Brando, M. Deppe, C. Geibel, F. Steglich, A. Krimmel, and A. Loidl. Search for Electronic Phase Separation at Quantum Phase Transitions. *Journal of Low Temperature Physics*, 161(1-2):167–181, September 2010. ISSN 0022-2291. doi: 10.1007/s10909-010-0214-3. URL http://link.springer.com/10.1007/s10909-010-0214-3

Bibliography

[1] M. A. Ruderman and C. Kittel. Indirect Exchange Coupling of Nuclear Magnetic Moments by Conduction Electrons. *Physical Review*, 96(1):99, 1954. doi: 10.1103/PhysRev.96.99.

[2] T. Kasuya. A Theory of Metallic Ferro- and Antiferromagnetism on Zener's Model. *Progress of Theoretical Physics*, 16(1):45–57, 1956. doi: 10.1143/PTP.16.45. URL http://ptp.ipap.jp/link?PTP/16/45/.

[3] Lev Davidovich Landau. The Theory of Phase Transitions. *Nature*, 138(3498): 840–841, 1936. ISSN 0028-0836. doi: 10.1038/138840a0.

[4] P. Mohn. *Magnetism in the Solid State*. Springer-Verlag Berlin Heidelberg, corrected edition, 2006. ISBN 9783540293842.

[5] T. Vojta. Quantenphasenübergänge: Von Ordnung zu Unordnung durch Quantenfluktuationen. *Physik in unserer Zeit*, 32(1):38–43, 2001. ISSN 1521-3943.

[6] M. Vojta. Quantum phase transitions. *Reports on Progress in Physics*, 66:2069, 2003.

[7] P. Coleman and A. J. Schofield. Quantum criticality. *Nature*, 433: 226–229, March 2005. ISSN 1476-4687. doi: 10.1038/nature03279. URL http://www.nature.com/nature/journal/v433/n7023/full/nature03279.htmlhttp://arxiv.org/abs/cond-mat/0503002.

[8] C. Pfleiderer. Why first order quantum phase transitions are interesting. *Journal of Physics: Condensed Matter*, 17(11):S987–S997, March 2005. ISSN 0953-8984. doi: 10.1088/0953-8984/17/11/031. URL http://stacks.iop.org/0953-8984/17/i=11/a=031?key=crossref.411e316d5d6e0fd3d902b83c90d2cfc7.

[9] D. Belitz and T. R. Kirkpatrick. Quantum Magnetism A watched pot on a quantum stove. *Nature Physics*, 3(January):15–16, 2007.

[10] J. A. Hertz. Quantum critical phenomena. *Physical Review B*, 14(3):1165–1184, 1976. URL http://link.aps.org/doi/10.1103/PhysRevB.14.1165.

[11] A. J. Millis. Effect of a nonzero temperature on quantum critical points in itinerant fermion systems. *Physical Review B*, 48(10):7183–7196, September 1993. ISSN 0163-1829. URL http://www.ncbi.nlm.nih.gov/pubmed/10006888.

[12] N. D. Mathur, F. M. Grosche, S. R. Julian, I. R. Walker, D. M. Freye, R. K. W. Haselwimmer, and G. G. Lonzarich. Magnetically mediated superconductivity in heavy fermion compounds. *Nature*, 394, 1998. ISSN 0028-0836.

[13] A. Schröder, G. Aeppli, R. Coldea, M. Adams, O. Stockert, H. v. Löhneysen, E. Bucher, R. Ramazashvili, and P. Coleman. Onset of antiferromagnetism in heavy-fermion metals. *Nature*, 407, 2000. ISSN 0028-0836.

[14] Qimiao Si, Silvio Rabello, Kevin Ingersent, and J Lleweilun Smith. Locally critical quantum phase transitions in strongly correlated metals. *Nature*, 413 (October), 2001.

[15] S. A. Grigera, R. S. Perry, A. J. Schofield, M. Chiao, S. R. Julian, G. G. Lonzarich, S. I. Ikeda, Y. Maeno, A. J. Millis, and A. P. Mackenzie. Magnetic field-tuned quantum criticality in the metallic ruthenate Sr3Ru2O7. *Science (New York)*, 294 (5541):329–32, October 2001. ISSN 0036-8075. doi: 10.1126/science.1063539. URL http://www.sciencemag.org/content/294/5541/329.short.

[16] B. Lake, H. M. R. Ronnow, N. B. Christensen, G. Aeppli, K. Lefmann, D. F. McMorrow, P. Vorderwisch, P. Smeibidl, N. Mangkorntong, T. Sasagawa, M. Nohara, H. Takagi, and T. E. Mason. Antiferromagnetic order induced by an applied magnetic field in a high-temperature superconductor. *Nature*, 415(January):0–3, 2002.

[17] J. Custers, P. Gegenwart, H. Wilhelm, K. Neumaier, Y. Tokiwa, O. Trovarelli, C. Geibel, F. Steglich, C. Pepin, and P. Coleman. The break-up of heavy electrons at a quantum critical point. *Nature*, 424, 2003.

[18] T. Park, F. Ronning, H. Q. Yuan, M. B. Salamon, R. Movshovich, J. L. Sarrao, and J. D. Thompson. Hidden magnetism and quantum criticality in the heavy fermion superconductor CeRhIn5. *Nature*, 440, March 2006. ISSN 1476-4687. doi: 10.1038/nature04571. URL http://www.ncbi.nlm.nih.gov/pubmed/16511490.

[19] P. Gegenwart, Q. Si, and F. Steglich. Quantum criticality in heavy-fermion metals. *Nature Physics*, 4(3):186–197, 2008. ISSN 1745-2473.

[20] C. de la Cruz, Q. Huang, J. W. Lynn, J. Li, W. Ratcliff, J. L. Zarestky, H. A. Mook, G. F. Chen, J. L. Luo, N. L. Wang, and P. Dai. Magnetic order close to superconductivity in the iron-based layered La O 1-x F x Fe As systems. *Nature*, 453(7197):899–902, June 2008. ISSN 1476-4687. doi: 10.1038/nature07057. URL http://www.ncbi.nlm.nih.gov/pubmed/18509333.

[21] Jun Zhao, D. T. Adroja, Dao-Xin Yao, R. Bewley, Shiliang Li, X. F. Wang, G. Wu, X. H. Chen, Jiangping Hu, and Pengcheng Dai. Spin Waves and Magnetic Exchange Interactions in CaFe2As2. *Nature Physics*, 5(July):18, 2009.

ISSN 1745-2481. doi: 10.1038/nphys1336. URL http://arxiv.org/abs/0903.2686.

[22] Heike Pfau, Stefanie Hartmann, Ulrike Stockert, Peijie Sun, Stefan Lausberg, Manuel Brando, Sven Friedemann, Cornelius Krellner, Christoph Geibel, Steffen Wirth, Stefan Kirchner, Elihu Abrahams, Qimiao Si, and Frank Steglich. Thermal and electrical transport across a magnetic quantum critical point. *Nature*, 484 (7395):493–7, April 2012. ISSN 1476-4687. doi: 10.1038/nature11072. URL http://www.ncbi.nlm.nih.gov/pubmed/22538612.

[23] J. G. Analytis, H-H. Kuo, Ross D. McDonald, Mark Wartenbe, P. M. C. Rourke, N. E. Hussey, and I. R. Fisher. Transport near a quantum critical point in Ba Fe 2 (As 1-x P x) 2. *Nature Physics*, 10(3):194–197, January 2014. ISSN 1745-2473. doi: 10.1038/nphys2869. URL http://www.nature.com/doifinder/10.1038/nphys2869.

[24] F. Malte Grosche. Quantum phase transitions: Magnetic islands. *Nature Physics*, 10(2):94–95, January 2014. ISSN 1745-2473. doi: 10.1038/nphys2884. URL http://www.nature.com/doifinder/10.1038/nphys2884.

[25] S. Kambe, H. Sakai, Y. Tokunaga, G. Lapertot, T. D. Matsuda, G. Knebel, J. Flouquet, and R. E. Walstedt. Degenerate Fermi and non-Fermi liquids near a quantum critical phase transition. *Nature Physics*, 10(11):840–844, September 2014. ISSN 1745-2473. doi: 10.1038/nphys3101. URL http://www.nature.com/doifinder/10.1038/nphys3101.

[26] K. Shimizu, T. Kimura, S. Furomoto, K. Takeda, K. Kontani, Y. Onuki, and K. Amaya. Superconductivity in the non-magnetic state of iron under pressure. *Nature*, 412(July):316–318, 2001. ISSN 0028-0836. doi: 10.1038/35085536.

[27] C. Pfleiderer, S. R. Julian, and G. G. Lonzarich. Non-Fermi-liquid nature of the normal state of itinerant-electron ferromagnets. *Nature*, 414, November 2001. ISSN 0028-0836. doi: 10.1038/35106527. URL http://www.ncbi.nlm.nih.gov/pubmed/11719799.

[28] N. Doiron-Leyraud, I. R. Walker, L. Taillefer, M. J. Steiner, S. R. Julian, and G. G. Lonzarich. Fermi-liquid breakdown in the paramagnetic phase of a pure metal. *Nature*, 425:595–599, 2003. ISSN 0028-0836. doi: 10.1038/nature01968.

[29] A. D. Huxley, V. Mineev, B. Grenier, E. Ressouche, D. Aoki, J.P. Brison, and J. Flouquet. Order parameter symmetry in the superconducting ferromagnets UGe2 and URhGe. *Physica C: Superconductivity*, 403(1-2):9–14, March 2004. ISSN 09214534. doi: 10.1016/j.physc.2003.11.001. URL http://linkinghub.elsevier.com/retrieve/pii/S0921453403016502.

[30] F. Lévy, I. Sheikin, B. Grenier, and A. D. Huxley. Magnetic field-induced superconductivity in the ferromagnet URhGe. *Science (New York, N.Y.)*, 309 (August):1343–1346, 2005. ISSN 0036-8075. doi: 10.1126/science.1115498.

[31] F. Lévy, I. Sheikin, and A. Huxley. Acute enhancement of the upper critical field for superconductivity approaching a quantum critical point in URhGe. *Nature Physics*, 3(July):460–463, 2007. ISSN 1745-2473. doi: 10.1038/nphys608.

[32] R. S. Keizer, S. T. B. Goennenwein, T. M. Klapwijk, G. Miao, G. Xiao, and A. Gupta. A spin triplet supercurrent through the half-metallic ferromagnet CrO2. *Nature*, 439(February):825–827, 2006. ISSN 0028-0836. doi: 10.1038/nature04499.

[33] Y. J. Uemura, T. Goko, I. M. Gat-Malureanu, J. P. Carlo, P. L. Russo, a. T. Savici, A. Aczel, G. J. MacDougall, J. a. Rodriguez, G. M. Luke, S. R. Dunsiger, A. McCollam, J. Arai, Ch. Pfleiderer, P. Böni, K. Yoshimura, E. Baggio-Saitovitch, M. B. Fontes, J. Larrea, Y. V. Sushko, and J. Sereni. Phase separation and suppression of critical dynamics at quantum phase transitions of MnSi and (Sr 1-x Ca x) Ru O 3. *Nature Physics*, 3(1):29–35, 2007. ISSN 1745-2473. doi: 10.1038/nphys488.

[34] V. Sidorov, V. N. Krasnorussky, A. E. Petrova, A. N. Utyuzh, W. M. Yuhasz, T. A. Lograsso, J. D. Thompson, and S. M. Stishov. High-pressure study of the phase transition in the itinerant ferromagnet CoS2. *Physical Review B - Condensed Matter and Materials Physics*, 83:3–6, 2011. ISSN 10980121. doi: 10.1103/PhysRevB.83.060412.

[35] R. Ritz, M. Halder, M. Wagner, C. Franz, A. Bauer, and C. Pfleiderer. Formation of a topological non-Fermi liquid in MnSi. *Nature*, 497(7448):231–4, 2013. ISSN 1476-4687. doi: 10.1038/nature12023. URL http://www.ncbi.nlm.nih.gov/pubmed/23636328.

[36] S. Lausberg, a. Hannaske, a. Steppke, L. Steinke, T. Gruner, L. Pedrero, C. Krellner, C. Klingner, M. Brando, C. Geibel, and F. Steglich. Doped YbRh2Si2: Not only ferromagnetic correlations but ferromagnetic order. *Physical Review Letters*, 110(June):1–5, 2013. ISSN 00319007. doi: 10.1103/PhysRevLett.110.256402.

[37] Naoyuki Tateiwa, Tatsuma D. Matsuda, Yoshinori Haga, and Zachary Fisk. Pressure-induced ferromagnetism with strong Ising-type anisotropy in YbCu 2 Si 2. *Physical Review B - Condensed Matter and Materials Physics*, 89:1–5, 2014. ISSN 10980121. doi: 10.1103/PhysRevB.89.035127.

[38] L. Schoop, M. Hirschberger, J. Tao, C. Felser, N. P. Ong, and R. J. Cava. Paramagnetic to ferromagnetic phase transition in lightly Fe-doped Cr 2 B. *Physical Review B*, 89(224417), 2014. doi: 10.1103/PhysRevB.89.224417.

[39] D. Belitz and T. Kirkpatrick. Fluctuation-Driven Quantum Phase Transitions in Clean Itinerant Ferromagnets. *Physical Review Letters*, 89(24):247202, November 2002. ISSN 0031-9007. doi: 10.1103/PhysRevLett.89.247202. URL http://link.aps.org/doi/10.1103/PhysRevLett.89.247202.

[40] D. Belitz and T. R. Kirkpatrick. A compilation of metallic systems that show a quantum ferromagnetic transition. *arXiv:cond-mat*, (1204.0873v1), April 2012. URL http://arxiv.org/abs/1204.0873.

[41] Thomas Vojta. Disorder-Induced Rounding of Certain Quantum Phase Transitions. *Physical Review Letters*, 90(10):107202, March 2003. ISSN 0031-9007. doi: 10.1103/PhysRevLett.90.107202. URL http://link.aps.org/doi/10.1103/PhysRevLett.90.107202.

[42] D. Belitz, T. Kirkpatrick, and Jörg Rollbühler. Tricritical Behavior in Itinerant Quantum Ferromagnets. *Physical Review Letters*, 94(24):247205, June 2005. ISSN 0031-9007. doi: 10.1103/PhysRevLett.94.247205. URL http://link.aps.org/doi/10.1103/PhysRevLett.94.247205.

[43] Y. Sang, D. Belitz, and T. R. Kirkpatrick. Disorder dependence of the ferromagnetic quantum phase transition. *Physical Review Letters*, 113(207201): 1–5, 2014. ISSN 10797114. doi: 10.1103/PhysRevLett.113.207201. URL http://arxiv.org/abs/1406.5745.

[44] T. Vojta and J. Schmalian. Quantum Griffiths effects in itinerant Heisenberg magnets. *Physical Review B*, 72(4):45438, July 2005. doi: 10.1103/PhysRevB.72.045438.

[45] Thomas Vojta. Rare region effects at classical, quantum and nonequilibrium phase transitions. *Journal of Physics A: Mathematical and General*, 39 (22):R143–R205, June 2006. ISSN 0305-4470. doi: 10.1088/0305-4470/39/22/R01. URL http://stacks.iop.org/0305-4470/39/i=22/a=R01?key=crossref.efb7d5f24dd1b89df653af8cd0da140b.

[46] Matthias Vojta, Ying Zhang, and Subir Sachdev. Quantum Phase Transitions in d -Wave Superconductors. *Physical Review Letters*, 85(23), 2000.

[47] G. J. Conduit, A. G. Green, and B. D. Simons. Inhomogeneous Phase Formation on the Border of Itinerant Ferromagnetism. *Physical Review Letters*, 103 (20):207201, November 2009. ISSN 0031-9007. doi: 10.1103/PhysRevLett.103.207201. URL http://link.aps.org/doi/10.1103/PhysRevLett.103.207201.

[48] Una Karahasanovic, Frank Krüger, and Andrew G. Green. Quantum order-by-disorder driven phase reconstruction in the vicinity of ferromagnetic quantum

critical points. *Physical Review B - Condensed Matter and Materials Physics*, 85(16):1–14, 2012. ISSN 10980121. doi: 10.1103/PhysRevB.85.165111.

[49] T. Chatterji. *Neutron Scattering from Magnetic Materials*. 2005. ISBN 0080457053. URL http://books.google.com/books?hl=de&lr=&id=ehBFD7mWCs8C&pgis=1.

[50] G. L. Squires. *Introduction to the Theory of Thermal Neutron Scattering*. 2012. ISBN 1107644062. URL http://books.google.com/books?hl=de&lr=&id=KUVD8KJt7_0C&pgis=1.

[51] N. Kardjilov, A. Hilger, I. Manke, M. Strobl, M. Dawson, and J. Banhart. New trends in neutron imaging. *Nuclear Instruments and Methods in Physics Research Section A: Accelerators, Spectrometers, Detectors and Associated Equipment*, 605(1-2):13–15, June 2009. ISSN 01689002. doi: 10.1016/j.nima.2009.01.162. URL http://www.sciencedirect.com/science/article/pii/S0168900209002150http://linkinghub.elsevier.com/retrieve/pii/S0168900209002150.

[52] O. Halpern and T. Holstein. On the Passage of Neutrons Through Ferromagnets. *Physical Review*, 59(12):960–981, 1941. ISSN 0031-899X.

[53] M. T. Rekveldt. Study of ferromagnetic bulk domains by neutron depolarization in three dimensions. *Zeitschrift für Physik A, Hadrons and Nuclei*, 259(5):391–410, 1973. ISSN 0939-7922. URL http://dx.doi.org/10.1007/BF01397376.

[54] A. Das, S. K. Paranjpe, S. Honda, S. Murayama, and Y. Tsuchiya. Neutron depolarization measurements on the reentrant spin-glass bcc Cr-Fe-Mn alloy. *Journal of Physics: Condensed Matter*, 11:5209–5217, 1999.

[55] L. Kõszegi, Z. Somogyvári, N.H. van Dijk, and M.Th. Rekveldt. Neutron depolarisation study of nanocrystalline Fe73.5Nb3Cu1Si13.5B9 alloy. *Physica B: Condensed Matter*, 335(1-4):140–142, July 2003. ISSN 09214526. doi: 10.1016/S0921-4526(03)00225-4. URL http://linkinghub.elsevier.com/retrieve/pii/S0921452603002254.

[56] I. Manke, N. Kardjilov, M. Strobl, a. Hilger, and J. Banhart. Investigation of the skin effect in the bulk of electrical conductors with spin-polarized neutron radiography. *Journal of Applied Physics*, 104(7):076109, October 2008. ISSN 00218979. doi: 10.1063/1.2992516. URL http://scitation.aip.org/content/aip/journal/jap/104/7/10.1063/1.2992516.

[57] Nikolay Kardjilov, Ingo Manke, Markus Strobl, André Hilger, Wolfgang Treimer, Michael Meissner, Thomas Krist, and John Banhart. Three-dimensional imaging of magnetic fields with polarized neutrons. *Nature Physics*, 4(5):399–403, March

2008. ISSN 1745-2473. doi: 10.1038/nphys912. URL http://dx.doi.org/10.1038/nphys912http://www.nature.com/doifinder/10.1038/nphys912.

[58] M. Schulz. *Radiography with Polarised Neutrons*. Phd thesis, Technische Universität München, 2010.

[59] M. Schulz, P. Schmakat, C. Franz, A. Neubauer, E. Calzada, B. Schillinger, P. Böni, and C. Pfleiderer. Neutron depolarisation imaging: Stress measurements by magnetostriction effects in Ni foils. *Physica B: Condensed Matter*, 406(12): 2412–2414, June 2011. ISSN 09214526. doi: 10.1016/j.physb.2010.10.079. URL http://linkinghub.elsevier.com/retrieve/pii/S0921452610010355.

[60] C. Pfleiderer, P. Böni, C. Franz, T. Keller, A. Neubauer, P. G. Niklowitz, P. Schmakat, M. Schulz, Y.-K. Huang, J. a. Mydosh, M. Vojta, W. Duncan, F. M. Grosche, M. Brando, M. Deppe, C. Geibel, F. Steglich, A. Krimmel, and A. Loidl. Search for Electronic Phase Separation at Quantum Phase Transitions. *Journal of Low Temperature Physics*, 161(1-2):167–181, September 2010. ISSN 0022-2291. doi: 10.1007/s10909-010-0214-3. URL http://link.springer.com/10.1007/s10909-010-0214-3.

[61] P. Schmakat. *Neutronen-Depolarisationsmessungen am Kondo-System CePd 1-x Rh x bei tiefen Temperaturen*. Diploma thesis, Technische Universität München, 2011.

[62] Wolfgang Treimer. Radiography and tomography with polarized neutrons. *Journal of Magnetism and Magnetic Materials*, 350:188–198, January 2014. ISSN 03048853. doi: 10.1016/j.jmmm.2013.09.032. URL http://linkinghub.elsevier.com/retrieve/pii/S0304885313006914.

[63] J. G. Sereni, R. Küchler, and C. Geibel. Evidence for a ferromagnetic quantum critical point in Ce Pd 1- x Rh x. *Physica B: Condensed Matter*, 359:41–43, 2005. ISSN 0921-4526.

[64] M. Deppe, P. Pedrazzini, N. Caroca-Canales, C. Geibel, and J. G. Sereni. Investigations of Ce Pd 1-x Rh x single crystals located near a ferromagnetic quantum critical point. *Physica B: Condensed Matter*, 378:96–97, 2006. ISSN 0921-4526.

[65] T. Westerkamp, M. Deppe, R. Küchler, M. Brando, C. Geibel, P. Gegenwart, A. P. Pikul, and F. Steglich. Kondo-Cluster-Glass State near a Ferromagnetic Quantum Phase Transition. *Physical Review Letters*, 102(20):206404, 2009. ISSN 1079-7114.

[66] M. Brando, T. Westerkamp, M. Deppe, P. Gegenwart, C. Geibel, and F. Steglich. Quantum Griffiths phase in Ce Pd 1- x Rh x with x=0.8. In *Journal of Physics: Conference Series*, volume 200, page 12016. IOP Publishing, October 2010.

doi: 10.1088/1742-6596/200/1/012016. URL http://arxiv.org/abs/0910.5840.

[67] P. Böni, S. M. Shapiro, and K. Motoya. Magnetic field dependence of the spin dynamics in the reentrant spin glass Fe 70.4 Al 29.6. *Physical Review B*, 37(1), 1988.

[68] J. A. Mydosh. *Spin glasses : an experimental introduction*. Taylor & Francis, London ; Washington, DC, 1993. ISBN 0748400389.

[69] T. Westerkamp. *Quantenphasenübergänge in den Schwere-Fermionen-Systemen Yb (Rh 1-x M x) 2 Si 2 und Ce Pd 1-x Rh x*. PhD thesis, 2009.

[70] M. Uhlarz, C. Pfleiderer, and S. Hayden. Quantum Phase Transitions in the Itinerant Ferromagnet ZrZn2. *Physical Review Letters*, 93(25):256404, December 2004. ISSN 0031-9007. doi: 10.1103/PhysRevLett.93.256404. URL http://link.aps.org/doi/10.1103/PhysRevLett.93.256404.

[71] M. Uhlarz, C. Pfleiderer, and S.M. Hayden. Quantum phase transitions in the itinerant ferromagnet ZrZn2. *Physica B: Condensed Matter*, 359-361:1174–1176, April 2005. ISSN 09214526. doi: 10.1016/j.physb.2005.01.324. URL http://linkinghub.elsevier.com/retrieve/pii/S0921452605003601.

[72] Shinya Takashima, Minoru Nohara, Hiroaki Ueda, Nao Takeshita, Chieko Terakura, Fumiko Sakai, and Hidenori Takagi. Robustness of Non-Fermi-Liquid Behavior near the Ferromagnetic Critical Point in Clean ZrZn 2. *Journal of the Physical Society of Japan*, 76(4):043704, April 2007. ISSN 0031-9015. doi: 10.1143/JPSJ.76.043704. URL http://journals.jps.jp/doi/abs/10.1143/JPSJ.76.043704.

[73] R. P. Smith, M. Sutherland, G. G. Lonzarich, S. S. Saxena, N. Kimura, S. Takashima, M. Nohara, and H. Takagi. Marginal breakdown of the Fermi-liquid state on the border of metallic ferromagnetism. *Nature*, 455, October 2008. ISSN 0028-0836. doi: 10.1038/nature07401. URL http://www.nature.com/doifinder/10.1038/nature07401.

[74] Noriyuki Kabeya, Hirotaka Maekawa, Kazuhiko Deguchi, Noriaki Kimura, Haruyoshi Aoki, and Noriaki K. Sato. Non-Fermi Liquid State Bounded by a Possible Electronic Topological Transition in ZrZn2. *Journal of the Physical Society of Japan*, 81:1–4, 2012. ISSN 00319015. doi: 10.1143/JPSJ.81.073706. URL http://journals.jps.jp/doi/abs/10.1143/JPSJ.81.073706.

[75] S. M. Shapiro, C. R. Fincher, A. C. Palumbo, and R. D. Parks. Anomalous spin-wave behaviour in the magnetic alloy Fe x Cr 1-x. *Physical Review B*, 24 (11), 1981.

[76] E. Fawcett, H. L. Alberts, V. Yu Galkin, D. R. Noakes, and J. V. Yakhmi. Spin-density-wave antiferromagnetism in chromium alloys. *Reviews of Modern Physics*, 66(1):25–127, 1994. ISSN 00346861. doi: 10.1103/RevModPhys.66.25.

[77] E. Fawcett and H. L. Alberts. Magnetic Gruneisen parameters in Cr alloys. *Journal of Physics: Condensed Matter*, 2:6251–6262, 1999. ISSN 0953-8984. doi: 10.1088/0953-8984/2/29/002.

[78] K. G. Wilson. Renormalization Group and Critical Phenomena. *Physical Review B*, 4(9), 1971.

[79] D. Belitz, T. Kirkpatrick, and Thomas Vojta. First Order Transitions and Multicritical Points in Weak Itinerant Ferromagnets. *Physical Review Letters*, 82(23):4707–4710, June 1999. ISSN 0031-9007. doi: 10.1103/PhysRevLett.82.4707. URL http://link.aps.org/doi/10.1103/PhysRevLett.82.4707.

[80] C. Pfleiderer and A. Faisst. Field dependence of the specific heat of single-crystalline ZrZn 2. *Journal of Magnetism and Magnetic Materials*, 230:258–260, 2001. URL http://www.sciencedirect.com/science/article/pii/S0304885300006557.

[81] S. Mühlbauer, B. Binz, F. Jonietz, C. Pfleiderer, A. Rosch, A. Neubauer, R. Georgii, and P. Böni. Skyrmion Lattice in a Chiral Magnet. *Science (New York)*, 323(September):915–920, March 2009. ISSN 1095-9203. doi: 10.1126/science.1166767. URL http://www.sciencemag.org/content/323/5916/915.short.

[82] W. Münzer, A. Neubauer, T. Adams, S. Mühlbauer, C. Franz, F. Jonietz, R. Georgii, P. Böni, B. Pedersen, M. Schmidt, A. Rosch, and C. Pfleiderer. Skyrmion lattice in the doped semiconductor Fe 1-x Co x Si. *Physical Review B*, 81(4):041203, January 2010. ISSN 1098-0121. doi: 10.1103/PhysRevB.81.041203. URL http://link.aps.org/doi/10.1103/PhysRevB.81.041203.

[83] T. Adams, A. Chacon, M. Wagner, A. Bauer, G. Brandl, B. Pedersen, H. Berger, P. Lemmens, and C. Pfleiderer. Long-Wavelength Helimagnetic Order and Skyrmion Lattice Phase in Cu 2 O Se O 3. *Physical Review Letters*, 108(23):237204, June 2012. ISSN 0031-9007. doi: 10.1103/PhysRevLett.108.237204. URL http://link.aps.org/doi/10.1103/PhysRevLett.108.237204.

[84] T. Goto, Y. Shindo, and H. Takahashi. Magnetic properties of the itinerant metamagnetic system Co (S 1-x Se x) 2 under high magnetic fields and high pressure. *Physical Review B*, 56(21):19–28, 1997. ISSN 0163-1829. doi: 10.1103/PhysRevB.56.14019.

[85] L. Wang, T. Chen, and C. Leighton. Spin-dependent band structure effects and measurement of the spin polarization in the candidate half-metal CoS2.

Physical Review B, 69(9):1–6, 2004. ISSN 1098-0121. doi: 10.1103/PhysRevB.69.094412.

[86] P. G. Niklowitz, F. Beckers, G. G. Lonzarich, G. Knebel, B. Salce, J. Thomasson, N. Bernhoeft, D. Braithwaite, and J. Flouquet. Spin-fluctuation dominated electrical transport of Ni3Al at high pressure. *Physical Review B*, 72:024424, 2005. doi: 10.1103/PhysRevB.72.024424. URL http://arxiv.org/abs/cond-mat/0411451.

[87] W. Wu, A. McCollam, S. A. Grigera, R. S. Perry, A. P. MacKenzie, and S. R. Julian. Quantum critical metamagnetism of Sr3Ru2O7 under hydrostatic pressure. *Physical Review B*, 83(4):1–7, 2011. ISSN 10980121. doi: 10.1103/PhysRevB.83.045106.

[88] C. Lester, S. Ramos, R. S. Perry, T. P. Croft, R. I. Bewley, T. Guidi, P. Manuel, D. D. Khalyavin, E. M. Forgan, and S. M. Hayden. Field tunable spin density wave phases in Sr3Ru2O7. *arXiv:cond-mat*, September 2014. URL http://arxiv.org/abs/1409.7054.

[89] S. S. Saxena, P. Agarwal, K. Ahilan, F. M. Grosche, R. K. Haselwimmer, M. J. Steiner, E. Pugh, I. R. Walker, S. R. Julian, P. Monthoux, G. G. Lonzarich, A. Huxley, I. Sheikin, D. Braithwaite, and J. Flouquet. Superconductivity on the border of itinerant-electron ferromagnetism in UGe2. *Nature*, 406, August 2000. ISSN 1476-4687. doi: 10.1038/35020500. URL http://dx.doi.org/10.1038/35020500.

[90] D. Aoki, A. Huxley, E. Ressouche, D. Braithwaite, J. Flouquet, J. P. Brison, E. Lhotel, and C. Paulsen. Coexistence of superconductivity and ferromagnetism in URhGe. *Nature*, 413, October 2001. ISSN 0028-0836. doi: 10.1038/35098048. URL http://www.ncbi.nlm.nih.gov/pubmed/11595943.

[91] N. T. Huy, A. Gasparini, D. E. De Nijs, Y. Huang, J. C P Klaasse, T. Gortenmulder, A. De Visser, A. Hamann, T. Görlach, and H. V. Löhneysen. Superconductivity on the border of weak itinerant ferromagnetism in UCoGe. *Physical Review Letters*, 99(6):3–6, 2007. ISSN 00319007. doi: 10.1103/PhysRevLett.99.067006.

[92] M. Nicklas, M. Brando, G. Knebel, F. Mayr, W. Trinkl, and A. Loidl. Non-Fermi-Liquid Behavior at a Ferromagnetic Quantum Critical Point in Ni x Pd 1-x. *Physical Review Letters*, 82(21), 1999.

[93] S. Drotziger, C. Pfleiderer, M. Uhlarz, H. V. Lohneysen, D. Souptel, W. Loser, and G. Behr. Suppression of ferromagnetism in CeSi 1.81 under temperature and pressure. *Physical Review B*, 73:214413, 2006. ISSN 1098-0121. doi: 10.1103/PhysRevB.73.214413. URL http://arxiv.org/abs/cond-mat/0604470.

[94] H. v. Löhneysen, A. Rosch, M. Vojta, and P. Wölfle. Fermi-liquid instabilities at magnetic quantum phase transitions. *Reviews of Modern Physics*, 79(3): 1015–1075, August 2007. doi: 10.1103/RevModPhys.79.1015.

[95] D. Aoki, A. Huxley, E. Ressouche, I. Sheikin, J. Flouquet, J. P. Brison, and C. Paulsen. Superconductivity in two itinerant uranium ferromagnets: UGe2 and URhGe. *Journal of Physics and Chemistry of Solids*, 63(6-8):1179–1182, 2002. ISSN 00223697. doi: 10.1016/S0022-3697(02)00152-X.

[96] T. C. Kobayashi, H. Hidaka, T. Fujiwara, M. Tanaka, K. Takeda, T. Akazawa, K. Shimizu, S. Kirita, R. Asai, H. Nakawaki, M. Nakashima, R. Settai, E. Yamamoto, Y. Haga, and Y. Onuki. Pressure-temperature phase diagrams of some heavy fermion systems. *Journal of Physics: Condensed Matter*, 19(12):125205, 2007. ISSN 0953-8984. doi: 10.1088/0953-8984/19/12/125205.

[97] M. Brando, D. Moroni-Klementowicz, C. Albrecht, and F.M. Grosche. Quantum criticality in NbFe2. *Physica B: Condensed Matter*, 378-380:111–112, May 2006. ISSN 09214526. doi: 10.1016/j.physb.2006.01.045. URL http://linkinghub.elsevier.com/retrieve/pii/S0921452606000421.

[98] D. Moroni-Klementowicz, M. Brando, C. Albrecht, W. J. Duncan, F. M. Grosche, D. Grüner, and G. Kreiner. Magnetism in Nb 1-y Fe 2+y: Composition and magnetic field dependence. *Physical Review B - Condensed Matter and Materials Physics*, 79(22):1–11, 2009. ISSN 10980121. doi: 10.1103/PhysRevB.79.224410.

[99] D. Rauch, M. Kraken, F. J. Litterst, S. Süllow, H. Luetkens, M. Brando, T. Förster, J. Sichelschmidt, A. Neubauer, C. Pfleiderer, W. J. Duncan, and F. M. Grosche. Spectroscopic study of metallic magnetism in single-crystalline Nb 1-y Fe 2+y. *Physical Review B*, 91(17):174404, 2015. ISSN 1098-0121. doi: 10.1103/PhysRevB.91.174404. URL http://link.aps.org/doi/10.1103/PhysRevB.91.174404.

[100] A. G. Green, S. A. Grigera, R. A. Borzi, A. P. MacKenzie, R. S. Perry, and B. D. Simons. Phase bifurcation and quantum fluctuations in Sr3Ru2O7. *Physical Review Letters*, 95(8):2–5, 2005. ISSN 00319007. doi: 10.1103/PhysRevLett.95.086402.

[101] P. Böni and S. M. Shapiro. Magnetic field dependence of the spin dynamics in Fe 28 Cr 72. *Journal of Physics: Condensed Matter*, 1:6123–6129, 1989.

[102] E. Fawcett and V. Y. Galkin. Magnetic phase diagrams and impurity resonance scattering of CrFe and CrSi and their ternary alloys with V and Mn. *Journal of Magnetism and Magnetic Materials*, 119:329–338, 1993. ISSN 03048853. doi: 10.1016/0304-8853(93)90419-3.

[103] S. K. Burke and B. D. Rainford. The evolution of magnetic order in CrFe alloys. I. Antiferromagnetic alloys close to the critical concentration. *Journal of Physics F: Metal Physics*, 13:441–450, 1983. ISSN 0305-4608. doi: 10.1088/0305-4608/13/2/021.

[104] S. K. Burke, R. Cywinski, J. R. Davis, and B. D. Rainford. The evolution of magnetic order in CrFe alloys. II. Onset of ferromagnetism. *Journal of Physics F: Metal Physics*, 13:451–470, 1983. ISSN 0305-4608. doi: 10.1088/0305-4608/13/2/020.

[105] S. K. Burke and B. D. Rainford. The evolution of magnetic order in CrFe alloys. III. Ferromagnetism close to the critical concentration. *Journal of Physics F: Metal Physics*, 13:471–482, 1983. ISSN 0305-4608. doi: 10.1088/0305-4608/13/2/021.

[106] M. Brando, D. Belitz, F. M. Grosche, and T. R. Kirkpatrick. Metallic Quantum Ferromagnets. *arXiv:cond-mat*, 2015.

[107] J. G. Sereni, T. Westerkamp, R. Küchler, N. Caroca-Canales, P. Gegenwart, and C. Geibel. Ferromagnetic quantum criticality in the alloy CePd 1-x Rh x. *Physical Review B*, 75(2):24432, 2007. ISSN 1550-235X.

[108] J. A. Blanco, M. de Podesta, J. I. Espeso, J. C. Gomez Sal, C. Lester, K. A. McEwen, N. Patrikios, and J. R. Fernandez. Specific heat of CeNi x Pt 1-x pseudobinary compounds and related dilute alloys. *Physical Review B*, 49(21): 126–132, 1994.

[109] D. Gignoux and J.C. Gomez Sal. Competition between the Kondo effect and exchange interactions in the CeNi x Pt 1-x compounds. *Physical Review B*, 30 (7):3967–3973, 1984.

[110] I. Kawasaki, K. Tenya, M. Yokoyama, and H. Amitsuka. Quantum critical phenomena of ferromagnetic CePt 1-x Rh x. *Physica B: Condensed Matter*, 403 (5-9):1284–1286, 2008. ISSN 09214526. doi: 10.1016/j.physb.2007.10.128.

[111] A. P. Pikul and D. Kaczorowski. Search for quantum criticality in a ferromagnetic system U Ni 1-x Co x Si 2. *Physical Review B - Condensed Matter and Materials Physics*, 85(4):1–7, 2012. ISSN 10980121. doi: 10.1103/PhysRevB.85.045113.

[112] Sara Ubaid-Kassis, Thomas Vojta, and Almut Schroeder. Quantum Griffiths phase in the weak itinerant ferromagnetic alloy Ni 1-x V x. *Physical Review Letters*, 104(6), 2010. ISSN 00319007. doi: 10.1103/PhysRevLett.104.066402.

[113] G. R. Stewart. Non-Fermi-liquid behavior in d- and f-electron metals. *Reviews of Modern Physics*, 73(4):797–855, 2001. doi: 10.1103/RevModPhys.73.797.

[114] G. R. Stewart. Addendum: Non-Fermi-liquid behavior in d-and f-electron metals. *Reviews of Modern Physics*, 78(3):743–753, 2006. ISSN 1539-0756.

[115] E. C. Stoner. Collective electron ferromagnetism. *Proceedings of the Royal Society of London. Series A, Mathematical and Physical Sciences*, 165(922): 372–414, 1938. ISSN 0080-4630.

[116] E. P. Wohlfarth. Thermodynamic aspects of itinerant electron magnetism. *Physica B*, 91:305–314, 1977.

[117] P. Mohn and E. P. Wohlfarth. The Curie temperature of ZrZn2. *Journal of Magnetism and Magnetic Materials*, 68:283–285, 1987.

[118] T. Moriya. On the possible mechanisms for temperature-induced ferromagnetism. *Journal of the Physical Society of Japan*, 55(1):357–366, 1986.

[119] G. G. Lonzarich and L. Taillefer. Effect of spin fluctuations on the magnetic equation of state of ferromagnetic or nearly ferromagnetic metals. *Journal of Physics C: Solid State Physics*, 18:4339–4371, 1985. URL http://www.iop.org/EJ/abstract/0022-3719/18/22/017.

[120] G. G. Lonzarich. The Magnetic Equation of State and Heat Capacity in Weak Itinerant Ferromagnets. *Journal of Magnetism and Magnetic Materials*, 54-57: 612–616, 1986. URL http://linkinghub.elsevier.com/retrieve/pii/0304885386901897.

[121] T. Moriya. *Spin Fluctuations in Itinerant Electron Magnetism*. Springer-Verlag Berlin Heidelberg New York Tokyo, 1985. ISBN 3-540-75422-1.

[122] G. G. Lonzarich. The magnetic electron. *Electron: a centenary volume*, 1999. URL http://books.google.com/books?hl=en&lr=&id=qUipZ0pXzfQC&oi=fnd&pg=PA109&dq=The+magnetic+electron&ots=fdm0JwoINi&sig=9KFJNtrmIQE7xu7V_V1hkxy53gw.

[123] P. Böni, W. Münzer, and a. Ostermann. Instrumentation with polarized neutrons. *Physica B: Condensed Matter*, 404(17):2620–2623, September 2009. ISSN 09214526. doi: 10.1016/j.physb.2009.06.031. URL http://linkinghub.elsevier.com/retrieve/pii/S0921452609003895.

[124] E. Babcock, A. Petoukhov, J. Chastagnier, D. Jullien, E. Lelièvre-Berna, K.H. Andersen, R. Georgii, S. Masalovich, S. Boag, C. D. Frost, and S. R. Parnell. AFP flipper devices: Polarized 3He spin flipper and shorter wavelength neutron flipper. *Physica B: Condensed Matter*, 397(1-2):172–175, July 2007. ISSN 09214526. doi: 10.1016/j.physb.2007.02.093. URL http://linkinghub.elsevier.com/retrieve/pii/S0921452607001561.

[125] V. Hutanu, S. Masalovich, M. Meven, O. Lykhvar, G. Borchert, and G. Heger. Scientific Review: Polarized 3 He Spin Filters for Hot Neutrons at the FRM II. *Neutron News*, 18(4):14–16, November 2007. ISSN 1044-8632. doi: 10.1080/10448630701623111. URL http://www.tandfonline.com/doi/abs/10.1080/10448630701623111#.VKwKjXtVVHA.

[126] W. H. Kraan. Instrumentation to handle thermal polarized neutron beams, November 2004. URL http://repository.tudelft.nl/view/ir/uuid:7c3c5919-e3c2-4146-89cd-5658b96e18f8/.

[127] N. Arend. *New Aspects of the MIEZE technique and Verification of the Multilevel MIEZE Principle*. Phd thesis, Technische Universität München, 2007.

[128] Stefan Mayerhofer. *Optimisation of the Magnetic Field Geometry for Neutron Depolarisation Measurements at the instrument ANTARES*. PhD thesis, Fachhochschule Müchen, 2014.

[129] O. Halpern and T. Holstein. On the Depolarization of Neutron Beams by Magnetic Fields. *Proceedings of the National Academy of Sciences*, 28(1), 1942.

[130] L. W. M. Schreurs, H. M. Weijers, A. P. J. van Deursen, and A. R. de Vroomen. Growth and electrical properties of ZrZn2 single crystals. *Materials Research Bulletin*, 24(9):1141–1145, September 1989. ISSN 00255408. doi: 10.1016/0025-5408(89)90072-X. URL http://www.sciencedirect.com/science/article/pii/002554088990072X.

[131] S.M. Hayden and C.C. Paulsen. THE LOW TEMPERATURE MAGNETIZATION OF ZrZn2. *Physica B*, 165:201–202, 1990.

[132] E. A. Yelland, S. J. Yates, O. Taylor, A. Griffiths, S. M. Hayden, and A. Carrington. Ferromagnetic properties of ZrZn2. *Physical Review B*, 72, 2005. ISSN 10980121. doi: 10.1103/PhysRevB.72.184436.

[133] M. Uhlarz and C. Pfleiderer. Pressure dependence of the ferromagnetic ordering temperature in single-crystal ZrZn2. *Physica B: Condensed Matter*, 313:487–488, 2002. URL http://www.sciencedirect.com/science/article/pii/S0921452601011747.

[134] T. F. Smith and C. W. Chu. Will Pressure Destroy Superconductivity. *Physical Review*, 159(2):353–358, July 1967. ISSN 0031-899X. doi: 10.1103/PhysRev.159.353. URL http://link.aps.org/doi/10.1103/PhysRev.159.353.

[135] Marco Halder. *Vibrating Sample Magnetometry for samples in a pressure cell*. Diploma thes, Technische Universität München, 2010.

[136] Andreas Bauer. *Quantenphasenübergänge und Skyrmion-Gitter in Mn 1-x Fe x Si und Mn 1-x Co x Si*. PhD thesis, 2009.

[137] F. Tasset. Zero field neutron polarimetry. *Physica B: Condensed Matter*, 156-157: 627–630, 1989. ISSN 09214526. doi: 10.1016/0921-4526(89)90749-7.

[138] B. Roessli and P. Böni. Polarized Neutron Scattering. *arXiv:cond-mat*, (0012180v1), December 2000. URL http://arxiv.org/abs/cond-mat/0012180.

[139] E. Lelièvre-Berna, E. Bourgeat-Lami, P. Fouilloux, B. Geffray, Y. Gibert, K. Kakurai, N. Kernavanois, B. Longuet, F. Mantegezza, M. Nakamura, S. Pujol, L. P. Regnault, F. Tasset, M. Takeda, M. Thomas, and X. Tonon. Advances in spherical neutron polarimetry with Cryopad. *Physica B: Condensed Matter*, 356(1-4 SPEC. ISS.):131–135, 2005. ISSN 09214526. doi: 10.1016/j.physb.2004.10.063.

[140] S. Masalovich. Method to measure neutron beam polarization with 2x1 Neutron Spin Filter. *Nuclear Instruments and Methods in Physics Research Section A: Accelerators, Spectrometers, Detectors and Associated Equipment*, 581(3): 1–13, November 2007. ISSN 01689002. doi: 10.1016/j.nima.2007.08.150. URL http://linkinghub.elsevier.com/retrieve/pii/S0168900207018700.

[141] Martin Klein and Christian J. Schmidt. CASCADE, neutron detectors for highest count rates in combination with ASIC/FPGA based readout electronics. *Nuclear Instruments and Methods in Physics Research, Section A: Accelerators, Spectrometers, Detectors and Associated Equipment*, 628(1):9–18, 2011. ISSN 01689002. doi: 10.1016/j.nima.2010.06.278. URL http://dx.doi.org/10.1016/j.nima.2010.06.278.

[142] W. Häussler, P. Böni, M. Klein, C. J. Schmidt, U. Schmidt, F. Groitl, and J. Kindervater. Detection of high frequency intensity oscillations at RESEDA using the CASCADE detector. *Review of Scientific Instruments*, 82(2011):10–16, 2011. ISSN 00346748. doi: 10.1063/1.3571300.

[143] J. P. Kappler, M. J. Besnus, A. Herr, A. Meyer, and J. G. Sereni. Crossover between intermediate valence and magnetic order in Ce Rh 1-x Pd x. *Physica B: Condensed Matter*, 171:346–349, 1991. ISSN 0921-4526.

[144] J. G. Sereni, T. Westerkamp, R. Kuechler, N. Caroca-Canales, P. Gegenwart, and C. Geibel. Quantum Criticality in doped Ce Pd 1-x Rh x Ferromagnet. *arXiv:cond-mat*, page 11, February 2006. doi: 10.1103/PhysRevB.75.024432. URL http://arxiv.org/abs/cond-mat/0602588.

[145] L. B. Ioffe and J. Millis. Critical behavior of the uniform susceptibility of a Fermi liquid near an antiferromagnetic transition with dynamic exponent z = 2. *Physical Review B*, 51(22):151–158, 1995.

[146] A. P. Pikul, N. Caroca-Canales, M. Deppe, P. Gegenwart, J. G. Sereni, C. Geibel, and F. Steglich. Non-Fermi-liquid behaviour close to the disappearance of

ferromagnetism in Ce Pd 1-x Rh x. *Journal of Physics: Condensed Matter*, 18 (42):L535–L542, October 2006. ISSN 0953-8984. doi: 10.1088/0953-8984/18/42/L01. URL http://stacks.iop.org/0953-8984/18/i=42/a=L01?key=crossref.4148ec8d1cc6a67488bbb52f32985a43.

[147] A. H. Castro Neto, G. Castilla, and B. A. Jones. Non-Fermi Liquid Behavior and Griffiths Phase in f -Electron Compounds. *Physical Review Letters*, 81(16): 3531–3534, 1998.

[148] A. H. Castro Neto and B. A. Jones. Non-Fermi-liquid behavior in U and Ce alloys: Criticality, disorder, dissipation, and Griffiths-McCoy singularities. *Physical Review B*, 62(22):14975–15011, 2000. ISSN 1550-235X.

[149] A. H. Castro Neto and B. A. Jones. Quantum Griffiths effects in metallic systems. *Europhysics Letters*, 71:790, 2005.

[150] Rastko Sknepnek and Thomas Vojta. Smeared phase transition in a three-dimensional Ising model with planar defects: Monte Carlo simulations. *Physical Review B - Condensed Matter and Materials Physics*, 69(17):1–9, 2004. ISSN 01631829. doi: 10.1103/PhysRevB.69.174410.

[151] V. Dobrosavljevic and E. Miranda. Absence of conventional quantum phase transitions in itinerant systems with disorder. *Physical Review Letters*, 94(18): 187203, 2005. ISSN 1079-7114.

[152] B. T. Matthias and R. M. Bozorth. Ferromagnetism of a zirconium-zinc compound. *Physical Review*, 109(2):604–605, 1958. ISSN 0031899X. doi: 10.1103/PhysRev.109.604.

[153] S. Foner, E. J. McNiff Jr., and V. Sadagopan. Magnetic Moment of ZrZn2 up to 150 kG: is "Pure" ZrZn2 Ferromagnetic? *Physical Review Letters*, 19 (21):1233–1236, 1967. URL http://journals.aps.org/prl/abstract/10.1103/PhysRevLett.19.1233.

[154] E. P. Wohlfarth. Very Weak Itinerant Ferromagnets; Application to ZrZn2. *Journal of Applied Physics*, 39(2):1061, 1968. ISSN 00218979. doi: 10.1063/1.1656163. URL http://scitation.aip.org/content/aip/journal/jap/39/2/10.1063/1.1656163.

[155] R. C. Wayne and L. R. Edwards. Effect of Pressure on the Curie Temperature of ZrZn2. *Physical Review*, 348, 1969. URL http://journals.aps.org/pr/abstract/10.1103/PhysRev.188.1042.

[156] E. P. Wohlfarth. The Theoretical and Experimental Status of the Collective Electron Theory of Ferromagnetism. *Reviews of Modern Physics*, 25(1), 1953.

[157] R. Viswanathan. Magnetic entropy of ZrZn2. *Journal of Physics F: Metal Physics*, 57:4–6, 1974. URL http://iopscience.iop.org/0305-4608/4/3/004.

[158] S. Ogawa. Electrical resistivity of weak itinerant ferromagnet ZrZn2. *Journal of the Physical Society of Japan*, 1976. URL http://journals.jps.jp/doi/abs/10.1143/JPSJ.40.1007.

[159] P. G. Mattocks and A. E. Dixon. De Haas-van Alphen oscillations in a single crystal of ZrZn2. *Journal of Physics F: Metal Physics*, 147, 1981. ISSN 03054608. doi: 10.1088/0305-4608/11/7/003. URL http://iopscience.iop.org/0305-4608/11/7/003.

[160] J. Inoue and M. Shimizu. Effect of spin fluctuations on the pressure dependence of the Curie temperature. *Physics Letters A*, 112(1):81–84, 1985. URL http://www.sciencedirect.com/science/article/pii/0375960185904712.

[161] N. R. Bernhoeft and S. A. Law. Magnetic excitations in ZrZn2 at low energies and long wavelengths. *Physica Scripta*, 191, 1988. URL http://iopscience.iop.org/1402-4896/38/2/015.

[162] S. Ogawa. Effect of alloying of Ti, Y, Nb and Hf on the band ferromagnetism in ZrZn2. *Physics Letters A*, 25(7):2–3, 1967. URL http://www.sciencedirect.com/science/article/pii/0375960167900187.

[163] S. Ogawa. Magnetic Properties of Zr 1-x Ti x Zn 2, Zr 1-x Y x Zn 2, Zr 1-x Nb x Zn 2 and Zr 1-x Hf x Zn 2. *Journal of the Physical Society of Japan*, 25(1), 1968.

[164] A. Arrott. Criterion for ferromagnetism from observations of magnetic isotherms. *Physical Review*, 108(6):1394–1396, 1957. ISSN 0031899X. doi: 10.1103/PhysRev.108.1394.

[165] Marc Philipp Uhlarz. *Magnetisierung von ZrZn2 unter hohem Druck*. PhD thesis, Universität Karlsruhe, 2004.

[166] B. Binz, H. Braun, T. Rice, and M. Sigrist. Magnetic Domain Formation in Itinerant Metamagnets. *Physical Review Letters*, 96(19):196406, May 2006. ISSN 0031-9007. doi: 10.1103/PhysRevLett.96.196406. URL http://link.aps.org/doi/10.1103/PhysRevLett.96.196406.

[167] C. Pfleiderer, D. Reznik, L. Pintschovius, H. v. Löhneysen, M. Garst, and A. Rosch. Partial order in the non-Fermi-liquid phase of MnSi. *Nature*, 427, 2004.

[168] J. O. Strom-Olsen, D. F. Wilford, S. K. Burke, and B. D. Rainford. The coexistence of spin density wave ordering and spin glass ordering in chromium

alloys containing iron. *Journal of Physics F: Metal Physics*, 9(5):L95–L98, 1979. ISSN 0305-4608. doi: 10.1088/0305-4608/9/5/002.

[169] Z. Barak and M. B. Walker. The effect of uniaxial compressive stress on the Neel transition in chromium. *Journal of Physics F: Metal Physics*, 12:483–495, 1981. ISSN 0305-4608. doi: 10.1088/0305-4608/14/5/021.

[170] ESS. ESS Website, 2014. URL http://www.europeanspallationsource.se.

[171] J. R. Santisteban, L. Edwards, M. E. Fitzpatrick, A. Steuwer, P. J. Withers, M. R. Daymond, M. W. Johnson, N. Rhodes, and E. M. Schooneveld. Strain imaging by Bragg edge neutron transmission. *Nuclear Instruments and Methods in Physics Research Section A: Accelerators, Spectrometers, Detectors and Associated Equipment*, 481(1-3):765–768, April 2002. ISSN 01689002. doi: 10.1016/S0168-9002(01)01256-6. URL http://www.sciencedirect.com/science/article/pii/S0168900201012566.

[172] J. R. Santisteban, L. Edwards, M. E. Fizpatrick, A. Steuwer, and P. J. Withers. Engineering applications of Bragg-edge neutron transmission. *Applied Physics A: Materials Science & Processing*, 74:s1433–s1436, December 2002. ISSN 0947-8396. doi: 10.1007/s003390101241. URL http://link.springer.com/10.1007/s003390101241.

[173] A. Steuwer, P. J. Withers, J. R. Santisteban, and L. Edwards. Using pulsed neutron transmission for crystalline phase imaging and analysis. *Journal of Applied Physics*, 97(7):074903, March 2005. ISSN 00218979. doi: 10.1063/1.1861144. URL http://scitation.aip.org/content/aip/journal/jap/97/7/10.1063/1.1861144.

[174] Michael Schulz, Peter Böni, Elbio Calzada, Martin Mühlbauer, Andreas Neubauer, and Burkhard Schillinger. A polarizing neutron periscope for neutron imaging. *Nuclear Instruments and Methods in Physics Research Section A: Accelerators, Spectrometers, Detectors and Associated Equipment*, 605(1-2):43–46, June 2009. ISSN 01689002. doi: 10.1016/j.nima.2009.01.125. URL http://linkinghub.elsevier.com/retrieve/pii/S0168900209002423.

[175] ISIS. ISIS Website, 2015. URL http://www.isis.stfc.ac.uk.

[176] SNS. SNS Website, 2014. URL http://neutrons.ornl.gov/facilities/SNS/.

[177] JPARC. JPARC Website, 2015. URL http://www.j-parc.jp/index-e.html.

[178] F. Mezei, M. Russina, and Gy. Kali. Time-of-Flight Neutron Diffraction for Long Pulse Neutron Sources. *Neutron News*, 23(1):29–31, January 2012. ISSN 1044-8632. doi: 10.1080/10448632.2012.645686. URL http://www.tandfonline.com/doi/abs/10.1080/10448632.2012.645686#.VJb0Tv_GUFA.

[179] Ferenc Mezei. Multiplexing Chopper Systems for Pulsed Neutron Sources: Practical Basics. *Journal of the Physical Society of Japan*, 82(Suppl.A):SA025, January 2013. ISSN 0031-9015. doi: 10.7566/JPSJS.82SA.SA025. URL http://journals.jps.jp/doi/10.7566/JPSJS.82SA.SA025.

[180] M. Strobl. Future prospects of imaging at spallation neutron sources. *Nuclear Instruments and Methods in Physics Research Section A: Accelerators, Spectrometers, Detectors and Associated Equipment*, 604(3):646–652, June 2009. ISSN 01689002. doi: 10.1016/j.nima.2009.03.075. URL http://www.sciencedirect.com/science/article/pii/S0168900209005300http://linkinghub.elsevier.com/retrieve/pii/S0168900209005300.

[181] M. Strobl, M. Bulat, and K. Habicht. The wavelength frame multiplication chopper system for the ESS test beamline at the BER II reactorâĂŤA concept study of a fundamental ESS instrument principle. *Nuclear Instruments and Methods in Physics Research Section A: Accelerators, Spectrometers, Detectors and Associated Equipment*, 705:74–84, March 2013. ISSN 01689002. doi: 10.1016/j.nima.2012.11.190. URL http://www.sciencedirect.com/science/article/pii/S0168900212016142http://linkinghub.elsevier.com/retrieve/pii/S0168900212016142.

[182] M. Russina, Gy. Káli, Zs. Sánta, and F. Mezei. First experimental implementation of pulse shaping for neutron diffraction on pulsed sources. *Nuclear Instruments and Methods in Physics Research Section A: Accelerators, Spectrometers, Detectors and Associated Equipment*, 654(1):383–389, October 2011. ISSN 01689002. doi: 10.1016/j.nima.2011.05.077. URL http://www.sciencedirect.com/science/article/pii/S0168900211011673http://linkinghub.elsevier.com/retrieve/pii/S0168900211011673.

[183] M. Russina, F. Mezei, and G. Kali. First Implementation of Novel Multiplexing Techniques for Advanced Instruments at Pulsed Neutron Sources. In *Journal of Physics: Conference Series*, volume 340, page 012018, February 2012. doi: 10.1088/1742-6596/340/1/012018. URL http://stacks.iop.org/1742-6596/340/i=1/a=012018?key=crossref.da9a164cfd809ea1402f2cc99eb3547chttp://stacks.iop.org/1742-6596/340/i=1/a=012018.

[184] A. A. van Well. Double-disk chopper for neutron time-of-flight experiments. *Physica B: Condensed Matter*, 180-181:959–961, 1992. ISSN 09214526. doi: 10.1016/0921-4526(92)90521-S.

[185] BIOREF. HZB BioRef, 2015. URL http://www.helmholtz-berlin.de/user/experimental-infrastructures/instruments-neutrons/index_en.html.

[186] AMOR. SINQ AMOR, 2015. URL http://www.psi.ch/sinq/amor/.

[187] FIGARO. FIGARO Website, 2015. URL https://www.ill.eu/instruments-support/instruments-groups/instruments/figaro/.

[188] D33. ILL Website, 2015. URL https://www.ill.eu/instruments-support/instruments-groups/instruments/d33/.

[189] REFSANS. Website, 2015. URL http://www.mlz-garching.de/instrumente/nanostrukturen/refsans.html.

[190] McStas. McStas Website, 2014. URL http://www.mcstas.org.

[191] A. P. Kaestner, S. Hartmann, G. Kühne, G. Frei, C. Grünzweig, L. Josic, F. Schmid, and E. H. Lehmann. The ICON beamline - A facility for cold neutron imaging at SINQ. *Nuclear Instruments and Methods in Physics Research Section A: Accelerators, Spectrometers, Detectors and Associated Equipment*, 659(1):387–393, December 2011. ISSN 01689002. doi: 10.1016/j.nima.2011.08.022. URL http://www.sciencedirect.com/science/article/pii/S0168900211016044http://linkinghub.elsevier.com/retrieve/pii/S0168900211016044.

[192] N. Kardjilov, a. Hilger, I. Manke, M. Strobl, M. Dawson, S. Williams, and J. Banhart. Neutron tomography instrument CONRAD at HZB. *Nuclear Instruments and Methods in Physics Research Section A: Accelerators, Spectrometers, Detectors and Associated Equipment*, 651(1):47–52, September 2011. ISSN 01689002. doi: 10.1016/j.nima.2011.01.067. URL http://linkinghub.elsevier.com/retrieve/pii/S0168900211001458http://www.sciencedirect.com/science/article/pii/S0168900211001458.

[193] A. Hilger, N. Kardjilov, I. Manke, C. Zendler, K. Lieutenant, K. Habicht, J. Banhart, and M. Strobl. Neutron guide optimisation for a time-of-flight neutron imaging instrument at the European Spallation Source. *Optics Express*, 23(1):301–311, 2015. doi: 10.1364/OE.23.000301.

[194] Marc Seifert. *Optimisation of a WFM Chopper system for the imaging instrument ODIN at the ESS*. Bachelor thesis, Technische Universität München, 2013.

[195] Ferenc Mezei. ESS Update Report, vol. III, Instruments and Scientific Utilisation. Technical report, European Spallation Source, 2006.

[196] C. Zendler, K. Lieutenant, D. Nekrassov, L.D. Cussen, and M. Strobl. Bi-spectral beam extraction in combination with a focusing feeder. *Nuclear Instruments and Methods in Physics Research Section A: Accelerators, Spectrometers, Detectors and Associated Equipment*, 704:68–75, March 2013. ISSN 01689002. doi: 10.1016/j.nima.2012.11.180. URL http:

//linkinghub.elsevier.com/retrieve/pii/S0168900212015276http://www.sciencedirect.com/science/article/pii/S0168900212015276.

[197] P. Schmakat, M. Seifert, M. Schulz, P. Böni, and M. Strobl. Wavelength frame multiplication chopper system for the multi-purpose imaging beamline ODIN at the European Spallation Source. *In Preparation*, 2015.

[198] P. Schmakat, M. Wagner, R. Ritz, A. Bauer, M. Brando, M. Deppe, W. Duncan, C. Duvinage, C. Franz, C. Geibel, F.M. Grosche, M. Hirschberger, K. Hradil, M. Meven, A. Neubauer, M. Schulz, A. Senyshyn, S. Süllow, B. Pedersen, P. Böni, and C. Pfleiderer. Spin dynamics and spin freezing at ferromagnetic quantum phase transitions. *The European Physical Journal Special Topics*, 224 (6):1041–1060, 2015. ISSN 1951-6355. doi: 10.1140/epjst/e2015-02445-4. URL http://link.springer.com/10.1140/epjst/e2015-02445-4.

[199] F. Kargl, M. Engelhardt, F. Yang, H. Weis, P. Schmakat, B. Schillinger, A. Griesche, and A. Meyer. In situ studies of mass transport in liquid alloys by means of neutron radiography. *Journal of physics. Condensed matter : an Institute of Physics journal*, 23(25):254201, 2011. ISSN 0953-8984. doi: 10.1088/0953-8984/23/25/254201.

Acknowledgements

Ich möchte allen Menschen die zur Entstehung dieser Arbeit beigetragen haben ganz herzlich danken. Falls ich jemanden vergessen habe, gilt auch ihm/ihr mein bester Dank!

Peter Böni Lieber Peter, ich danke Dir vielmals für die wunderbare Zeit am (besten) Lehrstuhl (der Welt) E21 und für Deine Unterstützung die zu dieser Arbeit geführt hat. Ich wünsche Dir weiterhin Alles Gute, insbesondere Gesundheit!

Christian Pfleiderer Lieber Christian, auch Dir meinen besten Dank für die tatkräftige Unterstützung bei meiner Arbeit. Ohne Dich wäre es nur halb so spannend und nur halb so schön gewesen!

Markus Strobl Lieber Markus, ich danke Dir sehr für die tatkräftige Unterstützung und unsere gute Zusammenarbeit. Durch Dich habe ich Einblick in ein sehr spannendes Grossforschungsprojekt bekommen. Ich bin davon überzeugt, dass ODIN an der ESS ein sehr erfolgreiches Instrument wird.

Gerhard Schmakat Mein lieber Vater, der mich stets aufgemuntert, unterstützt, mit besten Mahlzeiten versorgt und damit aus den Tiefs während dieser Arbeit geholt hat. Ich danke Dir für Alles!

Brigitte Schmakat Meine liebe Mutter, die mich ebenfalls stets unterstützt und aufgemuntert hat. Ohne Dich wäre ich niemals so weit gekommen und ich danke Dir für Alles!

Heiner Kolb, Peter Biber, Jürgen Peters Dem Team der Probenumgebung des FRM II danke ich für die vielen investierten Stunden um die Kryostaten zum laufen zu bringen. Heiner... Danke für deine Lektionen!

Marc Seifert Meinem Padawan, den ich bereits während seiner Bachelorarbeit betreute und nun bei der Masterarbeit betreue, danke ich sehr für die tatkräftige Unterstützung und unsere gute Zusammenarbeit.

Stefan Mayerhofer Meinem zweiten Padawan, den ich während seiner Bachelorarbeit betreute, danke ich sehr für die tatkräftige Unterstützung und unsere gute Zusammenarbeit.

Michael Schulz Meinem früheren Jedimeister danke ich für eine grossartige Zeit in der ich in Forschungsfeldern tätig war, dass ich erst durch ihn kennen und schätzen gelernt habe.

Tommy Reimann danke ich einfach so, weil er ein feiner Kerl ist und für hilfreiche Diskussionen und für seinen Magneten und überhaupt!

Lehrstuhl E21/E51 Dem besten Lehrstuhl der Welt danke ich für eine absolut fantastische Zeit die ich niemals missen möchte. Keep the spirit!

ANTARES Team Dem Team von ANTARES danke ich für eine tolle Zusammenarbeit. Dominik, es war eine Meisterleistung das Instrument auf den derzeitigen Stand zu bringen. Burkhard Schillinger danke ich für die unkomplizierte Organisation vieler Messzeiten.

MIRA Team Dem Team von MIRA danke ich für hervorragende Organisation und Betreuung meiner Experimente. Insbesondere Robert Georgii und Reinhard Schwikowski gilt mein Dank!

POLI Team Dem Team von POLI, insbesondere Vladimir Hutanu und Wolfgang Luberstetter meinen besonderen Dank für die Unterstützung meiner Testmessungen am POLI.

Georg Brandl Dem grossen Guru des mächtigen Python meinen umfassenden Dank für die Rettung so mancher Messzeit durch seinen spontanen Eingriff in die Matrix!?

Alex Lenz, Jörg Pulz, Jens Krüger Meinen besten Dank für die tatkräftige Unterstützung bei der Lösung software-technischer Probleme.

Werkstätten Den Werkstätten am FRM II und am Physik-Department danke ich ganz herzlich für eine saubere Arbeit. Dank Euch sind die Experimente in dieser Arbeit erst möglich geworden.

BBQ Gang Meiner Grillbande einen ewigen Dank für die wiederbelebenden Gourmet-Grillsamstage im Hirschgarten!

A. Appendix

A.1. ODIN Chopper Positions, Dimensions and Frequencies

chopper	position z
T0	9.0 m
BP	11.86 m
WFMC 1	6.5 m
WFMC 2	7.0 m
FOC 1	8.5 m
FOC 2	11.84 m
FOC 3	16.49 m
FOC 4	22.97 m
FOC 5	32.0 m

Table A.1.: Positions of the chopper discs, measured from the centre of the source.

chopper	outer radius r
T0	0.3 m
BP	0.4 m
WFMC 1	0.35 m
WFMC 2	0.35 m
FOC 1	0.4 m
FOC 2	0.5 m
FOC 3	0.6 m
FOC 4	0.9 m
FOC 5	0.9 m

Table A.2.: Outer radii of the chopper discs including the height of the window.

chopper	window height h
T0	0.09 m
BP	0.08 m
WFMC 1	0.07 m
WFMC 2	0.07 m
FOC 1	0.08 m
FOC 2	0.10 m
FOC 3	0.11 m
FOC 4	0.11 m
FOC 5	0.11 m

Table A.3.: Height of the chopper windows, measured from the outer radius.

chopper	frequency $f = \omega/2\pi$
T0	$2 \cdot f_{ESS} = 28$ Hz
BP	$1.5 \cdot f_{ESS} = 21$ Hz (six frames)
	$3 \cdot f_{ESS} = 42$ Hz (three frames)
WFMC 1	$4 \cdot f_{ESS} = 56$ Hz
WFMC 2	$4 \cdot f_{ESS} = 56$ Hz
FOC 1	$3 \cdot f_{ESS} = 42$ Hz
FOC 2	$3 \cdot f_{ESS} = 42$ Hz
FOC 3	$2 \cdot f_{ESS} = 28$ Hz
FOC 4	$1 \cdot f_{ESS} = 14$ Hz
FOC 5	$1 \cdot f_{ESS} = 14$ Hz

Table A.4.: Frequencies of the chopper discs.

A.2. ODIN Chopper Opening Windows and Phases

Chopper	T0	BP
θ	310.86°	127.7°
ϕ	195.07°	95.0°

Table A.5.: Opening angle θ and phase ϕ for the T0 and the BP chopper.

WFMC1	frame N=1	2	3	4	5	6
θ_{calc}	6.48°	10.14°	13.53°	16.69°	19.61°	22.33°
θ_{opt}	6.48°	10.14°	13.53°	16.69°	19.61°	21.88°
ϕ_{calc}	90.16°	139.51°	185.33°	227.87°	267.38°	304.07°
ϕ_{opt}	90.16°	139.51°	185.33°	227.87°	267.38°	304.29°

Table A.6.: Chopper angles for WFMC1 as calculated and after the optimisation. Only the last frame $N = 6$ was slightly changed due to an undesired wavelength contamination.

WFMC2	frame N=1	2	3	4	5	6
$\theta_{calc} = \theta_{opt}$	6.48°	10.14°	13.53°	16.69°	19.61°	22.33°
$\phi_{calc} = \phi_{opt}$	96.64°	149.65°	198.86°	244.56°	287.00°	326.40°

Table A.7.: The chopper angles for WFMC2 were used as calculated.

FOC1	frame N=1	2	3	4	5	6
θ_{calc}	13.72°	15.83°	17.79°	19.61°	21.29°	22.86°
θ_{opt}	13.72°	15.83°	17.79°	19.61°	19.80°	20.12°
ϕ_{calc}	82.64°	130.94°	175.78°	217.42°	256.08°	291.98°
ϕ_{opt}	82.64°	130.94°	175.78°	217.42°	256.83°	293.36°

Table A.8.: Chopper angles for FOC1 as calculated and after the optimisation.

FOC2	frame N=1	2	3	4	5	6
θ_{calc}	33.44°	34.14°	34.79°	35.40°	35.96°	36.48°
θ_{opt}	33.44°	34.14°	34.79°	35.40°	34.16°	34.65°
ϕ_{calc}	105.27°	172.58°	235.08°	293.12°	347.01°	397.05°
ϕ_{opt}	105.27°	172.58°	235.08°	293.12°	346.83°	397.14°

Table A.9.: Chopper angles for FOC2 as calculated and after the optimisation.

FOC3	frame N=1	2	3	4	5	6
θ_{calc}	40.60°	39.76°	38.98°	38.25°	37.58°	36.95°
θ_{opt}	40.60°	39.76°	38.98°	38.25°	36.45°	35.85°
ϕ_{calc}	91.18°	153.70°	211.76°	265.67°	315.73°	362.21°
ϕ_{opt}	91.18°	153.70°	211.76°	265.67°	315.17°	362.77°

Table A.10.: Chopper angles for FOC3 as calculated and after the optimisation.

FOC4	frame N=1	2	3	4	5	6
θ_{calc}	33.05°	31.72°	30.49°	29.34°	28.27°	27.28°
θ_{opt}	33.05°	31.72°	30.49°	29.04°	27.42°	26.19°
ϕ_{calc}	60.22°	103.78°	144.23°	181.79°	216.67°	249.05°
ϕ_{opt}	60.22°	103.78°	144.23°	181.64°	216.24°	249.60°

Table A.11.: Chopper angles for FOC4 as calculated and after the optimisation.

FOC5	frame N=1	2	3	4	5	6
θ_{calc}	50.83°	48.23°	45.81°	43.57°	41.49°	39.55°
θ_{opt}	50.83°	48.23°	44.89°	41.39°	36.51°	36.78°
ϕ_{calc}	80.61°	141.31°	197.67°	250.01°	298.61°	343.74°
ϕ_{opt}	80.61°	141.31°	197.22°	249.36°	298.19°	345.12°

Table A.12.: Chopper angles for FOC5 as calculated and after the optimisation.